Durham E-Theses

Galvanomagnetic effects in antimony and doped antimony single crystals

Oktu, Ozcan

How to cite:

Use policy

GALVANOMAGNETIC EFFECTS IN ANTIMONY AND

DOPED ANTIMONY SINGLE CRYSTALS

A thesis submitted to the University

of Durham for the Degree of Doctor

of Philosophy

by

Özcan Öktü

Department of Applied Physics,

Science Laboratories,

South Road,

Durham.

September, 1967.

A B S T R A C T

The twelve components of the magnetoresistivity tensor in antimony up to second order in magnetic field have been measured at 273°K, 225°K, 183°K, 139°K and 77°K. Results are interpreted in terms of a two carrier, multi-valley band model to obtain carrier mobilities and densities as a function of temperature and details of the nature of the Fermi surface. In agreement with recent theoretical band structure calculations the electrons are shown to be sited in pockets with a small tilt angle (5°) away from the trigonal axis, while the extrema containing holes have a large tilt angle (24°). The temperature dependence of mobilities of electrons and holes are found to be $T^{-1.42}$ and $T^{-1.48}$ respectively. Carrier densities are almost independent of temperature, ranging from 3.9×10^{19} cm^{-3} at 77°K to 4.2×10^{19} cm^{-3} at 273°K for both electrons and holes.

The Seebeck coefficient of antimony can be interpreted by inserting the mobility data obtained in a two parabolic band model. Results suggest that the Fermi energies are equal to 0.098 eV for electrons and 0.067 eV for holes giving a band overlap energy of 0.165 eV. These energy parameters are essentially temperature independent between 77°K and room temperature, but increase markedly at higher temperatures. Holes probably occupy six and electrons three pockets.

Conductivities, Hall coefficients and some of the magnetoresistivity coefficients have been measured in tin-antimony alloys of compositions 1.7 at.%, 2.0 at.%, 2.5 at.% 3.0 at% and 8 at.% tin at $77^{O}K$, $183^{O}K$ and $273^{O}K$ to obtain further knowledge of the valence band structure. Results cannot be explained quantitatively by a simple tilted ellipsoidal band model, although they evidence that holes are to be assigned to the highly tilted ellipsoids.

A C K N O W L E D G M E N T S

CONTENTS

CHAPTER   I

The Crystal and Band Structure of Antimony

1.1.   Introduction

The group V elements bismuth, antimony and arsenic are semimetals. All have a rhombohedral crystal structure (space group R$\bar{3}$m) with two atoms in each unit cell. Thus, the first five Brillouin zones contain just enough states to be filled completely by the ten electrons in the unit cell. However, the fifth zone just overlaps the sixth; a small amount of electrons (in Sb about 10^{-3} per atom) spill over into the conduction band, leaving an equal number of holes in the valence band, see figure 1.1.   The small carrier density and resultant low Fermi energies of the electrons and the holes give these elements a relatively different character from metals: electrical conductivities are less, while Hall, magnetoresistivity and Seebeck coefficients are greater. For these reasons they are called semimetals. Both electron and hole effective masses are small and at the same order of magnitude; the Fermi level remains pinned near the middle of the band overlap at all temperatures below the melting point: carrier polulations are degenerate. These features of the semimetals dominate the transport properties, the main object of this work.

FIGURE 1.1
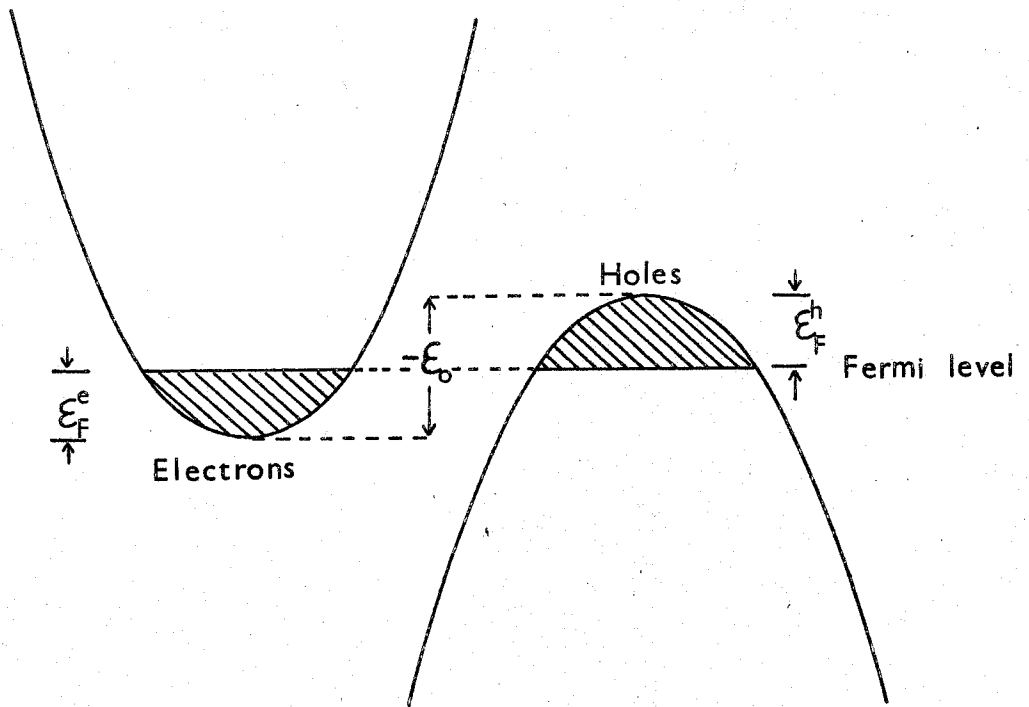
Schematic diagram of the electron and hole bands in
semimetals.   In antimony $-\mathcal{E}_o$ is about 0.2 eV.

To obtain details of carrier mobilities and densities and the band structure of antimony, the low field galvanomagnetic effects have been measured between $77^{O}K$ and $273^{O}K$. For quantitative assessment of the transport properties, a model of the Fermi surface is required in the solution of the Boltzmann equation. When the present studies were started, the band structure of antimony was a subject of controversy: although many experimental studies had indicated that the Fermi surface consists of two sets of ellipsoids, their number and arrangement in the Brillouin zone and in particular the true assignment of the electrons and the holes to these sets were not known. A three band model was also suggested. Because of this lack of knowledge experimental **data for room** temperature low field galvanomagnetic effects and thermoelectric power data (Saunders et al 1965) had not been fully explained.

During the progress of this work, a theoretical band structure calculation has been completed (Falicov and Lin 1966). Together with this theoretical work, experimental studies of the cyclotron resonance (Datars and Vanderkooy 1964) and the de Haas-Van Alphen effect in both pure (Windmiller and Priestley 1965) and tin and tellurium doped antimony (Ishizawa and Tanuma 1965) have established certain aspects of the band structure of antimony. These will be detailed in section 1.3. But further experimental evidence is desirable from which to assign the electrons and the holes to the correct sets of pockets, one aim of this work: experimental measurements of

the Hall coefficient and the Seebeck effect, both positive in
sign, should allow direct discrimination between the carriers.
In the present work the low field galvanomagnetic effects in
antimony have been explained by the band structure model
determined by Falicov and Lin (1966). The Seebeck coefficient
data is also explained using the carrier mobilities obtained
from the galvanomagnetic effects. Measurements of antimony-tin
alloys are also employed to give further evidence of the band
structure of antimony.

To analyse the galvanomagnetic effects, a model of the
Fermi surface must be assumed. Before discussion of this
model, the crystal structure and the Brillouin zone of the
group V semimetals will be described.

1.2   The Crystal Structure and Brillouin Zone

The group V semimetals bismuth, antimony and arsenic
all have the arsenic (A7) crystal structure, which is closely
related to the face centred cubic structure. The unit cell is
rhombohedral and contains two atoms. A rhombohedral lattice
can be constructed in a simple cubic structure so that each
cell contains two atoms, one at the corners and the other at the
body centre of the cell, figure 1.2.   In this case the
rhombohedral angle is 60°. The A7 structure can be obtained
from this cubic lattice by applying two independent distortions;
a shear and an internal displacement of the atoms. The shear

FIGURE 1.2
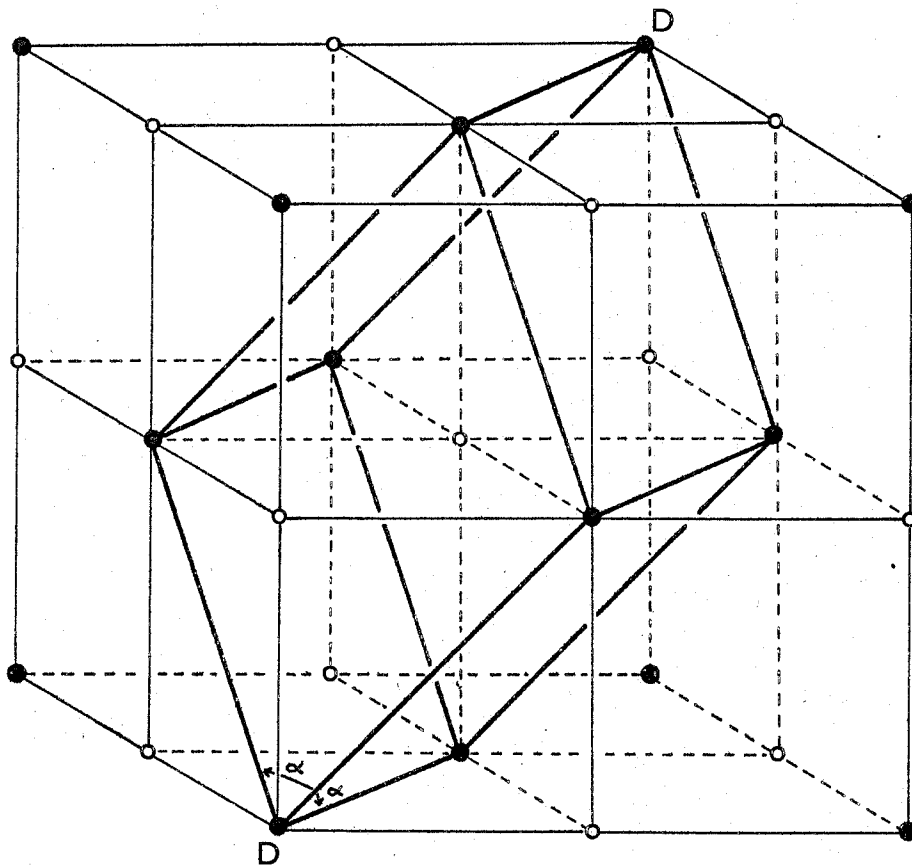
To construct the A7 structure: (i) apply a shear along
the body diagonal DD to reduce α and (ii) shift one of
the face centred lattices towards the other along the
sheared diagonal.

is applied along the body diagonal of the cube so that the rhombohedral angle α is reduced from 60° to the values shown, together with a parameter u, a measure of the internal displacement, in table 1.1.

Table 1.1.

Structure	α	u	ε
Simple cubic	60°	0.250	0
Bi	57° 14	0.237	0.0420
Sb	57° 14	0.234	0.0416
As	54° 10	0.226	0.0877

The internal displacement of the atoms can be visualised easily by considering the simple cubic structure as being composed of two interpenetrating face centered cubic lattices. If it is assumed that the shear along the body diagonal has already been applied, the face centred cubic lattices in fact form two face centred rhombohedral lattices. Then, the A7 structure is obtained by shifting one of these rhombohedral lattices towards the other along the sheared diagonal, which retains its symmetry and becomes the trigonal axis of the A7 structure. The parameter u is defined by

$$\underline{\tau} = u\underline{d} \quad ; \quad u \leq 1/4 \tag{1.1}$$

where $2\underline{\tau}$ is the smaller vector in the trigonal direction separating

the two interpretating lattices and $\underline{d}$ is the trigonal body
diagonal of one of the lattices. The value u = 1/4 corresponds
to that simple rhombohedral structure constructed in a simple
cubic lattice.

The rhombohedral primitive translation vectors of the
A7 structure can be expressed in the Cartesian co-ordinate system
formed by the cubic axes in the absence of shear. These are

$$\underline{a}_1 = a_o \{\varepsilon, \quad 1, \quad 1\}$$

$$\underline{a}_2 = a_o \{1, \quad \varepsilon, \quad 1\}$$

$$\underline{a}_3 = a_o \{1, \quad 1, \quad \varepsilon\} \tag{1.2}$$

where $\{\}$ indicates rectangular co-ordinates and ε is related
to the shear angle by

$$\varepsilon = \left[1 - (1 + \cos\alpha - 2 \cos^2\alpha)^{1/2} \right] / \cos\alpha$$

or $\cos\alpha = (1 + 2\varepsilon)/(2 + \varepsilon^2)$ (1.3)

The A7 structure retains some of the cubic symmetry
elements, including the trigonal axis along which the distor-
tion of the cubic system has taken place. In the cubic system
this axis has Miller indices $\begin{bmatrix} 111 \end{bmatrix}$. A stereographic projection
of the cubic system is shown in figure 1.3 and on which are
indicated the symmetry properties of antimony. The other
symmetry elements of the cubic system remaining after the dis-
tortion are the three binary axes perpendicular to the trigonal

FIGURE 1.3
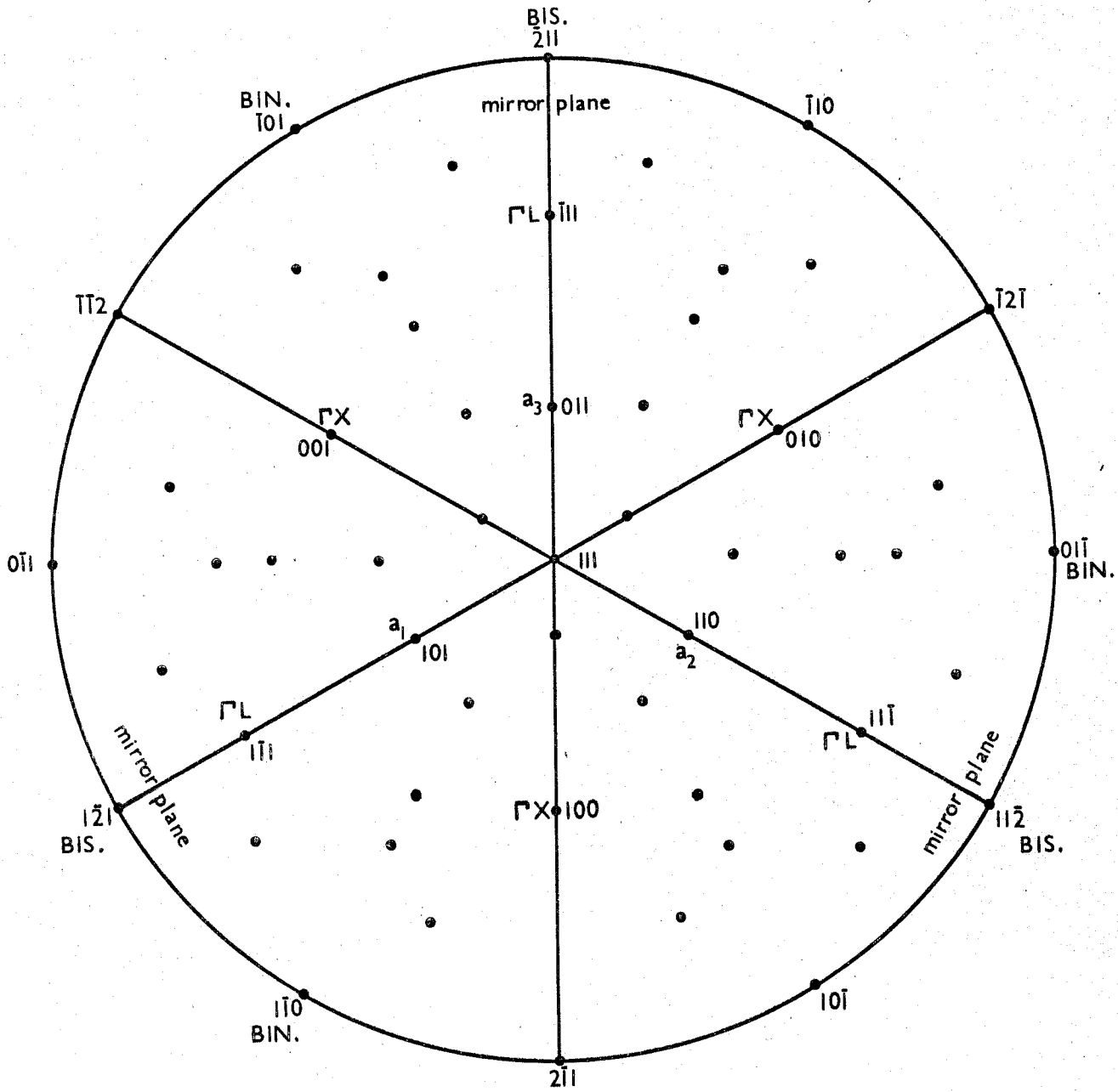
Standard (111) projection for cubic crystals showing those symmetry planes and directions used to describe the A7 structure

axis (in cubic indices $[1\bar{1}0]$, $[01\bar{1}]$, $[\bar{1}01]$) and three mirror
planes, containing the trigonal axis and perpendicular to the
binary axes, all are shown in figure 1.3. As α deviates from
60°, all the other symmetry elements of the cubic system lose
their symmetry although they retain some vestige of their
identity. For example, an X-ray photograph of antimony taken
along the direction corresponding to the $[100]$ direction of the
cubic system shows almost four-fold symmetry. Similarly the
$[11\bar{1}]$ direction has "pseudo-trigonal" symmetry. These two are
the interesting pseudo-symmetry elements of the A7 structure.
A set of X-ray photographs taken along the trigonal, the binary,
the bisectrix axes and these two pseudo-symmetry directions
are presented in figures 1.4. to 1.8.

The physical properties of group V semimetals are
usually referred to a right handed Cartesian co-ordinate system,
see figure 1.9., based on these symmetry elements. The (x)
and the (z) axes of the co-ordinate system are the binary and
the trigonal axes respectively of the crystal. The (y) axis,
called the bisectrix axis, is defined in the mirror plane to
form the right handed co-ordinate system. Since the binary
axis cannot be defined uniquely (figure 1.3), there are two
independent co-ordinate systems. However by means of the pseudo-
symmetry elements of the crystal, the two co-ordinate systems can
be distinguished. This will now be discussed particularly in
relation to the Brillouin zone which shows all these symmetry
elements of the A7 structure.

FIGURE 1.5 X-ray photograph taken along the binary axis.

FIGURE 1.4 X-ray photograph taken along the trigonal axis.

FIGURE 1.7 X-ray photograph taken
along the pseudo-trigonal direction.

FIGURE 1.6 X-ray photograph taken
along the bisectrix axis.

FIGURE 1.9   The relationship between lattice vectors $\underline{a}_1, \underline{a}_2$ and $\underline{a}_3$ of the rhombohedral unit cell and the Cartesian coordinate system defined by the binary bisectrics and trigonal axes.

FIGURE 1.8   X-ray photograph taken along the pseudo-fourfold symmetry direction.

Once the crystal structure is known, the Brillouin zone can be obtained by geometrical construction in k-space. The first Brillouin zone of the A7 structure with the symmetry points in standard notations is shown in figure 1.10.(Jones 1960). This can be considered as the Brillouin zone of the face centred cubic structure compressed along the trigonal direction ΓT. The square faces in the Brillouin zone of face centred cubic structure now became rectangular and the hexagonal faces not normal to the trigonal direction now have unequal adjacent sides. The faces normal to the trigonal axis remain hexagons. One of the mirror planes is exemplified by UTZLNXUΓ in the Brillouin zone. The binary ΓK, and the bisectrix ΓN, axes are also shown. ΓX and ΓL correspond to the pseudo-four fold and pseudo-three fold directions of the crystal structure respectively.

An important feature is that in the mirror plane rotation from the trigonal axis ΓT towards the bisectrix axis can be taken in one of the two senses, either through the point X or through the point L (Windmiller 1966). The ambiguity, arising from the fact that binary axes cannot be uniquely defined, can be resolved through consideration of the sense of this rotation. Thus, one rotational Cartesian co-ordinate system can be defined so that the rotation sense is that from the trigonal axis ΓT towards the bisectrix axis passing through ΓL. Equally the system could be defined in the sense passing through ΓX. In this work, the former definition is employed while Windmiller (1966) and Falicov and Lin (1966) used the latter. Once the Brillouin zone is known the band structure can be discussed and

FIGURE 1.11 Cross section of an
ellipsoid in the y-z plane.

FIGURE 1.10 The Brillouin zone of
antimony.

we now turn to this.

1.3.   The Band Structure:

The many studies of semimetals have shown that the
Fermi surface consists of a number of pieces in each band.
These pockets are located at equivalent points in the Brillouin
zone so that they have in total the same symmetry as the
reciprocal lattice. The Fermi surface of antimony consists of
two sets of closed, somewhat warped prolate ellipsoids, one which
corresponds to electrons, the other to holes. Development of
this model has followed from extensive experimental studies of
the de Haas-van Alphen effect (Shoenberg 1952, Saito 1964,
Windmiller and Priestley 1965, Ishizawa and Tanuma 1965), the
de Haas - Shubnikov effect (Ketterson and Eckstein 1963, Rao et
al 1964), the ultrasonic attenuation (Eriksson et al 1964), the
cyclotron resonance (Datars and Dexter 1961, Datars and Vanderkooy
1964), the infra-red absorption (Nanney 1963), and the low
field galvanomagnetic effects (Freedman and Juretschke 1961,
Epstein and Juretschke 1963). In particular the recent experi-
ments on the cyclotron resonance (Datars and Vanderkooy 1964)
and the de Haas-van Alphen effect (Windmiller and Priestly 1965
and Windmiller 1966) clearly show the presence of the two sets
of pockets.

The experimental information can be summarized in the
following way (Falicov and Lin 1966):

(i)   Both sets of pockets have at least binary or mirror
symmetry.

(ii)   Both sets of pockets are tilted in the trigonal-bisectrix plane, i.e. exemplified by UTZLNXUΓ   in figure 1.10. The de Haas-van Alphen data of Windmiller (1966) shows that one set gives a maximum area for a magnetic field direction of about 6.5^O from the trigonal axis in the quadrant containing ΓT, ΓL and ΓN (henceforth these will be described as the small tilt pockets), see figures 1.10 and 1.11. The other set gives a maximum area at a magnetic field direction of about 31° in the same quadrant (to be described as the large tilt pockets). But the pockets are not true ellipsoids: the directions of the minumum areas are 87.7^O and 52.6^O respectively in the adjacent quadrant containing ΓT, ΓX and ΓN. The deviation of pockets from ellipsoids is clear: for true ellipsoids the sum of the two angles of minimum and maximum area directions measured in the two adjacent quadrants would be equal to 90°, see figure 1.11.

(iii)   The ratio of the volumes between single pockets of small and large tilt angles is 2:1 within experimental error.

A theoretical calculation of the band structures of semimetals has been carried out by Cohen, Falicov and Golin (1964). Their calculation is based on the crystal structure and chemistry of group V elements and uses the pseudo-potential technique. More recently Falicov and Lin (1966) have completed the pseudo-potential calculations for antimony. Results show that the location of the holes is at or near the point T and that of the electrons should be at or close to the point L in the Brillouin zone. Group theoretical arguments (Falicov and Lin 1966)

have given the possible location, number and symmetry properties

of the pockets.   The holes can be located

(a) in a single pocket of symmetry $\bar{3}$m centred at T;

(b) in two equivalent pockets centred at Λ along the trigonal

axis (each pocket having a symmetry 3m and the net symmetry is

then $\bar{3}$ m):

(c) in six equivalent pockets, each of symmetry 2, centred at Q

along the binary axis;

(d) in six equivalent pockets, each of symmetry m, centred on

the mirror plane close to T;

(e) in twelve equivalent pockets of no symmetry at a general

point in the vicinity of T.

The electrons can be located

(A) in three equivalent pockets each of symmetry 2/m, centred

at the points L;

(B) in six equivalent pockets, each of symmetry 2, centred at Y

along the binary axis:

(C) in six equivalent pockets,each of symmetry m, centred on the

mirror plane near L;

(D) in twelve equivalent pockets of no symmetry at a general point

close to L.

From comparison of experimental and group theoretical

arguments, the Fermi surface of antimony has resulted. Possibilities

(e) and (D) which have no symmetry are eliminated by reference

to the experimental results. Furthermore, since the ratio of

the volumes of the single pockets of small and large tilt is 2:1,

the result is restricted to cases (A) for the electrons and
(c) or (d) for the holes. Thus, there should be six hole
pockets close to T each having either binary or mirror symmetry
and three electron pockets with 2/m symmetry centred at L .
This can only be true, if the holes are assigned to the large
tilt pockets and the electrons to the small tilt pockets. Thus,
because the number of electrons is equal to the number of holes,
in this model the volume of small tilt pockets must be twice
that of the large tilt pockets. Experimental evidence for this
predicted model of Falicov and Lin (1966) has been provided by
Ishizawa and Tanuma (1965). They find, when antimony is doped
with tin, a decrease in the period of the de Haas-van Alphen
oscillations corresponding to carriers in the large-tilt
pockets while the periods due to extrema with small tilt angle
increase. Tin doping introduces holes. Now the period of the
de Haas-van Alphen oscillations is related to the cross-sectional
area of the Fermi surface by

$$P = \frac{2 \pi e}{\hbar c A} \tag{1.4}$$

Therefore, since the cross-sectional area of the large tilt
angle pockets increases on tin doping, thus suggest that these
are the pockets containing holes. Further experimental evidence
of the placement of the carriers to the correct pockets arise from
the present work; the galvanomagnetic effects both in pure and
tin-doped crystals can only be explained by assigning the holes

to the large tilt pockets. Verification of this point is of some importance: it is contrary to previous assumption.

Previously the large-tilt ellipsoids, which were first observed by Shoenberg (1952), have been taken to contain electrons. If the large-tilt pockets are assumed to contain electrons, it is not possible to explain the low field galvanomagnetic effects (Juretschke et al 1961, 1963) and the Seebeck coefficient data of antimony (Saunders et al 1965) by the two band model. To explain the galvanomagnetic effects, with the assumption that Shoenberg carriers are electrons, Hall and Koenig (1964) had to postulate a three band model for antimony. Their model was based on the finding of heavy holes by a cyclotron resonance experiment (Datars and Dexter 1961). However in the later cyclotron resonance experiment by Datars and Vanderkooy (1964) and in the de Haas-van Alphen experiment of Windmiller (1966) there is no evidence of a third carrier.

From further theoretical procedures, Falicov and Lin (1966) have shown that the case (d) and not (c) correspond to the true structure for the hole pockets in antimony, i.e. there are six pockets of mirror symmetry located on the mirror planes, close to T. Their calculated, cross-section of the electron and the hole pockets in the mirror plane are reproduced in figures 1.12 and 1.13 respectively. The tilt angles shown on the figures correspond to the minimum and maximum area of the pockets and are compared in table 1.2. with the data of Windmiller (1966).

Electrons

t = $\overrightarrow{\Gamma T}$
x = $\overrightarrow{\Gamma X}$
l = $\overrightarrow{\Gamma L}$
bis = Bisectrix

t

x

l

bis

7°

2.5°

.05 au

L
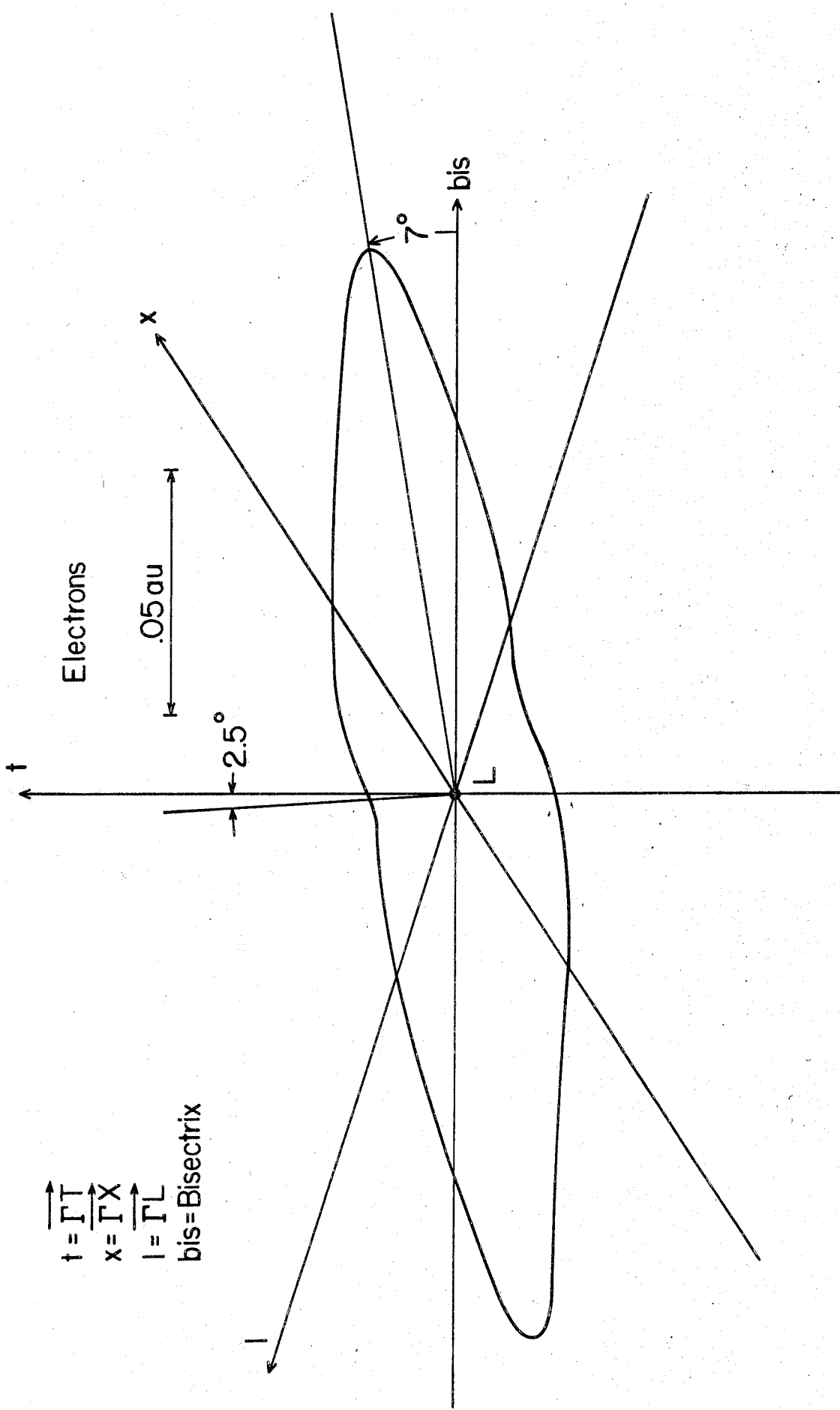
FIGURE 1.12   Calculated corss-section of electron
pockets in the mirror plane (Falicov and Lin 1966).

$t = \overrightarrow{\Gamma T}$
$x = \overrightarrow{\Gamma X}$
$l = \overrightarrow{\Gamma L}$

bis = Bisectrix

49°

bis

H

Holes

.05 au
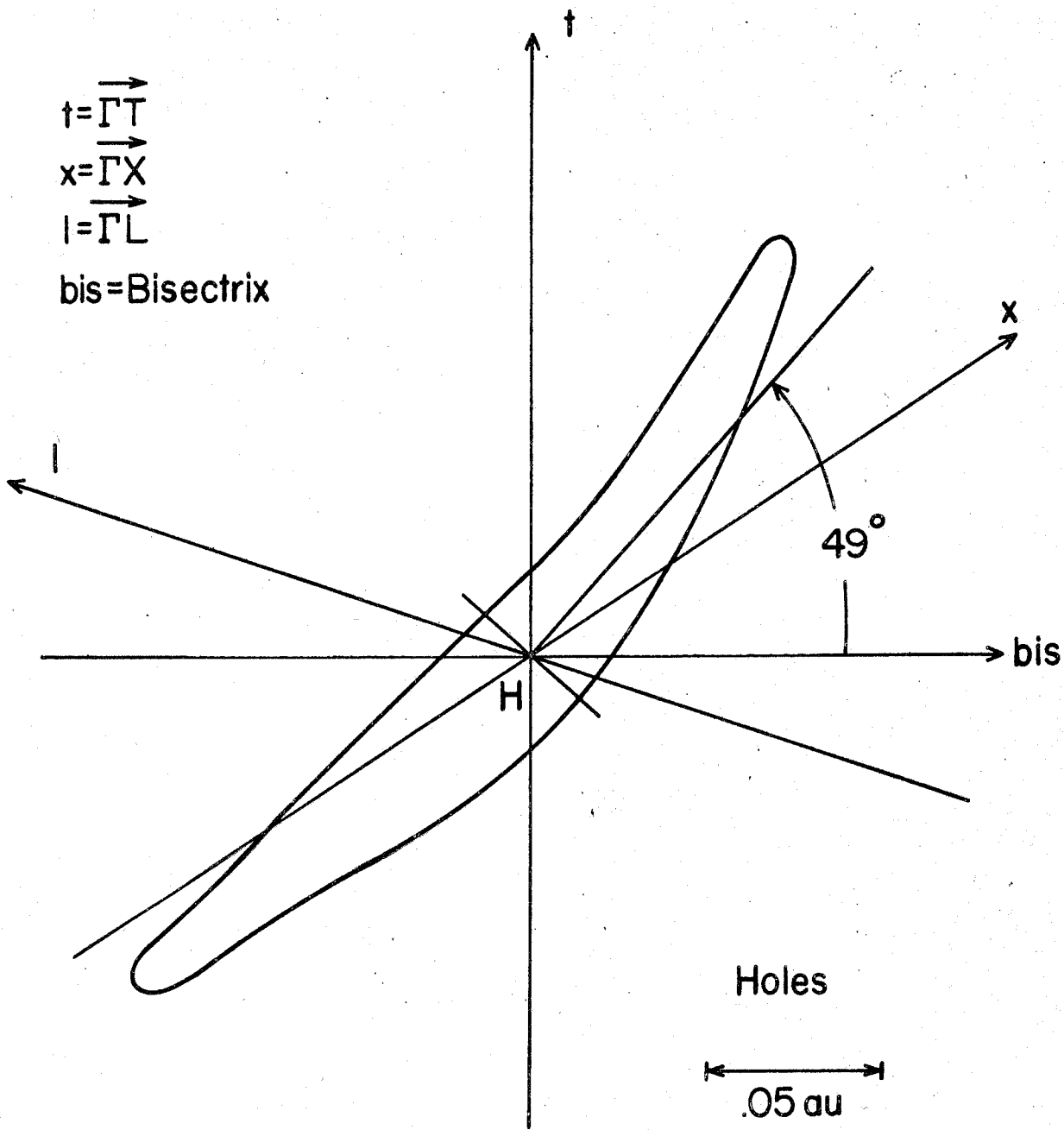
FIGURE 1.13   Calculated cross-section of hole pockets in the mirror plane (Falicov and Lin 1966)

Table 1.2.

The comparison of the calculated (Falicov and Lin 1966) and
measured (Windmiller 1966) tilt angles of the electron and the
hole pockets

	Electron		Hole	
	Exp.	The.	Exp.	The.
Tilt angle of max. area	$+6.5^{\circ}$	$+7^{\circ}$	31°	--
Tilt angle of min. area	-87.7°	-87.5°	-52.6°	-41°

Now to summarise the recent theoretical and experi-
mental predictions. The electron and the hole pockets, can both
be approximated to ellipsoids, this can be seen from figures
1.12 and 1.13, and lie in the sets of three trigonal-bisectrix
planes exemplified by ΓZLNUXΓ in the Brillouin zone. There
appear to be three electron ellipsoids located at points
L and six hole ellipsoids placed close to T. A further result
is that one principal axis of the ellipsoids is coincident with
the binary axis of the crystal, while the other two lie in the
mirror plane, figure 1.11. A photograph of a model of the
Fermi surface of antimony contructed in the Brillouin zone of the
face centred cubic crystal structure is shown in figure 1.14.

The two properties of antimony, the crystal and the
band structure essential for the discussion of the galvanomagnetic
effects in antimony have now been described. In the next chapter
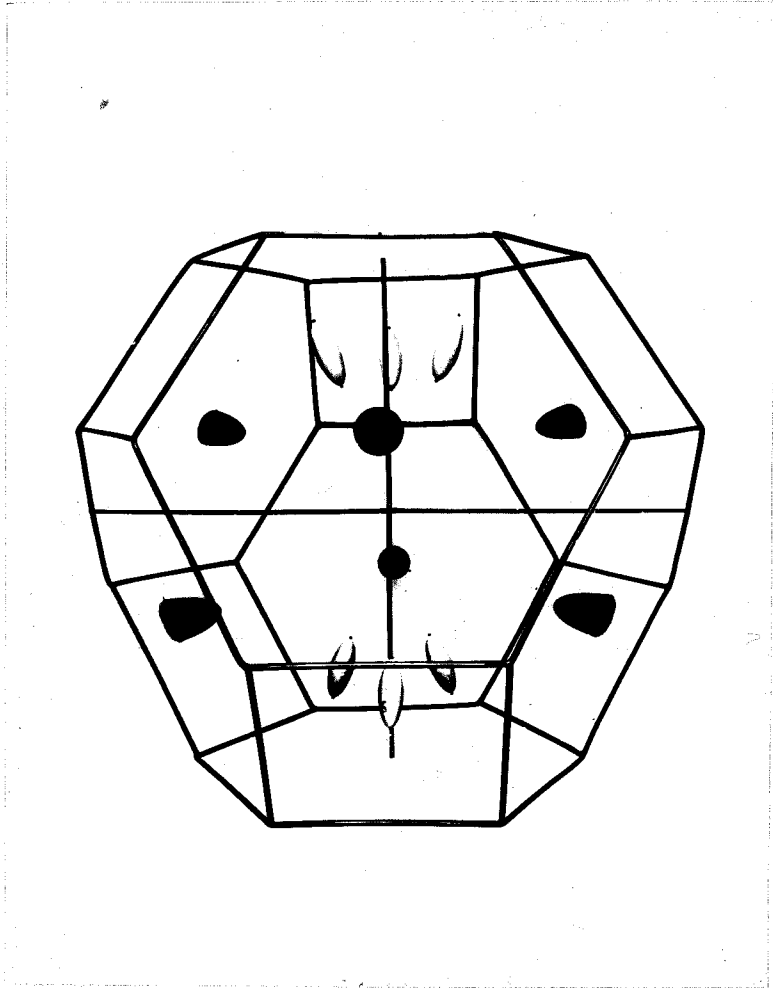
FIGURE 1.14 A model of the Fermi surface of
antimony. Dark surfaces contain electrons
and the others holes.

the theory of the galvanomagnetic effects, the basis of the

interpretation of the experimental data, is to be discussed.

CHAPTER II

The Theory of the Galvanomagnetic Effects

in Antimony.

2.1.   Introduction

Measurements of electrical resistivity, Hall coefficient
and magnetoresistivity provide basic information about the
conduction processes in solids. As a starting point, for an
isotropic solid the mobilities and carrier densities can be
derived for a simple band model composed of spherical energy
surfaces centred at $\underline{k} = 0$. Such a model does not apply for an
anisotropic material like antimony. Even many cubic semiconductors
have a complicated, multivalley band structure and show, for example,
a finite longitudinal magnetoresistance (see Putley 1960), which
on the simple model should be zero. Of course, this model is
useful for first analysis of transport data on new materials.

When the band structure is described by a multivalley
system with quadratic constant energy surfaces as in antimony,
the Boltzmann equation is to be solved to relate the galvano-
magnetic coefficients to the carrier mobilities and densities.
The procedure for solving the Boltzmann equation for a
multivalleyed band structure is developed in this chapter. But
before this discussion a description of the relationship between
crystal structure and galvanomagnetic effects is introduced in

the next section, followed by the experimental design used for measurement of the galvanomagnetic coefficients.

2.2.   Phenomenological Theory

In an anisotropic solid the relation between the current density $\underline{J}$, and applied electric field $\underline{E}$ involves a tensor, and in the Cartesian co-ordinate system it takes the form

$$J_i = \tilde{\sigma}_{ij} E_j \tag{2.1}$$

$$\text{or} \quad E_i = \rho_{ij} J_j \tag{2.2}$$

where $\tilde{\sigma}_{ij}$ and ρ_{ij} are called the conductivity and the resistivity tensors respectively, and repeated indices indicate summation over 1, 2, 3, i.e. $E_i = \rho_{ij} J_j = \sum_{j=1}^{3} \rho_{ij} J_j$. The number of independent tensor components depends upon the crystal structure and symmetry. For an uniaxial crystal, such as antimony, two components are needed to define the resistivity completely, one along (ρ_{33}) and the other perpendicular (ρ_{11}) to the trigonal axis. Thus

$$\rho_{ij} = \begin{vmatrix} \rho_{11} & 0 & 0 \\ 0 & \rho_{11} & 0 \\ 0 & 0 & \rho_{33} \end{vmatrix}$$

In a magnetic field $\underline{H}$, the components of the resistivity and conductivity tensors are general functions of $\underline{H}$ and Ohm's

law can be written as

$$J_i = \tilde{\sigma}_{ij} (\underline{H}) E_j \tag{2.3}$$

or $\qquad E_i = \rho_{ij} (\underline{H}) J_j \tag{2.4}$

$\tilde{\sigma}_{ij}(\underline{H})$ and $\rho_{ij}(\underline{H})$ are called magnetoconductivity and magneto-resistivity tensors respectively and obey the Onsager relation, i.e.

$$\tilde{\sigma}_{ij} (\underline{H}) = \tilde{\sigma}_{ji}(-\underline{H}) \quad \text{and} \quad \rho_{ij}(\underline{H}) = \rho_{ji}(-\underline{H}) \tag{2.5}$$

$\tilde{\sigma}_{ij}(\underline{H})$ and $\rho_{ij}(\underline{H})$ also are subject to the restrictions imposed by the crystal symmetry.

Any second-rank tensor can be devided into two parts; one (s_{ij}) is symmetrical and the second (a_{ij}) antisymetrical. Therefore, equation (2.4) can be written as

$$E_i = s_{ij}(\underline{H}) J_j + a_{ij}(\underline{H}) J_j \tag{2.6}$$

and $\qquad s_{ij} = 1/2 \ (\rho_{ij} + \rho_{ji}) = s_{ji},$

$$a_{ij} = 1/2 \ (\rho_{ij} - \rho_{ji}) = -a_{ji} \tag{2.7}$$

also hold. Then Onsager's relations can be written for $s_{ij}(\underline{H})$ and $a_{ij}(\underline{H})$ as

$$s_{ij}(\underline{H}) = s_{ij}(-\underline{H}) = s_{ji}(\underline{H})$$

$$a_{ij}(\underline{H}) = - a_{ij}(-\underline{H}) = - a_{ji}(\underline{H}) \qquad (2.8)$$

For low magnetic fields, when $\mu H \ll 1$, where μ is the carrier mobility, $s_{ij}(\underline{H})$ and $a_{ij}(\underline{H})$ can be expanded in terms of a rapidly converging series of increasing powers of the magnetic field H, i.e.

$$s_{ij}(\underline{H}) = \rho_{ij} + A_{ijkl} H_k H_l + F_{ijklmn} H_k H_l H_m H_n + ------;$$

$$a_{ij}(\underline{H}) = R_{ijk} H_k + T_{ijklm} H_k H_l H_m + -------. \qquad (2.9)$$

The coefficients ρ_{ij}, R_{ijk}, A_{ijkl} are called galvanomagnetic coefficients. In general, the coefficients of the antisymmetrical part of the magnetoresistivity tensor components, i.e. R_{ijk}, T_{ijklm}, etc., are called Hall, and coefficients of the symmetrical part, i.e. A_{ijkl}, F_{ijklmn}, etc., magnetoresistivity coefficients. They have the following symmetry relations (Juretschke 1955)

$$\rho_{ij} = \rho_{ji}$$

$$A_{ijkl} = A_{jikl} = A_{ij} \text{ (all permutations of k l)}$$

$$R_{ijk} = -R_{jik} \qquad (2.10)$$

$$T_{ijklm} = -T_{jiklm} = T_{ij} \text{ (all permutations of k l m)}$$

These symmetry relations reduce the number of independent

coefficients which also depend upon the crystal structure. For example, the explicit expression of $\rho_{\parallel}(\underline{H})$ up to H^2 is

$$\rho_{11}(\underline{H}) = \rho_{11} + R_{111}\,H_1 + R_{112}\,H_2 + R_{113}\,H_3 +$$

$$A_{1111}\,H_1^2 + A_{1122}\,H_2^2 + A_{1133}\,H_3^2 + A_{1112}\,H_1\,H_2 +$$

$$A_{1113}\,H_1\,H_3 + A_{1121}\,H_2\,H_1 + A_{1123}\,H_2\,H_3 +$$

$$A_{1131}\,H_3\,H_1 + A_{1132}\,H_3\,H_2.$$

This contains 13 coefficients. If the symmetry relations (2.10) are applied, i.e.

$$R_{111} = -R_{111} = 0 \quad \text{together with } R_{112} = R_{113} = 0$$

$$A_{1112} = A_{1121}$$

$$A_{1113} = A_{1131}$$

$$A_{1123} = A_{1132} ,$$

the number of independent coefficients reduces to seven. For a cubic system all but four coefficients vanish. The nonvanishing coefficients are ρ_{11}, A_{1111}, A_{1122} and A_{1133}, and furthermore cubic symmetry implies that A_{1122} equals to A_{1133}. Therefore, three constants are sufficient to express the magnetoresistivity tensor component $\rho_{11}(\underline{H})$. For the rhombohedral system (R$\bar{3}$m), two

of the seven coefficients vanish A_{1112} and A_{1113}, leaving five independent coefficients in $\rho_{11}(\underline{H})$.

Juretschke (1955) has detailed the results for the rhombohedral structure and gives the following expressions for all the magnetoresistivity tensor components, for terms up to second order in magnetic field:

$$\rho_{11}(\underline{H}) = \rho_{11} + A_{11}H_1^2 + A_{12}H_2^2 + A_{13}H_3^2 - 2A_{24}H_2H_3,$$

$$\rho_{22}(\underline{H}) = \rho_{11} + A_{12}H_1^2 + A_{11}H_2^2 + A_{13}H_3^2 + 2A_{24}H_2H_3,$$

$$\rho_{33}(\underline{H}) = \rho_{33} + A_{31}H_1^2 + A_{31}H_2^2 + A_{33}H_3^2, \qquad (2.11)$$

$$\rho_{23}(\underline{H}) = R_{231}H_1 - A_{42}H_1^2 + A_{42}H_2^2 + 2A_{44}H_2H_3,$$

$$\rho_{31}(\underline{H}) = R_{231}H_2 + 2A_{44}H_3H_1 - 2A_{42}H_1H_2,$$

$$\rho_{12}(\underline{H}) = R_{123}H_3 - 2A_{24}H_3H_1 + (A_{11} - A_{12})H_1H_2.$$

The remaining components of $\rho_{ij}(\underline{H})$ are obtainable from the Onsager relation $\rho_{ij}(H) = \rho_{ji}(-H)$. Antimony then has twelve independent, isothermal, galvanomagnetic coefficients to second order in the magnetic field, there being two resistivity components, ρ_{11} and ρ_{33}, two Hall coefficients R_{231} and R_{123}, taken as the negatives of the conventionally defined Hall coefficients, and eight magnetoresistance coefficients A_{11} (the short notation for $A_{11, 11}$) $A_{12}(A_{11, 22})$, $A_{13}(A_{11, 33})$, $A_{31}(A_{33, 11})$, $A_{44}(A_{23, 23})$,

$A_{24}(A_{22,23})$, $A_{33}(A_{33,33})$, and $A_{42}(A_{23,22})$. These coefficients are defined conveniently with respect to the usual orthogonal co-ordinate system described in the first chapter, having 1 along the binary (x-) axis, 2 along the bisectrix (y-) axis and 3 along the trigonal (z-) axis.

The magnetoresistivity coefficients are the experimentally measured quantities. However, theoretical calculations are more conveniently carried out in terms of the conductivity tensor. There is a complete correspondence between the magnetoresistivity and magnetoconductivity tensor components. In fact the same discussion just carried out for the magnetoresistivity tensor can be applied to the magnetoconductivity tensor, one being the reciprocal tensor of the other. Thus, magnetoconductivity tensor components can also be expanded in terms of increasing powers of H, i.e.

$$\widetilde{\sigma}_{ij}(\underline{H}) = \widetilde{\sigma}_{ij} - P_{ijk}H_k - B_{ijkl}H_kH_l - \ldots\ldots \qquad (2.12)$$

where $\widetilde{\sigma}_{ij}$ are the conductivity, P_{ijk} are Hall conductivity and B_{ijkl} are the magnetoconductivity coefficients. The reason why negative signs are used in the expansion (2.12) is as follows: the magnetoresistivity coefficients are positive (as they must be since the applied magnetic field increases the resistance) and thus the magnetoconductivity coefficients must be negative. But, because it is more convenient to deal with positive quantities, the expansion, in general, is represented in the above form (2.12) and the coefficients defined in this way

have positive signs.

One can relate the coefficients $\widetilde{\sigma}_{ij}$, P_{ijk}, B_{ijkl} to ρ_{ij}, R_{ijk}, A_{ijkl} by solving the equation

$$\widetilde{\sigma}_{ij}(\underline{H}) \; \rho_{ij}(\underline{H}) = \delta_{ij} \tag{2.13}$$

where δ_{ij} is the Kronecker delta, being equal to 1 for $i = j$ and zero for $i \neq j$. The calculations have been completed by Juretschke (1955) for the rhombohedral ($R\bar{3}m$) structure for terms up to second order in magnetic field. With the assumption that the expressions are in the form (2.9) and (2.12), the results are given by

$$\widetilde{\sigma}_{11} = \frac{1}{\rho_{11}}, \qquad \widetilde{\sigma}_{33} = \frac{1}{\rho_{33}}, \qquad P_{123} = \frac{R_{123}}{\rho^2_{11}}$$

$$P_{231} = \frac{R_{231}}{\rho_{11}\rho_{33}}, \qquad B_{11} = \frac{A_{11}}{\rho^2_{11}}, \qquad B_{33} = \frac{A_{33}}{\rho^2_{33}},$$

$$B_{24} = \frac{A_{24}}{\rho^2_{11}}, \qquad B_{42} = \frac{A_{42}}{\rho_{11}\rho_{33}}$$

$$B_{12} = \frac{A_{12}}{\rho^2_{11}} + \frac{R^2_{231}}{\rho^2_{11}\rho_{33}}, \qquad B_{13} = \frac{A_{13}}{\rho^2_{11}} + \frac{R^2_{123}}{\rho^3_{11}}$$

$$B_{31} = \frac{A_{31}}{\rho^2_{33}} + \frac{R^2_{231}}{\rho_{11}\rho^2_{33}}, \qquad B_{44} = \frac{A_{44}}{\rho_{11}\rho_{33}} - \frac{1}{2} \frac{R_{123} R_{231}}{\rho^2_{11} \rho_{33}} \tag{2.14}$$

These equations remain valid when ρ_{ij}, R_{ijk}, A_{ijkl} and $\widetilde{\sigma}_{ij}$, P_{ijk}, B_{ijk} are interchanged throughout.

In the present work, the twelve components of the resistivity tensor of antimony, have been measured as a function of temperature both in pure and tin doped single crystal specimens. In the following section the experimental configurations necessary for the measurements will be described.

2.3.   Design of Experiments

Different experimental configurations have been employed by various workers to measure the low field galvanomagnetic coefficients in antimony and bismuth. In the present work, the experimental configuration is based upon those described by Epstein and Juretschke (1963) who obtained all the 12 coefficients at room temperature from two differently orientated, long single crystal rods with rectangular cross-section. The two convenient sample orientations are, one having the trigonal axis perpendicular (90° orientation) and the other having the trigonal axis parallel (0° orientation) to the rod axis. The rod axis of the sample determines the current direction and the measured galvanomagnetic fields are either parallel or perpendicular to this axis. The magnetic field direction is fixed and the specimens are rotated about the vertical axis (see figure 2.1). All the twelve coefficients can be obtained from the following three sets of measurements

(1)   The first set of measurements

A 90° – specimen is placed in the magnetic field $\underline{H}$

FIGURE 2.1
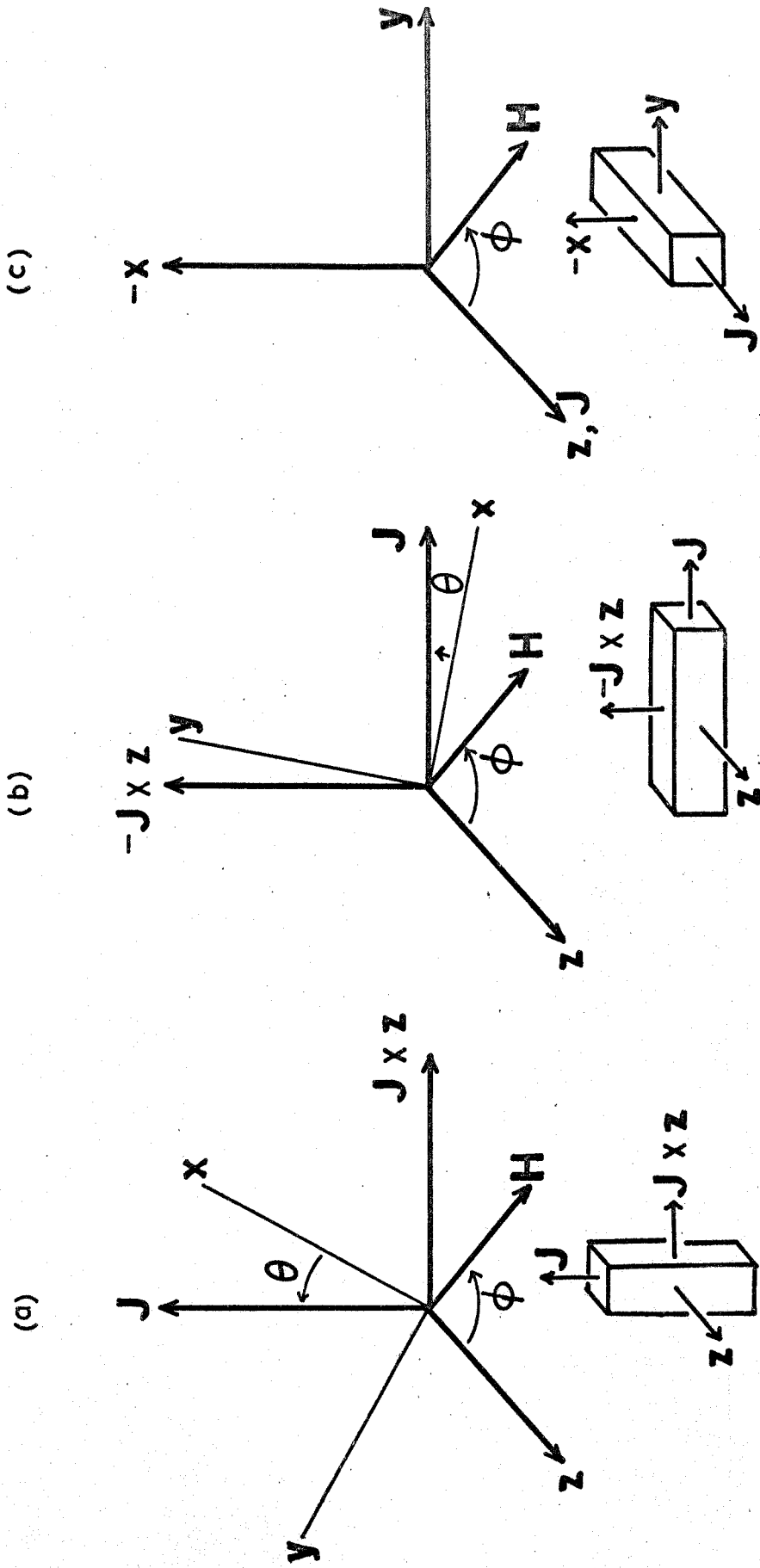
(a)

(b)

(c)

The specimen configurations relative to the directions of the current and
the applied magnetic field

as shown in figure 2.1 - (a) and is rotated about its long axis, which makes an angle Θ with the binary axis of the crystal. $\emptyset$ is the angle between the trigonal axis and the magnetic field direction. Then the components of the current density $\underline{J}$ and magnetic field $\underline{H}$ with respect to the crystallographic axes are:

$$J_1 = J \cos \Theta \qquad\qquad H_1 = -H \sin \Theta \sin \emptyset$$

$$J_2 = J \sin \Theta \qquad\qquad H_2 = H \cos \Theta \sin \emptyset \qquad (2.15)$$

$$J_3 = 0 \qquad\qquad H_3 = H \cos \emptyset$$

The measured galvanomagnetic fields $E_{\underline{J}}$, $E_{\underline{z}}$ and $E_{\underline{J} \times \underline{z}}$ can be written in terms of the components of the electric field $\underline{E}$ as

$$E_{\underline{J}} = E_1 \cos \Theta + E_2 \sin \Theta$$

$$(2.16)$$

$$E_{\underline{z}} = E_3$$

$$E_{\underline{z} \times \underline{J}} = E_1 \sin \Theta + E_2 \cos \Theta$$

These fields (2.16) are obtained in terms of the galvanomagnetic coefficients by substituting the components of $\underline{J}$ and $\underline{H}$ from equations (2.15) in the relation

$$E_i = \rho_{ij} (\underline{H}) J_j$$

where ρ_{ij} (H) is given by the equations (2.11). By algebraic

manipulation the following results are obtained:

$$E_{\underline{J}} = \rho_{11}J + JH^2(A_{12}\sin^2\phi + A_{13}\cos^2\phi - A_{24}\cos3\Theta\sin2\phi)$$

$$E_{\underline{z}} = JHR_{231}\sin\phi + JH^2A_{42}\sin3\Theta\sin^2\phi \qquad\qquad (2.17)$$

$$E_{\underline{z}\times J} = -JHR_{123}\cos\phi + JH^2A_{24}\sin3\Theta\sin2\phi$$

From the measurements of these fields, seven coefficients $(\rho_{11}, R_{231}, R_{123}, A_{12}, A_{13}, A_{24}$ and $A_{42})$ can be determined. The optimum value for Θ is 15°: in this case the contributions of the terms containing A_{24} and A_{42} are maximized. The dependence of the fields on ϕ permits the separation of the measured field into contributions from the various coefficients.

(2)   The second set of measurements

A 90° - specimen is placed in the magnetic field as shown in figure 2.1 - (b). Now the rotation axis is perpendicular one of the lateral faces. The measured fields are obtained in terms of the galvanomagnetic coefficients as above with these results

$$E_{\underline{J}} = \rho_{11}J + JH^2(A_{11}\sin^2\phi + A_{13}\cos^2\phi + A_{24}\sin3\Theta\sin2\phi)$$

$$E_{\underline{z}} = JH^2(-A_{42}\sin3\Theta\sin^2\phi - A_{44}\sin2\phi)$$

$$E_{\underline{z}\times\underline{J}} = -JHR_{123}\cos\phi + JH^2A_{24}\cos3\Theta\sin2\phi \qquad\qquad (2.18)$$

Two additional coefficients A_{11} and A_{44} are obtained as well as duplicates of some of the coefficients measured from the first arrangement, which serve to check the two sets of results.

This experimental configuration can be obtained from the arrangement shown in fig 2.1 -(a) by rotating the sample 90° along the trigonal axis. Thus the two sets of measurements can be taken on the same sample.

(3)   The Third Set of Measurements

A 0° - specimen is rotated in a plane containing $\underline{H}$ and $\underline{J}$, see figure 2.1 -(c). The lateral faces of the sample are chosen parallel to the binary and bisectrix axes of the crystal, although this is not essential to obtain the remaining three coefficients (ρ_{33}, A_{31} and A_{33}), but does enable a checking determination of the coefficient A_{44}. The fields are related to the galvanomagnetic coefficients by

$$E_{\underline{J}} = \rho_{33}J + JH^2 (A_{31}\sin^2\emptyset + A_{33}\cos^2\emptyset)$$

$$E_{\underline{x}} = -JHR_{231}\sin\emptyset$$

$$E_{\underline{y}} = JH^2(A_{42}\sin^2\emptyset + A_{44}\sin2\emptyset) \qquad (2.19)$$

R_{231} and A_{42} can be measured besides ρ_{33}, A_{31}, A_{33} and A_{44}.

The equations (2.17), (2.18) and (2.19) are not invariant under the transformation $\Theta \longrightarrow \Theta + 1/3n\pi$, where n can be 1, 3, 5 etc., when the coefficients A_{24} and A_{42} change sign. Θ is defined as the angle between the current direction

and a binary axis. Therefore, this transformation changes the selection of the binary axis. Thus the sign of these two coefficients depends upon the choice of this axis which can be defined conveniently by referring to one of the two rotational right handed Cartesian co-ordinate systems described in the first chapter.

This experimental design allows determination of the 12 magnetoresistivity coefficients of antimony. Further details of how the experimental measurements were made will be deferred until chapter 4.

2.4   The Boltzmann Equation

When an external field, either electric or magnetic, or a temperature gradient is applied to a solid, then the equilibrium distribution function of the carriers is continually being disturbed through acceleration of the carriers. Balance of the electron distribution function is restored by scattering of the electrons with lattice vibrations, foreign atoms or other defects in the lattice. When the local concentration of carriers in the state $\underline{k}$ in the neighbourhood of the point $\underline{r}$ in space is written as $f_{\underline{k}}(\underline{r},t)$, then the condition for the steady state, known as the Boltzmann equation, is

$$\left[\frac{\partial f_k}{\partial t}\right]_{\text{diff.}} + \left[\frac{\partial f_k}{\partial t}\right]_{\text{fields}} + \left[\frac{\partial f_k}{\partial t}\right]_{\text{scatt.}} = 0 \qquad (2.20)$$

The explicit forms of the first two terms are given by

$$\left[\frac{\partial f}{\partial t}\right]_{\text{diff.}} = -\underline{V}_{\underline{k}} \cdot \frac{\partial f}{\partial \underline{r}} = -\underline{V}_{\underline{k}} \cdot \text{grad}_{\underline{r}} f \qquad (2.21)$$

and

$$\left[\frac{\partial f}{\partial t}\right]_{\text{field}} = -\frac{e}{\hbar} (\underline{E} + \frac{1}{c} \underline{V}_{\underline{k}} \times \underline{H}) \text{grad}_{\underline{k}} f \qquad (2.22)$$

where $\underline{V}_{\underline{k}}$ is the velocity of the carrier in the state $\underline{k}$, e is the electronic charge, $\underline{E}$ and $\underline{H}$ are the applied electric and magnetic fields respectively. If $Q(\underline{k},\underline{k}')$ is the probability per unit time that an electron makes a transition from the state $\underline{k}$ to the state $\underline{k}'$ (equals to $Q(\underline{k}', \underline{k})$ a measure the transition rate from $\underline{k}'$ to $\underline{k}$), the rate of change of $f_{\underline{k}}(\underline{r}, t)$ will be

$$\left[\frac{\partial f}{\partial t}\right]_{\text{scatt.}} = \iint \left\{ f_{\underline{k}'}(1-f_{\underline{k}}) - f_{\underline{k}}(1-f_{\underline{k}'}) \right\} Q(\underline{k},\underline{k}') d\underline{k}' \qquad (2.23)$$

a general form of the scattering term. Here to take into account the effect of the exclusion principle, $Q(\underline{k},\underline{k}')$ is multiplied by $f_{\underline{k}}$, the number of carriers in the state $\underline{k}$ and $(1 - f_{\underline{k}'})$, the number of vacancies available in the final state. In the equilibrium state, when no fields and temperature gradients are present, this expression, as it must, vanishes and $f_{\underline{k}}$ is replaced by $f_{\underline{k}}^{o}$, the equilibrium distribution function, which for a metal is the Fermi distribution function,

$$f(\mathcal{E}) = \frac{1}{\exp\left\{(\mathcal{E} - \mathcal{E}_F)/kT\right\} + 1} \qquad (2.24)$$

When the scattering processes in the solid are representable by a relaxation time, the Boltzmann equation reduced to the form,

$$-\frac{e}{\hbar}\left(\underline{E} + \frac{1}{c}\,\underline{V} \times \underline{H}\right)\text{grad}_{\underline{k}}f + \underline{V} \cdot \text{grad}_{\underline{r}}\,f = -\frac{f - f^{o}}{\tau} \qquad (2.25)$$

The relaxation time τ, in general, is a function of wave vector $\underline{k}$ and should have the same symmetry of the crystal as energy-wave vector relation $\mathcal{E}(\underline{k})$.

2.5 Electrical Conductivity

Electrical conductivity is measured in a conductor to which an electric field $\underline{E}$ is applied in the absence of a temperature gradient and magnetic fields. Now $\text{grad}_{\underline{r}}f$ and $\underline{H}$ can both be put equal to zero in equation (2.25) which then reduces to the form

$$-\frac{e}{\hbar}\,\underline{E} \cdot \text{grad}_{\underline{k}}\,f = -\frac{f - f^{o}}{\tau} \qquad (2.26)$$

If the applied electric field is small, then the distribution function in the steady state will not be far from f^{o} and therefore f can be replaced by f^{o} in the left hand side of the equation (2.26). However, $f - f^{o}$ has a finite value, which is in fact the measure of the deviation from the equilibrium state. Therefore from equation (2.26), the steady

state distribution function

$$f = f^0 + \frac{e}{\hbar} \cdot \tau \ \underline{E} \ \text{grad}_{\underline{k}} \ f^0 \tag{2.27}$$

is obtained. From the relations

$$\text{grad}_{\underline{k}} \ f^0 = \frac{\partial f^0}{\partial \underline{k}} = \frac{\partial f^0}{\partial \varepsilon} \cdot \frac{\partial \varepsilon}{\partial \underline{k}} \ ,$$

and $\quad \underline{v} = \frac{1}{\hbar} \ \frac{\partial \varepsilon}{\partial \underline{k}}$

equation (2.27) takes the form

$$f_{\underline{k}} = f^0 + e \ \tau \ \underline{v} \cdot \underline{E} \ \frac{\partial f^0}{\partial \varepsilon} \tag{2.28}$$

The number of electrons per unit volume of the crystal, whose wave vectors lie in the interval $d\underline{k} = (dk_1, \ dk_2, \ dk_3)$, is

$$\frac{1}{4\pi^3} \ f_{\underline{k}} \ d\underline{k} \tag{2.29}$$

Then the current density is given by

$$\underline{J} = - \frac{e}{4\pi^3} \int \underline{v}_{\underline{k}} \ f_{\underline{k}} \ d\underline{k} \tag{2.30}$$

and using the equation (2.28) it becomes

$$\underline{J} = - \frac{e^2}{4\pi^3} \int \tau \ \underline{v} \cdot (\underline{v} \cdot \underline{E}) \ \frac{\partial f^0}{\partial \varepsilon} \cdot d\underline{k} \tag{2.31}$$

Writing Ohm's law in an anisotropic solid

$$J_i = \widetilde{\sigma}_{ij} \, E_j$$

and using the equation (2.31), the conductivity tensor takes the form

$$\widetilde{\sigma}_{ij} = - \frac{e^2}{4\pi^3} \int \tau \, v_i \, v_j \, \frac{\partial f^o}{\partial \mathcal{E}} \, d\underline{k} \qquad (2.32)$$

The integration is carried out over constant energy surfaces in $\underline{k}$-space. If $d\underline{k}$ is the element of $\underline{k}$-space between the surfaces $\mathcal{E}$ and $\mathcal{E} + d\mathcal{E}$, then

$$d\underline{k} = \frac{dS \, d\mathcal{E}}{\left| grad_k \mathcal{E} \right|} \quad , \qquad (2.34)$$

where dS is an element of the surface $\mathcal{E}(\underline{k})$.
Therefore equation (2.32) becomes

$$\widetilde{\sigma}_{ij} = - \frac{e^2}{4\pi^3} \int \frac{\partial f^o}{\partial \mathcal{E}} \, d\mathcal{E} \int \frac{\tau v_i v_j \, dS}{\left| grad_k \mathcal{E} \right|} \qquad (2.35)$$

For a metal $\dfrac{\partial f^o}{\partial \mathcal{E}}$ behaves like a delta function at the Fermi level $\mathcal{E}_F$ and equation (2.35) takes the form

$$\widetilde{\sigma}_{ij} = \frac{e^2}{4\pi^3} \int \frac{\tau v_i v_j \, dS}{\left| grad_k \mathcal{E} \right|} \qquad (2.36)$$

The integration is carried out over the Fermi surface. To evaluate this integral for a particular material a specific model

of the Fermi surface must be considered, for antimony, for instance, the ellipsoidal model. For an isotropic metal with spherical energy surfaces in which the energy is related to the wave vector by $\mathcal{E} = \frac{1}{2}\hbar^2 k^2/m^*$, the conductivity equation reduces to

$$\sigma = \frac{Ne^2 \tau_F}{m^*} \tag{2.37}$$

where N is the number of carriers, τ_F is the relaxation time appropriate to the Fermi energy and m^* is the effective mass of the carriers.

2.6 A Relaxation Time Expression for Semimetals

The rate of change of f_k due to scattering, $\left[\frac{\partial f}{\partial t}\right]_{scatt.}$, given by the integral (2.23) can be evaluated for metals and semimetals to obtain an expression for the relaxation time with the following assumptions (Wilson 1953):

(i)   Only elastic scattering between electrons and lattice waves is to be considered,

(ii) $\mathcal{E}(\underline{k})$ is a quadratic function of $\underline{k}$ and so has spherical symmetry (free electron model with effective mass m^*)

(iii) The frequencies of the lattice vibrations are the same as those of an elastic continuum.

The relaxation time τ for a metal then becomes for temperatures $T \gg \Theta$ where Θ is the Debye temperature

$$\tau = \frac{2\hbar^2 \Lambda}{(1/2 \, m^*)^{1/2} \, D} \cdot \frac{\Theta}{T} \, \mathcal{E}^{3/2}. \tag{2.38}$$

Here Λ and D are constants of the crystal.

If the carrier density $N < \frac{1}{4} N_a$, where N_a is the number of atoms per unit volume, the relaxation time τ is given by

$$\tau = \frac{h^2 D \Lambda}{2(1/2\ m^*)^{1/2}} \cdot \frac{\Theta}{T} \cdot \frac{1}{\mathcal{E}^{1/2}} \qquad (2.39)$$

for temperatures $T \gg (2/D)^{1/2} \Theta$. For semimetals with small number of carriers, the latter expression is applicable: briefly the reason for this is as follows. In the derivation of the equation (2.38), it is assumed that electrons can be scattered by lattice vibrations with all wave vectors $|\underline{q}| \leq q_o$, where q_o is the Debye cut-off frequency and proportional to the number of atoms per unit volume of the crystal. However to **conserve** the energy and momentum in any collision $|\underline{k}| = |\underline{k} \pm \underline{q}|$ and, therefore, an electron in the state $\underline{k}$ can only interact with phonons having momentum $|\underline{q}| \leq 2|\underline{k}|$. In a metal electron with $|\underline{k}| = k_o$, where k_o is the wave vector of the electrons on the Fermi surface, is to be considered. Thus, if $2k_o < q_o$, $2k_o$ is taken as the upper limit for the evaluation of the integral (2.23) which leads to the equation (2.39) (Sondheimer 1952). Sondheimer shows that $2k_o < q_o$ is satisfied when $n_a < 1/4$, where n_a is the number of conduction electrons per atom. This is true for the semimetals As, Bi, Sb and graphite, i.e. for antimony n_a is of the order of 10^{-3}. Therefore, in semimetals the carriers are scattered by only long-wave phonons.

2.7.   Isothermal Galvanomagnetic Effects in Anisotropic

Conductors.

The Boltzmann equation can be written conveniently by defining the distribution function $f_{\underline{k}}$ in the form

$$f_{\underline{k}} \equiv f_{\underline{k}}^{O} - \Phi_{\underline{k}} \frac{\partial f_{\underline{k}}^{O}}{\partial \mathcal{E}_{\underline{k}}} \tag{2.40}$$

The new function $\Phi_{\underline{k}}$ is a measure of the deviation from equilibrium of the electron distribution in the steady state, and it is weighted with $\frac{\partial f^{O}}{\partial \mathcal{E}}$ which depends upon the form of that distribution. In the case of Fermi – Dirac statistics, $\frac{\partial f^{O}}{\partial \mathcal{E}}$ is equal to

$$\frac{f^{O} (1 - f^{O})}{kT} \quad ,$$

which maximizes sharply at the Fermi surface. Introducing f_{k} in this form into equation (2.25), reduces the Boltzmann equation for an isothermal metal to the form (Wilson 1953)

$$\frac{1}{\tau} \Phi + \frac{e}{\hbar} \underline{E} \cdot \text{grad} \mathcal{E} + \frac{e}{\hbar^{2}c} \underline{H} \Omega \Phi = 0 \tag{2.41}$$

where $\Omega = \text{grad}_{\underline{k}} \mathcal{E} \times \text{grad}_{\underline{k}}$, an operator. The operator Ω is conveniently written in tensor notation as

$$\Omega_{i} \equiv \epsilon_{ikl} \frac{\partial \mathcal{E}}{\partial k_{k}} \cdot \frac{\partial}{\partial k_{l}} \tag{2.42}$$

where the tensor ϵ_{ikl} is defined by

$$\epsilon_{123} = \epsilon_{231} = \epsilon_{312} = 1$$

$$\epsilon_{231} = \epsilon_{132} = \epsilon_{321} = -1$$

and all the other components are zero.

A solution for the equation (2.41) has been given by Jones and Zener (1934) as a series of increasing powers of the magnetic field H in the form

$$\Phi = -\frac{e}{\hbar}\left[\tau \underline{E} \, \text{grad}\mathcal{E} - \frac{e}{\hbar^2 c} \, \tau \underline{H} \quad \Omega(\tau\underline{E}.\text{grad}\mathcal{E})\right.$$
$$\left. + \frac{e^2}{\hbar^4 c^2} \, \tau\underline{H}.\Omega\{\tau\underline{H}\Omega(\tau\underline{E}.\text{grad}\mathcal{E})\} + \dots \right] \qquad (2.43)$$

Then the electric current density previously given by equation (2.30) becomes

$$\underline{J} = \frac{e}{4\pi^3\hbar} \int \text{grad}\mathcal{E} \, \Phi \, \frac{\partial f^o}{\partial \mathcal{E}} \quad d\underline{k} \ . \qquad (2.44)$$

Becuase Φ is given by a series of increasing powers of H, then $\underline{J}$ can be written in the form

$$J_i = \sigma_{ij}E_j + P_{ijk}E_jH_k + B_{ijkl}E_jH_kH_l + \dots \qquad (2.45)$$

This is equivalent to the series (2.12) of the phenomonological

theory and $\widetilde{\sigma}_{ij}$, P_{ijk}, B_{ijkl}, ... are the magnetoconductivity tensor coefficients. Using equations (2.44) and (2.45) these coefficients up to second order in the magnetic field can be expressed in the following form (Abeles and Meiboom 1954)

$$\widetilde{\sigma}_{ij} = \frac{-e^2}{4\pi^3\hbar^2} \int \tau \frac{\partial f^o}{\partial \mathcal{E}} \frac{\partial \mathcal{E}}{\partial k_i} \frac{\partial \mathcal{E}}{\partial k_j} \, d\underline{k}$$

$$P_{ijk} = \frac{-e^2}{4\pi^3\hbar^4 c} \int \tau \frac{\partial f^o}{\partial \mathcal{E}} \cdot \frac{\partial \mathcal{E}}{\partial k_i} \frac{\partial \mathcal{E}}{\partial k_l} \frac{\partial}{\partial k_m} (\tau \frac{\partial \mathcal{E}}{\partial k_j}) \epsilon_{klm} d\underline{k}$$

$$B_{ijkl} = \frac{-e^4}{4\pi^3\hbar^6 c^2} \int \tau \frac{\partial f^o}{\partial \mathcal{E}} \cdot \frac{\partial \mathcal{E}}{\partial k_i} \frac{\partial \mathcal{E}}{\partial k_p} \frac{\partial}{\partial k_q} \left[\tau \frac{\partial \mathcal{E}}{\partial k_m} \frac{\partial}{\partial k_n}(\tau \frac{\partial \mathcal{E}}{\partial k_j}) \right]$$

$$\times \frac{1}{2} \left[\epsilon_{qpl} \epsilon_{nmk} + \epsilon_{qpk} \epsilon_{nml} \right] d\underline{k} \tag{2.46}$$

If v_i and v_j in equation (2.32) in section 2.5 are replaced by $\frac{1}{\hbar}\frac{\partial \mathcal{E}}{\partial k_i}$ and $\frac{1}{\hbar}\frac{\partial \mathcal{E}}{\partial k_j}$ respectively, then the result for $\widetilde{\sigma}_{ij}$ is obtained.

These integrals (2.46) can be evaluated in principle if $\mathcal{E}(\underline{k})$, $\tau(\underline{k})$ and f^o, the equilibrium distribution function, are known. Probably for all crystals $\mathcal{E}(\underline{k})$ and $\tau(\underline{k})$ are complicated functions of the wave vector $\underline{k}$. But to evaluate the above integrals for such a case is prohibitively difficult. However, if an isotropic relaxation time is assumed, then τ can be taken outside to simplify the integrals. In fact,

when $\tau(\underline{k})$ is not too anisotropic, and the magnitudes of the tensor components of $\tau(\underline{k})$ differ by only as much as a factor of 2, this approach is a good approximation (Herring and Vogt 1956). Further simplification of the calculations is obtained by assuming a simple shape for the surfaces of constant energy in $\underline{k}$-space. For low carrier densities, the constant energy surfaces near the extrema can usually be described by ellipsoids; the band structure of antimony will be treated this way. Then the above integrals can be evaluated so that the magnetoconductivity coefficients are related to the band parameters, such as mobilities μ_i (equal to $e\tau/m_i^*$), which are defined along the principal axes of the ellipsoids and N, number of carriers.

This method was first applied to bismuth by Jones (1936) to explain the observed large magnetoresistivity. He used a single-valleyed band model, with ellipsoidal, constant energy surfaces, and obtained some qualitative features of the galvanomagnetic effects. Abeles and Meiboom extended the problem to a many-valleyed system, and explained quantitatively the experimental observations in n-type germanium (1954) and in bismuth (1956).

A clear discussion and evaluation of the integrals (2.46) for a many-valleyed ellipsoidal band model in the rhombohedral crystal system has been developed by Drabble and Wolfe (1956). The following explanation leans heavily on their work. For the calculations the following assumptions

are made.

(a)   Only one type of carrier is considered at a time.

(b)   The energy surfaces in k-space have a number of minima at equivalent points k_o^i . The whole set of surfaces in a given band must have the rhombohedral ($\overline{3}$m) symmetry of the crystal.

(c)   Constant energy surfaces in k-space are a set of similar ellipsoids centred at points k_o^i . With appropriate choice of the co-ordinate system, they can be written as

$$\mathcal{E} = \mathcal{E}_o + \frac{h^2}{2} \left[\frac{(k_1^i - k_{10}^i)^2}{m_1} + \frac{(k_2^i - k_{20}^i)^2}{m_2} + \frac{(k_3^i - k_{30}^i)^2}{m_3} \right] \qquad (2.47)$$

where $\mathcal{E}_o$ is the minimum energy in the band and m_1, m_2 and m_3 are the effective masses along the principal axes of the ellipsoids.

(d)   A relaxation time exists and it does not depend upon k and can be written in the form

$$\tau = b\mathcal{E}^{-\lambda} \qquad (2.48)$$

where λ and b depend upon the scattering mechanism. b, generally, is a function of temperature, as shown, for instance, by equations (2.38) and (2.39).

(e)   Intervalley scattering is neglected. In other words the relaxation process only takes place for transitions between states belonging to the same extremum. Thus, each

pocket can be treated independently, and the total current can be obtained as the sum of the contributions from all of them.

Then, for each valley, in its own principal axes system, the evaluation of the integrals (2.46) leads to the following expressions:

$$\sigma_{ij}^{(i)} = \frac{A}{m_i} \, \delta_{ij}$$

$$P_{ijk}^{(i)} = \frac{-B}{m_i m_j} \, \epsilon_{ijk}$$

$$B_{ijkl}^{(i)} = \frac{C}{m_i m_j m_n} \left[\epsilon_{nil} \epsilon_{jnk} + \epsilon_{njk} \epsilon_{jnl} \right] \qquad (2.49)$$

where A, B and C are constants whose values depend upon f^o, b and λ, and for a completely degenerate conductor are given by

$$A = \frac{e^2}{3\pi^2} \, b \, \left(\frac{2m^T}{\hbar^2}\right)^{3/2} \, (\mathcal{E}_F)^{3/2 - \lambda}$$

$$B = \frac{e^3}{3\pi^2} \, \frac{b^2}{c} \, \left(\frac{2m^T}{\hbar^2}\right)^{3/2} \, (\mathcal{E}_F)^{3/2 - 2\lambda}$$

$$C = \frac{e^4}{6\pi^2} \, \frac{b^3}{c^2} \, \left(\frac{2m^T}{\hbar^2}\right)^{3/2} \, (\mathcal{E}_F)^{3/2 - 3\lambda} \qquad (2.50)$$

Here $\mathcal{E}_F$ is the Fermi energy and m^T is $(m_1 m_2 m_3)^{1/3}$, the density of states effective mass. Drabble and Wolfe also give the results for the non-degenerate case.

To obtain the conductivity tensor coefficients of the crystal as a whole, the contributions of a single valley are transformed to a common co-ordinate system and then they are summed over all the valleys. This procedure involves two orthogonal matrices; one of them carries the transformation of the valley (i) into each of the other valleys and the second specifies the transformations of valleys to the principal crystal axes. In order to complete the calculations a specific crystal structure and band model have to be considered. The problem has been solved for the rhombohedral structure (A7) with a band model of six tilted ellipsoidal valleys centred on the mirror planes of the Brillouin zone (i.e. the valence band structure of antimony) by Drabble and Wolfe (1956). Their general results for the twelve magnetoconductivity tensor coefficients can be written in the following form for a degenerate carrier population:

$$\widetilde{\sigma}_{11} = \frac{N}{2} e^2 \tau \left(\frac{1}{m_1} + \frac{\alpha^2}{m_2} + \frac{\beta^2}{m_3} \right)$$

$$\widetilde{\sigma}_{33} = N e^2 \tau \left(\frac{\beta^2}{m_2} + \frac{\alpha^2}{m_3} \right)$$

$$P_{231} = \frac{N e^3 \tau^2}{2c} \left(\frac{1}{m_2 m_3} + \frac{\beta^2}{m_1 m_2} + \frac{\alpha^2}{m_1 m_3} \right)$$

$$P_{123} = \frac{Ne^3\tau^2}{c} \quad \frac{1}{m_1} \quad (\frac{\alpha^2}{m_2} + \frac{\beta^2}{m_3})$$

$$B_{11} = \frac{Ne^4\tau^3}{8c^2} \left[\frac{\beta^2}{m_2} (\frac{1}{m_1} - \frac{1}{m_3})^2 + \frac{\alpha^2}{m_3} (\frac{1}{m_1} - \frac{1}{m_2})^2 \right.$$

$$\left. + \frac{3\alpha^2\beta^2}{m_1} (\frac{1}{m_2} - \frac{1}{m_3})^2 \right]$$

$$B_{12} = \frac{Ne^4\tau^3}{8c^2} \left[\frac{3\beta^2}{m_2}(\frac{1}{m_1^2} + \frac{1}{m_3^2}) + \frac{3\alpha^2}{m_3} (\frac{1}{m_1^2} + \frac{1}{m_2^2}) \right.$$

$$\left. + \frac{\alpha^2\beta^2}{m_1} (\frac{1}{m_2} - \frac{1}{m_3})^2 + \frac{2}{m_1 m_2 m_3} \right]$$

$$B_{13} = \frac{Ne^4\tau^3}{2c^2} \left[\frac{1}{m_1} + \frac{\alpha^2}{m_2} + \frac{\beta^2}{m_3} \right] \left[\frac{1}{m_1} (\frac{\alpha^2}{m_2} + \frac{\beta^2}{m_3}) \right]$$

$$B_{31} = \frac{Ne^4\tau^3}{2c^2} \left[\frac{\beta^2}{m_2} + \frac{\alpha^2}{m_3} \right] \left[\frac{1}{m_2 m_3} + \frac{1}{m_1} (\frac{\beta^2}{m_2} + \frac{\alpha^2}{m_3}) \right]$$

$$B_{33} = \frac{Ne^4\tau^3}{c^2} \cdot \frac{\alpha^2\beta^2}{m_1} (\frac{1}{m_2} - \frac{1}{m_3})^2$$

$$B_{24} = \frac{Ne^4\tau^3}{4c^2} \quad \frac{\alpha\beta}{m_1} \quad (\frac{1}{m_2} - \frac{1}{m_3}) (-\frac{1}{m_1} + \frac{\alpha^2}{m_2} + \frac{\beta^2}{m_3})$$

$$B_{42} = \frac{Ne^4\tau^3}{4c^2} \, \alpha\beta \left[\frac{1}{m_2} - \frac{1}{m_3} \right] \left[\frac{1}{m_2 m_3} - \frac{1}{m_1} \left(\frac{\beta^2}{m_2} + \frac{\alpha^2}{m_3} \right) \right]$$

$$-B_{44} = \frac{Ne^4\tau^3}{2c^2} \left[\frac{\beta^2}{m_2} + \frac{\alpha^2}{m_3} \right] \left[\frac{1}{m_1} \left(\frac{\alpha^2}{m_2} + \frac{\beta^2}{m_3} \right) \right] \tag{2.51}$$

where N is the total density of electrons, given by the relation

$$N = \frac{1}{3\pi^2} \left(\frac{2m^T}{\hbar^2} \right)^{3/2} (\mathcal{E}_F)^{3/2} \tag{2.52}$$

and $\alpha = \cos\psi$, $\beta = \sin\psi$ are the tilt angles defined in figure 1.11. These equations apply equally to sets of either 3 or 6 ellipsoids in the mirror planes, UTZLNXUΓ in figure 1.10, arranged in the Brillouin zone to produce in total $\overline{3}$m symmetry.

2.8.   The Relevant Relationship Between the Magnetoconductivity Tensor Components and Band Parameters of Antimony.

The relations (2.51) can be applied to antimony by extending them to the two carrier case. By introducing

$$\mu_i = \frac{e\tau}{m_i^{(el)}} \quad \text{and} \quad \nu_i = \frac{e\tau}{m_i^{(h)}} \, ,$$

defined as the mobilities along the principal axes of the ellipsoids containing electrons and holes respectively, the relevant equations become

$$2\widetilde{G}_{11} = Ne\left[(\mu_1 + \alpha_1^2\mu_2 + \beta_1^2\mu_3) + (\nu_1 + \alpha_2^2\nu_2 + \beta_2^2\nu_3)\right]$$

$$\widetilde{G}_{33} = Ne\left[(\beta_1^2\mu_2 + \alpha_1^2\mu_3) + (\beta_2^2\nu_2 + \alpha_2^2\nu_3)\right]$$

$$-2cP_{231} = Ne\left\{\left[\nu_2\nu_3 + \nu_1\,(\beta_2^2\nu_2 + \alpha_2^2\nu_3)\right]\right.$$

$$\left. - \left[\mu_2\mu_3 + \mu_1(\beta_1^2\mu_2 + \alpha_1^2\mu_3)\right]\right\}$$

$$-cP_{123} = Ne\left\{\left[\nu_1(\alpha_2^2\nu_2 + \beta_2^2\nu_3)\right] - \left[\mu_1(\alpha_1^2\mu_2 + \beta_1^2\mu_3)\right]\right\} \qquad (2.53\ -a)$$

The rest of the equations are written more conveniently by including only the contributions from electrons, those from the holes being identical in form and simply added on:

$$2c^2B_{13} = Ne\left[\mu_1 + \alpha_1^2\mu_2 + \beta_1^2\mu_3\right]\left[\mu_1(\alpha_1^2\mu_2 + \beta_1^2\mu_3)\right]$$

$$2c^2B_{31} = Ne\left[\beta_1^2\mu_2 + \alpha_1^2\mu_3\right]\left[\mu_2\mu_3 + \mu_1(\beta_1^2\mu_2 + \alpha_1^2\mu_3)\right]$$

$$-2c^2B_{44} = Ne\left[\beta_1^2\mu_2 + \alpha_1^2\mu_3\right]\left[\mu_1(\alpha_1^2\mu_2 + \beta_1^2\mu_3)\right]$$

$$c^2(3B_{12} -B_{11} -2B_{44}) = Ne\left[\mu_1 + \alpha_1^2\mu_2 + \beta_1^2\mu_3\right]\left[\mu_2\mu_3 + \mu_1(\beta_1^2\mu_2 + \alpha_1^2\mu_3)\right]$$

$$8c^2B_{11} = Ne\left[\beta_1^2\mu_2(\mu_1 - \mu_3)^2 + \alpha_1^2\mu_3(\mu_1 - \mu_2)^2 + 3\alpha_1^2\beta_1^2\mu_1(\mu_2 - \mu_3)^2\right]$$

$$8c^2B_{12} = Ne\left[3\beta_1^2\mu_2(\mu_1^2 + \mu_3^2) + 3\alpha_1^2\mu_3(\mu_1^2 + \mu_2^2) + \alpha_1^2\beta_1^2\mu_1(\mu_2 - \mu_3)^2\right.$$

$$\left. + 2\mu_1\mu_2\mu_3\right]$$

$$2c^2B_{33} = c^2(-B_{12} + 3B_{11} - 2B_{44}) = 2Ne\ \alpha_1^2\beta_1^2\mu_1(\mu_2 - \mu_3)^2$$

$$4c^2B_{24} = Ne\ \alpha_1\beta_1\mu_1(\mu_2 - \mu_3)\ (-\mu_1 + \alpha_1^2\mu_2 + \beta_1^2\mu_3)$$

$$4c^2B_{42} = Ne\ \alpha_1\beta_1\ (\mu_2 - \mu_3)\left[\mu_2\mu_3 - \mu_1(\beta_1^2\mu_2 + \alpha_1^2\mu_3)\right] \qquad (2.53 -)$$

Here the carrier densities N of holes and electrons are assumed equal and α and β are the cosine and sine of the tilt angles ψ_e and ψ_h. These equations are invariant under the operations

$$\alpha \rightleftharpoons \beta$$
$$\mu_2 \rightleftharpoons \mu_3$$
$$\nu_2 \rightleftharpoons \nu_3$$

except for simultanious changes of signs of B_{24} and B_{42}. In figure 2.2. the cross-section of an ellipsoid in the mirror plane is presented; if, before this transformation

FIGURE 2.2
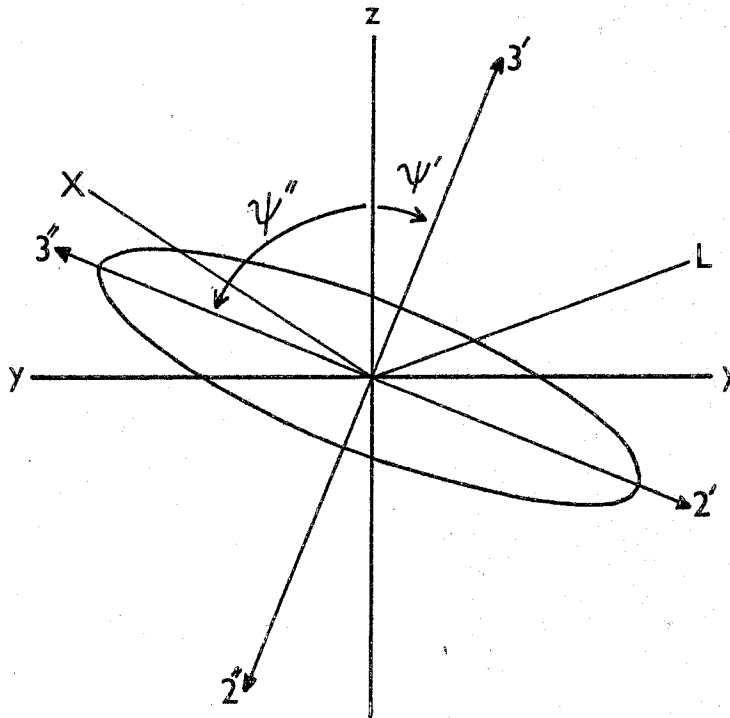
Cross-section of an ellipsoid in the y-z plane.

The binary axis is towards the viewer for the
quadrant containing L, but in the opposite
direction for the adjacent quadrant.

the tilt angle is ψ' and the principal mobilities in the mirror plane are $\mu_{2'}$ and $\mu_{3'}$, then after the transformation the tilt angle will be ψ'' and the corresponding principal mobilities will lie along the axes $2''$ and $3''$. Therefore, this transformation changes the algebraic representation of the ellipsoids, and so the equations (2.53), from one rotational system to the other in the y-z plane. The only differences between the representation of the equations (2.53) in one or other co-ordinate system are the signs of B_{24} and B_{42}, which accords with the result of the phenomonological theory; the signs of the two magneto-resistivity tensor coefficients A_{24} and A_{42} depend upon the selection of the co-ordinate system.

These twelve equations contain nine parameters, i.e. N numbers of carriers, three principal electron mobilities μ_i and three principal hole mobilities ν_i, where i is 1, 2 or 3. There must be three identities connecting the equations. Two of them are known (Freedman and Juretschke 1961);

$$2B_{33} \equiv 3B_{11} - B_{12} - 2B_{44}$$

and
$$4P_{231}\left[\widetilde{\sigma_{11}}(-2B_{44}) - \widetilde{\sigma_{33}} B_{13} \right]$$

$$\equiv P_{123}\left[4\widetilde{\sigma_{11}} B_{31} - \widetilde{\sigma_{33}}(3B_{12} - B_{11} - 2B_{44}) \right]$$

$$(2.54).$$

They have some importance since they allow ready experimental verification of the band model.

The equations (2.53) have been employed by Freedman and Juretschke (1961) and Epstein and Juretschke (1963) to explain the room temperature low field galvano-magnetic effects in antimony. In the present work the galvanomagnetic effects have been measured between 77^OK and 273^OK; results have been analysed on the basis of the theory discussed in this chapter. Before introducing these results, the growth of single crystals and the methods of measurements will be described.

CHAPTER   III

Growth of Single Crystals of Antimony and

Antimony-Tin Alloys

3.1.   Introduction

Square - sectioned (0.25 cm x 0.25 cm), pure and tin doped, antimony single crystal rods up to 10 cm long were grown in a nitrogen atmosphere by a method due to Epstein (1962). Precast rods were seeded in the two major crystallographic directions, with the (111) plane perpendicular or parallel to the rod axis. A distinct feature of the method in comparison with that of earlier workers (Kapitza 1928, Hasler 1933, Rausch 1947) was the use of high growth rates, from 2 cm. per minute to 10 cm. per minute. Epstein could not grow single crystal rods with c-plane perpendicular to rod axis, when the growth rate was smaller than 2 cm. per minute. Similar attempts in this work were also unsuccessful.

Although high growth rates may introduce some imperfections to the crystals, this method was used to obtain pure and heavily doped antimony samples for the following two reasons.

(i)   Difficulty in cutting samples without introducing mechanical stress. Particularly it is difficult to cut single crystal rods with c-plane perpendicular to the long axis because of easy cleavage of antimony along (111) planes.

(ii)   Tin has a very small equilibrium segregation coef-
ficient ($\sim$0.2). Thus, by employing fast growth rates, the
effective segregation coefficient can be made close to unity.

Epstein and Juretschke (1963) grew their pure and
doped (0.2% and 0.8% at tin) samples by this method and
obtained comparable results for magnetoresistivity coefficients
at room temperature to those measured on specimens grown at
slow rates by Bridgman method (Freedman and Juretschke 1961).

For succesfull growth of single crystals it is neces-
sary to use a crucible material having a low heat conductivity
relative to antimony. Antimony expands during solidification.
Therefore, the crucible must be designed in such a way as to
minimise strain in the growing crystals. The furnace and
crucible are kept stationary. To obtain high growth rates,
the temperature gradient is swept along the furnace axis
by reducing the heater power.

99.999% pure antimony as supply by Johnson, Matthey
and Co. Ltd., was used for the experiments. Tin dopant
(99.99% pure) was also obtained from the same company.

3.2.   Description of Apparatus.

Furnace The furnace was constructed from two concentric tubes,
figure 3.1. Kanthal wire was wound openly, about 6 turns per
inch between L and G, and about 12 turns per inch between G
and H, on the inner clear quartz tube to allow development of
a steep temperature gradient around G. It was found that a

FIGURE 3.1

silica rod
to push seed

thermocouple

add 4 in.

N₂
inlet

N₂
outlet

L   G   H

clear silica
tube

kanthal wire
heater

pyrex tube

0   1   2 in

Details of furnace
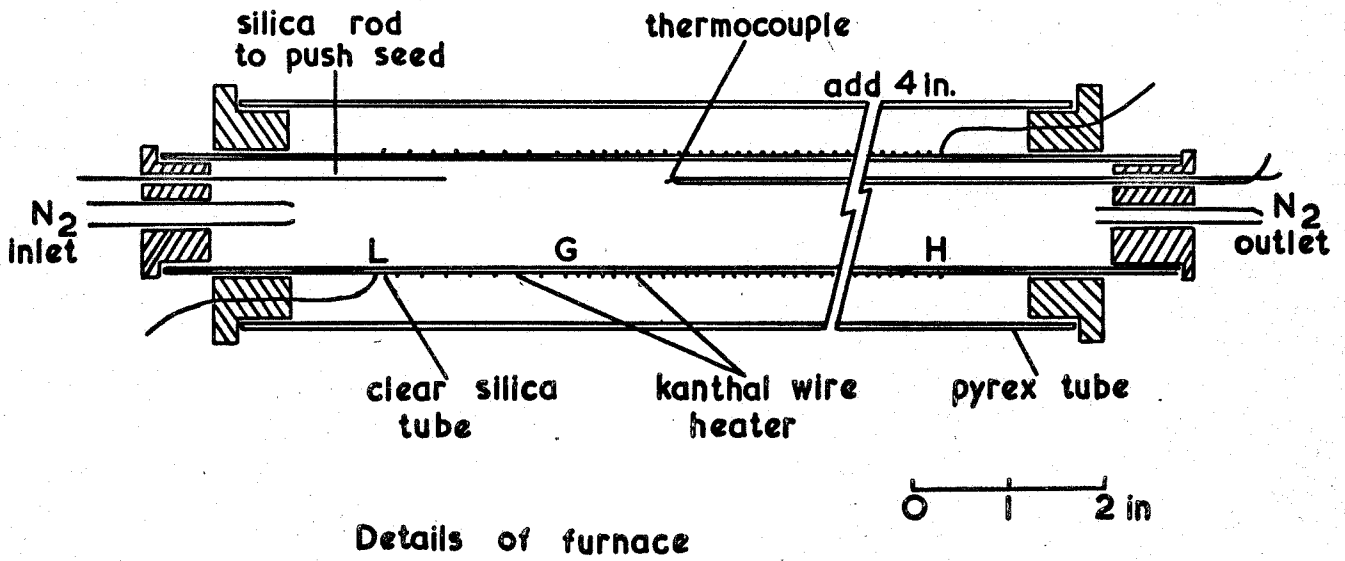
FIGURE 3.2
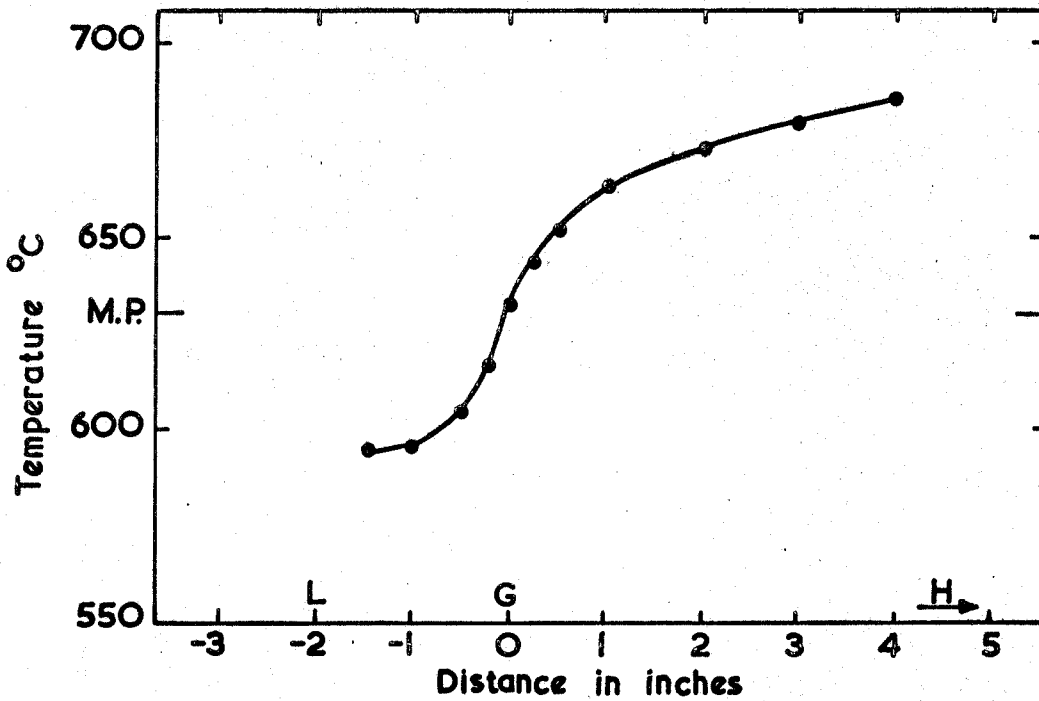
Temperature gradient in the furnace

slight temperature gradient ($\sim 5^O$C per cm.) along the axis of the higher temperature zone (GH) was convenient for growth of longer single crystal rods. This temperature gradient along GH was obtained by pushing the windings towards H, so having more turns per inch near to H. The wires between G and H, where transparency was not essential, were covered by alumina cement to fix them. The resistance of the heater was 50 ohms.

The temperature gradient in the furnace depends upon the nitrogen flow and applied heater power. An approximate plot is shown in figure 3.2. The temperature gradient at G was about 30^OC per cm. and along GH between 3 to 5^OC per cm. The gas flow was measured by an uncalibrated, oil manometer which read the pressure difference between the two end points of a capillary tube. Suitable flow rates were found by experience. Temperature was measured by a chromel-alumel thermocouple.

Crucible - Three long (15 cm.), thin (0.25 cm.) slats made of pyrophyllite, and then baked at 1150^OC, were used as the crucible mould. They were rigidly held together by two channelled, pyrophyllite blocks, leaving a square cross-sectioned (0.25 cm. x 0.25 cm.) channel, figure 3.3. A lid (0.7 x 0.3 x 10 cm) was used to cover the channel into which was placed the precast antimony rod. Pyrophyllite neither adheres to nor reacts with antimony at or below 700^OC. It has also a low heat conductivity relative to antimony. The design of the crucible mould from three thin slats has two

FIGURE 3.3
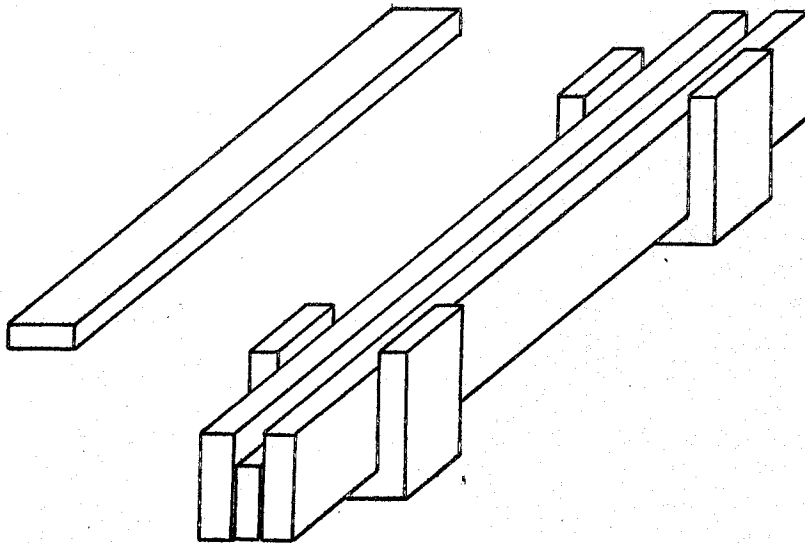
The pyrophyllite crucible

motives: firstly, it minimises straining of the growing crystal and secondly, removes the possibility of damaging the crystallized rod while removing it from the crucible.

3.3.   Growth Procedure

The following steps were followed to grow the single crystal rods.

(1)   The slats of the crucible mould were rubbed with a fine emery cloth, washed in concentrated nitric acid followed by distilled water and then baked at about 700°C to remove any traces of small crystallites and oxide.

(2)   The precast antimony rod, prepared under nitrogen atmosphere, cleaned by etching in CP4 for a few seconds and, subsequently, washed in distilled water, was placed in the crucible channel and covered with the pyrophyllite lid. About 2 mm. of the rod was left exposed to view at the place where the seed junction would be. A single crystal seed, accurately orientated and cut to be a snug fit in the groove, was placed about 1 cm. away from the exposed end of the rod. This seed was of sufficient size to allow about 2 mm. of it to melt, yet leave enough solid to maintain orientation.

(3)   The crucible mould was placed in the furnace so that the exposed end of the rod was at G, the highest temperature gradient point of the furnace. Nitrogen was passed for some 20 minutes to remove any oxygen present in the system, then the flow almost reduced to zero.

(4)   The furnace temperature was increased, while the

protruding end of the melt was observed. The furnace current
was about 3.5 amps. This applied power (about 500 W.) sufficed
to melt the antimony rod (M.P. 630°C) in about ten minutes.
At the instant when the exposed end melted, the seed was pushed
by a tin silica rod, s in figure 3.1., along the groove up to
the molten metal. If the seed was pushed right into the melt,
a blob formed at the seed-melt junction and orientation was
lost. To preserve seed orientation, the blob size was kept
to a minimum by pushing the seed just into contact with
the melt so that surface tension drew the melt over the seed
face. When about 1 to 2 mm of the seed had melted, the furnace
power was sharply reduced to about 50 watts so as to sweep
the temperature gradient along the rod.

(5)   When crystallization was completed, the furnace power
was further reduced and the crystal was cooled slowly to
room temperature under a nitrogen atmosphere. The rod was
removed by taking the two holding blocks away from the slats and
moving out the slats. Usually, any grain structure could be
seen on the grown rod, probably due to thermal etching.
Dilute aqua regia (50% HCL – 50% H_2NO_3) was also used to
show grain boundaries. The most frequent defect consisted of
a few small grains of less then 1 mm^2.along the faces of the
rod. These were attributed to nucleation at the slat inter-
face. Therefore, the slats were cleaned, as described above.
The crystals grew up to a length of about 8 cm., beyond this
a polycrystalline section at the far end of the rod was

common. It was found that when the antimony melted completely,
if the furnace was tapped gently before seeding, the final
crystal would have a more uniform cross-section along its
length.

3.4.   Pure Antimony Samples.

To obtain better crystals the growth rate was kept
close to the minimum rate (2 cm./min.) by not cutting off
the heater power but reducing it to about 50 watts. The growth
rate was estimated as 3 - 5 cm./min.

X-ray back reflection Laue photographs were taken
of each single crystal rod to determine the crystallographic
directions relative to rod faces and axis. The crystals obtained
were relatively unstrained: the lack of splitting of the
Laue spots of the X-ray photographs taken from the two samples
can be seen in figures 1.4 to 1.8 of the first chapter. Crystals
were etched with CP4 etching reagent, as described by Wernick
et al (1958) who obtained etch pits on zone-refined, slowly
grown crystals. The number of dislocation etch pits on the
(111) cleaveage planes was found between $3x10^4$ cm^{-2}. to
$7x10^4$ cm^{-2}. in accord with their results of the order of
10^4 cm^{-2}. Figure 3.4. shows the triangular etch pits
obtainable on the (111) faces.

To fit the experimental requirements, 18 mm. and
25 mm. long specimens were prepared by cleaving (c-plane
perpendicular rods) or by trimming with a spark erosion cutter
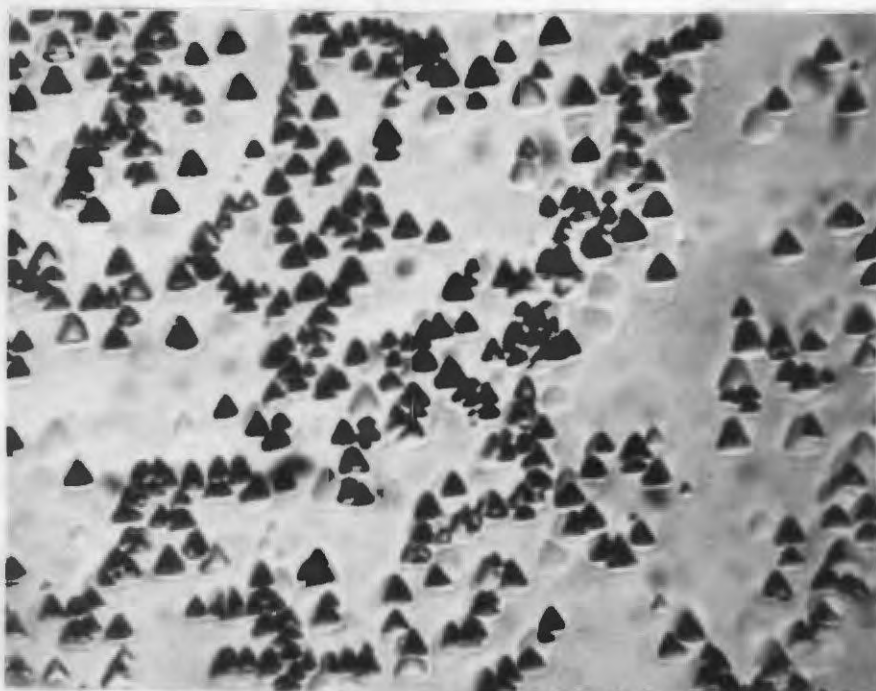
x 250
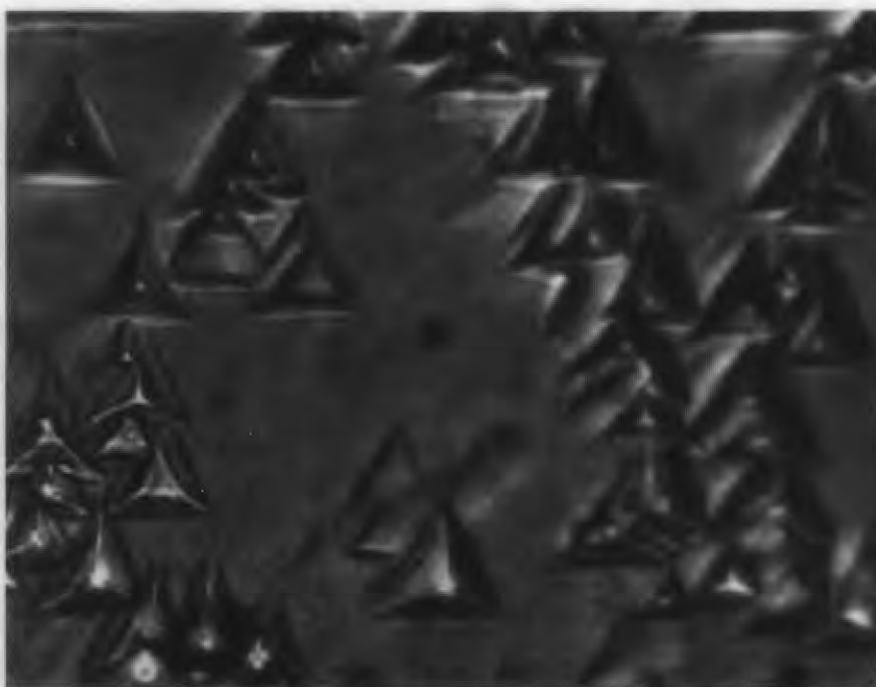
x 1000

FIGURE 3.4 Triangular etch pits obtainable
on the (111) planes of antimony.

(c-plane parallel rods). Sample dimensions were measured by a travelling microscope.

3.5. Growth of tin-antimony alloys

The tin-antimony phase diagram can be found in Hansen (1958). Crystals of these alloys having the antimony structure can be grown containing up to about 8% tin. It is usual when growing alloys by normal freezing methods to have difficulty in preparing homogeneous samples. In the present case, the equilibrium segregation coefficient has been estimated from the phase diagram as about 0.2. Epstein (1962) found that by use of the fast growing method, described in this chapter, it is possible to grow apparently homogeneous alloy crystals. He observed, for instance, less than 1% change in electrical resistivity measured along single crystal rods of 0.2% and 0.8% tin alloys.

Alloy single crystal rods, containing 1.7%, 2.0%, 2.5%, 3.0% and 8.0% tin, were grown using the following procedure.

(i) A weighed amount of tin was placed evenly along the crucible mould containing the antimony pieces.

(ii) The mould was covered with the lid and heated to $700^{o}C$ under nitrogen atmosphere and left in order to allow diffusion of tin into antimony. After about 30 minutes the furnace power was cut off and the nitrogen flow increased to cause rapid solidification.

(iii)   The precast rod obtained was about 10 to 12 cm. long. This rod was cut into two pieces. Each piece was seeded – doped seeds were used – with the two principal orientations. The growth rate was about 5 cm. per minute.

Microscopic examination particularly of the 8% tin alloy reveals regions in the crystal of somewhat different appearance than the surrounding material. These crystals still remain single, as evidenced by back reflection Laue photographs. Plausibly, there are segregation zones (see Guinier 1963), consisting of domains of solid solution of composition different from the surrounding matrix but coherent with it. These have been considered as extended defects of the solid solution and not as a grain of a second phase introduced into the matrix.

Tin concentration along the rod axis of c-plane perpendicular crystals was examined by the X-ray fluorescence technique. A piece was cleaved from the each end of the specimens. Antimony $K\alpha$ and tin $K\alpha$ X-ray radiation was assessed by a scintillation counter. Relative compositions for these end pieces were compared and the results are summarized in table 3.1. The total statistical error could not be reduced below 4% because the samples were rather small and the count depends upon the specimen position in the instrument cavity, in which the intensity is not uniform. Samples were centralized in the cavity. These results demonstrate that the crystals are homogeneous within experimental error on a macroscopic scale.

Table 3.1.

Composition (at %)	Tin counts/Antimony counts	
	Seed end	Far end
2.0%	0.030	0.034
2.5%	0.043	0.055
3.0%	0.073	0.072
8.0%	0.149	0.156

Total statistical error is 4% for all the ratios.

CHAPTER IV

Details of the Apparatus and the

Experimental Procedure

4.1.   The Cryostat and the Sample Holder.

Potentiometric measurements were made on single crystal specimens placed in a cryostat designed to give a constant temperature bath between $77^{O}K$ and $273^{O}K$. This cryostat, shown in figure 4.1., was a metal Dewar constructed from two concentric, german silver tubes. A brass tail was hard-soldered onto the bottom of the outer tube. The upper half of the thick walled (1 mm), inner, german silver tube was machined to about half the original thickness to reduce heat conduction. The metal Dewar interspace was evacuated by a standard pumping system and the pressure measured by a Pirani gauge sensitive to pressures of the order of 10^{-3} mm. Hg. A heater, made of 40 gauge copper wire, was wound onto the tail of the inner tube and coated with araldite. The heater power, up to 2 watts, was obtained from a 4 volt battery regulated by a variable series resistance. The cryostat was placed inside an outer glass Dewar filled with liquid nitrogen.

The sample holder was made of a heavy copper cylinder with a flat face, machined onto it, on which to mount the

FIGURE 4.1 THE CRYOSTAT

rotation head
(∓180°)

lead and thermocouple
outlets

levelled horizontal
support plate

to vacuum
system

heater lead outlets

stainless steel support rod

german silver Dewar

add 5 in.

liquid air

coolant liquid

O ½ 1 in.

copper sample
holder

heater
(araldite coated)
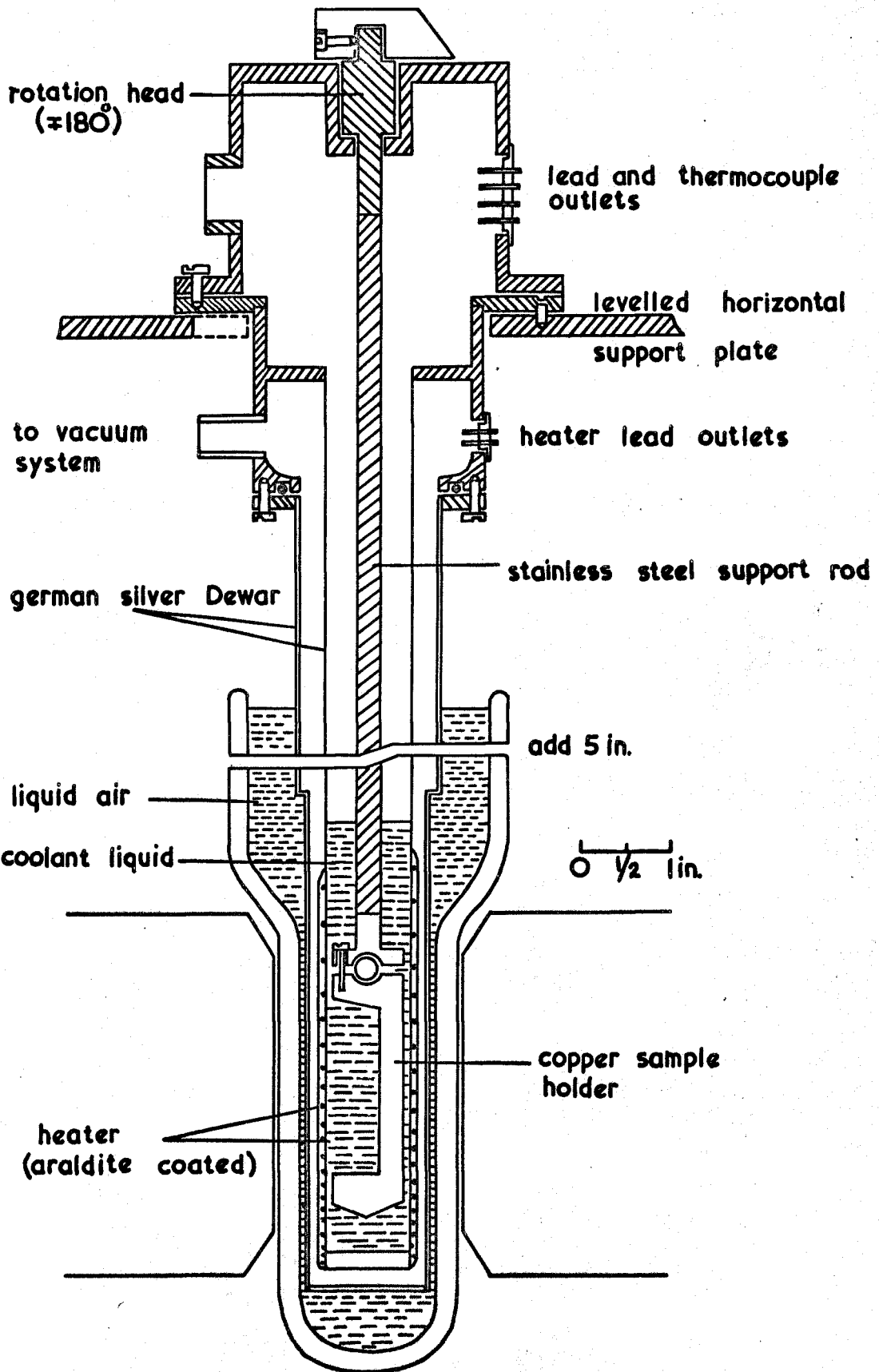
samples, figures 4.1. and 4.2. Samples were insulated from the
sample holder by fine paper and nail polish. Rotation of the
sample holder in the magnetic field, and consequently of the
specimens, was performed by a rotation head, shown in figure
4.1., whose axis was accurately perpendicular to a levelled
horizontal support plate on which the cryostat was mounted.
To ensure that the support rod axis at the bottom rotated
in the vertical, a kinematic adjustment was placed between the
support rod and the sample holder. This allowed accurate
specimen alignment in the magnetic field. By using the kinematic
adjustment the cylinder axis of the sample holder was made
parallel to the magnet poles for any rotation position; samples
were mounted along the cylinder axis.

For measurements at $139^{O}K$ and $183^{O}K$ the samples were
immersed in the non-flammable, five component, organic liquid
mixture of 14.5% chloroform, 25.3% methylene chloride, 33.4%
ethyl bromide, 10.4% transdichloroethylene and 16.4% trichloro-
methylene which remains liquid to below $130^{O}C$ (White 1959).
Because this mixture develops an appreciable conductivity above
about $200^{O}K$, normal hexane was used as the liquid bath at
$225^{O}K$ and $273^{O}K$. Two precalibrated, copper-constantan
thermocouples, one at each end of the sample, were used to
measure the sample temperature. The bath temperature was
controlled by adjustment of the pressure in the metal Dewar
interspace through a needle valve, and fine control was
achieved with the heater. To reach thermal equilibrium just
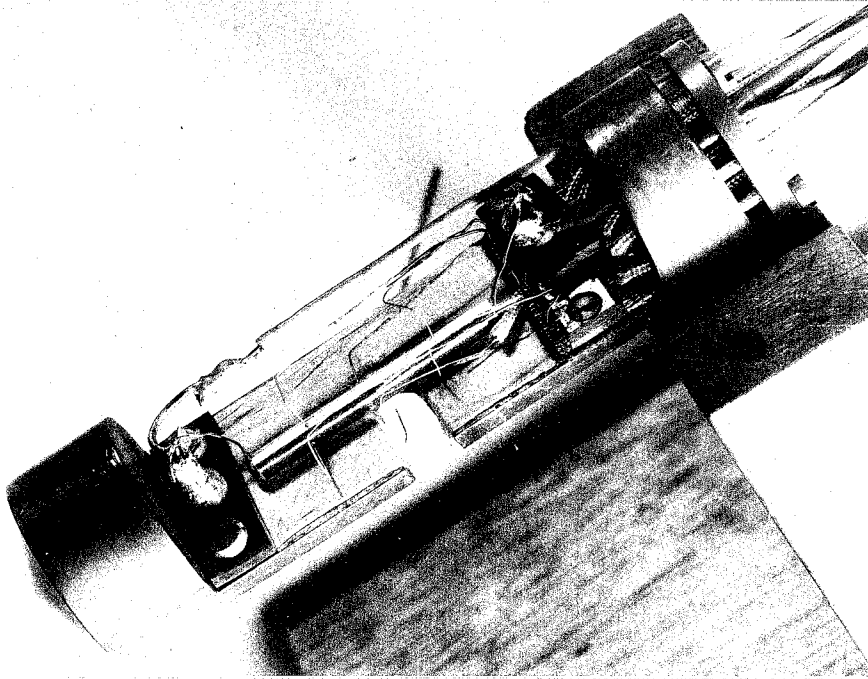
FIGURE 4.2   The sample holder;   the sample
shown is a 3.0 at.% tin alloy (S-90°).
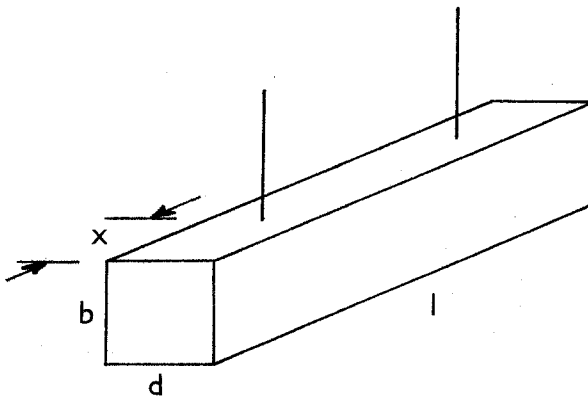
FIGURE 4.3   Geometry of the probes positions.

at the required temperature, although possible was a rather long
process and not essential. Therefore, a limiting value of
$\mp$ 0.5 degK was accepted. Because the measured magnetoresistivity
coefficients are not a very strong function of temperature, the
error arising from this temperature variation is negligible in
comparison with other errors.

The large thermal capacity of the system facilitated
control of the bath temperature to better than 0.05 degK over
long intervals. Measured magnetoresistivity coefficients for
undoped antimony were of the order of 10^{-9} ohm – cm per square
kilogauss. For example, at $183^{O}K$ the temperature dependence of
the resistivity ($\rho_{\parallel}$) was estimated as about 2 x 10^{-9} ohm – cm
per 0.01 degK. Therefore, it was necessary to keep the bath
temperature constant to better than 0.01 degK for measurements
at low magnetic fields. This was also achieved for shorter
periods of about 10 to 20 minutes.

4.2.   Current and Potential Contacts to Crystals

Current leads were soldered to the crystal ends by
60% tin/lead solder using tricene flux. Subsequently, samples
were washed with distilled water to remove any tricene present.
 Two sets of three voltage probes of enamelled, 36 gauge,
copper wire were spot welded to each pair of opposite faces,
figures 4.2 and 4.3, each probe being aligned on the centre
line.

To prevent shorting out of the Hall field, the potential contacts must be far from the ends. For any rectangular specimen with Hall voltage probes at a distance x from the ends, the measured Hall voltage is (Volger 1950)

$$V_H = R_H \; (\frac{HI}{d}) \; f(1/b, \; x/1) \tag{4.1}$$

where R_H is the Hall coefficient, H the magnetic field, I the current, and 1,b and d the length, width and thickness of the sample, figure 4.3. The function f, determined by the relative dimensions of the sample and the position of the probes on it, has values between 0 and 1 and measures the non-shorted fraction of the Hall field. Some calculated values of f for different values of 1/b and x/1 are presented in table 4.1.

Table 4.1.

Some values of function f (Volger 1950)

x/1 \ 1/b	2.0	4.0	∞
0.250	0.82	0.98	1.00
0.500	0.92	1.00	1.00

To obtain the true values of the Hall and magnetoresistivity coefficients directly, f ought to be made equal to unity. The values of 1/b of the samples used in the experiments are between 8 and 10. Thus, from the table 4.1. it can be seen that placing the probes at one fourth of the sample length away from the ends is sufficient to prevent end effects. For pure

antimony specimens the potential probes are placed at about 1/3 and for doped specimens at 1/4 of the sample length away from the ends.

4.3.   The Measuring System.

Magnetic fields were obtained from 4" electromagnet and measured by a fluxmeter. The cryostat size limited to pole gap to 2" and, consequently, the magnetic fields up to 6000 gauss, quite adequate for the low field galvanomagnetic effect measurements.

Figure 4.4. represents the main features of the system for measuring sample potentials necessary for deter-mination of the resistivity and the Hall and magnetoresistivity coefficients. Potential measurements were made using a precision decade potentiometer (Pye, Cat.No. 7600), a galvanometer preamplifier (Pye, Cat.No. 11330) and a galvanometer (Pye, Cat.No. 7903/S). On the lowest range of the potentiometer, potentials below 0.02 volts were measurable in steps of $0.1\mu V$. The overall sensitivity of the preamplifier - galvanometer pair is about 2000 mm. per μA on the most sensitive range. A 10 turn helical 1 ohm slide wire, kept in a closed tufnol box, was used to balance out the "IR drop" occurring in the transverse galvanomagnetic field measurements. All electrical connections were sited in a closed box to keep them at a constant temper-ature and minimize contact e.m.f.'s. Screened copper wires to prevent capacitive pick-up were used for electrical connections

FIGURE 4.4 THE MEASURING CIRCUIT
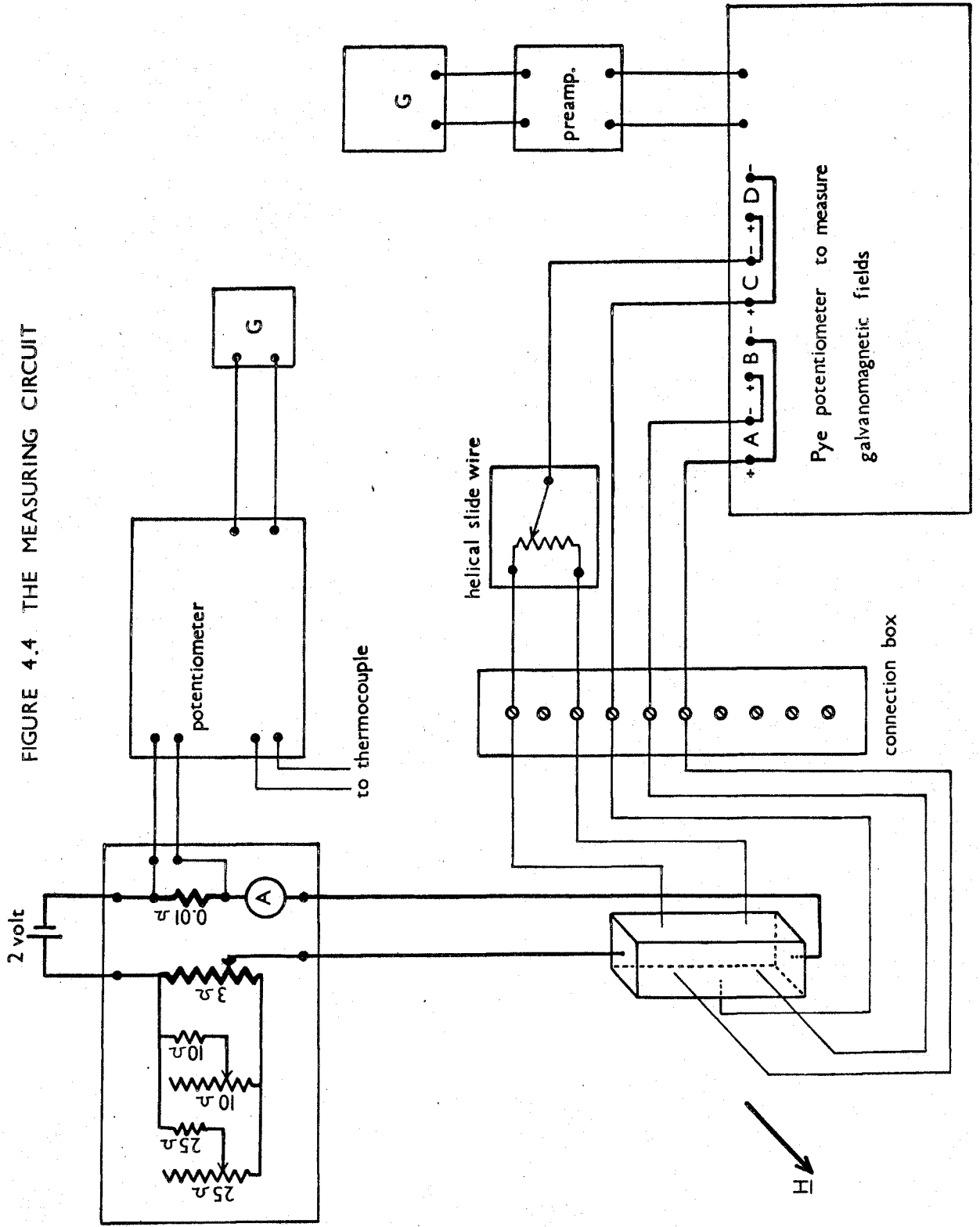
from the connections box to the potentiometer and from the
potentiometer to the galvanometer preamplifier.

Sample current, usually about 40 A per cm^2 and cons-
tant to better than 1 part in 10^4, was obtained from two 2V
batteries connected in parallel, figure 4.4. A separate
potentiometric system was used to measure the current by
monitoring across a 0.01 ohm standard resistance. Any change
in the current was corrected manually. For tin doped specimens
a current density of about 75 A per cm^2 was employed. A $_{42}$ and
$-A_{44}$ were also measured for antimony specimens with this current
density.

4.4.   Experimental Procedure.

4.4.1.   Measurements on Pure Antimony Samples.

The types of experimental configurations necessary
for measurement of the twelve magnetoresistivity coefficients
up to second order in magnetic field have been described in
section 2.3 (page 23) and are shown in figure 2.1. The
coefficients were obtained from two different sets of one
S - 0° and two S - 90° specimens. The six particular experi-
mental specimen orientations used are shown in figure 4.5.
Here are shown the orientation of the crystals, the galvano-
magnetic fields, which were measured, and the directions of the
current $\underline{J}$ and the magnetic field $\underline{H}$. For specimen s - 0°- 1
only, the experimental configuration differs from that shown
in figure 2.1-(c). During the experiments, the magnetic field
is fixed and the samples are rotated about the vertical axis.
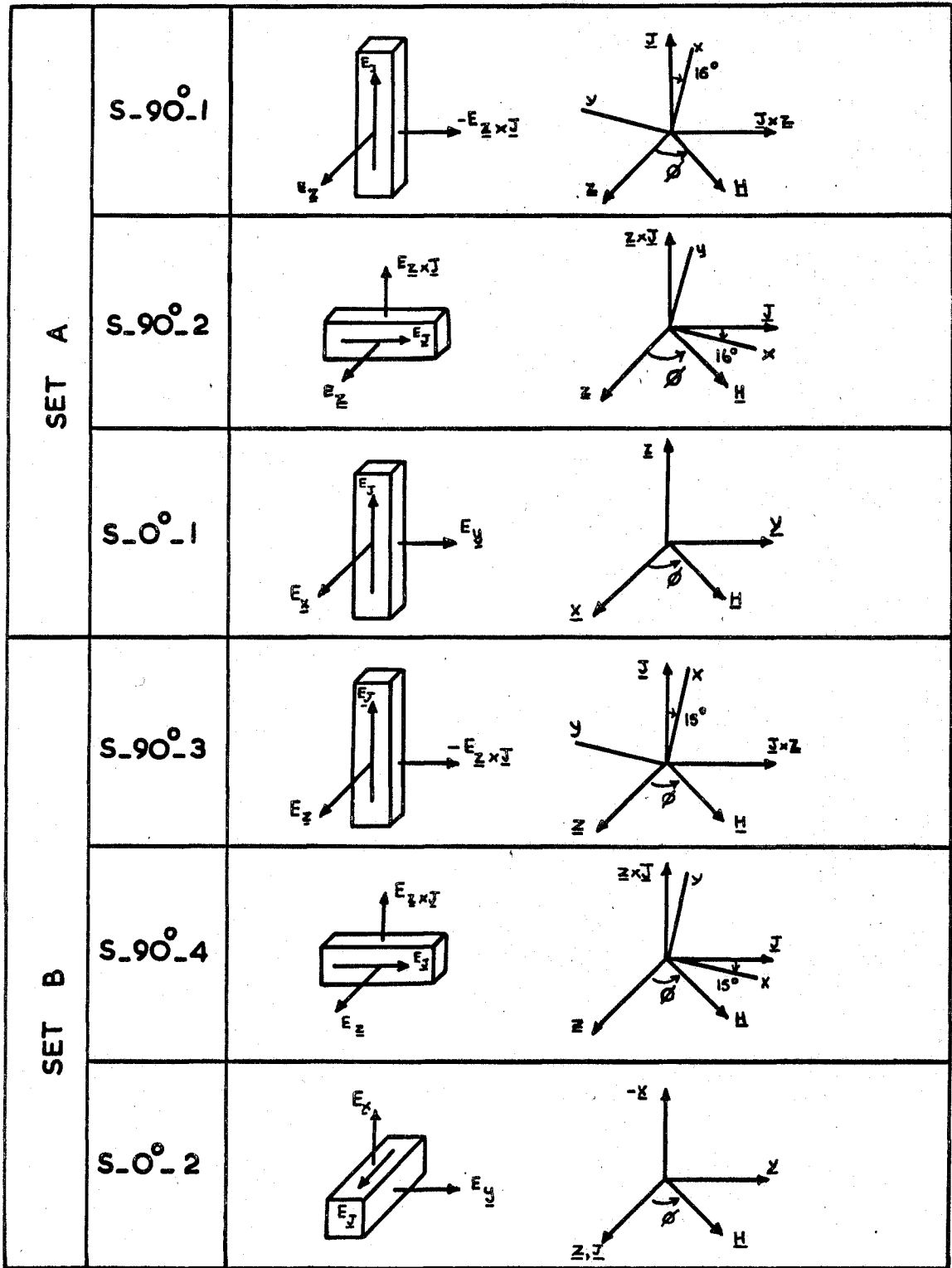
FIGURE 4.5 Specimen orientations showing the measured galvanomagnetic fields, the magnetic field and the current directions.

For particular selected values of the angle $\emptyset$, only one coefficient contributes markedly to the measured galvanomagnetic field E and such values of $\emptyset$ were chosen for measurements. However, some of the coefficients cannot be separated from others by changing $\emptyset$; in these cases the galvanomagnetic field E is measured for different suitable values of $\emptyset$ and the required coefficients calculated from the configuration equations 2.17, 2.18, and 2.19 (pages 25 and 26).

Arbitrary choice of co-ordinate systems of the x, y, and z axes were made during the experiments. All magneto-resistivity coefficients including the absolute values of A_{24} and A_{42} can be determined without referring to a particular rotational co-ordinate system. The necessity to define a specific co-ordinate system arises when the signs of A_{24} and A_{42} are significant. In the right handed Cartesian co-ordinate system defined by rotation in the y-z plane away from the trigonal axis through the pseudo-trigonal point towards the bisectrix axis, A_{24} and A_{42} have positive signs. An experiment to find out the sign of A_{42} is presented in detail in section 4.5, because of its importance in determination of the sense of the tilt angle of the ellipsoidal surfaces in $\underline{k}$-space through calculated signs of B_{24} and B_{42}. The sign of the other magnetoresistivity coefficients are positive except that of A_{44}.

Generally, one or more galvanomagnetic coefficients higher than second order in magnetic field contribute to

each measured galvanomagnetic field. The contribution of
higher order terms increases with decreasing temperature.
These contributions have to be eliminated, and this is done
conveniently by a graphical method.

<u>The transverse galvanomagnetif fields: determination</u>
<u>of the Hall coefficients R_{123} and R_{231}, and the</u>
<u>magnetoresistivity coefficients A_{42} and $-A_{44}$</u>

The measured, transverse galvanomagnetic field, in
general, contains both symmetrical and antisymmetrical terms
and can be written symbolically in the form

$$E_t = JHR(\emptyset) + JH^2A(\Theta, \emptyset) + JH^3T(\Theta, \emptyset) + \ldots \ldots \qquad (4.2)$$

where J is the current density and H the magnetic field. $R(\emptyset)$
and $A(\Theta, \emptyset)$ are some function of coefficients R_{ijk} and A_{ij}
respectively, depend upon the angles Θ and $\emptyset$, and have the
explicit form given by the configuration equations (2.17 to
2.19). $T(\Theta, \emptyset)$ and higher order functions relating to higher
powers of magnetic field are the contributions which are to be
removed. E_t is set equal to zero for H = O and the symmetrical
and antisymmetrical terms are separated by taking measurements
for $\mp\underline{H}$. The intercept of the graph $\left[E_t(\underline{H}) + E_t(-\underline{H}) \right] / JH^2$
plotted against H^2 determines $2A(\Theta, \emptyset)$. The value of $2R(\emptyset)$
is found as the intercept on the graphs of $\left[E_t(\underline{H}) - E_t(-\underline{H}) \right] / JH$
versus H^2; if the value of the function $T(\Theta, \emptyset)$ is required,
it can be readily found from the slope of the linear region
of this curve. But no systematic measurements of the higher

order terms have been made. Any contribution of the Nernst field due to a temperature gradient along the specimen is eliminated by taking measurements for $\mp$ $\underline{J}$ and averaging the results.

Antimony has two independent low field Hall coefficients, $-R_{123}$ (where the last indice shows the magnetic field direction) and $-R_{231}$, measurable when the magnetic field is parallel and perpendicular to the trigonal axis respectively. $-R_{123}$ can only be measured from $s - 90^{\circ}$ samples. For the experimental configuration of samples $s - 90^{\circ} - 1$ and $s - 90^{\circ} - 3$, shown in figure 4.5., the galvanomagnetic field $E_{\underline{z} \times \underline{J}}$, including the terms up to H^3, is given by (Juretschke 1955)

$$E_{\underline{z} \times \underline{J}} = -JHR_{123} \cos \emptyset + JH^2 A_{24} \sin 3\theta \sin 2\emptyset$$

$$- JH^3 (T_{322} \cos 3\theta \sin^3\emptyset + 3T_{331} \sin^2\emptyset \cos\emptyset + T_{333} \cos^3\emptyset). \tag{4.3}$$

This takes the form, for $\emptyset = o$

$$E_{\underline{z} \times \underline{J}} = - JH(R_{123} + H^2 T_{333}) \tag{4.4}$$

Equation 4.4 also applies to the configuration of samples $s - 90^{\circ} - 2$ and $s - 90^{\circ} - 4$, for $\emptyset = o$.

$-R_{123}$ was measured from samples $s - 90^{\circ} - 1$ and $s - 90^{\circ} - 3$ for $\emptyset = o$ and π. The plot of $E_{\underline{z} \times \underline{J}}/JH$ against H^2 is shown in figure 4.6. for sample $s - 90^{\circ} - 1$. No contribution of the phenomonological coefficient T_{333} was present up to a magnetic field of 4000 gauss, even at $77^{\circ}K$. Similar straight lines were obtained for specimen $s - 90^{\circ} - 3$.

FIGURE 4·6
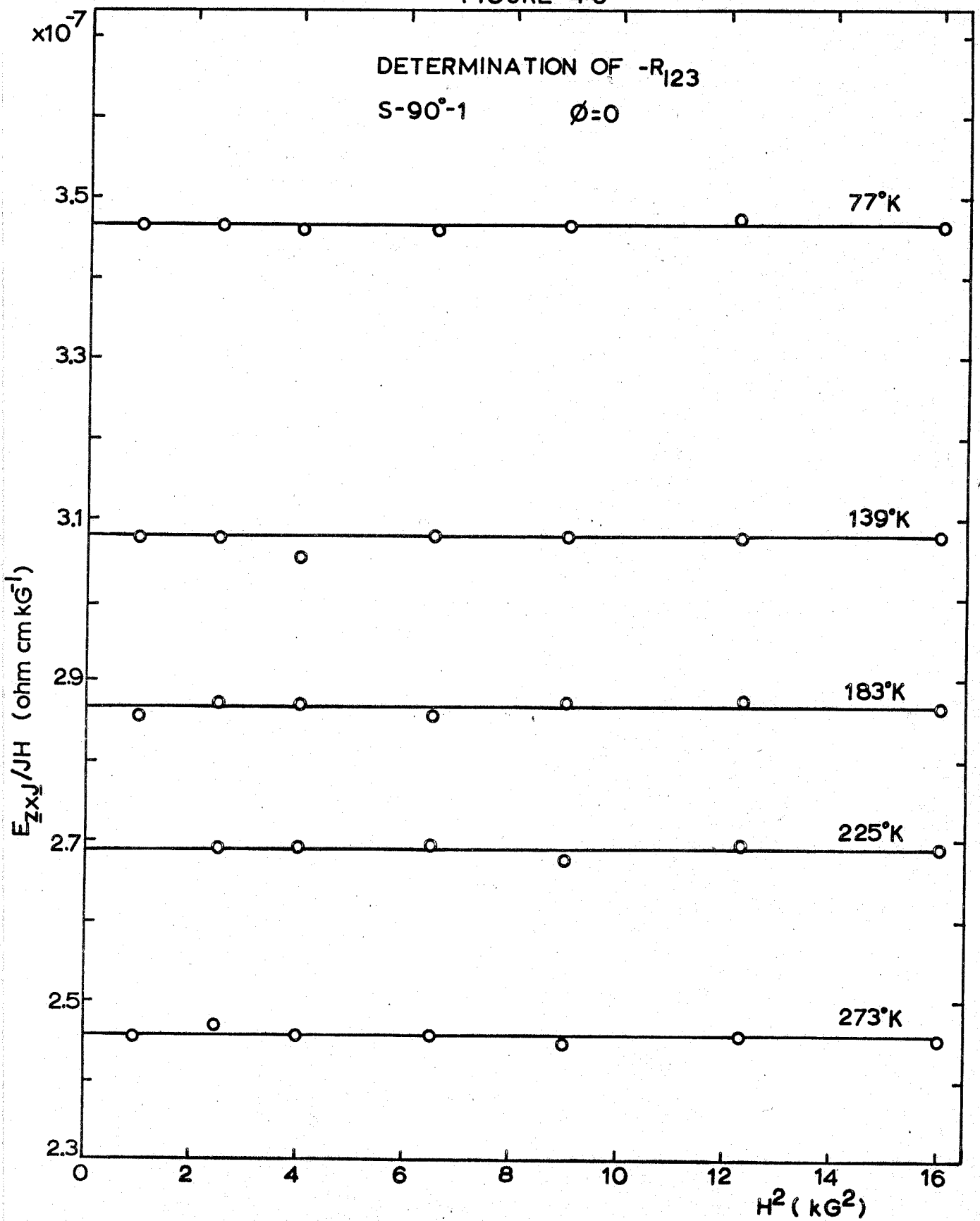
The agreement between the measured values of $-R_{123}$ from the two specimen was within 1.5%. At $77^O K$ carrier mobilities have been estimated as of the order of 5×10^6 e.s.u. Then, for instance, for H = 3 Kgauss μH is 0.5; thus the condition $\mu H \ll 1$ is not satisfied. Therefore one might expect to observe contributions of higher order terms : T_{333} must be close to zero.

$-R_{231}$ can be determined from both types of sample. For samples s - 90° - 1 and s - 90° - 3 the measured galvano-magnetic field $E_{\underline{z}}$ is given by

$$E_{\underline{z}} = JHR_{231}\sin\phi + JH^2 A_{42}\sin 3\theta \, \sin^2\phi$$

$$+JH^3 (3T_{112}\sin^3\phi + 3T_{113}\sin\phi\cos^2\phi + 3T_{224} \cos 3\theta\sin^2\phi$$

$$\cos\phi) \qquad (4.5)$$

and takes the form for $\phi = \frac{\pi}{2}$

$$E_{\underline{z}} = JHR_{231} + JH^2 A_{42}\sin 3\theta + 3JH^3 T_{112} \qquad (4.6)$$

The galvanomagnetic field $E_{\underline{x}}$ for samples s - 0° - 1 and s - 0° - 2, measured at $\phi = \frac{\pi}{2}$, has the form of equation (4.6) except in the second term which vanishes. $-R_{231}$ was determined from specimens s - 0° - 1 and s - 90° - 3 at all temperatures and from other specimens at some temperatures. The spread of values was about 4%. The graph of $E_{\underline{z}}/JH$ against H^2 as a function of temperature for sample s - 0° - 1 is shown in figure 4.7. The curves evidence the contribution, particularly at lower temperatures, of higher-order coefficients. From

FIGURE 4.7

DETERMINATION OF $-R_{231}$

$S \cdot 0 \cdot 1$ $\phi = 1/2\pi$
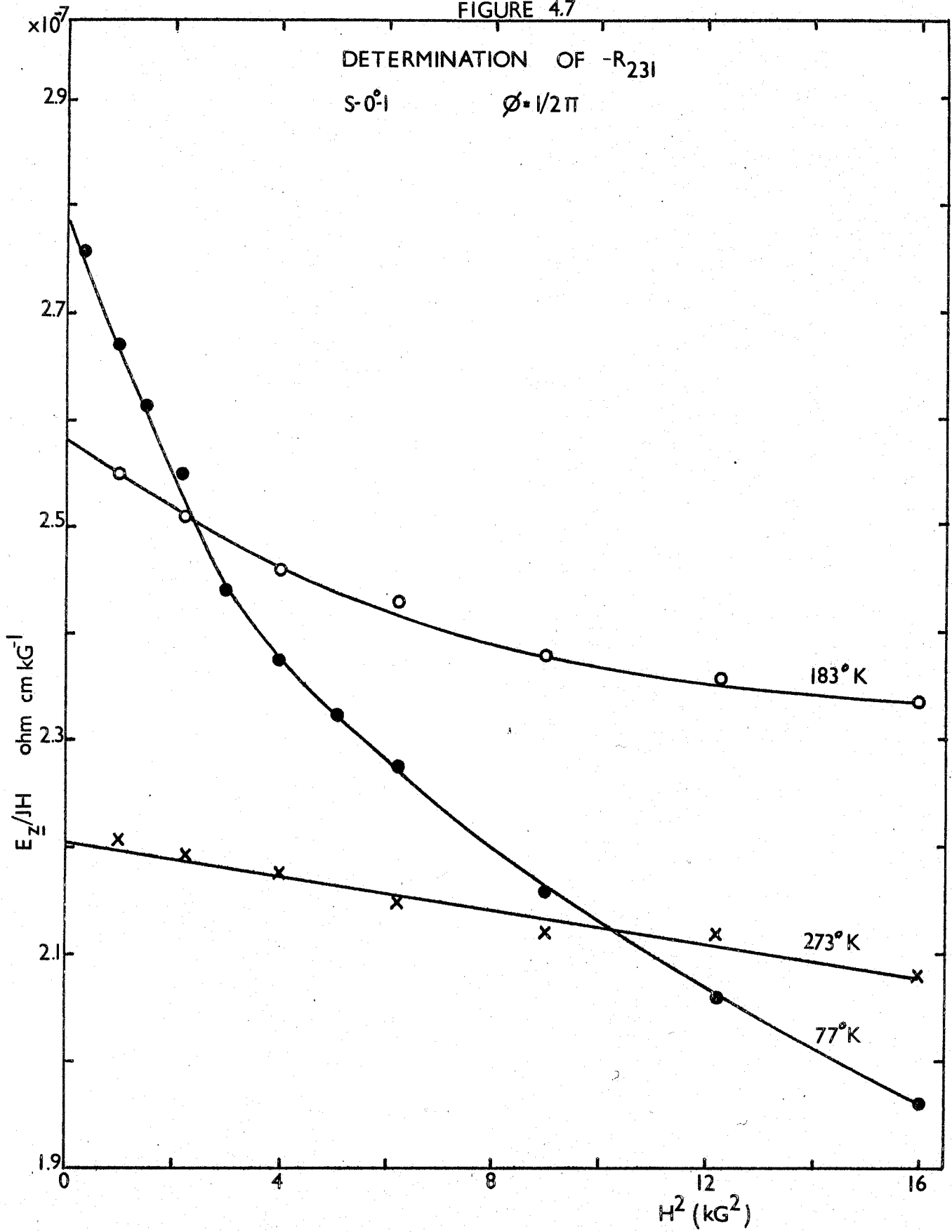
the linear region of the curves, the value of T_{112} was determined and is presented in table 4.2.

<div align="center">Table 4.2.</div>

Temp. $^{\circ}K$	T_{112} (s – 0° – 1)	T_{112} (s – 90° – 3)
273	0.23	0.23
183	1.1	1.0
77	5.5	4.0

Units; 10^{-9} ohm – cm –kG^{-3}.

The values of A_{42} and $-A_{44}$ can only be determined from the transverse field measurements. It was not possible to determine accurately the value of A_{42} when the components of $-R_{ijk}$ were present in the measured field. However, for two experimental configurations, shown in figure 2.1-(b) and (c), the Hall coefficients do not contribute to the transverse fields $E_{\underline{z}}$ and $E_{\underline{y}}$ respectively. These fields allow determination of A_{42} and $-A_{44}$. The coefficients A_{42} and $-A_{44}$ were determined from the samples s – 90° – 4 and s – 0° – 2. The galvanomagnetic field $E_{\underline{z}}$, for experimental configuration of s – 90° – 4, is given by

$$E_{\underline{z}} = -JH^2(A_{42}\sin3\Theta\sin^2\emptyset + A_{44}\sin2\emptyset). \qquad (4.7)$$

Suitable values of the angle $\emptyset$, for the measurements, are $\frac{\pi}{2}$ and $\frac{\pi}{4}$. For $\emptyset = \frac{\pi}{2}$, only A_{42} contributes to field $E_{\underline{z}}$ and was

FIGURE 4.8

DETERMINATION OF A_{24} AND A_{44}
S-90°-4
77°K
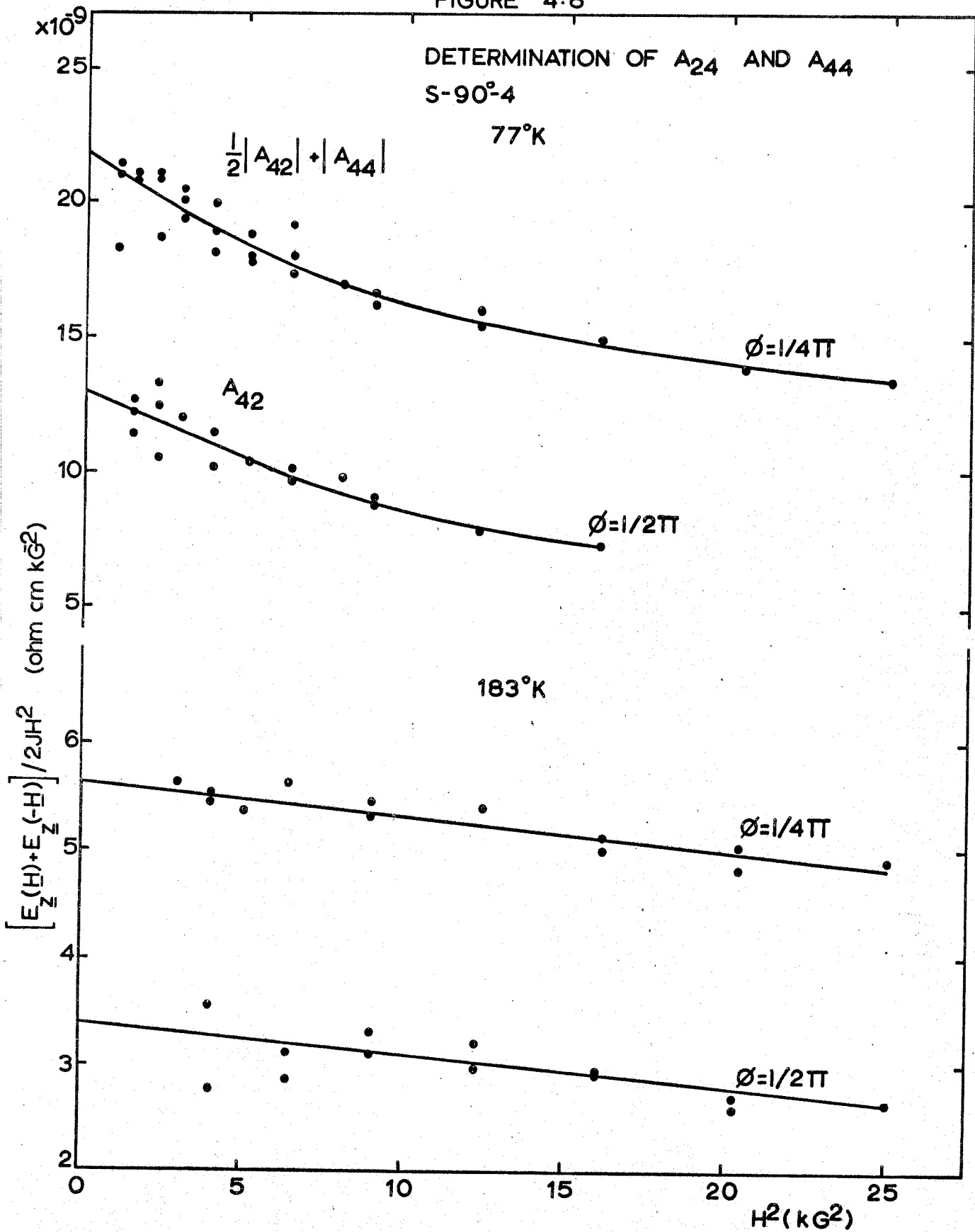
obtained as the intercept of the graph $\left[E_z(H) + E_z(-H)\right]/2JH^2$

against H^2, figure 4.8.   The intercept should be equal to

$\frac{1}{2}\left|A_{42}\right| + \left|A_{44}\right|$ for measurements at $\emptyset = \frac{\pi}{2}$. A_{44} was calculated

from this intercept by using the already determined value of

A_{42}. E_z has a maximum value at $\emptyset = \frac{\pi}{4}$ and a minimum at

$\emptyset = \frac{\pi}{4} + \frac{\pi}{2}$ in the co-ordinate system where A_{42} is positive.

In the second co-ordinate system, in which A_{42} is negative,

the maximum occurs at $\emptyset = \frac{\pi}{4} + \frac{\pi}{2}$ and the minimum at $\emptyset = \frac{\pi}{4}$.

Thus, the absolute value of A_{42} can be determined by finding

out the maximum value of E_z without defining the co-ordinate

system.   This discussion applies equally to sample s - 0° - 2

from which A_{42} and A_{44} have been determined through measurements

of the galvanomagnetic field E_y.

The longitudinal galvanomagnetic fields: determination of the magnetoresistivity coefficients A_{11}, A_{12}, A_{13}, A_{31}, A_{33}, and A_{24}.

The longitudinal galvanomagnetic field E_1, which

contains only symmetrical terms, for any experimental

configuration can be written symbolically in the form

$$E_1 = \rho J + JH^2 A(\Theta,\emptyset) + JH^4 F(\Theta,\emptyset) + \ldots \ldots \qquad (4.8)$$

where ρ is the resistivity.   The intercept of the graph

$\left[E_1(H) - E_1(O)\right]/JH^2$ plotted against H^2 determines the function

$A(\Theta,\emptyset)$ and the value of the function $F(\Theta,\emptyset)$ can be found

from the slope of the linear region of the curve.   But $F(\Theta,\emptyset)$

bears a complicated relationship with the band structure

parameters and cannot be used to extract information. Any contributions of Hall coefficients to the longitudinal galvano-magnetic field due to misalignment of the contact probes were cancelled out by measuring $E_1(H)$ for both magnetic field directions and averaging. In the present measurements $E_1(H)$ were determined in the order, $E_1(O)^{in\cdot}$, $E_1(H)$, $E_1(-H)$, $E_1(O)^{fin\cdot}$ for a given current direction and angle $\emptyset$. The mean value of $E_1(H) - E_1(O)^{in\cdot}$ and $E_1(-H) - E_1(O)^{fin\cdot}$ were calculated and used in the plot. If any significant change was observed in the readings $E_1(O)^{in}$ and $E_1(O)^{fin}$, these were discarded. Measurements have been taken for $\emptyset$ and $\emptyset + \pi$ and for both current directions, and the results obtained were plotted separately.

The values of A_{12}, A_{13} and A_{24} were determined through the galvanomagnetic field $E_{\underline{J}}$ for samples s $- 90^O - 1$ and S $- 90^O - 3$. The field $E_{\underline{J}}$, given in terms of the phenomonological coefficients up to second order in H in equation 2.17.(page 25), takes the form for $\emptyset = O$

$$E_{\underline{J}} = \rho_{11}J + JH^2 A_{13} \qquad\qquad (4.9)$$

and for $\emptyset = \frac{\pi}{2}$

$$E_{\underline{J}} = \rho_{11}J + JH^2 A_{12} \qquad\qquad (4.10)$$

Thus, A_{13} and A_{12} were determined as the intercept of the graph $\left[E_{\underline{J}}(H) - E_{\underline{J}}(O)\right] /JH^2$ plotted against H^2 for $\emptyset = O$ and

$\emptyset = \frac{\pi}{2}$ respectively. For $\emptyset = \frac{\pi}{4}$ and $\emptyset = \frac{3\pi}{4}$ the field $E_{\underline{J}}$, depending on the sign of A_{24}, is given by

$$E_{\underline{J}} = \rho_{11}J + JH^2(\frac{1}{2}A_{12} + \frac{1}{2}A_{13} \mp A_{24}\cos3\Theta) \qquad (4.11)$$

Once the values of A_{12} and A_{13} were known, A_{24} was determined from the intercept obtained from the measurements of the field $E_{\underline{J}}$ at both the suitable values of angle $\emptyset$ and the results were averaged. The graph, necessary to determine these coefficients, obtained for sample s - 90° - 1 at 139^OK is presented in figure 4.9. The plot of the intercepts obtained from figure 4.9. against $\emptyset$ is shown in figure 4.10., together with the values of the intercepts determined from similar graphs at the other temperatures. The curves were fitted by using the equation 2.17 with the average value obtained for A_{24}.

A_{11} was found from the measurements of the field $E_{\underline{J}}$ at $\emptyset = \frac{\pi}{2}$ for samples s - 90° - 2 and s - 90° - 4. The graph of $\left[E_{\underline{J}}(H) - E_{\underline{J}}(O)\right] /JH^2$ against H^2 plotted at different temperatures for sample s - 90° - 4 is shown in figure 4.11; the intercept gives the value of A_{11}, see equation 2.18 (page 25). A_{13} and A_{24} could also be found from these samples. They have been determined at several temperatures in order to compare them with the results obtained from the first experimental configuration.

The remaining two coefficients A_{31} and A_{33} were obtained from the sample s - 0° - 2 with suitable selections

FIGURE 4.9

DETERMINATION OF A_{12}, A_{13} AND A_{24}

S-90° -4

139° K

A_{12}

$\phi = 1/2\pi$

$\phi = 1/4\pi$

$\phi = 3/4\pi$

A_{13}

$\phi = 0$

$\left| [E_j(H) - E_j(0)] \right| / JH^2$ (ohm cm kG^{-2})

$\times 10^8$

H^2 (kG^2)
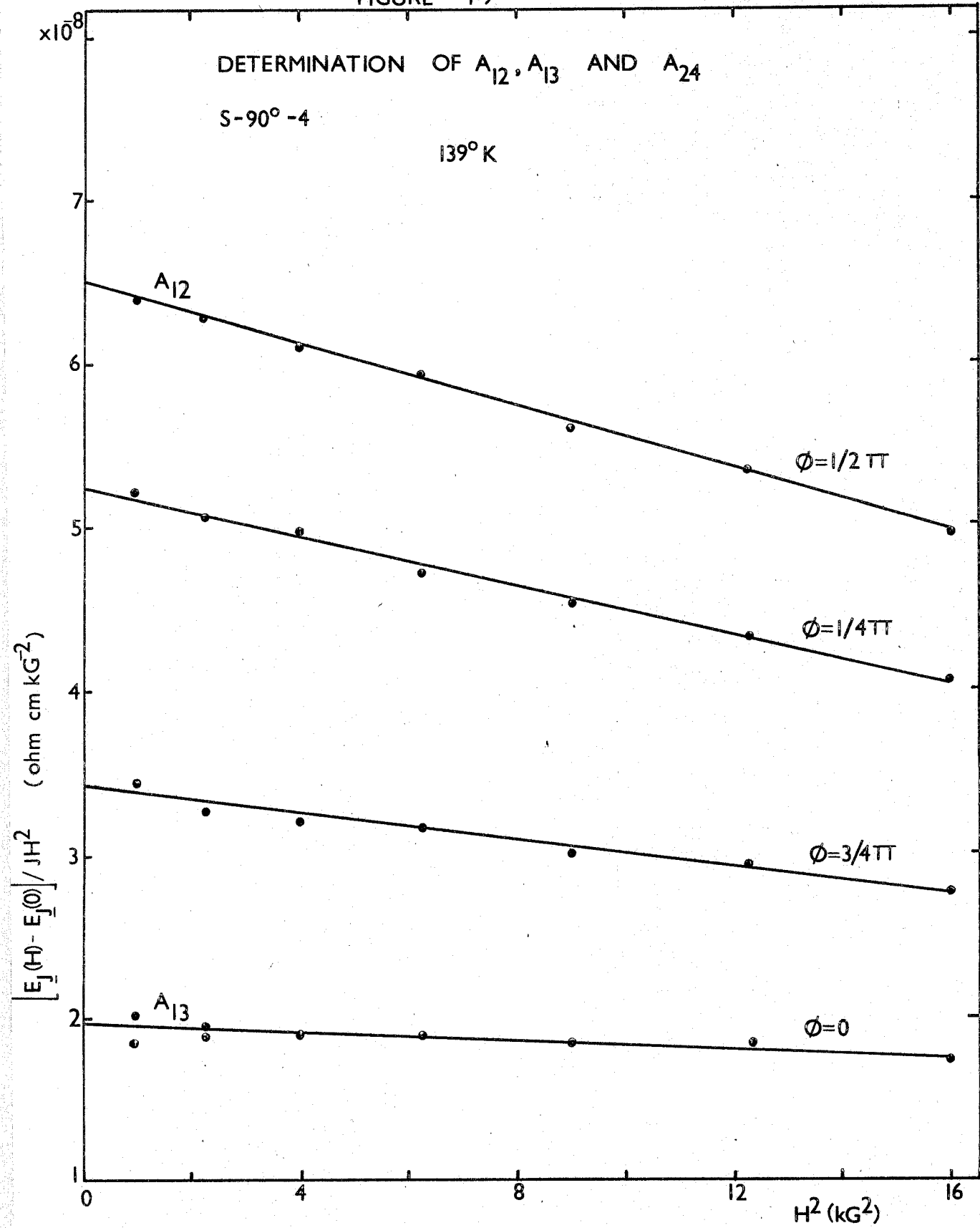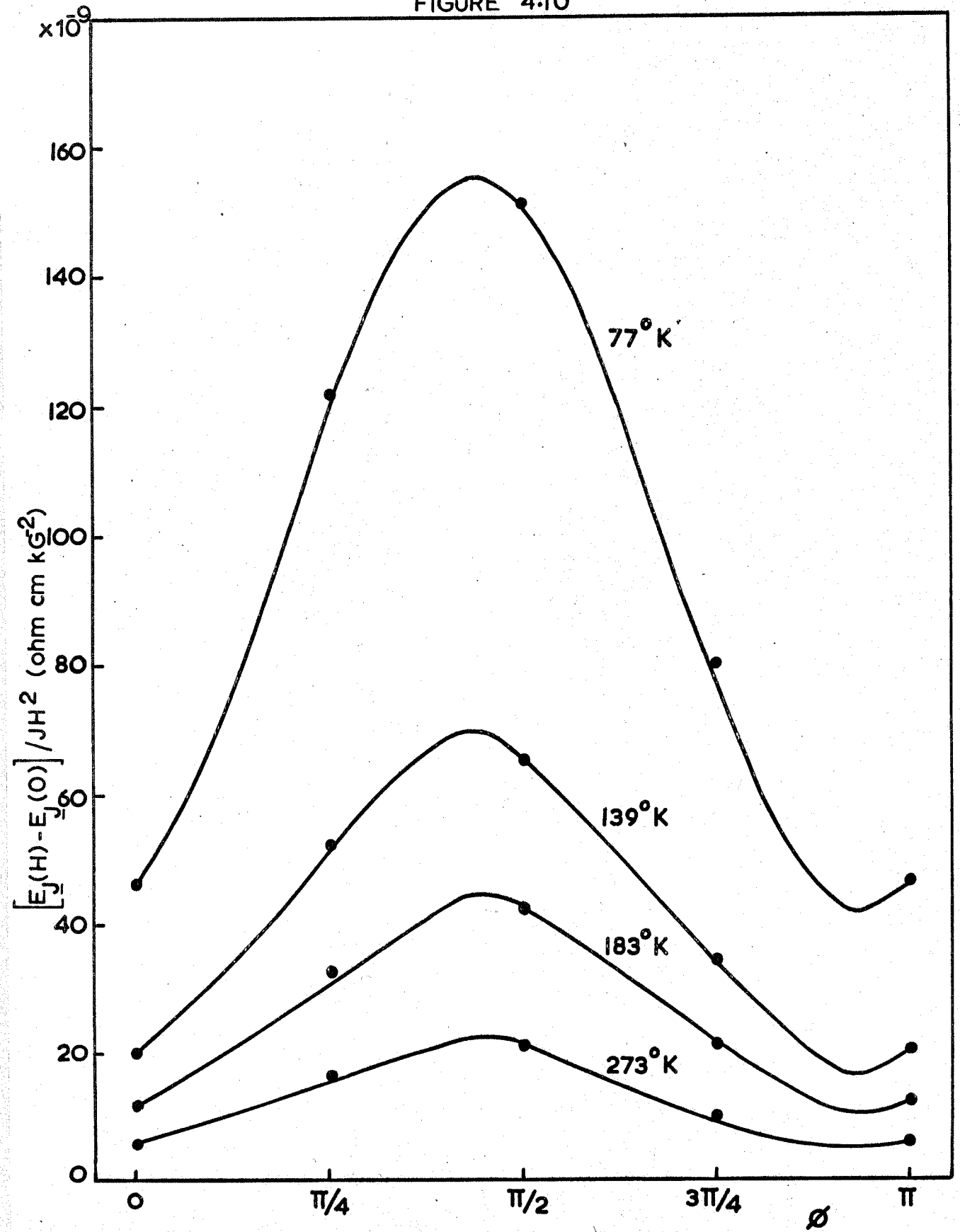
FIGURE 4.10

FIGURE 4.11

DETERMINATION OF $A_{||}$

S-90°-4 $\emptyset = 1/2\pi$
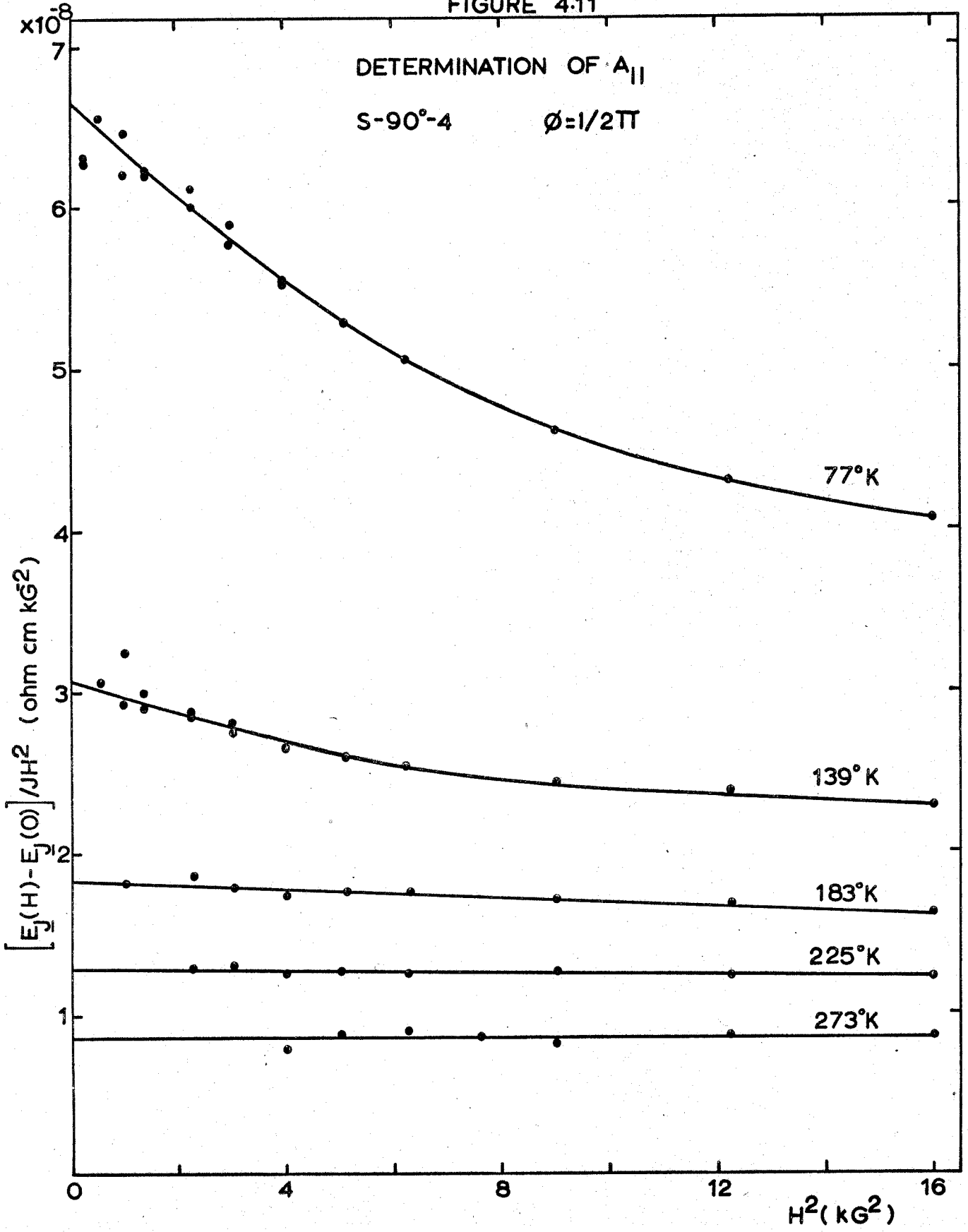
FIGURE 4·12

DETERMINATION OF A_{31} AND A_{33}

S-0°-2

77°K
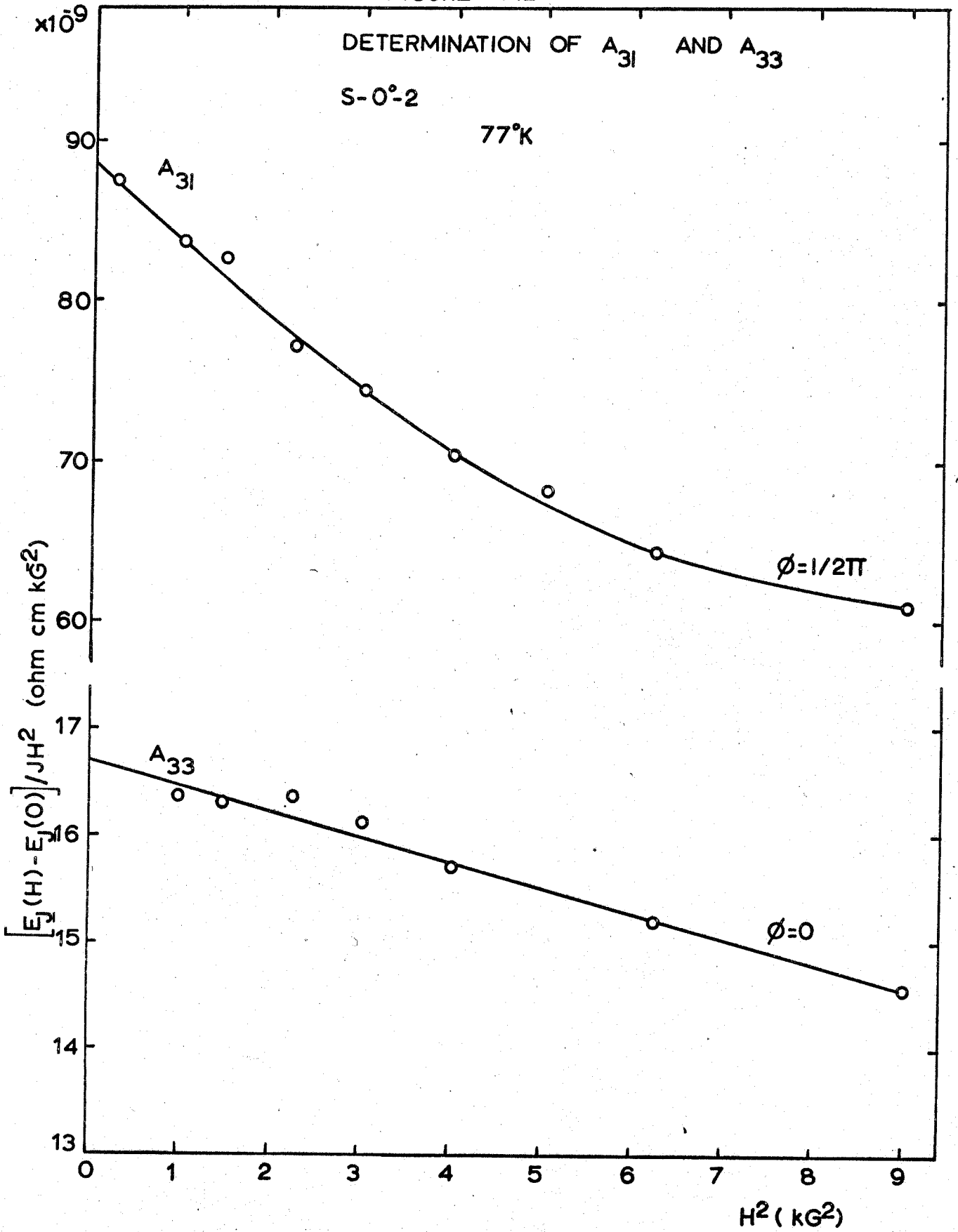
of the angle $\emptyset$. An example of the determination of these coefficients at 77^OK is presented in figure 4.12. A_{31} was also found from specimen s - 0° - 1.

The contributions to the galvanomagnetic field of higher order phenomonological coefficients, particularly at 77^OK are substantial, as can be seen from the figures presented here. Although, from the slope of the linear region of the curves some of the coefficients F_{ijklmn} could be found, no attempt was made to determine them.

4.4.2.   Measurements in Tin Alloyed Specimens

Two samples at each composition, one s - 90° and one s - 0°, were employed to determine some of the coefficients in tin-alloy single crystals at 77^OK, 183^OK and 273^OK. The experimental configuration used for s - 90° samples was that shown in figure 2.1-(a) and for s -0° samples that in (c). These coefficients measured were ρ_{11}, ρ_{33}, $-R_{123}$, $-R_{231}$, A_{12}, A_{13}, A_{31}, and A_{33}. $-R_{231}$ could be measured from both s - 90° and s - 0° specimens; this enables assesment of the matching of each pair of alloyed specimens.

For tin-alloy specimens, the carrier mobilities were relatively small; the higher order terms were not observed even at 77^OK with the maximum applied magnetic field of 6 kilogauss. Therefore, to obtain the values of the galvano-magnetic coefficients, the quantities $\left[E_1(H) - E_1(O) \right] / JH^2$ and $\left[E_t(H) - E_t(-H) \right] / 2JH$ determined from different magnetic field values were simply averaged.

There was a slight, steady change of temperature of

the coolant liquid with time. The rate of temperature change
was generally about 0.01 deg.K per 15 minutes. If the measured
longitudinal galvanomagnetic field was of the order of a few
μV, this temperature change introduced an error of up to
10% in the measured potential difference $E_1(H) - E_1(O)$. This
error was usually negligible in pure antimony but it was
important in tin-alloy specimens where the coefficients
measured were of the order of 10^{-10} ohm $-$ cm/kG^2. When this
effect was important, the procedure of determination of
$E_1(H) - E_1(O)$ was carried out in the following way $E_1(O)^{in}$,
$E_1(H)$, $E_1(O)^{mid}$, $E_1(-H)$, $E_1(O)^{fin}$ were measured for each value
of $\underline{H}$; and $E_1(H) - E_1(O)$ was found by appropriate averaging
of the two results for each magnetic field direction.

4.5. Determination of the Sign of the Coefficient A_{42}

The sign of A_{42} can be conveniently determined from
the galvanomagnetic field E_y for sample s $-$ O^O $-$ 2, figure
4.5. For $\emptyset = \frac{\pi}{2}$ (i.e. bisectrix axis parallel to the applied
magnetic field) E_y is given simply by

$$E_y = JH^2 A_{42} \tag{4.12}$$

The sign of E_y determines the sign of the coefficient A_{42}.
In figure 4.13-(a) the experimental configuration is shown
relative to the major crystallographic directions on which
the rotational co-ordinate systems are based. The symbol $\triangle$
refers to the right handed co-ordinate system defined by

FIGURE 4.13

Determination of the sign A_{42}
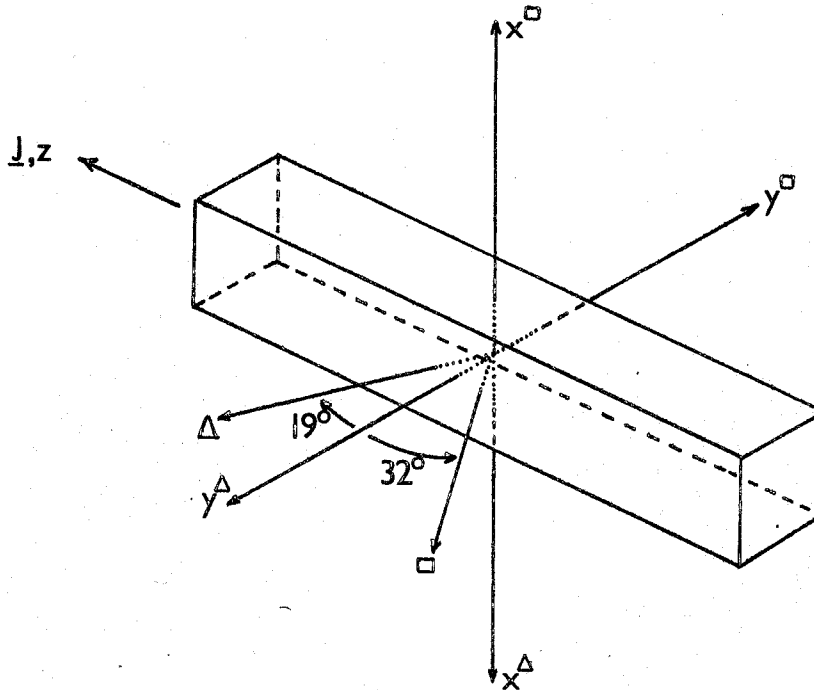
(a)   Sample orientation relative to major
crystallographic directions
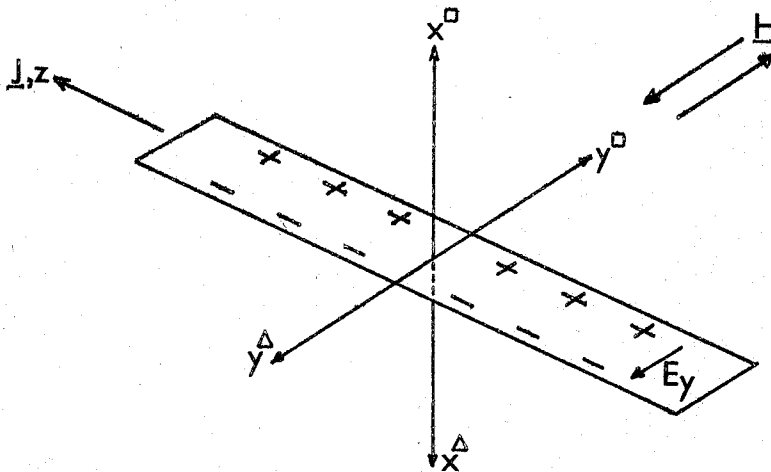
(b)   The polarization obtained when a magnetic
field is applied.

rotation through the pseudo-trigonal direction and the symbol □ to a rotation through the pseudo-fourfold direction. The z-axis is common in both systems and is determined by the direction of the current $\underline{J}$. Since E_y is proportional to H^2, the sign of the magnetic field, applied along the y-axis, need not be considered.

The experiment was carried out at liquid nitrogen temperature for magnetic fields between 3 and 5 k.gauss. The polarization obtained in the magnetic field is shown in figure 4.13-(b). E_y is positive in the co-ordinate system of axes x^Δ, y^Δ and z , giving a positive sign for A_{42} in this system. In the other co-ordinate system of axes $x^\square$, $y^\square$ and z , A_{42} has a negative sign. If the current direction is altered, the sign of E_y changes, together with the direction chosen for the z-axis: the system defined are now rotated 180° about the x-axis. Results are the same.

4.6.   Estimation of Errors.

The following errors were present in each measured galvanomagnetic field E:

(i)   a systematic geometrical error arrising from the determination of the cross sectional area of the rods ($\mp$ 2%) and the distance between the potential probes ($\mp$ 0.5%);

(ii)   an error of about $\mp$ 2% in the magnetic field;

(iii)   an error of $\mp$ 0.2 μV in reading the potential difference.

Other sources of error were present in the galvano-

magnetic field measurements. These include misalignment of the sample in the magnetic field, thermomagnetic effects, fluctuation of sample current and temperature variation of the coolant liquid; for pure antimony specimens these were negligible in comparison to the errors detailed above. However in alloy specimens fluctuation of sample current (a high current density of about 75 A per cm^2 was employed) and temperature variations of the coolant liquid were important in longitudinal galvanomagnetic field measurements. For these two sources of error and relatively large error in the smaller potential difference readings, the spread of values of the coefficients A_{ij} obtained from different measurements were between 15% to 30%.

In pure antimony specimens, the values of $-R_{ijk}$ and A_{ij} were estimated graphically from many measurements taken at different magnetic field. This ought to reduce the unsystematic errors. Some of the intercepts on the graphs were calculated by the least square method from the linear region of the curves. The calculated standard deviations for the intercepts were between $\mp$ 1% to $\mp$ 3%.

The value of the angle Θ was only needed in determination of three coefficients A_{24}, A_{42} and $-A_{44}$. The error on determination of the angle Θ was estimated as $\mp$ 1^O. Since the relations are proportional to 3Θ, an additional error of about $\mp$ 5% is present in the values of these coefficients.

CHAPTER   V

Experimental Results from Antimony

Single Crystals

5.1.   Introduction

The twelve coefficients of the magnetoresistivity
tensor components up to second order in magnetic field have
been measured at 77^OK, 139^OK, 183^OK, 225^OK and 273^OK.   The
experimental results are presented in this chapter and compared
with the previous data of Freedman and Juretschke (1961),
Epstein and Juretschke (1963) and Kechin et al (1966).   Kechin
et al have measured the galvanomagnetic coefficients at 293^OK,
273^OK, 195^OK and 77^OK and their results were published during
the progress of the present work.   Specimen galvanomagnetic
coefficients obtained at all temperatures are given in Appendix
A and in table 5.1. collected representative values.

Table 5.1.

Experimental values of the magnetoresistivity

tensor components of antimony between 77°K and 273°K

Temp.	Resistivity		Hall		Magnetoresistivity							
°K	ρ_{11}	ρ_{33}	$-R_{123}$	$-R_{231}$	A_{11}	A_{12}	A_{13}	A_{31}	A_{33}	$-A_{44}$	A_{42}	A_{24}
273	41.3	31.7	2.47	2.22	8.35	21.0	6.1	13.6	2.2	1.8	2.4	3.4
225	31.5	24.0	2.69	2.42	12.0	30.8	8.3	18.0	3.1	2.1	3.2	6.0
183	23.8	18.0	2.88	2.62	18.3	42.5	12.1	25.5	4.5	3.0	4.5	7.8
139	16.5	12.2	3.09	2.80	30.5	64.4	18.6	38.5	7.0	5.3	6.5	12.7
77	7.15	5.27	3.43	3.00	63.5	151	45.2	91.0	16.6	13.5	16.5	30.0
Estimated error %	3	6	5	7	7	7	7	7	15	20	20	20

Units: Resistivity, 10^{-6} ohm.cm; Hall, 10^{-7} ohm cm kG^{-1}; Magnetoresistivity, 10^{-9} ohm.cm.kG^{-2}.

5.2.   The Components of the Resistivity, ρ_{ij}

The temperature dependence of the resistivity tensor components, ρ_{11} and ρ_{33}, obtained from two samples for each direction are shown in figure 5.1. The spread of measured values of ρ_{11} is 2%, which is comparable with the estimated geometrical error of 2.5%. Within experimental error, the results agree with those of Lane and Dodd (1942), and Kechin et al (1966). The average value of ρ_{11} (45.0 x 10^{-6} ohm cm) at 293°K is in accord with Epstein and Juretschke's room temperature results of 44.3 x 10^{-6} ohm cm.

The measured values of ρ_{33} for the two samples are in disagreement by about 9%, more than the estimated error. A third specimen, prepared by cutting with a spark erosion cutter from a slowly grown, Bridgman crystal, has values of ρ_{33} of 33.3 x 10^{-6} ohm cm at 293°K and 5.6 x 10^{-6} ohm cm at 77°K, almost equal to the results obtained from sample s - 0° - 2, figure 5.1. Epstein and Juretschke, and other investigaters also observed more spread in ρ_{33} than ρ_{11}. Epstein and Juretschke's average value of ρ_{33} at room temperature is 34.6 x 10^{-6} ohm cm and lies between the two results obtained in the present measurements at 293°K. The values of ρ_{33} given by Kechin et al and Freedman and Juretschke agree within 2% with that of sample s - 0° - 2.

FIGURE 5.1

TEMPERATURE DEPENDENCE OF
THE RESISTIVITY COMPONENTS
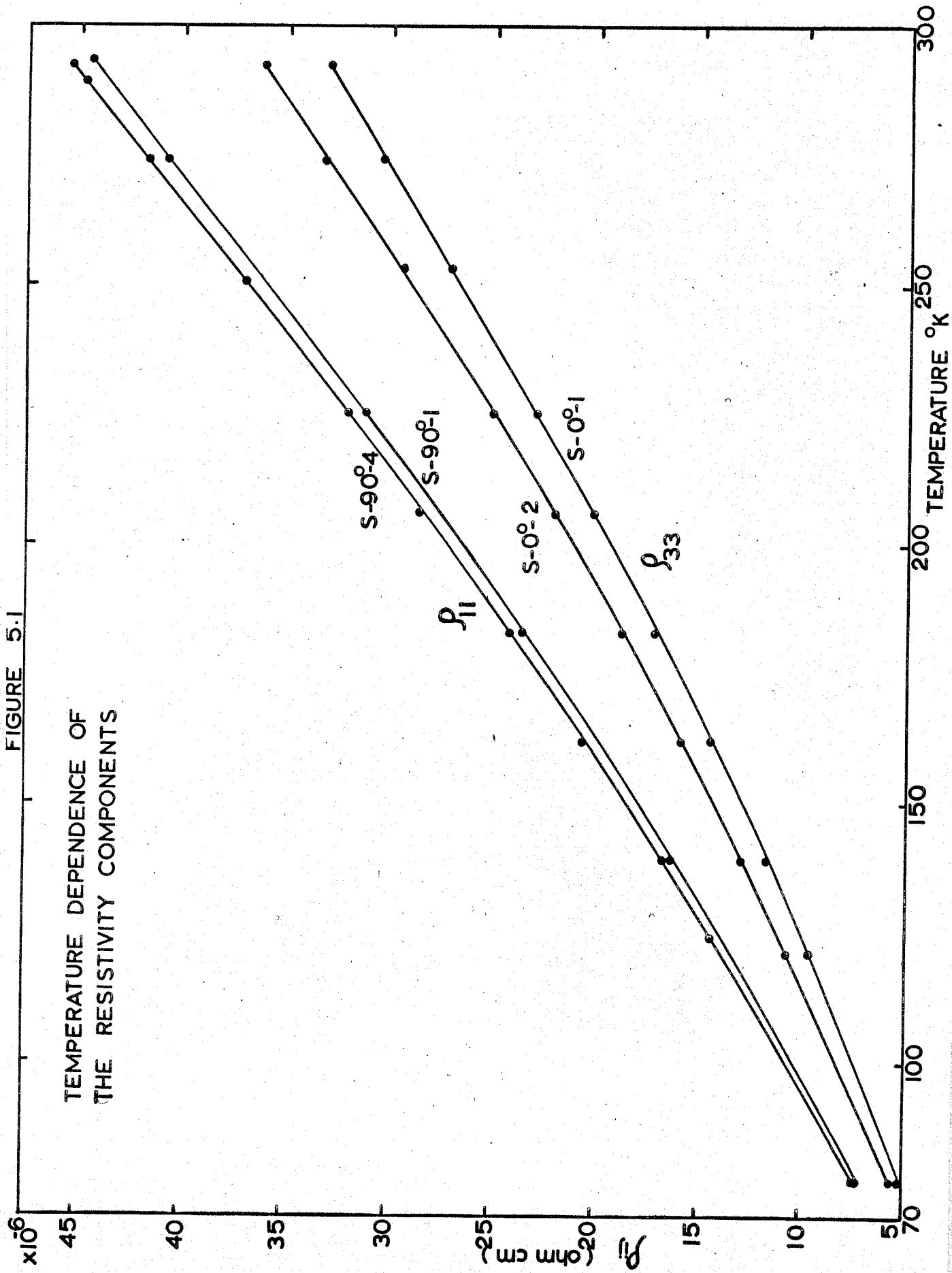
5.3.   The Hall Coefficients, R_{ijk} .

The temperature dependences of the Hall coefficients R_{123} and R_{231} of antimony are shown in figure 5.2. Both coefficients are positive in sign and are of the same order of magnitude. The Hall coefficients, when extrapolated to room temperature, agree with those obtained by Epstein and Juretschke (1963). Both are about 10% less than the results of Kechin et al over the temperature range. At $77^{O}K$ Kechin et al give $-R_{231}$ as 2.46×10^{-7} ohm cm kG^{-1} which is about 15% less than their measured value at $195^{O}K$ and equal to their room temperature value. However in the present measurements all samples show a steady increase in the measured value of $-R_{231}$ with decreasing temperature, figures 4.7 and 5.2.

5.4.   The Magnetoresistivity Coefficients, A_{ij}.

All magnetoresistivity coefficients show similar temperature dependences between $77^{O}K$ and $273^{O}K$, as shown in figure 5.3. The values of A_{ij} used in the fugure are the representative values at each temperature taken from table 5.1. They are strongly temperature dependent. The ratio A_{ij}(at $77^{O}K$)/A_{ij}(at $273^{O}K$) is the same for all the coefficients being 7.1 ∓ 0.4. The values of A_{ij} extrapolated to room temperature are smaller (up to about 10%) than those of Epstein and Juretschke (1963). The results of Kechin et al (1966) at $273^{O}K$ agree with the present values but at $77^{O}K$

FIGURE 5.2

TEMPERATURE DEPENDENCE OF THE
HALL COEFFICIENTS

$-R_{123}$ (S-90°-1)

$-R_{231}$ (S-0°-1)

TEMPERATURE °K

$-R_{ijk}$ (ohm cm kG^{-1})

×10^7
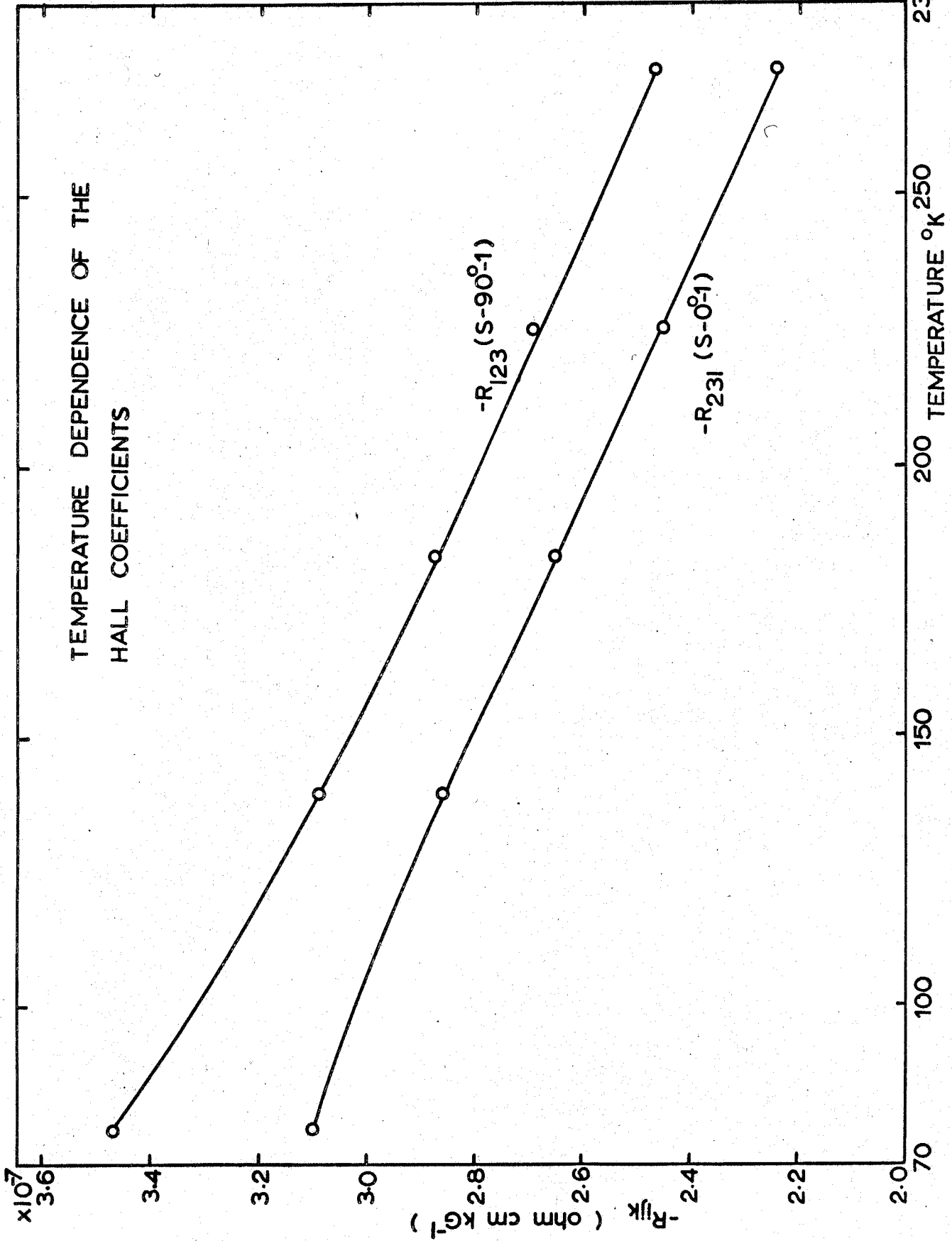
FIGURE 5.3 Temperature dependence of the magnetoresistivity components
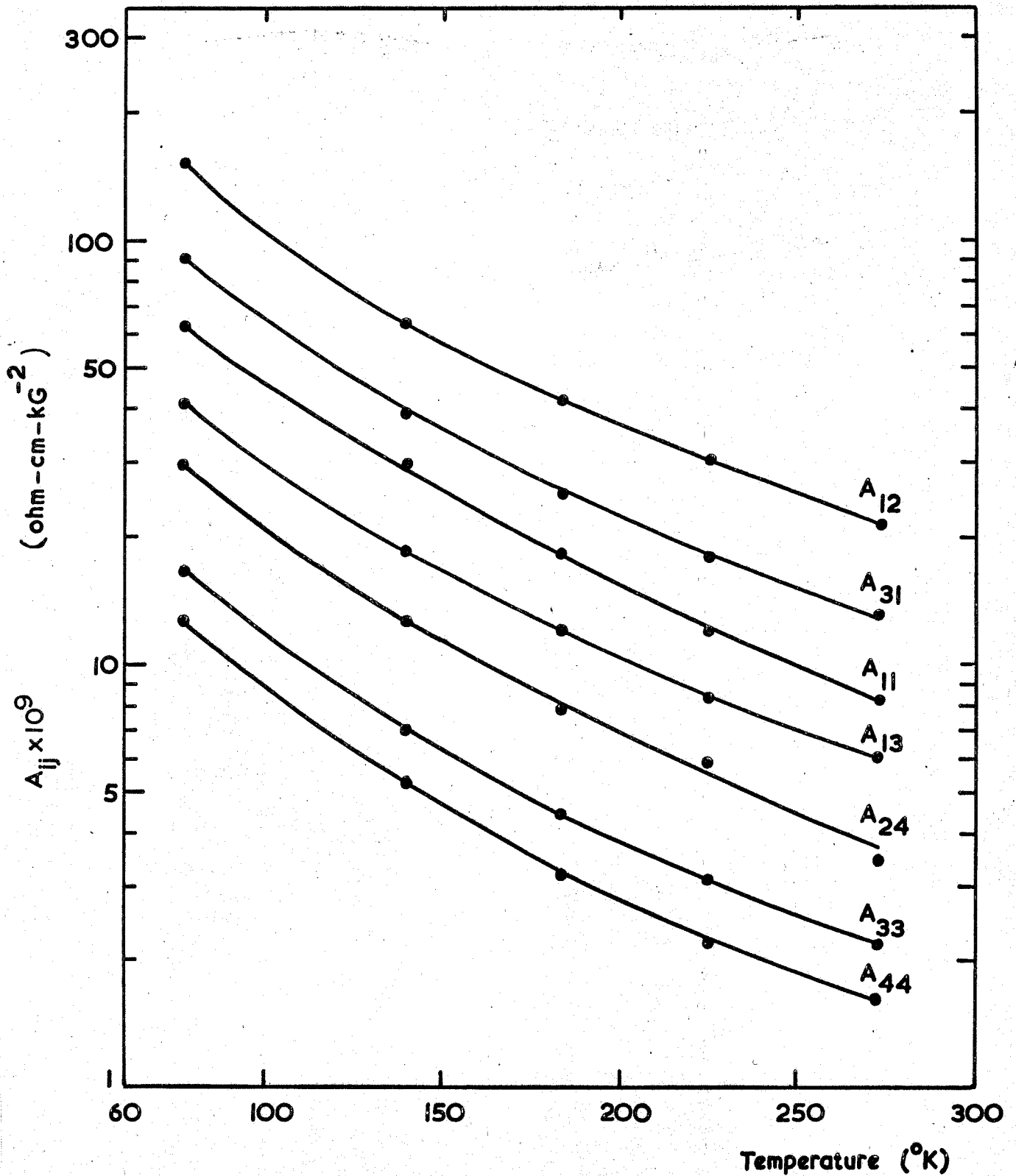
are up to 30% smaller for some coefficients (A_{11}, A_{12} and A_{31}).

5.5.   The Magnetoconductivity Coefficients.

The magnetoconductivity coefficients have been calculated from the average values of the magnetoresistivity coefficients in table 5.1. by using the equations 2.14 (page 22) and are presented in table 5.2. The maximum errors are included. The values of the coefficients B_{ij} are proportional to μ^3 and ν^3, while the P_{ijk} depends upon μ^2 and ν^2 and $\widetilde{\sigma_{ij}}$ are determined by μ and ν. Therefore, if N, the number of carriers, is constant over the temperature range and μ and ν have similar temperature dependences, then $\log B_{ij}$ versus $\log T$ plots should be straight lines with slopes determined by the temperature dependences of mobilities. Such plots are presented in figures 5.4 to 5.7, and the temperature dependences of average mobilities have been estimated from the B_{ij} 's as $T^{-1.42}$, from the P_{ijk} 's as $T^{-1.50}$ and from the $\widetilde{\sigma_{ij}}$'s as $T^{-1.39}$. These results indicate constant carrier densities and similar temperature dependences for both carriers. This will be confirmed by detailed computations in Chapter 6.

Table 5.2.

Magnetoconductivity tensor components

Temp.	Conductivity		Inverse Hall		Magnetoconductivity							
$^{\circ}$K	σ_{11}	σ_{33}	$-P_{123}$	$-P_{231}$	B_{11}	B_{12}	B_{13}	B_{31}	B_{33}	$-B_{44}$	B_{42}	B_{24}
273	2.42	3.15	1.45	1.70	0.49	1.32	0.44	1.47	0.22	0.19	0.18	0.19
225	3.17	4.16	2.71	3.20	1.20	3.35	1.07	3.45	0.54	0.42	0.42	0.60
183	4.20	5.56	5.08	6.12	3.23	8.20	2.75	8.76	1.38	1.07	1.05	1.38
139	6.06	8.20	11.4	13.9	11.2	26.0	8.96	29.0	4.7	3.9	3.2	4.6
77	13.9	18.9	67.1	79.5	124	329	120	374	59.9	54.9	43.7	58.7
Estimated error %	3	6	11	16	13	13	13	19	27	35	35	30

Units : Conductivity, 10^4 ohm^{-1}cm^{-1}; Inverse Hall, 10^2 ohm^{-1} cm^{-1} kG^{-1};

Magnetoconductivity, 10 ohm^{-1} cm^{-1} kG^{-2}.

FIGURE 5.4 TEMPERATURE DEPENDENCES OF THE σ_{ij} AND $-P_{ijk}$
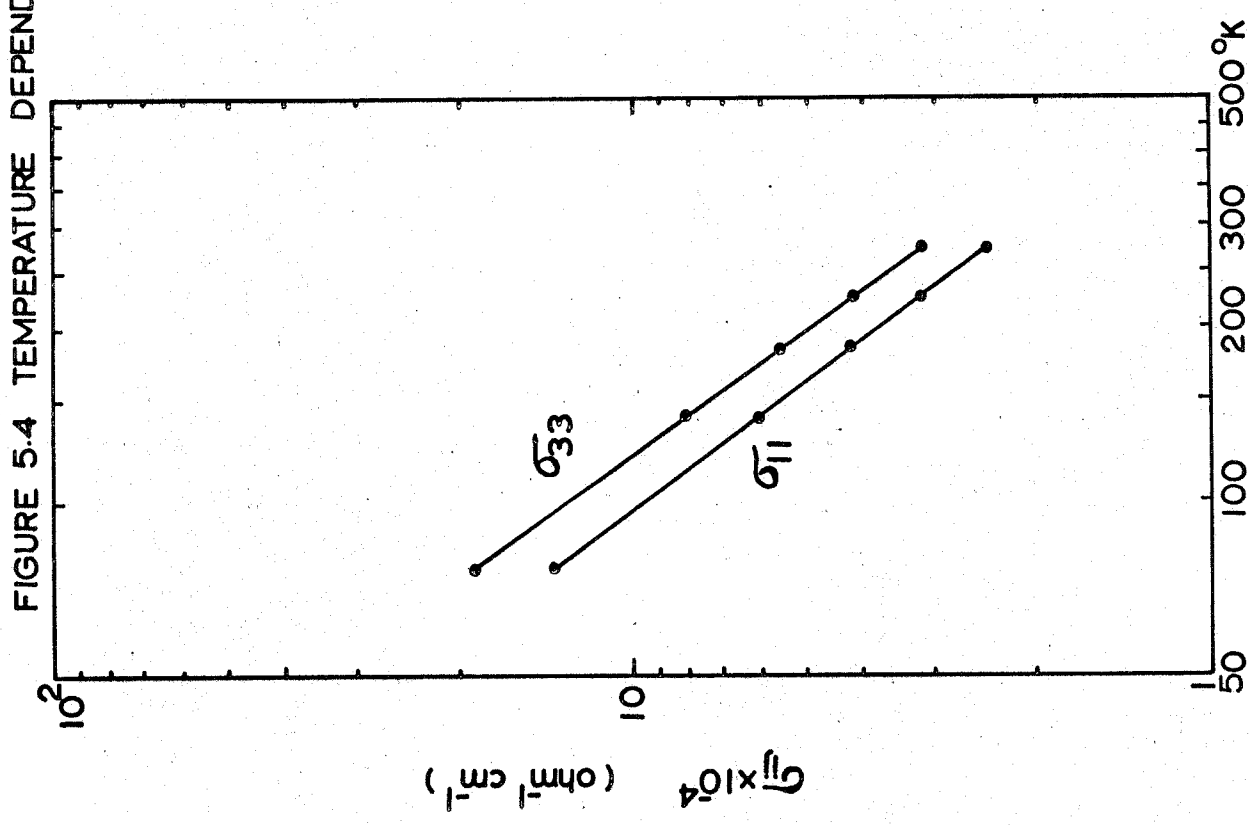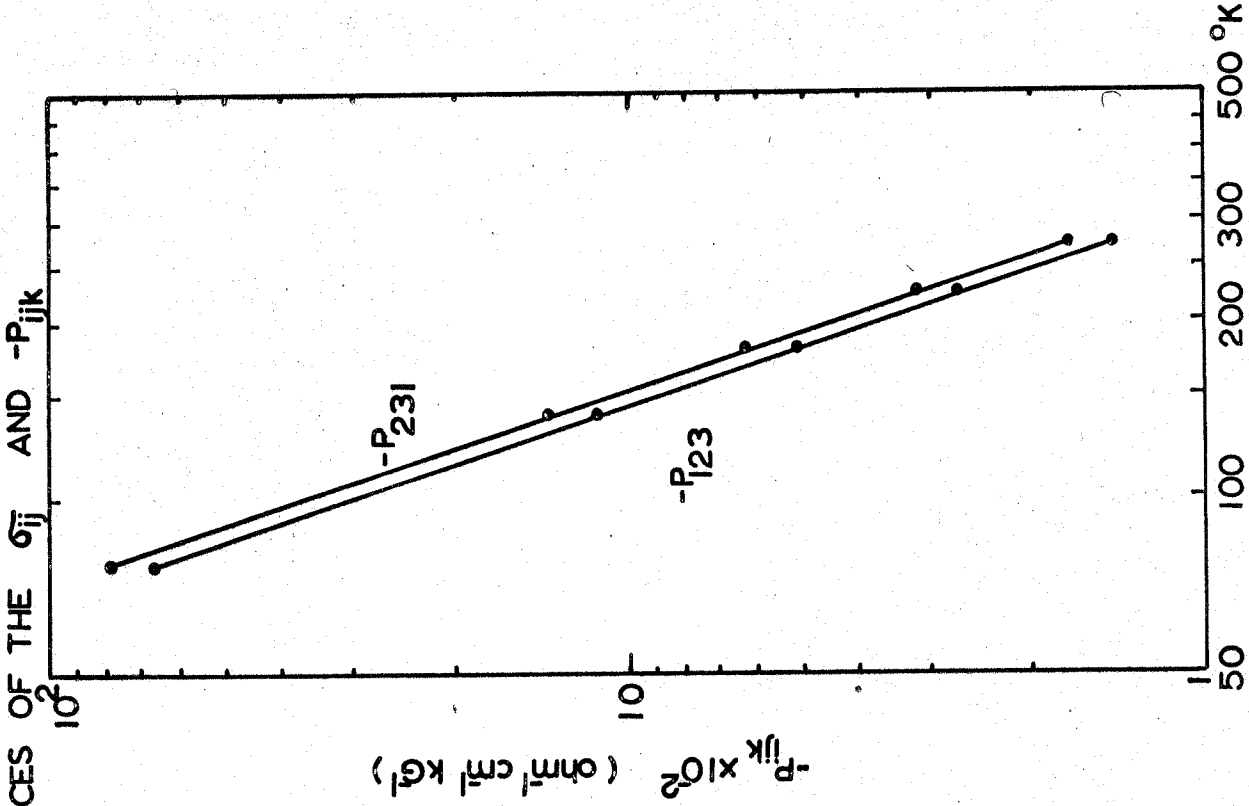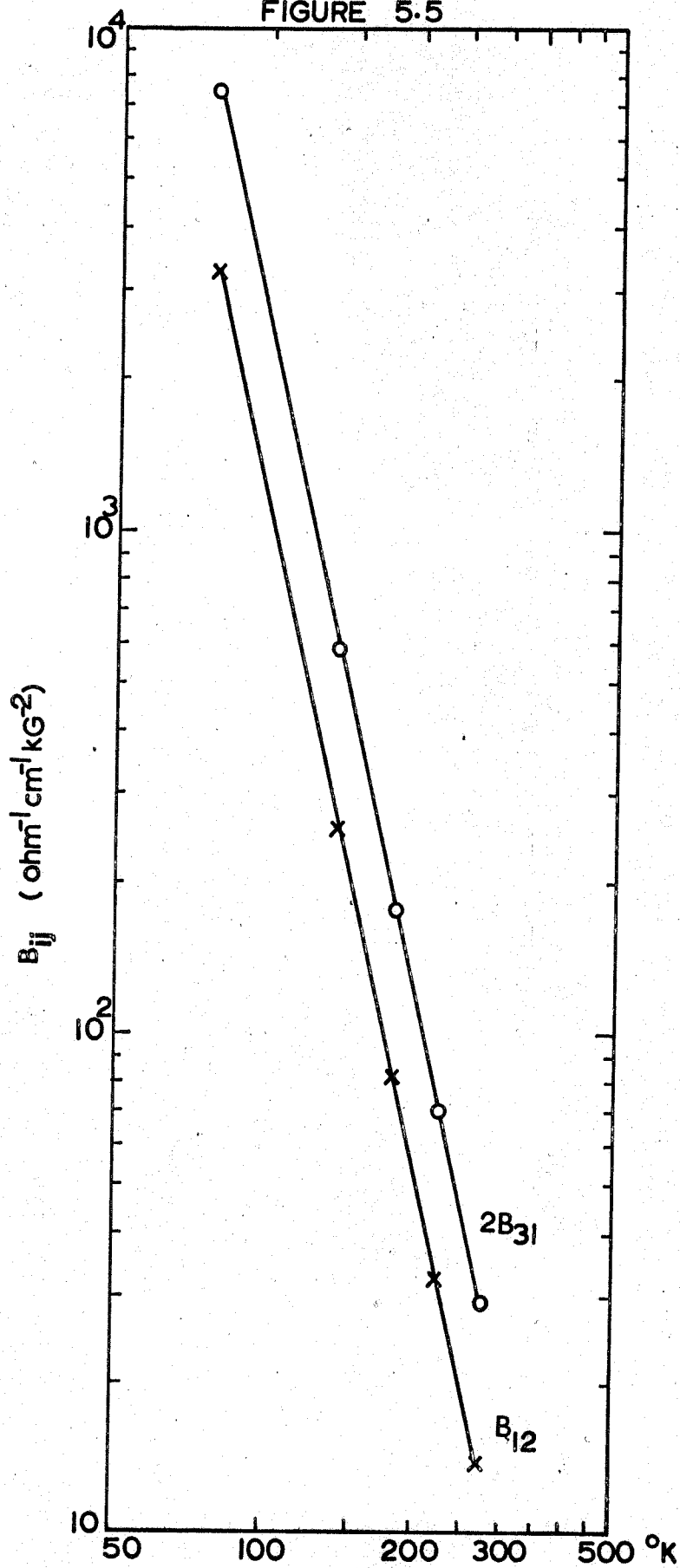
FIGURE 5.5

TEMPERATURE DEPENDENCES OF B_{12} AND B_{31}

FIGURE 5.6
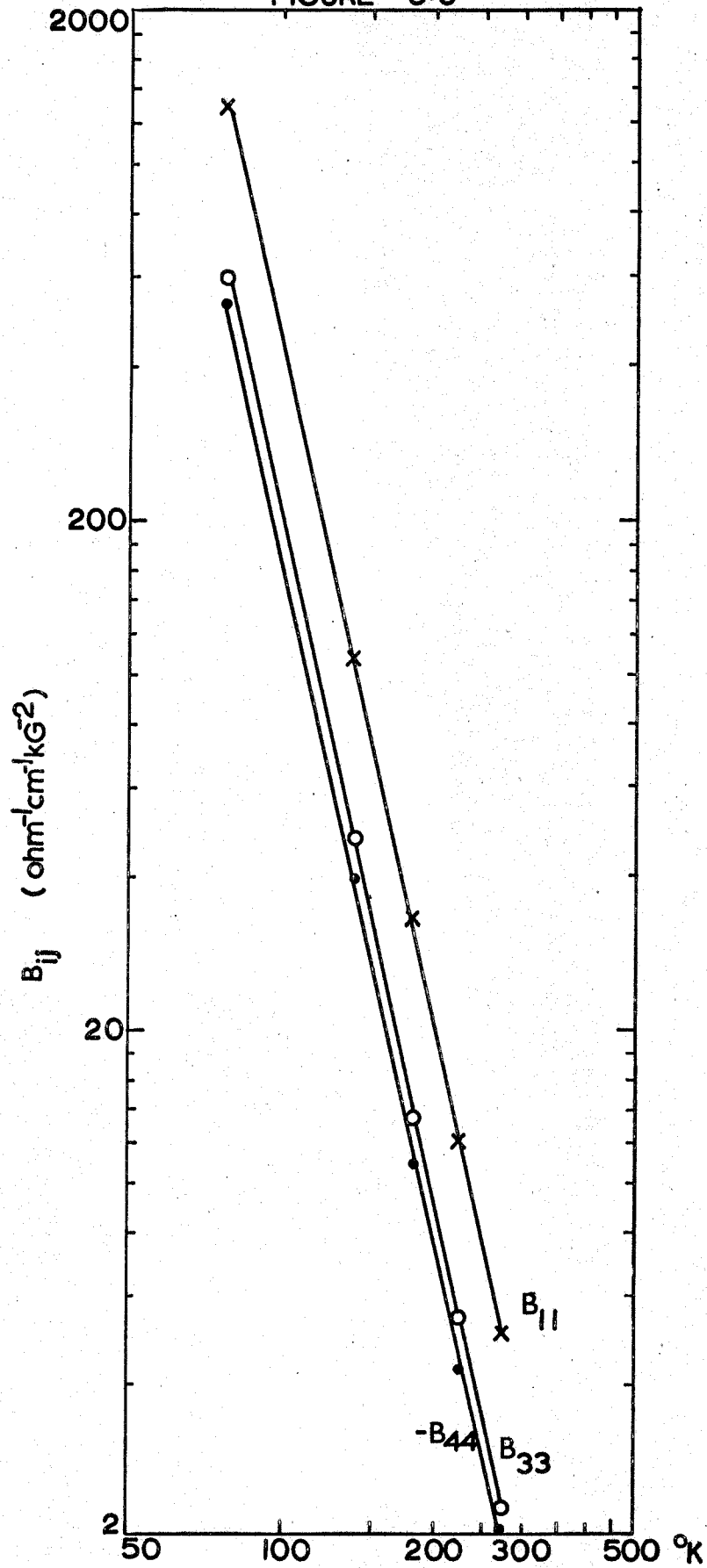
TEMPERATURE DEPENDENCES OF B_{11}, B_{33} AND B_{44}

FIGURE 5.7
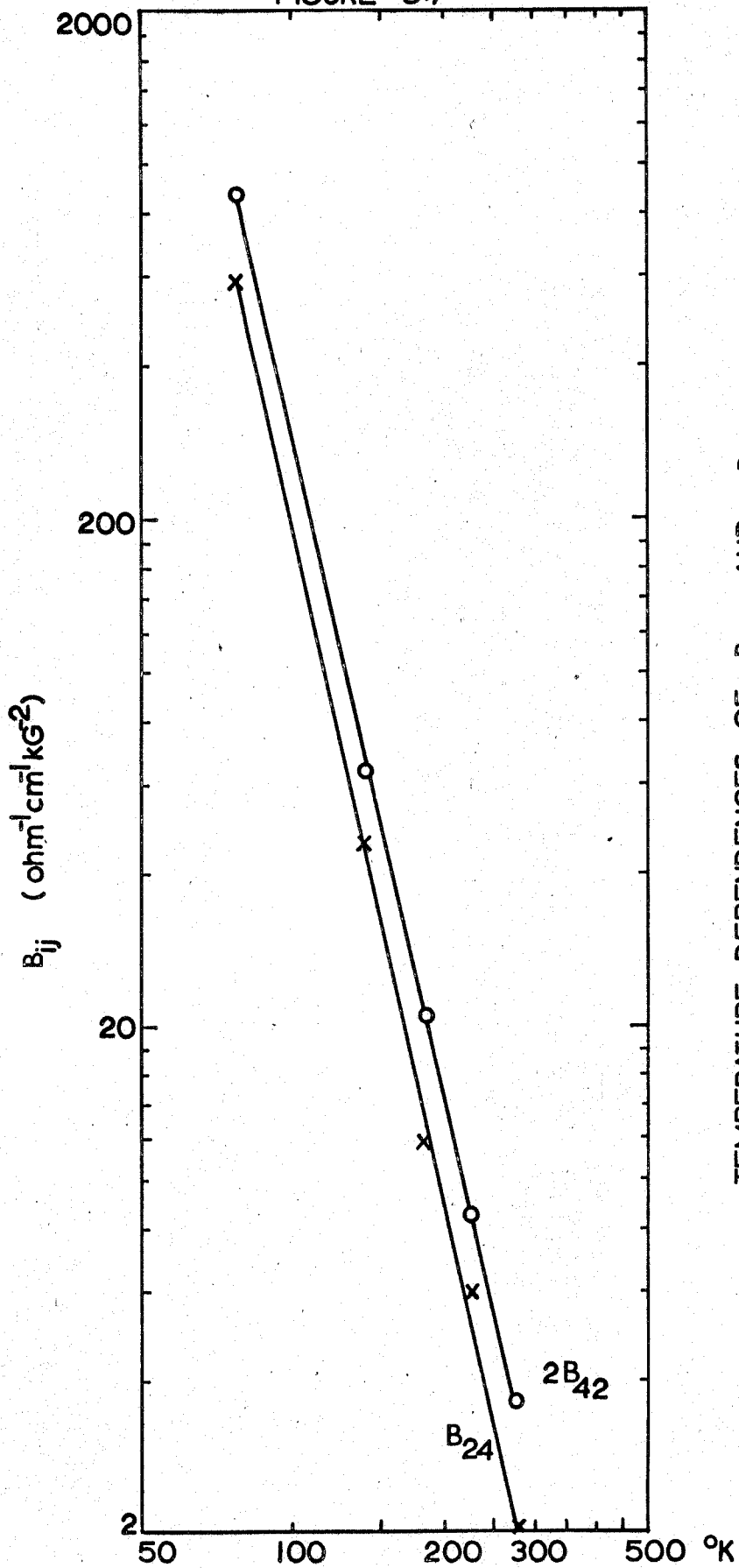
TEMPERATURE DEPENDENCES OF B_{24} AND B_{42}

5.6.   Experimental Verification of the Two Identities

Imposed by the Band Model Assumed.

The equations (2.53) relating the parameters of the band structure to the magnetoconductivity tensor coefficients of antimony predict three identities of which two are known. These identities, also given in chapter 2, are

$$2B_{33} \equiv 3B_{11} - B_{12} - 2B_{44} \qquad (5.1)$$

and
$$4P_{231} \left[\frac{\sigma_{11}}{\sigma_{33}} (-2B_{44}) - B_{13} \right]$$

$$\equiv P_{123} \left[\frac{4\sigma_{11}}{\sigma_{33}} (B_{31}) - (3B_{12} - B_{11} - 2B_{44}) \right] \qquad (5.2)$$

The left and right-hand sides of these identities have been calculated and are presented in tables 5.3 and 5.4 respectively.

<div align="center">Table 5.3.</div>

Temp. $^{\circ}K$	$2B_{33}$	$3B_{11}-B_{12}-2B_{44}$
273	0.44	0.53
225	1.08	1.09
183	2.76	3.63
139	9.4	15.4
77	119.8	152.8

Unit : 10 ohm cm kG^{-2}

Table 5.4.

Temp. $^{\circ}$K	$4P_{231}\left[\dfrac{\tilde{\sigma}_{11}}{\tilde{\sigma}_{33}}(-2B_{44})-B_{13}\right]$	$P_{123}\left[\dfrac{4\tilde{\sigma}_{11}}{\tilde{\sigma}_{33}}B_{31}-(3B_{12}-B_{11}-2B_{44})\right]$
293^{F-J}	$-\ 0.30 \times 10^{3}$	0.37×10^{3}
293^{E-J}	$-\ 0.55 \times 10^{3}$	0.52×10^{3}
273	-1.00×10^{3}	0.97×10^{3}
225	$-\ 5.50 \times 10^{3}$	2.40×10^{3}
183	$-\ 27.7 \times 10^{3}$	14.9×10^{3}
139	$-\ 17.7 \times 10^{4}$	12.7×10^{4}
77	$-\ 12.5 \times 10^{6}$	8.56×10^{6}

Unit : $\text{ohm}^{2}\ \text{cm}^{2}\ \text{kG}^{-3}$

The first identity (5.1) is satisfied within experimental
error. For the second identity, values taken at the centres
of the ranges of experimental error in the coefficients lead
to negative quantity for the left-hand side but a positive
value for the right-hand side. This is common for all
temperatures, and also for the room temperature results
of Freedman and Juretschke (1961) and Epstein and Juretschke
(1963), see table 5.4. However, if the coefficients are
changed within experimental error (up to 15% for the B_{ij} 's)
the identity can be satisfied for all temperatures. An
example, showing how the identity 5.2 can be verified by
altering the coefficients within experimental error is shown
in table 5.5.

Table 5.5.

To show the steps in the computations necessary to satisfy the identity 5.2. Each coefficient in turn is altered within the experimental error. The results are those for 183^OK but almost identical percentage changes are required at the other temperatures and for the results of Juretschke et al (1961), (1963).

$(1 + \delta)B_{ij}$	Left hand side	Right hand side
$0.88\ B_{13}$	-19.6	14.9
$1.15(-B_{44})$	-13.5	13.3
$0.88\ B_{31}$	-13.5	-2.8
$1.08\ B_{12}$	-13.5	-12.7
$0.95\ P_{231}$	-12.7	-12.7

Unit: $10^3\ ohm^2\ cm^2\ kG^{-3}$.

The important feature is that it is necessary to change the same coefficients about the same fraction for each set, including those of the previous workers. Therefore, one concludes that this systematic descrepancy arises either from the inadequacies of the model assumed in the development of the equations 2.53 or a systematic experimental error. The latter case must be omitted; the three experimental determinations of the magnetoconductivity tensor coefficients (Juretschke et al 1961, 1963 and the present work) have been

made in different experimental conditions and on single crystal specimens prepared by different methods. Thus, the systematic discrepancy must be attributed to the assumptions made in the derivation of the equations 2.53. However, because both identities are verified within experimental error, the equations can be considered a good approximation from which to explain the galvanomagnetic effects in antimony.

CHAPTER   VI

Computation of the Band Parameters

of Antimony

6.1.   Introduction

The nine parameters of the band structure, that is

the principal electron and hole mobilities μ_i and ν_i

respectively (where i = 1, 2 and 3), the number of carriers

N, and the tilt angles ψ_e and ψ_h can be obtained as a

function of temperature from the experimental values of the

magnetoconductivity tensor coefficients through solving the

equations 2.53 (page 43). Although a direct solution of

these equations can be found, this is impracticable

because the magnetoconductivity coefficients depend on

the parameters in a most complicated way. Therefore, it

is necessary to develop a different method of solution.

By making use of a computer, many possibilities arise. One

can estimate the order of magnitude of the parameters, then

calculate the twelve magnetoconductivity coefficients for an

arbitrary set of parameters selected from this estimated

range and then compare the calculated coefficients with the

experimental values. This procedure is repeated until a satisfactory fit is obtained. A faster computer than was available is necessary for this method. An alternative method is to estimate some of the parameters by solving some of the equations among the set 2.53, and then changing the rest arbitrarily. Such a method was developed by Freedman and Juretschke (1961) to analyse their room temperature results. In the present work these lines have been followed. The procedure will be detailed in the next section.

6.2. The Method for Calculation

The equations for the conductivities (σ_{11} and σ_{33}), the inverse Hall coefficients (P_{123} and P_{231}), and the magnetoresistivity coefficients (B_{13}, B_{31}, B_{44} and the combination $3B_{12} - B_{11} - B_{44}$) can be written in a comparatively simple form by defining the following eight new variables;

$$\mu_{1C} = \mu_1 + \alpha_1^2 \mu_2 + \beta_1^2 \mu_3$$

$$\mu_{3C} = \beta_1^2 \mu_2 + \alpha_1^2 \mu_3$$

$$\nu_{1C} = \nu_1 + \alpha_2^2 \nu_2 + \beta_2^2 \nu_3$$

$$\nu_{3C} = \beta_2^2 \nu_2 + \alpha_2^2 \nu_3$$

$$\mu_{1H} = \mu_2\mu_3 + \mu_1(\beta_1^2\mu_2 + \alpha_1^2\mu_3)$$

$$\mu_{3H} = \mu_1(\alpha_1^2\mu_2 + \beta_1^2\mu_3)$$

$$\nu_{1H} = \nu_2\nu_3 + \nu_1(\beta_2^2\nu_2 + \alpha_2^2\nu_3)$$

$$\nu_{3H} = \nu_1(\alpha_2^2\nu_2 + \beta_2^2\nu_3) \qquad (6.1)$$

One now obtains eight equations in nine variables, namely the newly defined, combined mobilities and N, number of carriers. Since an identity 5.2 (page 80) exists between the equations, there are in fact only seven independent equations in nine variables. By selecting two variables arbitrarily, the equations can be solved. Freedman and Juretschke started at this point . They then defined further new variables to reduce the equations to a yet simpler form. They defined a function f, which measures the contribution of electrons and holes to the conductivities, by

$$\mu_1 + \mu_2 + \mu_3 = fS \qquad (6.2)$$

$$\nu_1 + \nu_2 + \nu_3 = (1 - f)S \qquad (6.3)$$

where $\quad S = \dfrac{2\,\widetilde{\sigma}_{11} + \widetilde{\sigma}_{33}}{eN} \qquad (6.4)$

This arises from the property of the conductivity relations that

$$\frac{2\sigma_{11} + \sigma_{33}}{Ne} = \mu_1 + \mu_2 + \mu_3 + \nu_1 + \nu_2 + \nu_3 = S \qquad (6.5)$$

The value of f must lie between 0 and 1 and measures the electron contribution to the conductivity, while (1-f) measures the hole contribution. It is also convenient to introduce the following dimensionless parameters, which measure the principal mobilities

$$x_e = \frac{\mu_1}{fS} \qquad y_e = \frac{\mu_2}{fS} \qquad z_e = \frac{\mu_3}{fS}$$

$$x_h = \frac{\nu_1}{(1-f)S} \qquad y_h = \frac{\nu_2}{(1-f)S} \qquad z_h = \frac{\nu_3}{(1-f)S} \qquad (6.6)$$

Therefore, from the relations 6.2 and 6.3,

$$x_e + y_e + z_e = 1 = x_h + y_h + z_h \qquad (6.7)$$

The physically meaningful ranges of x, y and z are between 0 and 1. By using these dimensionless quantities, a new set of variables is defined instead of the relations 6.1;

$$K_{1e} = x_e + \alpha_1^2 y_e + \beta_1^2 z_e$$

$$K_{3e} + \beta_1^2 y_e + \alpha_1^2 z_e$$

$$L_{1e} = y_e z_e + x_e (\beta_1^2 y_e + \alpha_1^2 z_e)$$

$$L_{3e} = x_e (\alpha_1^2 y_e + \beta_1^2 z_e)$$

$$K_{1h} = x_h + \alpha_2^2 y_h + \beta_2^2 z_h$$

$$K_{3h} = \beta_2^2 y_h + \alpha_2^2 z_h$$

$$L_{1h} = y_h z_h + x_h (\beta_2^2 y_h + \alpha_2^2 z_h)$$

$$L_{3h} = x_h (\alpha_2^2 y_h + \beta_2^2 z_h) \tag{6.8}$$

Here $\quad K_{1e} + K_{3e} = 1$

and $\quad K_{1h} + K_{3h} = 1 \tag{6.9}$

With these new variables the first eight equations of 2.53 can be rewritten in the following form to obtain two sets of four equations in ten variables; the first set is

$$f K_{1e} + (1-f) K_{1h} = \frac{2 \widetilde{\sigma}_{11}}{2 \widetilde{\sigma}_{11} + \widetilde{\sigma}_{33}} = S_1$$

$$f^2 L_{1e} - (1-f)^2 L_{1h} = \frac{2eNcP_{231}}{(2\tilde{\sigma}_{11} + \tilde{\sigma}_{33})^2} = NS_4$$

$$f^3 L_{1e} K_{3e} + (1-f)^3 L_{1h} K_{3h} = \frac{2(eNc)^2 B_{31}}{(2\tilde{\sigma}_{11} + \tilde{\sigma}_{33})^3} = N^2 S_5$$

$$f^3 L_{1e} K_{1e} + (1-f)^3 L_{1h} K_{1h} = \frac{(eNc)^2(3B_{12}-B_{11}-2B_{44})}{(2\tilde{\sigma}_{11} + \tilde{\sigma}_{33})^3} = N^2 S_6$$

(6.10)

where in the third equation K_{3e} and K_{3h} can be removed by replacing with $(1-K_{1e})$ and $(1-K_{1h})$ respectivdy. Then, for a given value of N and f, these equations can be solved to obtain K_{1e}, K_{1h}, L_{1e} and L_{1h}.

The second set of equations is

$$fK_{3e} + (1-f)K_{3h} = \frac{\tilde{\sigma}_{33}}{2\tilde{\sigma}_{11} + \tilde{\sigma}_{33}} = S_3$$

$$f^2 L_{3e} - (1-f)^2 L_{3h} = \frac{eNc\, P_{123}}{(2\tilde{\sigma}_{11} + \tilde{\sigma}_{33})^2} = NS_7$$

$$f^3 L_{3e} K_{3e} + (1-f)^3 L_{3h} K_{3h} = \frac{(eNc)^2(-2B_{44})}{(2\tilde{\sigma}_{11} + \tilde{\sigma}_{33})^3} = N^2 S_8$$

$$f^3 L_{3e} K_{1e} + (1-f)^3 L_{3h} K_{1h} = \frac{(eNc)^2\, 2B_{13}}{(2\tilde{\sigma}_{11} + \tilde{\sigma}_{33})^3} = N^2 S_9$$

(6.11)

In the last equation K_{1e} and K_{1h} can be removed by replacement with $(1-K_{3e})$ and $(1-K_{3h})$. Then K_{3e}, K_{3h}, L_{3e} and L_{3h} can be obtained by solving these equations for a given pair of values of f and N.

The two sets of equations are not independent, because of the identity 5.2, which can be rewritten in terms of S_1 through to S_9 (defined in the equations 6.10 and 6.11) as

$$S_4(S_1 S_8 - S_3 S_9) \equiv S_7(S_1 S_5 - S_3 S_6) \tag{6.12}$$

and the relation

$$S_1 + S_3 = 1 \tag{6.13}$$

Therefore, when the two sets are considered together there are six independent equations with eight independent unknowns N, f, K_{1e}, K_{1h}, L_{1e}, L_{1h}, L_{3e} and L_{3h}. Because the relation 6.12 is not satisfied exactly by the experimental data, it is somewhat difficult to solve the two sets of equations simultaniously; the values calculated for K_{1e} and K_{3e} (similarly K_{1h} and K_{3h}) do not satisfy the relations 6.9. Therefore, Freedman and Juretschke used a method of least-squares distribution of errors to determine the most probable values of the coefficients which satisfy the identity 6.12, and at the same time to find a consistent

set of parameters for the eight equations. This is not
essential to solve these equations, since when the two
sets are solved independently for the same value of N and f
the values obtained for K_{1e}, K_{3e}, K_{1h} and K_{3h} almost satisfy
the relation 6.9. The equality range is estimated as 0.8
to 1.2. Therefore, in the present work, the two sets were
solved separately for the same value of N and f by using
the experimental data as obtained, and then the results
averaged.

Once the values of K_{1e}, K_{3e}, K_{1h}, K_{3h}, L_{1e}, L_{1h},
L_{3e}, L_{3h} are known, the dimensionless parameters x_e, y_e, z_e,
x_h, y_h and z_h, and the tilt angle of the ellipsoids can be
determined from the following relations

$$x_e = \frac{1}{2} K_{1e} \left[1 \mp (1 - 4L_{3e}/K_{1e}^2)^{1/2} \right]$$

$$y_e = \frac{1}{2}(1 - x_e)\left\{1 - \left[1 - 4(L_{1e} - x_e K_{3e})/(1-x_e)^2 \right]^{1/2}\right\}$$

$$z_e = \frac{1}{2}(1 - x_e)\left\{1 + \left[1 - 4(L_{1e} - x_e K_{3e})/(1-x_e)^2 \right]^{1/2}\right\}$$

$$\alpha_1^2 = (K_{3e} - y_e)/(z_e - y_e) \tag{6.14}$$

These relations, pertaining to the electron ellipsoids,
have been obtained from the equations 6.7 and 6.8. A
set of relationships identical in form hold for the hole

ellipsoids and can be obtained on replacing K_{1e} by K_{1h}, L_{3e} by L_{3h} etc. The principal mobilities are easily obtained from the relations 6.6.

Two important features of the solutions obtained in this way are firstly, that x_e and x_h have two distinct, physically acceptable values each and therefore, the method predicts four separate solutions for a given value of f and N. Secondly, y and z are obtained as the two roots of a quadratic equation; the selection of these in the form 6.14 is arbitrary and corresponds to a particular choice of co-ordinate system; the operations

$$ y \rightleftharpoons z $$

$$ z \rightleftharpoons y $$

transform the representation from one rotational co-ordinate system to the other. This is true for both electrons and holes and can be applied separately; the number of possible solution increases to eight in a particular system. However, the de Haas-van Alphen data of Windmiller and Priestley (1965) shows that both electron and hole ellipsoids are tilted in the same sense in antimony. Therefore, in the calculations the arbitrary selection of y and z has been made in the same sense for both electrons and holes. Hence

the number of possible solutions to be considered is four
in a given rotational co-ordinate system.

The calculations are conveniently carried out by a
computer. For a given f and N, the mobilities and tilt angles
are determined and then all magnetoconductivity coefficients
are calculated by means of the equations 2.53. and compared
with the experimental data. The computer is programmed so
that the unphysical answers are automatically rejected. This
can be done easily: the physically meaningful range of values
of x_e, y_e, z_e, x_h, y_h, and z_h are between 0 and 1. It is
also convenient to restrict acceptable solutions to those
whose calculated coefficients are within a certain limit.
The range of N is taken as 10^{19} cm^{-3}. Since holes dominate
the conductivity, the physically acceptable range of f must
be smaller than 0.5.

6.3   Calculations

An ALGOL programme has been prepared and run on an
Elliot 803 computer. The computer programme is presented in
Appendix B1 and a typical output in Appendix B2. In particular,
extensive calculations for all four types of solution have
been performed for the experimental data obtained at $183^{O}K$.
The four solutions, denoted by A, B, C and D, have been
searched through to find the best fit to the experimental
data. The band parameters of all the solutions obtained for

the best fit are shown in table 6.1. In table 6.2, the
recalculated coefficients of these solutions are compared
with the experimental data.

The solution type -B and type -C cover broad
ranges of f and N: for type -B values of f lie between 0.370
to 0.400 and N between 3.6×10^{19} to 4.0×10^{19} cm^{-3}. The
ranges of f and N are even wider for solution C, 0.370 to
0.430 and 3.6×10^{19} to 4.3×10^{19} cm^{-3} respectively.
For the other two types of solution A and D, the physically
acceptable solutions lie only in a very narrow range of
f and N. These ranges have been found to be f = 0.390 $\pm$ 0.005
and N = 4.0×10^{19} $\mp$ 0.2×10^{19} cm^{-3} for both solutions.
This narrow range results from small tilt angle of the
electron ellipsoids of these solutions.

Although in the calculations a somewhat different
procedure than that of Freedman and Juretschke (1961) was
used, the solution C given in table 6.1 is identical in form
to the result obtained from their room temperature galvano-
magnetic data. Their solution is presented in table 6.3,
together with the results of Epstein and Juretschke (1963),
who give the two types of solution C and D.

It is not possible to select the true solution
from the four types without taking into account other experi-
mental results. From table 6.2, it can be seen that the fit
for solution types A and B are poorer than C and D. However,
because they are solutions of the equations 2.53, one could

Table 6.1

Calculated band parameters of antimony for solutions type
A, B, C and D at 183^OK

	A	B	C	D
N	4.0	3.7	3.8	4.0
f	0.390	0.380	0.420	0.390
μ_1	4.57	0.30	0.11	4.59
μ_2	0.10	2.59	2.37	0.10
μ_3	3.18	6.33	7.20	3.81
ψ_e	6°	53°	51°	6°
ν_1	1.19	1.08	7.20	7.20
ν_2	3.67	2.97	0.39	0.26
ν_3	8.42	10.5	5.80	5.83
ψ_h	60°	56°	23°	24°

Units: mobilities, 10^3 cm^2 volt^{-1} sec^{-1}:
N, 10^{19} cm^{-3}.

Table 6.2

Comparison for all types of solutions of the recalculated

magnetoconductivity tensor coefficients with the experimental values

at 183°K.

	A		B		C		D	
	cal	cal/exp	cal	cal/exp	cal	cal/exp	cal	cal/exp
σ_{11}	4.19	1.00	4.19	1.00	4.19	1.00	4.19	1.00
σ_{33}	5.55	0.99	5.54	0.99	5.55	0.99	5.55	0.99
$-P_{123}$	5.08	1.00	5.08	1.00	5.08	1.00	5.08	1.00
$-P_{231}$	6.12	1.00	6.12	1.00	6.12	1.00	6.12	1.00
B_{11}	1.99	0.62	2.32	0.72	3.01	0.93	3.24	1.00
B_{12}	8.08	0.99	8.19	1.02	8.42	1.02	8.50	1.04
B_{13}	2.39	0.87	2.39	0.87	2.32	0.87	2.40	0.87
B_{31}	7.88	0.90	7.86	0.90	7.88	0.90	7.88	0.90
B_{33}	0.37	0.27	0.81	0.59	1.72	1.24	2.02	1.45
$-B_{44}$	1.41	1.32	1.41	1.32	1.41	1.32	1.41	1.31
B_{24}	0.12	0.10	0.40	0.29	1.25	0.91	1.22	1.13
B_{42}	0.73	0.69	1.76	1.68	0.40	0.38	1.55	1.16

Units: σ, 10^4 ohm^{-1} cm^{-1}; P, 10^2 ohm^{-1} cm^{-1} kG^{-1}; B, 10 ohm^{-1} cm^{-1} kG^{-2}

Table 6.3

The solutions given by Freedman and Juretschke (1961) and Epstein and Juretschke (1963) obtained from the room temperature galvanomagnetic effects data.

	Solution given by Freedman and Juretschke	Solutions given by Epstein and Juretschke	
	type $-$C	type $-$C	type $-$D
N	3.7	4.3	4.3
μ_1	0.15	0.17	1.45
μ_2	1.18	1.63	0.18
μ_3	4.05	2.43	2.68
ψ_e	60°	54°	10°
ν_1	3.56	3.80	4.07
ν_2	0.13	0.13	0.20
ν_3	3.30	2.42	2.4
ψ_h	27°	22°	20°

Units : mobilities, 10^3 cm^2 volt^{-1} sec^{-1};

N, 10^{19} cm^{-3}.

by many more calculations obtain a better fit. Changing the input data within experimental error does not alter the main structure of the solutions: the tilt angles and mobilities are only slightly changed.

The true physical answer is believed to be solution D. In table 6.4 this solution is presented at all temperatures, and in table 6.5 recalculated magnetoconductivity coefficients are compared with the experimental results. Agreement is very good at all temperatures. The number of carriers increases slightly with temperature but the tilt angles are not temperature dependent.

Solution D is referred to the rotational system in the y-z plane taken from the trigonal axis through ΓL; then the calculated values of B_{24} and B_{42} are positive, in agreement with the experimental data for A_{24} and A_{42}. The tilt angles of the electron ellipsoids (5°) and the hole ellipsoids, although rather smaller (24°), accord with the other experimental and theoretical results summarized in the first chapter. Furthermore, the mobilities equal to $\frac{e\tau}{m^{*}}$ compare qualitatively along each ellipsoid axis with the effective mass data of Windmiller (1966); the largest mobilities lie along the equivalent direction to the smallest effective masses, figures 6.1 and 6.2.

Table 6.4.

Calculated band parameters of
antimony for solution type D.

Temp. $^{\circ}$K	273	225	183	139	77
N	4.22	4.12	4.00	3.92	3.86
f	0.405	0.397	0.390	0.387	0.385
μ_1	2.74	3.34	4.59	6.91	16.2
μ_2	0.11	0.09	0.10	0.17	0.38
μ_3	1.95	2.90	3.81	5.46	12.6
ψ_e	3°	5°	6°	6°	5°
ν_1	3.63	5.34	7.20	10.2	23.6
ν_2	0.18	0.33	0.26	0.44	1.70
ν_3	3.22	3.93	5.83	9.16	2.14
ψ_h	24°	22°	24°	24°	24°

Units: N, 10^{19} cm^{-3}; Mobilities, 10^3 cm^2 volt^{-1} sec^{-1}.

Table 6.5

To compare the recalculated magnetoconductivity tensor components for solution type D with the experimental values

	273°K		225°K		183°K		139°K		77°K	
	cal.	cal/exp	cal.	cal/exp	cal.	cal/exp	cal.	cal/exp	cal.	cal/exp
σ_{11}	2.41	0.99	3.17	1.00	4.19	0.99	6.05	0.99	13.9	1.00
σ_{33}	3.15	1.00	4.16	1.00	5.55	0.99	8.20	1.00	18.9	1.00
$-P_{123}$	1.44	0.99	2.70	0.99	5.08	1.00	11.3	0.99	67.0	1.00
$-P_{231}$	1.69	0.99	3.19	0.99	6.12	1.00	13.9	1.00	79.5	1.00
B_{11}	0.49	1.02	1.16	0.96	3.24	1.00	10.2	0.91	120	0.97
B_{12}	1.37	1.04	3.43	1.02	8.50	1.04	26.7	1.02	339	1.03
B_{13}	0.38	0.87	0.95	0.89	2.40	0.87	7.85	0.88	106	0.89
B_{31}	1.33	0.90	3.14	0.91	7.88	0.90	26.3	0.90	340	0.91
B_{33}	0.30	1.40	0.56	1.04	2.02	1.45	7.01	1.48	78.6	1.31
$-B_{44}$	0.24	1.30	0.53	1.28	1.41	1.31	4.98	1.27	68.2	1.24
B_{42}	0.18	1.00	0.38	0.91	1.22	1.16	4.13	1.28	47.5	1.08
B_{24}	0.21	1.08	0.53	0.89	1.55	1.13	4.75	1.02	54.1	0.92

Units: σ, 10^4 ohm^{-1} cm^{-1}; P, 10^2 ohm^{-1} cm^{-1} kG^{-1}; B, 10 ohm^{-1} cm^{-1} kG^{-2}.

FIGURE 6.1

(a)

Cross-section of an electron ellipsoid in the mirror plane. The angles shown correspond to the pocket area maxima and minima (Windmiller 1966).

(b)

The electron mobility ellipsoid obtained in solution D in the trigonal-bisectrix plane (not to scale).

FIGURE 6.2

(a)
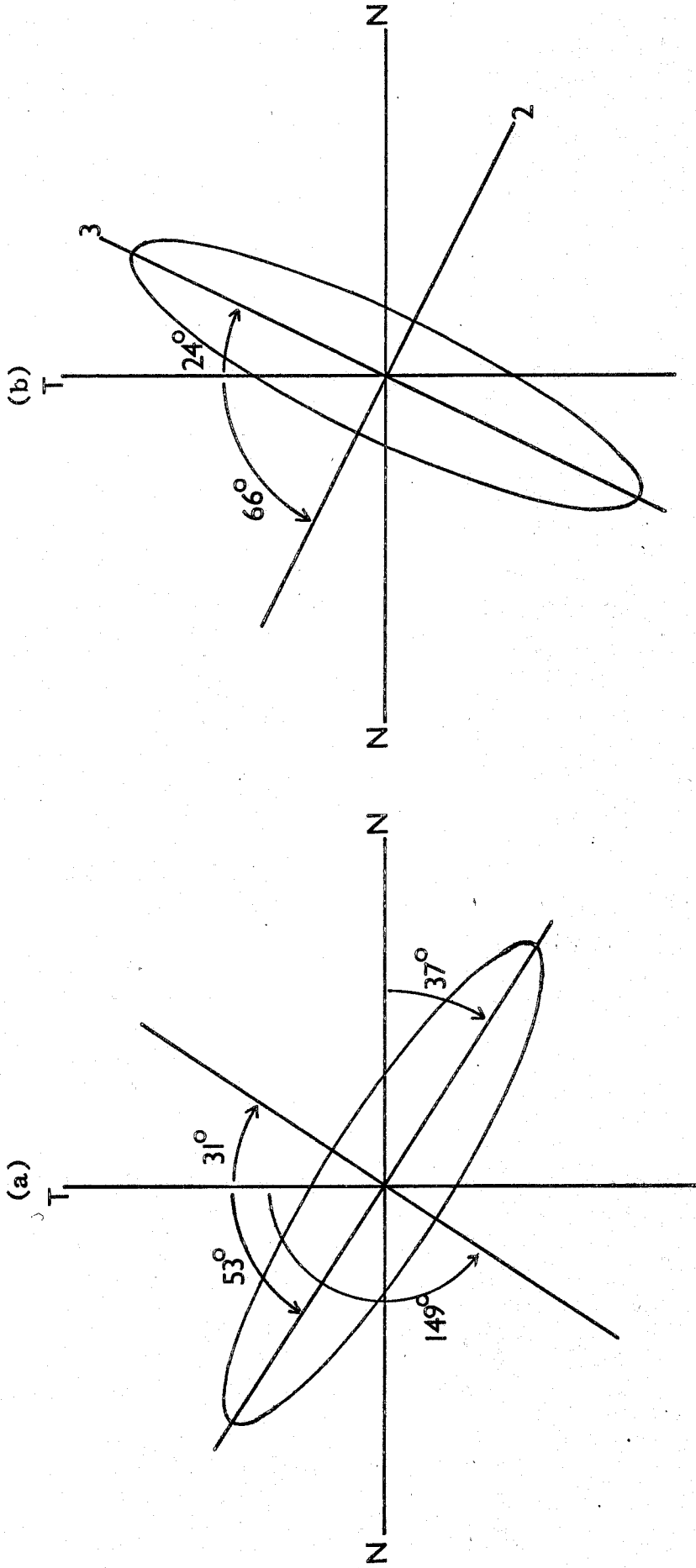
Cross-section of a hole ellipsoid
in the mirror plane. The angles shown
correspond to the pocket area maxima
and minima (Windmiller 1966).

(b)

The hole mobility ellipsoid
obtained in solution D in the
trigonal-bisectrix plane (not to scale).

Only solution D and solution C, presented in table 6.6, were obtained at all temperatures. The effect of change of input data within experimental error on solution D was examined at $183^{O}K$. The tilt angles and the number of carriers remain practically unaltered. However, the mobilities do change slightly. This can be readily seen by reference to the ratios of the mobilities μ_x/ν_x and μ_z/ν_z, where μ_x and ν_x, and μ_z and ν_z are the electron and hole mobilities along the x and the z axes of the crystals and are given by the equations

$$\mu_x = \frac{1}{2} (\mu_1 + \alpha_1^2 \mu_2 + \beta_1^2 \mu_3)$$

$$\mu_z = \beta_1^2 \mu_2 + \alpha_1^2 \mu_3$$

$$\nu_x = \frac{1}{2} (\nu_1 + \alpha_2^2 \nu_2 + \beta_2^2 \nu_3)$$

$$\nu_z = \beta_2^2 \nu_2 + \alpha_2^2 \nu_3 \tag{6.15}$$

The range of solutions with a good fit to the experimental data gives μ_x/ν_x between 0.45 to 0.56 and μ_z/ν_z between 0.75 to 0.95. The solution given in table 6.1 gives values for $\mu_x/\nu_x = 0.56$ and $\mu_z/\nu_z = 0.76$, and represents one end of the range. A solution at the other limit is presented in table 6.7. It is not possible to assess from the galvano-magnetic effects alone where the true solution lies in the range of D. However, the thermoelectric power data of antimony very much depends upon the values of the ratios μ_x/ν_x and
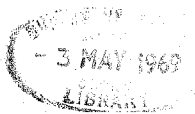
Table 6.6

Calculated band parameters of antimony

for solution type C (f = 0.420).

Temp. $^{\circ}$K	273	225	183	139	77
N	4.13	3.90	3.78	3.70	3.60
μ_1	0.11	0.10	0.11	0.19	0.37
μ_2	1.54	1.86	2.37	3.43	7.66
μ_3	3.43	5.13	7.20	10.7	26.1
ψ_e	59°	51°	51°	52°	52°
ν_1	3.60	5.42	7.20	10.1	23.6
ν_2	0.26	0.28	0.39	0.77	2.20
ν_3	3.15	4.06	5.80	8.96	21.3
ψ_h	23°	23°	23°	23°	23°

Units: N, 10^{19} cm^{-3}; Mobilities, 10^3 cm^2 volt^{-1} sec^{-1}.

Table 6.7 -(a)

A solution type -D obtained at 183°K and towards the end of the region of physical acceptibility.

N	3.98		f	0.385
μ_1	4.12		ν_1	7.94
μ_2	0.09		ν_2	0.27
μ_3	4.22		ν_3	5.23
ψ_e	0°		ψ_h	23°
μ_x/ν_x	0.47		μ_z/ν_z	0.94

Units : N, 10^{19}cm^{-3}, mobilities, 10^3cm^{2}volt^{-1}sec^{-1}.

Table 6.7 -(b)

To compare the solution given in table 6.7 -(a) with the experimental data.

	Cal.	Cal/Exp		Cal.	Cal/Exp
σ_{11}	4.20	1.00	B_{13}	2.43	0.88
σ_{33}	5.54	0.99	B_{31}	7.66	0.88
$-P_{123}$	5.05	0.99	B_{33}	1.64	1.20
$-P_{231}$	6.13	1.00	$-B_{44}$	1.23	1.15
B_{11}	3.24	1.00	B_{24}	1.57	1.13
B_{12}	8.90	1.07	B_{42}	0.98	0.94

Units: σ, 10^4ohm^{-1}cm^{-1}; P, 10^2ohm^{-1}cm^{-1}kG^{-1}; B, 10 ohm^{-1}cm^{-1}kG^{-2}.

μ_z/ν_z and can be explained by taking certain values of these ratios. This will be discussed in the last chapter.

6.4.   Discussion.

For electron ellipsoids the tilt angle is in very good agreement with that of obtained by Windmiller (1966). He gives a tilt angle of 6.5^O, corresponding to the larger cross-section in the quadrant containing ΓL and 87.7^O for the smaller cross-section in the adjacent quadrant, figure 6.1 -(a). Therefore, one would expect, in the ellipsoid approximation to the warped pockets, that the tilt angle should be between 2.3^O $(= 90^O - 87.7^O)$ and 6.5^O, which accords with the results $(3^O$ to $6^O)$ given in table 6.4. For hole ellipsoids the agreement is not so good. For figure 6.2 -(a), with similar discussion, one would expect an average tilt angle between 31° to 37° $(90^O - 53^O)$, not in good agreement with the value of 24° calculated in solution D.

This discrepancy between the two answers for the tilt angle for hole pockets was first atributed to the method of calculations. It was thought that, if the mobilities obtained were altered arbitrarily within maximum calculation error, about 30%, the recalculated magnetoconductivity coefficients would fit to the experimental data for fixed values of tilt angles; for instance, ψ_e equal to 4° and ψ_h between 30° to 36°, an angle closer to the value obtained from the other

measurements. A new computer programme was prepared (presented in Appendix C1 and a typical output in Appendix C2) and the magnetoconductivity coefficients were recalculated for $\psi_h = 26^O$ to 36° and results compared with the experimental data. The best fits obtained for $\psi_h = 30^O$ and 36° are shown in table 6.8 and the recalculated coefficients are compared with the experimental data in table 6.9. Fits become poorer as the tilt angle of the hole ellipsoids is increased towards 36°. The anisotropy of the recalculated coefficients also deviate from the observed values. Particularly the ratio P_{123}/P_{231}, which has an experimental value of 0.83 ∓ 0.17, shows a steady increase with a larger value of ψ_h. A satisfactory fit to the experimental data can only be obtained when ψ_e is between 0° to 7°, and ψ_h is between 22° to 26°. Therefore, the discrepancy between the tilt angles of the hole ellipsoids obtained in the present work and the other measurements is believed to originate from physical differences between the properties measured and their relationship to the Fermi surface.

The carrier densities are essentially temperature independent, and in agreement with those obtained by other methods, see table 6.10. The temperature dependences of the principal electron mobilities μ_1 and μ_3 are plotted in logarithmic scale, figure 6.3. Both μ_1 and μ_3 show same temperature dependences, as expected from the uniform relaxation time assumption. Similarly the hole

Table 6.8

Solution type D obtained as the closest fit to the experimental data for a given ψ_e and ψ_h at 183°K.

	Solution D $\psi_h = 30^{\circ}$	Solution D $\psi_h = 36^{\circ}$
N	4.4	4.3
f	0.380	0.380
μ_1	2.86	3.01
μ_2	0.23	0.18
μ_3	4.43	4.44
ψ_e	7°	4°
ν_1	6.63	6.91
ν_2	0.28	0.17
ν_3	5.37	5.48

Units: N, 10^{19} cm^{-3}; mobilities, 10^3 cm^2 volt^{-1} sec^{-1}.

Table 6.9

To compare the recalculated magnetoconductivity tensor coefficients for solutions given in table 6.8 with the experimental values.

	Solution D $\psi_h = 30^{\circ}$		Solution D $\psi_h = 36^{\circ}$	
	Cal.	Cal/Exp	Cal.	Cal/Exp
σ_{11}	4.00	0.95	4.19	0.99
σ_{33}	5.96	1.07	5.55	0.99
$-P_{123}$	6.65	1.31	9.10	1.79
$-P_{231}$	5.33	0.87	4.03	0.66
B_{11}	2.76	0.85	2.87	0.89
B_{12}	6.28	0.76	6.16	0.75
B_{13}	3.06	1.11	4.32	1.57
B_{31}	6.20	0.71	5.46	0.62
B_{33}	2.31	1.67	3.05	2.21
$-B_{44}$	1.61	1.50	1.83	1.71
B_{24}	1.37	0.99	1.51	1.09
B_{42}	1.09	1.04	1.12	1.06

Units: σ, 10^4 ohm^{-1} cm^{-1}; P, 10^2 ohm^{-1} cm^{-1} kG^{-1};

B, 10 ohm^{-1} cm^{-1} kG^{-2}.

Table 6.10

Carrier densities in antimony

Reference	Carrier density per cm^3	Temperature
Erik̑sson et al (1964)	N_e = 4.2 x 10^{19} N_h = 4.4 x 10^{19}	1.5^OK 1.5^OK
Epstein and Juretschke (1963)	$N_e = N_h$ = 4.3 x 10^{19}	293^OK
Ketterson and Eckstein (1963)	$N_e = N_h$ = 4.07 x 10^{19}	1.15^OK
Rao et al (1964)	$N_e = N_h$ = 5.05 x 10^{19}	4.2^OK
Present work (solution D)	$N_e = N_h$ = 4.22 x 10^{19} = 4.12 x 10^{19} = 4.00 x 10^{19} = 3.92 x 10^{19} = 3.86 x 10^{19}	273^OK 225^OK 183^OK 139^OK 77^OK
Windmiller and Priestley (1965)	$N_e = N_h$ = 5.5 x 10^{19}	1.26^OK

FIGURE 6.4

The temperature dependences of the

principal hole mobilities

ν_1
ν_3

Mobility (cm² V⁻¹ sec⁻¹)

Temperature (°K)

FIGURE 6.3

The temprature dependences of the

principal electron mobilities

μ_1
μ_3

Mobility (cm² V⁻¹ sec⁻¹)
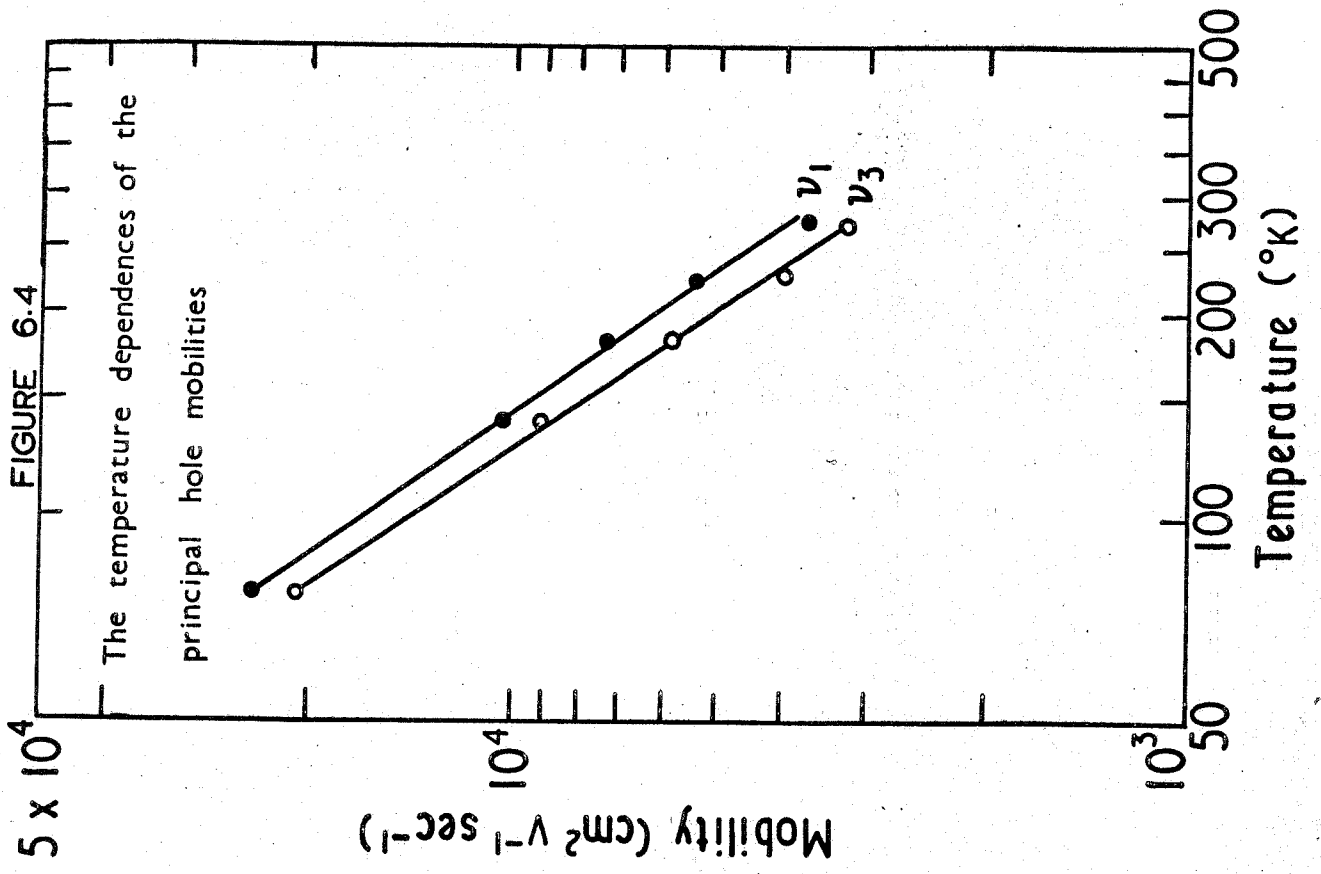
Temperature (°K)

mobilities are illustrated in figure 6.4. Both sets of carriers have almost identical temperature dependences of mobility, $T^{-1.42}$ for electrons and $T^{-1.48}$ for holes.

Before going into further discussion of the carrier mobilities and band structure of antimony the results obtained from tin-antimony alloys, relevant to the overall picture, will be presented in the next chapter.

CHAPTER VII

Experimental Results in Antimony-Tin Alloys

and Computation of Valence Band Parameters.

7.1.   Introduction

Further verification of the new assignment of the carriers (electrons to low tilt angle pockets and the holes to the highly tilted extrema) has come from the low field galvano-magnetic effects in tin-antimony alloys. Tin (Group $\overline{IV}$) has one fewer valency electron than antimony, and when substituted for antimony in the lattice, removes electrons from the conduction band. In the simplest case each tin atom would remove one electron from the conduction band. However, to adjust the Fermi level a number of electrons from the lower Brillouin zone must spill over into the conduction band. The number of spilled electrons depends upon the density of states in the two zones. If the density of states are the same in both bands, then after the addition of 2δ tin atoms, there will be $N - \delta$ electrons in the conduction band and $N + \delta$ holes in the valence band. For a parabolic band, the density of states $g(\mathcal{E})d\mathcal{E}$ in the energy interval $(\mathcal{E} + d\mathcal{E}) - \mathcal{E}$ is given by

$$g(\mathcal{E}) \ d\mathcal{E} = 4\pi(\frac{2m_o}{h^2})^{3/2} \ (m^T)^{3/2} \ \mathcal{E}^{1/2} \ d\mathcal{E} . \qquad (7.1)$$

Here $m^T = (m_1 m_2 m_3)^{1/3}$ is the density of states effective mass

in units of m_o and energy ε is measured from the band edge.

Therefore, on this basis in antimony, where m^T is larger for

electrons than for holes, the density of states at the Fermi

level should be greater in the conduction band than in the

valence band. In this case the addition of 2δ tin atoms

should introduce slightly less than δ holes for small concentra-

tions of tin. However, the density of states decreases as the

band edge is approached, and the addition of a high concentration

of tin atoms is less effective in removing electrons from the

conduction band than in creating holes in the valence band.

Thus, for high doping levels, the situation is the reverse

from that at low doping. Although, this discussion shows some

qualitative features of the nature of what happens when semi-

metals are alloyed, the actual process is complicated. For

instance, when bismuth is doped with the group $\overline{IV}$ elements

tin or lead, both introduce holes, but tin is three times more

efficient than lead (see Wilson 1953, p. 229). Therefore, it

is difficult to asses the amount of tin necessary to produce a

purely p-type alloy of antimony. From the galvanomagnetic

effect data of Epstein and Juretschke (1963) for tin doped

antimony (0.2 at.% and 0.8 at. % Sn), it turns out that 1% or

more tin is required to ensure conduction by holes alone.

Samples have been prepared with compositions of 1.7 at.%

2.0 at.%, 2.5 at.%, 3.0 at.% and 8 at.% tin. In these samples,

the resistivities ρ_{11} and ρ_{33}, the Hall coefficients $-R_{123}$ and $-R_{231}$, and four magnetoresistivity coefficients up to second order in magnetic field A_{12}, A_{13}, A_{31} and A_{33} have been measured at 273°K, 183°K and 77°K.

By assuming that the six tilted ellipsoidal model still holds for the valence band of antimony with the pockets simply being expanded, the band parameters are related to the selected measured coefficients by

$$2\widetilde{\sigma_{11}} = Pe\ (\nu_1 + \alpha^2\nu_2 + \beta^2\nu_3)$$

$$\widetilde{\sigma_{33}} = Pe\ (\beta^2\nu_2 + \alpha^2\nu_3)$$

$$-2cP_{231} = Pe\ \left[\nu_2\nu_3 + \nu_1\ (\beta^2\nu_2 + \alpha^2\nu_3)\right]$$

$$-cP_{123} = Pe\ \nu_1\ (\alpha^2\nu_2 + \beta^2\nu_3)$$

$$8c^2B_{12} = Pe\ \left[3\beta^2\nu_2(\nu_1^2 + \nu_3^2) + 3\alpha^2\nu_3(\nu_1^2 + \nu_2^2)\right.$$

$$\left. + \alpha^2\beta^2\nu_1(\nu_2 - \nu_3)^2 + 2\nu_1\nu_2\nu_3\right]$$

$$2c^2B_{13} = Pe(\nu_1 + \alpha^2\nu_2 + \beta^2\nu_3)\ \nu_1(\alpha^2\nu_2 + \beta^2\nu_3)$$

$$2c^2\beta_{31} = Pe(\beta^2\nu_2 + \alpha^2\nu_3)\left[\nu_2\nu_3 + \nu_1(\beta^2\nu_2 + \alpha^2\nu_3)\right]$$

$$2c^2 B_{33} = 2Pe\ \alpha^2\beta^2\nu_1\ (\nu_2 - \nu_3)^2 \qquad\qquad (7.2)$$

Here P is the number of holes, α and β are the cosine and sine of the tilt angle ψ_h and ν_1, ν_2 and ν_3 are the principal mobilities defined along the principal axes of the hole ellipsoids. These eight equations can be solved in a number of ways to obtain the five parameters (P, ν_1, ν_2, ν_3 and ψ_h). Two identities imposed by the equations 7.2 are useful. These are

$$Pec = \frac{\widetilde{\sigma_{11}}\ (-P_{123})}{B_{13}} \qquad\qquad (7.3)$$

and $\qquad Pec = \dfrac{\widetilde{\sigma_{33}}\ (-P_{231})}{B_{31}} \qquad\qquad (7.4)$

The number of holes can be obtained from the identities 7.3 and 7.4 separately, and if the model holds the two values must be compared within experimental error. Once P is known, the first four equations ($\widetilde{\sigma_{11}}$, $\widetilde{\sigma_{33}}$, $-P_{123}$ and $-P_{231}$) of the set 7.2 are solved to obtain the principal mobilities and the tilt angle. Recalculated magnetoconductivity coefficients from these parameters serve as a check.

7.2   Experimental Results

Experimental results obtained from the two specimens of different orientation at each composition are shown in table 7.1.   The values of $-R_{231}$ measured from different specimen orientations agree within about 10 % for all the compositions, except for the set determined from the samples of composition 2.0 at.% Sn.   For this composition the disagreement is about 40%, well above the estimated experimental error of about 6%. For the other compositions the matching of each pair of alloyed specimens is reasonable: the Hall coefficients are strongly dependent on composition.   The temperature dependences of conductivities ($\widetilde{\sigma_{11}}$ and $\widetilde{\sigma_{33}}$) between 77°K and room temperature are shown logarithmically in figure 7.1.   Tangents to the curves at room temperature, which assume $\widetilde{\sigma_{ij}} \propto T^{-x}$, give the values presented in table 7.2 for the exponent x, which decreases for higher doping level.   The values of x obtained from the both components of conductivity are the same for each composition : there is no anisotropy in the temperature dependence of the carrier mobilities.

Table 7.1

Experimental Values of the Magnetoresistivity Tensor

Components of Antimony-Tin Alloys between 77°K and 273°K

Concentration % sn	Sample Orientation	Temp. °K	Resistivity ρ_{11}	ρ_{33}	Hall $-R_{123}$	$-R_{231}$	Magnetoresistivity A_{12}	A_{13}	A_{31}	A_{33}
1.7%	s-90°	273	39.5		7.6	13.6	~8	~5		
		183	29.2		8.4	15.2	~14	~10		
		77	18.9		9.7	16.2	27.2	22.0		
	s – 0°	273		55.0		14.3			36.0	9.0
		183		41.2		15.4			44.2	13.5
		77		25.9		17.0			64.4	27.0
2.0%	S-90°	273	43.5		3.7	9.8	~6	~6		
		183	34.0		4.1	10.5				
		77	24.0		4.6	11.0	9.2	8.3		
	s – 0°	273		57.6		14.0			32.0	7.5
		183		43.5		15.2			38.2	12.
		77		28.1		16.7			52.0	23.0

Concentration %Sn	Sample orientation	Temp. °K	Resistivity		Hall		Magnetoresistivity			
			ρ_{11}	ρ_{33}	$-R_{123}$	$-R_{231}$	A_{12}	A_{13}	A_{31}	A_{33}
2.5%	S-90°	273	44.5		3.80	8.90				
		183	34.8		3.94	9.60				
		77	24.8		4.40	10.0	9.0	6.2		
	S – 0°	273		70.6		9.90				
		183		55.0		10.5				
		77		38.5		11.2			19	
3.0%	S-90°	273	45.0		2.4	7.6				
		183	36.6		2.5	7.3				
		77	26.5		2.7	7.5	5.6	5.2		
	S – 0°	273		85.4		6.0				
		183		70.0		6.0				
		77		52.0		6.3			12	4.0
8.0%	S-90°	273	47.3		0.60	1.40				
		183	39.6		0.65	1.60				
		77	32.0		0.57	1.37				
	S – 0°	273		85.0		1.35				
		183		72.7		1.28				
		77		59.3		1.24			∠0.5	

Units: ρ_{ij}, 10^{-6} ohm cm; R_{ijk}, 10^{-8} ohm cm kG^{-1}; A_{ij}, 10^{-10} ohm cm kG^{-2}.

FIGURE 7.1

Temperature dependence of the coductivities σ_{11} and σ_{33} in antimony-tin alloys

Table 7.2
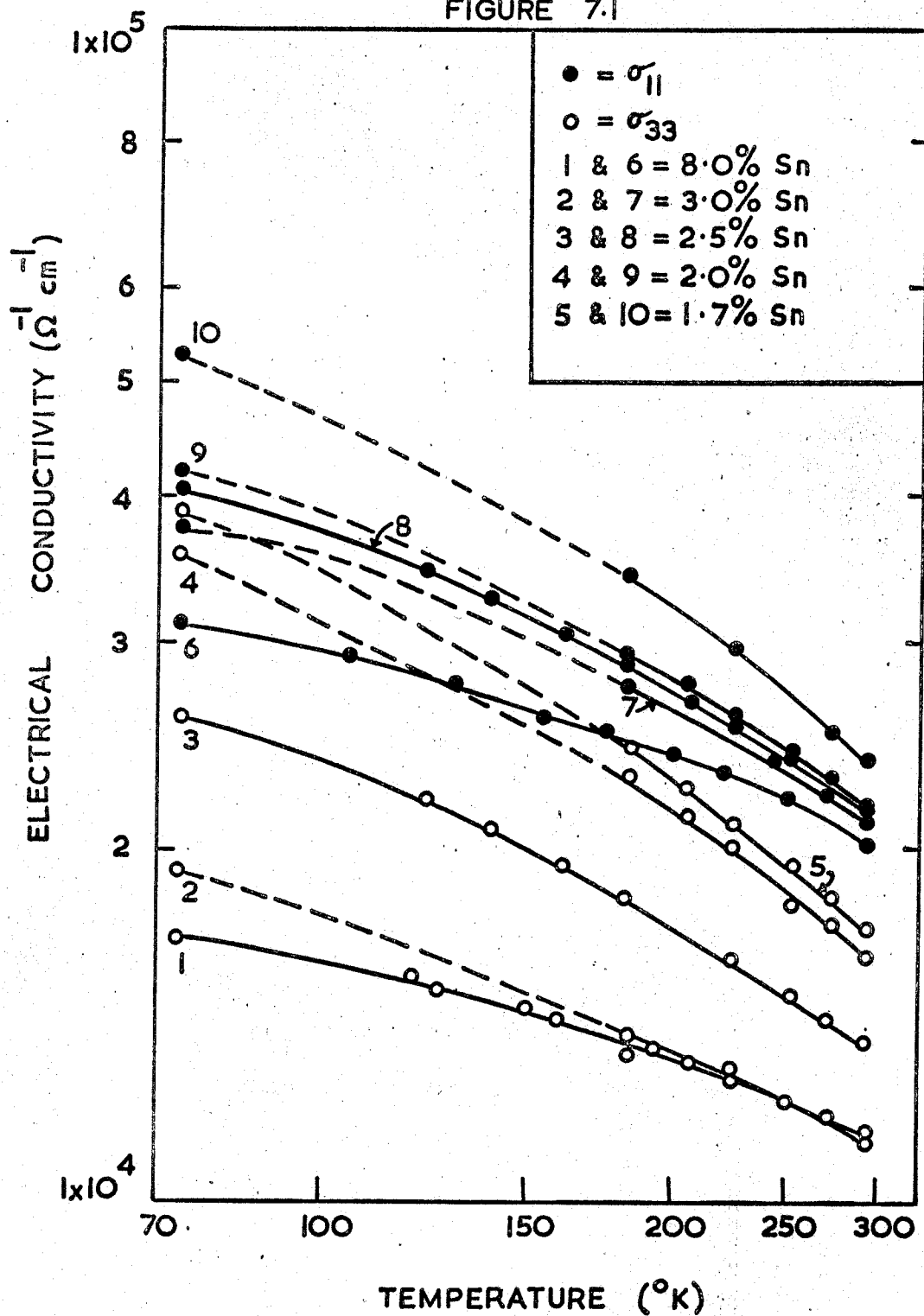
The values at 293°K of the exponent x estaimated
from the temperature dependence of the conductivities.

Composition (% Sn)	Exponent x	
	$\widetilde{\sigma_{11}}$	$\widetilde{\sigma_{33}}$
pure	-1.39	-1.39
1.7	-0.84	-0.85
2.0	-0.73	-0.75
2.5	-0.64	-0.63
3.0	-0.62	-0.59
8.0	-0.49	-0.49

Figure 7.2 illustrates the composition dependence
of the two components of resistivity at room temperature.
The values for the compositions 0.2 at. % and 0.8 at. %
tin are taken from the data of Epstein and Juretschke (1963).
ρ_{33} increases continuously with increasing tin concentra-
tion, while ρ_{11} decreases first and passes through a minimum.
This concentration dependence of resistivities can be
explained by considering the mobility ratios $\mu x/\nu x = 0.47$
and $\mu z/\nu z = 0.94$ obtained for antimony given in table 6.7 -(a)

FIGURE 7·2

Tin Concentration Dependence of the Resistivities at Room Temperature.
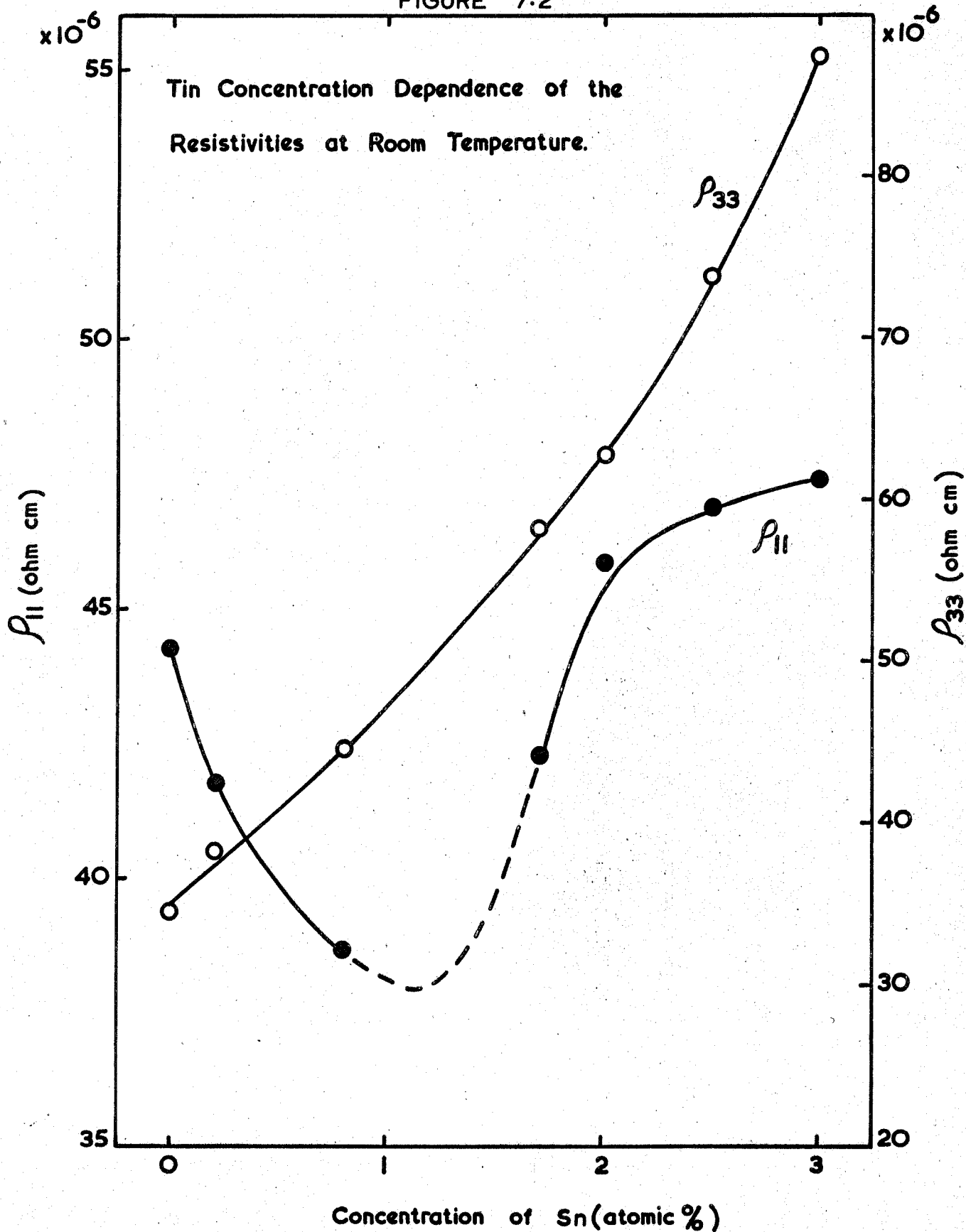
(page 103) for the solution type D. To simplify the discussion these ratios can be taken as 0.50 and 1.00 respectively: thus, $\mu_x = \nu_x/2 = \eta_x$ and $\mu_z = \nu_z = \eta_z$. Then the resistivity components for pure antimony can be written in the form

$$\rho_{11} \approx \frac{1}{Ne\eta_x + 2Pe\,\eta_x} = \frac{1}{(N + 2P)\eta_x}$$

$$\rho_{33} \approx \frac{1}{(N + P)\,e\eta_z} \qquad\qquad (7.5)$$

where N and P, equal in pure antimony, are the number of electrons and holes respectively. On alloying, the number of electrons becomes $(N - \delta)$ and holes $(N + \delta)$. The resistivity components then take the form

$$\rho'_{11} \approx \frac{1}{(N - \delta + 2(N + \delta))e\,\eta'_x} = \frac{1}{(3N + \delta)\,e\eta'_x}$$

$$\rho'_{33} \approx \frac{1}{(N - \delta + N + \delta)\,e\,\eta'_z}\ \ \frac{1}{2Ne\,\eta'_z} \cdot \qquad (7.6)$$

The origin of the difference in behaviour of ρ_{11} and ρ_{33} can be seen by inspection of equations 7.5 and 7.6. Since $\eta'_z < \eta_z$ (due to increased scattering), then $\rho'_{33} > \rho_{33}$. However, for the other component (ρ_{11}) although $\eta'_x < \eta_x$ holds, the increment of carriers outweighs the mobility decrease at

small concentrations and, therefore, the resistivity curve shows a minimum. Further increase of tin concentration enhances scattering, and $\eta_x^!$ decreases rapidly : $\rho_{11}^!$ begins to rise again. At low temperatures, below about 200^OK, where the impurity scattering dominate, this minimum is not observable. In figure 7.3 a set of similar curves are shown for the resistivity component ρ_{11} at temperatures 4.2^OK, 100^OK, 200^OK and 300^OK. The values have been taken from the data of Lane and Dodd (1942).

Similarly the composition dependence of Hall coefficients are shown in figure 7.4. $-R_{231}$ has a maximum at about 0.2% tin concentration, while $-R_{123}$ decreases monotonically with increasing tin.

Magnetoconductivity coefficient calculated from the magnetoresistivity coefficients given in table 7.1 are shown in table 7.3. The number of carriers has been estimated from the two identities 7.3 and 7.4, and are presented in table 7.4.

FIGURE 7·3

Tin concentration dependence of ρ_{11}
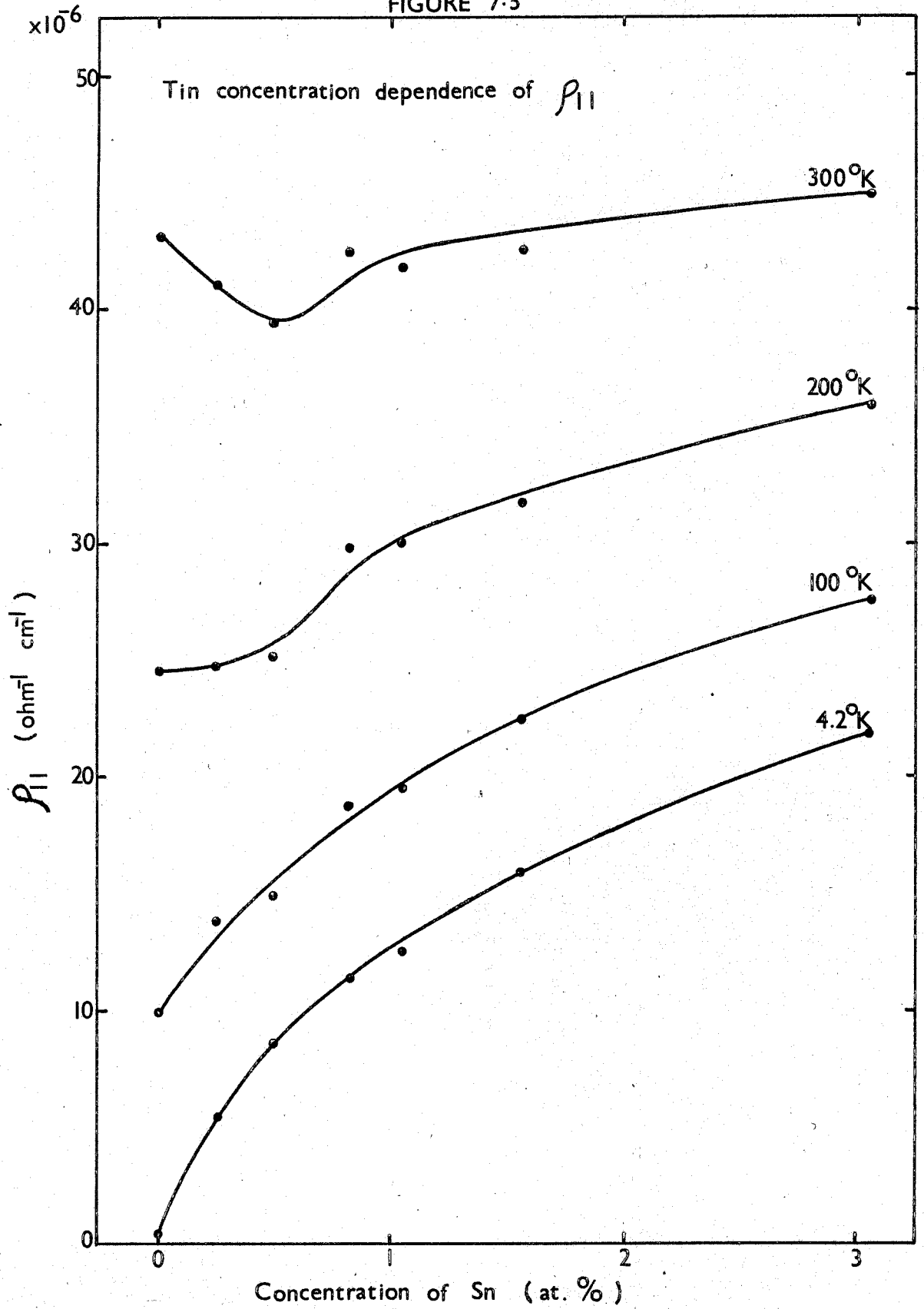
FIGURE 7.4

Tin Concentration Dependence of the Hall Coefficients at Room Temperature.
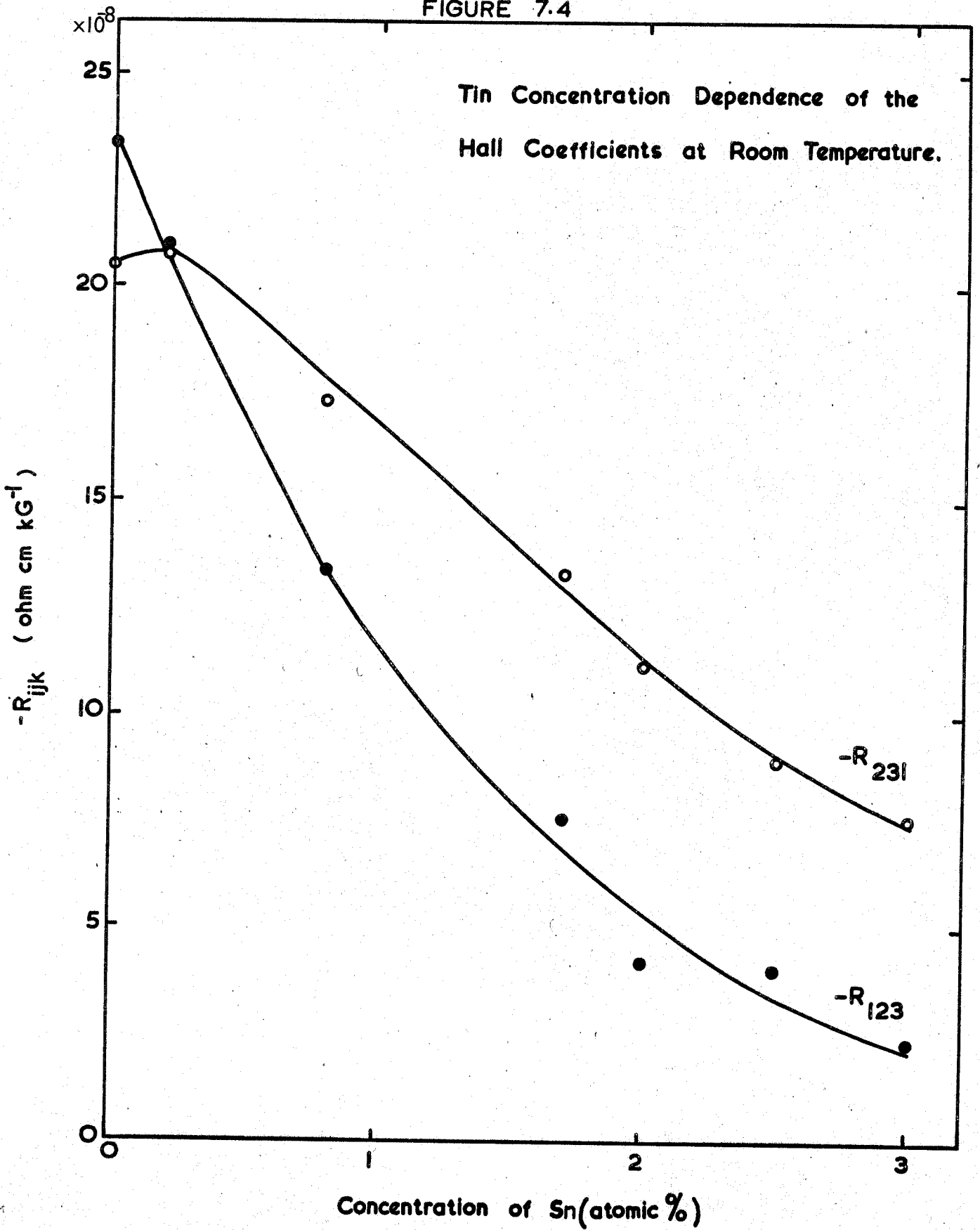
Table 7.3

Magnetoconductivity tensor coefficients.

Composition (at.% Sn)	Temp. °K	Magnetoconductivity coefficients							
		σ_{11}	σ_{33}	P_{123}	P_{231}	B_{12}	B_{13}	B_{31}	B_{33}
1.7%	273	2.53	1.82	0.49	0.62	0.7	0.4	1.3	0.30
	183	3.47	2.43	1.01	1.28	2.3	1.5	3.1	0.80
	77	5.29	3.80	3.37	3.32	10.7	7.6	11.8	4.03
2.0%	273	2.30	1.73	0.20	0.39			1.0	0.23
	183	2.94	2.30	0.36	0.71	0.8	0.56	2.3	0.63
	77	4.11	3.57	0.77	1.60	2.3	1.6	7.3	2.91
2.5%	273	2.33	1.44	0.19	0.36				
	183	2.88	1.82	0.32	0.52				
	77	4.04	2.60	0.71	1.11	2.0	1.13	1.61	
3.0%	273	2.22	1.17	0.12	0.18				
	183	2.73	1.43	0.19	0.27				
	77	3.78	1.92	0.38	0.50	0.94	0.78	0.52	0.15

Units: σ_{ij}, 10^4 ohm^{-1} cm^{-1}; P_{ijk}, 10^2 ohm^{-1} cm^{-1} kG^{-1}; B_{ij}, ohm^{-1} cm^{-1} kG^{-2}.

Table 7.4

Calculation of number of holes from the

two identities 7.3 and 7.4.

Composition (atomic %)	$\dfrac{\sigma_{11}\,(-P_{123})}{ecB_{13}}$ $P =$	$\dfrac{\sigma_{33}(-P_{231})}{ecB_{31}}$ $P=$
1.7%	1.20	0.71
2.0%	1.30	0.68
2.5%	1.63	1.17
3.0%	1.25	1.24

P is quoted in units of 10^{20} cm^{-3}.

7.3   Computation of the Band Parameters of Antimony-
Tin Alloys.

The method of solution of the first four equations of
the set 7.2 is presented in Appendix D1 together with the
computer programme by which the calculations were carried out
for various values of P. In particular extensive calculations
were performed for the data obtained at 77^OK for the composi-
tions 1.7 at.% and 2.5 at.% tin. No solutions were found
for the estimated range of P, shown in table 7.4, from the
identities 7.3 and 7.4. However, when the input data had
been altered within experimental error, some solutions were
obtained with values of P about 2 or 3 times larger than
those of shown in table 7.4. The solutions with best fit
to the experimental data found for both compositions are
presented in table 7.5, and the comparison of the calculated
coefficients to the experimental data is shown in table 7.6.
These solutions can be compared with the valence band structure
of antimony given in tables 6.4 and 6.7 -(a); the tilt angles
found are 31° for 1.7 % and 30° for 2.5% composition, in
accord with that of 24° : the principal mobilities in each
direction are in good qualitative agreement. However, the fit,
demonstrated in table 7.6, is poor, particularly for the
components of the coefficients B_{ij}.

The calculations for the rest of the compositions
and at all temperatures were carried out by Dr. G.A. Saunders

Table 7.5

Band parameters of antimony-tin alloys for compositions of 1.7 at.% and 2.5 at.% tin.

Composition	1.7 at.%	2.5 at.%
P	2.5	4.0
ν_1	2.12	1.00
ν_2	0.05	0.01
ν_3	1.18	0.51
ψ_h	31°	30°

Units: P, 10^{20} cm^{-3}; mobilities, 10^3 cm^2 volt^{-1} sec^{-1}.

Table 7.6

To compare the recalculated values of the
magnetoconductivity coefficients for the
solutions given in table 7.5 with the
experimental data.

Composition	1.7 at.%		2.5 at.%	
	Cal.	Cal./Exp	Cal.	Cal./Exp
$\widetilde{\sigma_{11}}$	4.94	0.93	3.61	0.90
$\widetilde{\sigma_{33}}$	3.46	0.90	2.44	0.94
$-P_{123}$	3.01	1.10	0.83	1.15
$-P_{231}$	3.77	1.09	1.22	1.10
B_{12}	6.22	0.58	0.95	0.48
B_{13}	3.72	0.49	0.47	0.42
B_{31}	3.26	0.28	0.46	0.29
B_{33}	2.14	0.53	0.31	---

Units: $\widetilde{\sigma_{ij}}$, 10^4 ohm^{-1} cm^{-1}; P_{ijk}, 10^2 ohm^{-1} cm^{-1} kG^{-1};

B_{ij}, ohm^{-1} cm^{-1} kG^{-2}.

with the assumption that ν_2 is equal to zero. Since ν_2
is much smaller than ν_1 and ν_3 as found for antimony, this
is a good approximation and allows estimation of the number
of carriers from the equations relating band parameters to
the components of conductivities ($\widetilde{G}_{11}$ and $\widetilde{G}_{33}$) and inverse
Hall coefficients ($-P_{123}$ and $-P_{231}$). The calculated band
parameters are detailed in table 7.7. This different
method of calculation neither changes the main structure
of the solution given in table 7.5 nor improves the fit
to the experimental data. The tilt angles then are found
to be $30^{\circ} \mp 3^{\circ}$ and are invariant with temperature and
composition, even out to 8 at.% tin. But the calculated
values of B_{ij} are about the half of those found by experiment.
Carrier densities indicate that, for alloys containing between
1.7% and 3.0% tin, each tin atom contributes 0.75 ∓ 0.15
carrier to the holes.

Table 7.7

Calculated Band Parameters of Antimony-Tin Alloys

Composition (% Sn)	Temperature $^{\circ}K$	Hole Mobilities		Carrier Density	Tilt Angle (ψ_h)
		ν_1	ν_3		
1.7%	77	1.75	1.03	3.2	32.5°
	183	1.05	0.60	3.5	32.5°
	273	0.68	0.40	4.0	32.1°
2.0%	77	0.90	0.54	5.1	26.8°
	183	0.62	0.33	5.4	26.9°
	273	0.45	0.23	5.6	26.9°
2.5%	77	0.85	0.40	5.3	29.5°
	183	0.57	0.26	5.6	29.0°
	273	0.49	0.21	5.5	27.2°
3.0%	77	0.52	0.20	8.2	31.8°
	183	0.37	0.14	8.8	30.7°
	273	0.30	0.12	8.3	30.4°
8%	77	0.079	0.033	33.0	32.9°

Units: Hole mobilities, 10^3 cm^2 $volt^{-1}$ sec^{-1};

carrier density, 10^{20} cm^{-3}.

7.4   Discussion

Discrepancies between experimental and calculated values of B_{ij} give notice that the band structure is more complex than the model employed. By introducing more holes the volumes of the ellipsoid-like pockets are increased: the ellipsoidal approximation may no longer hold, as a result of the extention of the pockets. In fact the hole ellipsoids in antimony are already warped. The carrier densities in these alloys are of the same order as that of arsenic (2.1×10^{20} cm^{-3}). The holes in arsenic are contained in a multiply-connected surface of six warped, ellipsoid-like pockets joined by necks (Priestley et al 1967). The antimony-tin alloys may have a similar band structure. Effects of inhomogeneity of the samples have been neglected. This may have profound effect on observed coefficients.

Addition of 1.7% or more tin depresses the Fermi level well below that of pure antimony. Therefore, it is possible to assume a second valence band as in bismuth (see Morimoto and Takamura 1967 for references), in which the carriers have different effective masses. Some preliminary calculations carried out by Dr. G. A. Saunders have shown that a very good fit to the experimental data can be obtained by assuming a second valence band consisting

of either one or two ellipsoids of revolution about the trigonal axis. The carrier density in the second band is about two orders of magnitude smaller and carriers are more mobile than those in the primary band, which keeps its original structure.

CHAPTER   VIII

Discussion

In chapter 6 it was shown that the low field galvano-magnetic effects in antimony, measured between $77^{O}K$ and $273^{O}K$, can be explained by the multi-valleyed band model with holes occupying highly tilted ellipsoids, while electrons are contained in the extrema of low tilt angle. The nine band and mobility parameters have been determined: temperature dependences of carrier densities and mobilities are then resolved. These now be discussed in the first section of this chapter. At the onset of this work, the Seebeck coefficient could not be explained quantitatively (Saunders et al 1965): the band model was not then complete and the temperature dependences of the carrier mobilities in antimony were not known. With the aid of the present data, the Seebeck coefficient has been fitted by a two parabolic band model. The calculations were mainly carried out by Dr. G. A. Saunders. However, since the findings are interesting and closely related to the results obtained

from the galvanomagnetic effects, a short summary of these
calculations and conclusions are given in section 8.2. Finally,
the band structure of antimony will be summarized.

8.1.   Carrier Mobilities and Densities

In section 2.6. it was shown that, when the number of
conduction electrons per atom n_a is smaller than 1/4, the
relaxation time is given by

$$\tau = a \; T^{-1} \; \mathcal{E}^{-1/2} \qquad\qquad (8.1.)$$

where a is a constant. This expression is equivalent to
equation 2.39 (page 33) and applies to semimetals. The present
finding of $T^{-1.42}$ and $T^{-1.48}$ laws for scattering of electrons
and holes respectively evidence a similar scattering mechanism
for both types of carriers. The exponent may be compared
with that of -2.1 for bismuth (Gallo et al 1963) and -1.2 for
single crystal graphite (Soule 1958). In a semiconductor,
the mean energy of the non-degenerate carrier is proportional to
$T^{-1/2}$ and, hence, for acoustic mode lattice scattering, the
relaxation time and carrier mobilities obey a $T^{-1.5}$ law. In
metals and semimetals, where degenerate statistics is applicable,
only carriers on the Fermi surface need be considered. The
Fermi level in semimetals has only a weak temperature dependence
and is constant in metals. The Seebeck coefficient data of
antimony, which will be discussed in the next section, show that

the Fermi energies of electrons and holes are constant between $77^{o}K$ and $300^{o}K$ and then increase above room temperature. Thus, for acoustic mode intravalley scattering, a mobility temperature dependence closer to $T^{-1.0}$ between $77^{o}K$ and $300^{o}K$ would be expected. To examine this discrepancy further, the measurements of the conductivity component $\widetilde{\sigma}_{11}$ have been extended up to about $700^{o}K$ and are shown, plotted on a logarithmic scale in figure 8.1. Inspection of this figure reveals that only a slight change takes place in the slope above room temperature where the Fermi energy and density of both carriers increase. Assuming $\widetilde{\sigma}_{ij} \propto T^{-x}$, the exponent x gives a value of 1.39 at low temperatures but reduces to 1.16 towards $700^{o}K$. The $T^{-1.5}$ dependence of mobilities does not appear to have a simple explanation. Further theoretical studies should clarify the situation and assess possible contributions from other mechanisms such as intervalley scattering and electron-hole collisions.

From the effective mass tensor data of Datars and Vanderkooy (1964) and the principal mobilities determined in solution D (see table 6.4, page 99), the carrier relaxation times have been estimated and are shown in table 8.1. Carrier signs assumed by Datars and Vanderkooy were inverted. These relaxation times are not highly anisotropic, and are an order of magnitude larger than those in metals at the same temperature (i.e. for copper at $0^{o}C$, $\tau \sim 3 \times 10^{-14}$ sec. Mott and Jones 1936,

FIGURE 8·1

Sample S-90°-1
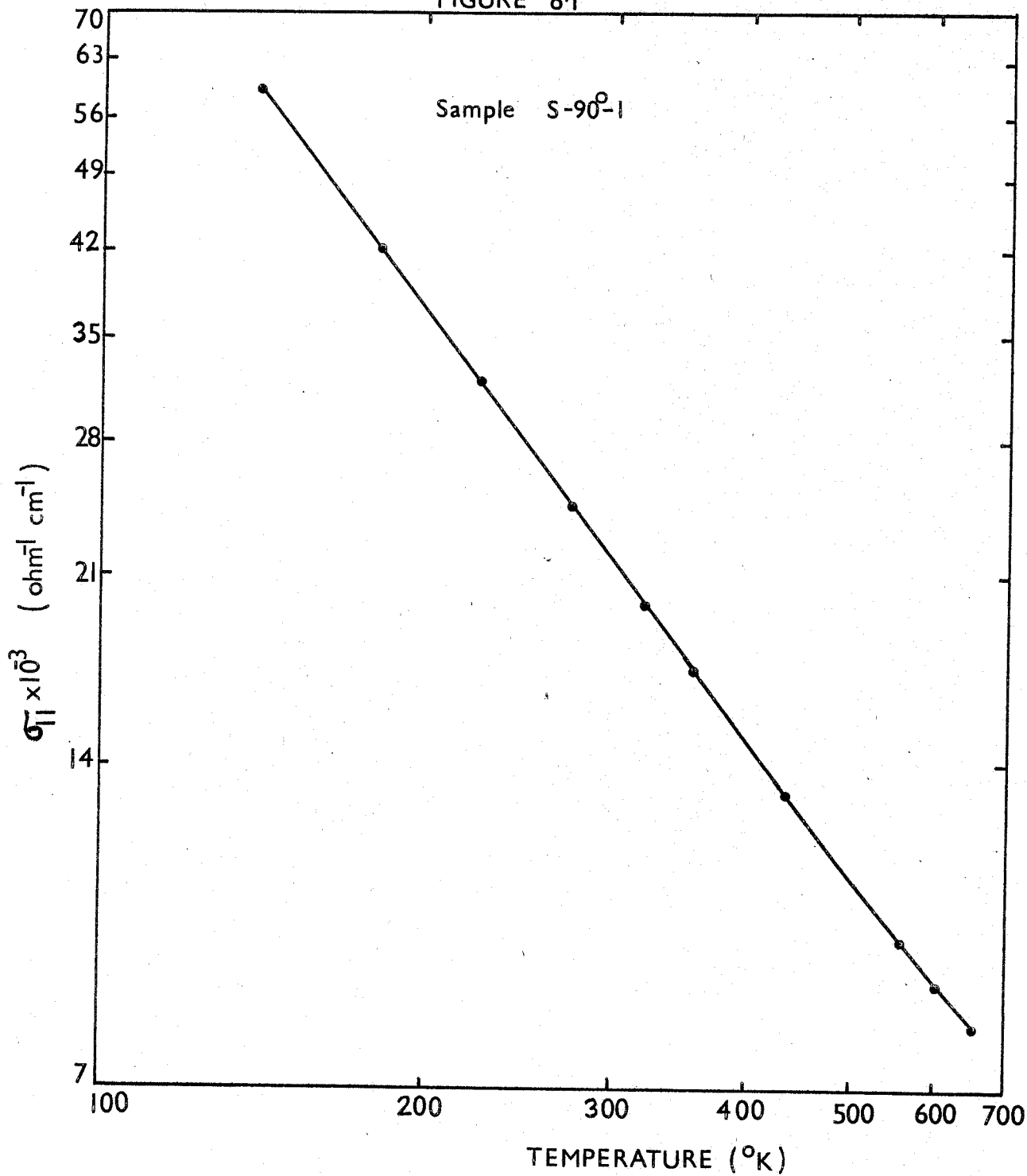
The conductivity σ_{11} as a function of temperature

Table 8.1

Relaxation times for electrons and holes in antimony calculated from the cyclotron effective masses (Datars and Vanderkooy 1964) and mobility data from solution D.

Relaxation Times	273°K	225°K	183°K	139°K	77°K
Electrons					
τ_1	1.4	1.7	2.4	3.6	8.6
τ_2	0.7	0.6	0.7	1.1	2.5
τ_3	1.0	1.5	1.9	2.7	6.3
Holes					
τ_1	1.4	2.0	2.7	3.9	9.1
τ_2	1.0	1.7	1.4	2.3	8.9
τ_3	0.9	1.1	1.6	2.6	6.1

Relaxation times are quoted in units of 10^{-13} sec.

page 286). This arises since in semimetals only the longest-wavelength phonons can scatter the carriers, as discussed in section 2.6. Sondheimer (1952) has shown that the relaxation time is proportional to $(4n_a)^{-4/3}$. A decrease in relaxation time follows qualitatively through the sequence of semimetals, at 77°K, with increasing carrier density

bismuth: $n_a = 1.7 \times 10^{-5}$ $\tau_{av} \sim 10^{-11}$ sec.

graphite: $n_a = 5 \times 10^{-5}$ $\tau_{av} \sim 2 \times 10^{-12}$ sec.

and antimony: $n_a = 1.2 \times 10^{-3}$ $\tau_{av} \sim 7 \times 10^{-13}$ sec.

The long relaxation time coupled with the small carrier effective masses accounts for the comparatively high mobilities found for semimetals, which in turn provides measurable galvanomagnetic coefficients of high order.

Carrier densities, calculated in solution D as 3.9×10^{-19} cm^{-3} at 77^OK and 4.2×10^{-19} cm^{-3} at 273^OK, are essentially temperature independent in this temperature range. These values are about 25% less than that (5.5×10^{-19} cm^{-3}) obtained by the de Haas-van Alphen effect measurements of Windmiller and Priestley (1965), while in agreement with that from the de Haas-Shubnikov effect data (4.07×10^{-19} cm^{-3}) of Ketterson and Eckstein (1963) and the ultrasonic attenuation measurements (4.2×10^{-19} cm^{-3}) of Eriksson et al (1964).

8.2.   The Seebeck Coefficient of Atimony Single Crystals

and the Fermi Energies of Electrons and Holes.

The Seebeck coefficients S_{33} and S_{11}, which can be obtained respectively from measurements made along the trigonal axis and in the plane perpendicular to this axis, have been measured between 77^OK and 300^OK by Saunders et al (1965). Measurements have now been extended up to 700^OK. Using the carrier mobilities obtained from solution D, the results have been

FIGURE 8·2
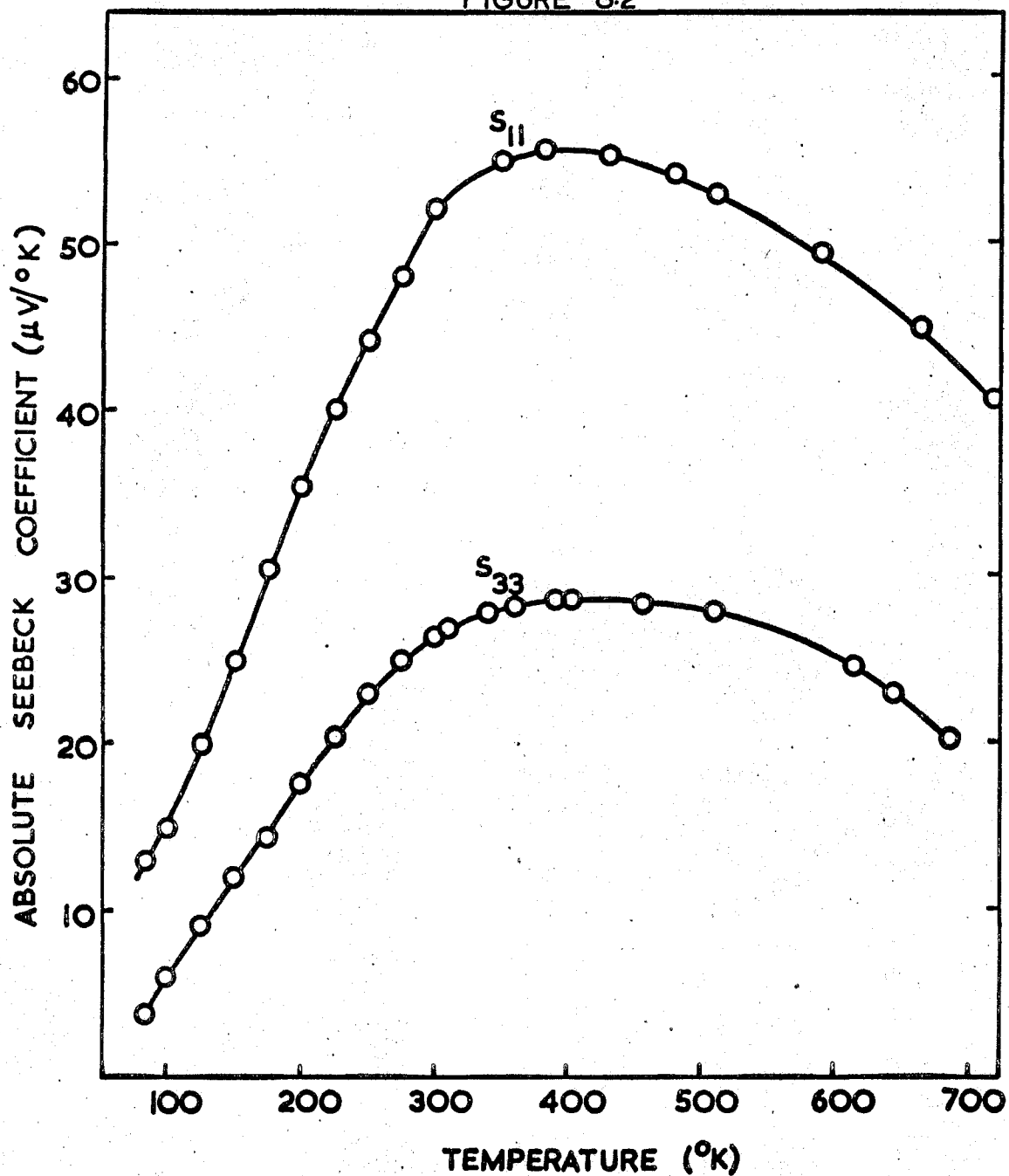
The experimental values of the absolute Seebeck coefficients in antimony as a function of temperature.

analysed by the transport theory methods employed in the study
of bismuth (Chandrasekhar 1959, Gallo et al 1963). The
experimental results are plotted as a function of temperature
in figure 8.2. Experimental errors are estimated as $\mp$ 4% at
low temperatures but about $\mp$ 6% above room temperature. For
both components a maximum is extant at about $400^{\circ}K$.

Assuming isotropic ralaxation time, which can be
written as $\tau = \tau_o \mathcal{E}^s$, for both electrons and holes, the
isotropic, partial Seebeck coefficients S_e and S_h are obtained
from

$$S_{11} = \frac{(\sigma_e)_{11} S_e + (\sigma_h)_{11} S_h}{(\sigma_e)_{11} + (\sigma_h)_{11}} = \frac{(\mu_x/\nu_x) S_e + S_h}{(\mu_x/\nu_x) + 1} \qquad (8.2)$$

$$S_{33} = \frac{(\sigma_e)_{33} S_e + (\sigma_h)_{33} S_h}{(\sigma_e)_{33} + (\sigma_h)_{33}} = \frac{(\mu_z/\nu_z) S_e + S_h}{(\mu_z/\nu_z) + 1} \qquad (8.3)$$

Here σ_e and σ_h are the partial conductivities of electrons
and holes. The partial Seebeck coefficients are related to the
reduced Fermi energies of electrons $\xi_e = \mathcal{E}_F^e/kT$ and holes
$\xi_h = \mathcal{E}_F^h/kT$ by

$$S_e = \frac{k}{e} \left[\frac{(5/2 + s) F_{3/2 + s} (\xi_e)}{(3/2 + s) F_{1/2 + s} (\xi_e)} - \xi_e \right] \qquad (8.4)$$

$$S_h = \frac{k}{e} \left[\frac{(5/2 + s) \ F_{3/2 + s} \ (\bar{\xi}_h)}{(3/2 + s) \ F_{1/2 + s} \ (\bar{\xi}_h)} - \bar{\xi}_h \right] \qquad (8.5)$$

where s is taken as -1/2 for acoustic mode intravalley scattering.
These equations lead to the calculation of the Fermi energies in
both bands and the overlap energy $(-\mathcal{E}_o)$, measured from the top
of the valence band to the bottom of the conduction band. The
negative sign arises from use of the same convention employed
for semiconductors.

For quantitative resolution of the Seebeck coefficient,
it is necessary to know the electron and hole mobility ratios
$L_x = \mu_x/\nu_x$ and $L_z = \mu_z/\nu_z$ and their temperature dependences. It
was shown in chapter 6 that it is not possible to assess the
values of these ratios uniquely from solution D: they cover
a physically acceptable range of between 0.47 and 0.56 for L_x
and between 0.76 to 0.94 for L_z. However, since the hole and
electron mobilities show almost identical temperature dependences
between 77^oK and 273^oK, the mobility ratios can be assumed
independent of temperature. When the electron-hole mobility
ratios L_x and L_z are taken as 0.50 $\mp$ 0.03 and 0.90 $\mp$ 0.03
respectively, the calculated values of $\mathcal{E}_F^e$, $\mathcal{E}_F^h$ and $-\mathcal{E}_o$,
which are sensitive to the mobility ratios, agree with the
results found by other methods. The effect of changes in the
electron-hole mobility ratio L_x and L_z on the calculated Fermi
energies and the band overlap are summarized in table 8.2.

Table 8.2

To show the effect of changes in the electron/
hole mobility ratio L_x and L_z on the calculated
Fermi energies and the band overlap.

Energy (eV)	Temp °K	$L_x = 0.50$ $L_z = 0.90$	$L_x = 0.47$ $L_z = 0.87$	$L_x = 0.47$ $L_z = 0.92$
$\mathcal{E}_F^e$	100	0.098	0.10	0.12
	300	0.099	0.10	0.12
	500	0.17	0.18	0.16
	700	0.31	0.31	0.37
$\mathcal{E}_F^h$	100	0.067	0.070	0.070
	300	0.067	0.070	0.070
	500	0.083	0.089	0.11
	700	0.16	0.18	0.20
$-\mathcal{E}_o$	100	0.16	0.17	0.19
	300	0.16	0.17	0.19
	500	0.25	0.27	0.27
	700	0.47	0.49	0.57

For the pair ($L_x = 0.50$ and $L_z = 0.90$) the results are plotted
as a function of temperature in figure 8.3 and in figure 8.4
the partial Seebeck coefficients are shown.

FIGURE 8·3
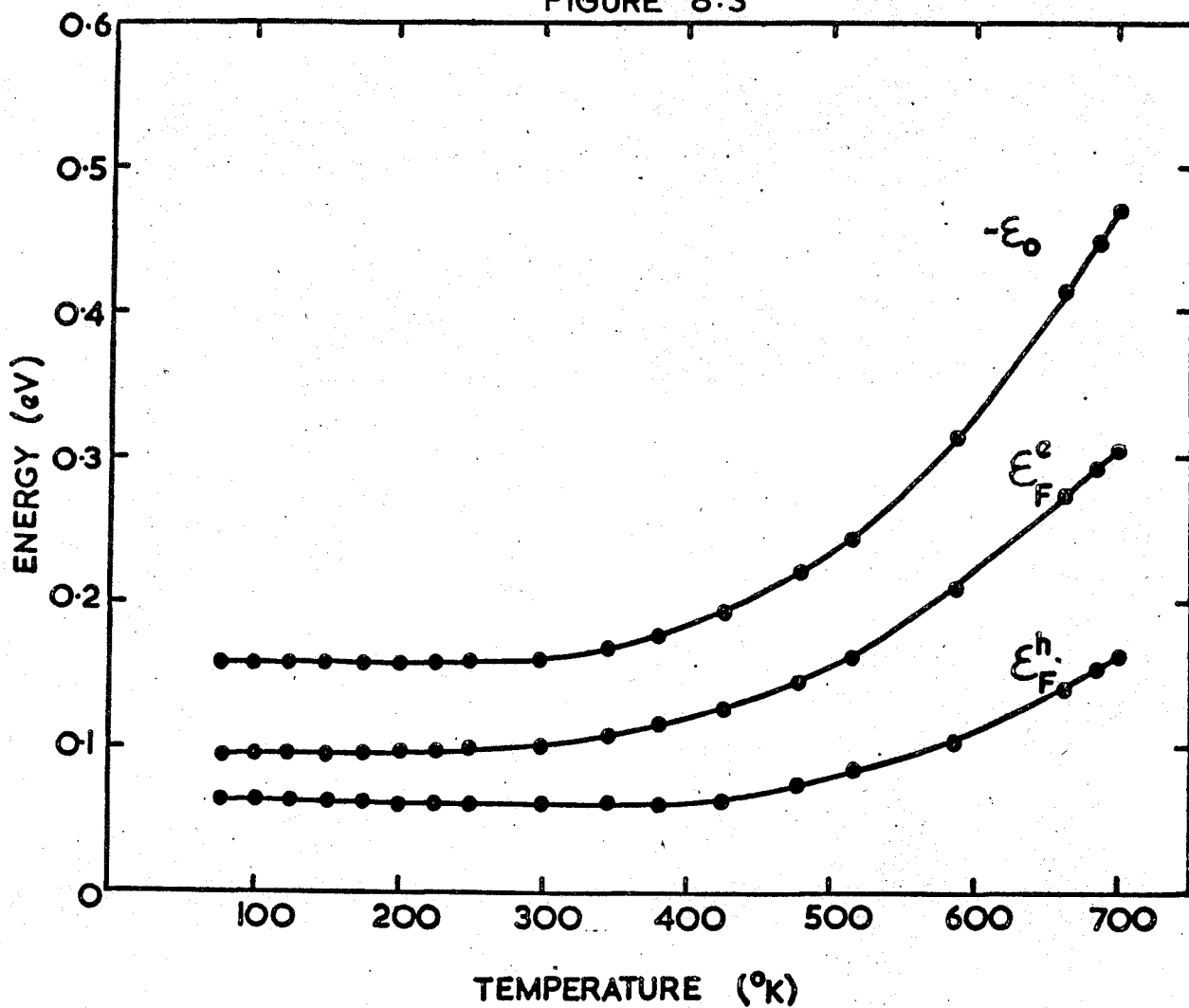
Calculated values of the overlap energy $-\mathcal{E}_o$ and the Fermi energies of electrons $\mathcal{E}_F^e$ and holes $\mathcal{E}_F^h$ in antimony as a function of temperature. The mobility ratios L_x and L_z used are 0.50 and 0.90 respectively.

FIGURE 8.4
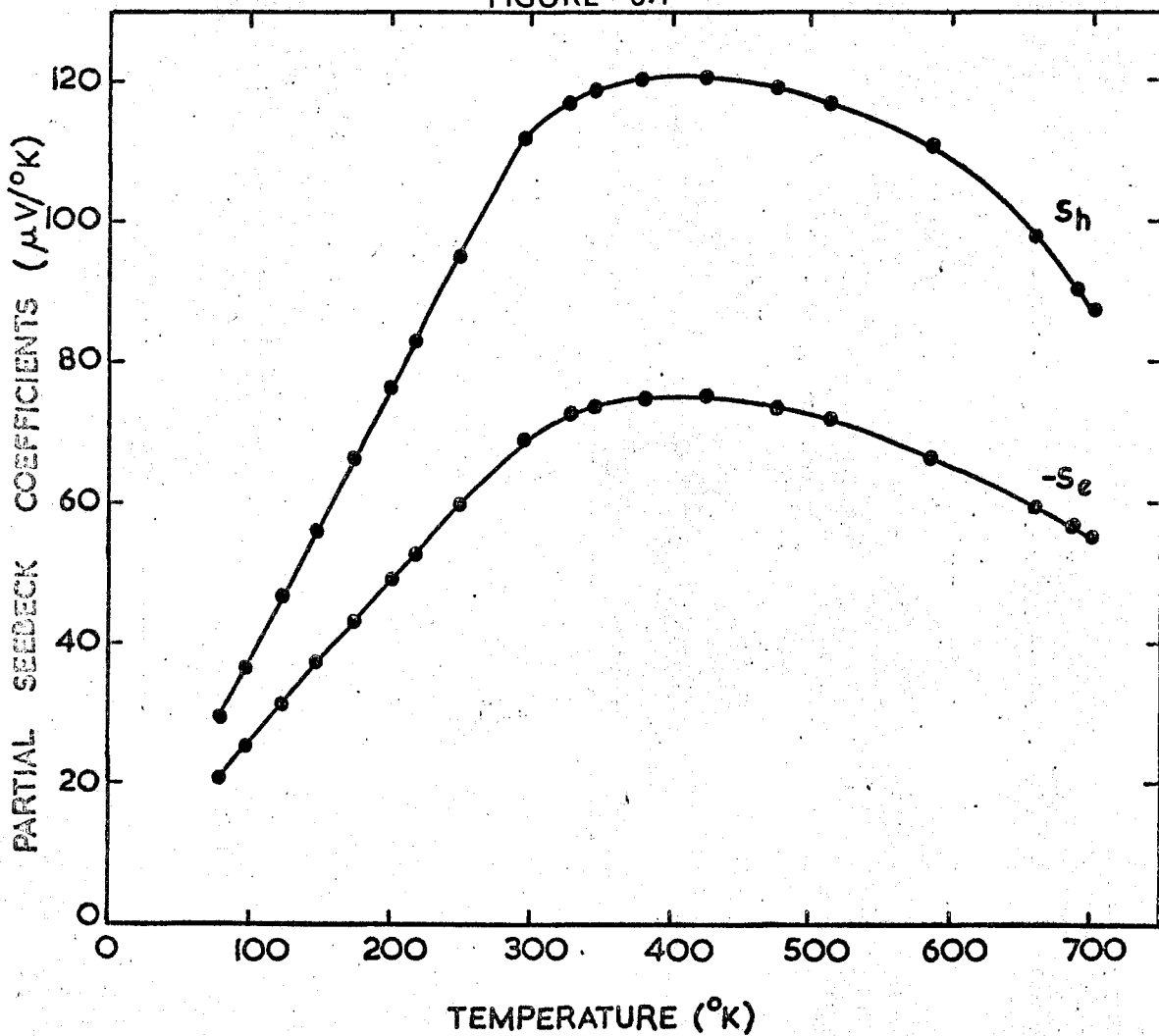
The isotropic, partial Seebeck coefficients as a function of temperature.

Between 77^OK and room temperature $\mathcal{E}_F^e$ is 0.098 eV and $\mathcal{E}_F^h$ is 0.067 eV. The overlap energy, estimated as 0.165 eV, agrees with that obtained at liquid helium temperatures from the de Haas-Shubnikov effect (0.20 eV) by Rao et al (1964). The Fermi energies and the band overlap energy are esentially temperature independent up to 300^OK and then increase markedly. The assumption of constant mobility ratios might not be quite correct beyond 300^OK: the results obtained at higher tempera-tures must be treated cautiously. However, this does not change the general behaviour.

Falicov and Lin (1966) predict location of the holes in six and the electrons in three pockets. This can be verified through comparing the Fermi energies obtained from the Seebeck coefficient with that calculated from the carrier density taking various numbers of ellipsoids. For a parabolic band containing n ellipsoids

$$\frac{N}{n} = \frac{4\pi}{h^3} (2m_o kT)^{3/2} (m^T)^{3/2} F_{1/2} (\xi) \qquad (8.6)$$

where N is total number of carriers, being equal for electrons and holes, and m^T (in units of m_o) is the density of states effective mass per ellipsoid, given by $(m_1 m_2 m_3)^{1/3}$. m_e^T and m_h^T, the electron and hole density of states effective masses, have been estimated from the cyclotron resonance data of Datars and Vanderkoy (1964) as 0.2 ± 0.01 and 0.15 ± 0.01 respectively. On the assumption that each band contains three or six

ellipsoids, the Fermi energies $\mathcal{E}_F^e$ and $\mathcal{E}_F^h$ have been calculated by Dr. G. A. Saunders and results are shown in table 8.3, together with that estimated from the Seebeck coefficient. Reasonable agreement obtains only for the model with six extrema in the valence band and three in the conduction band, verifying the prediction of Falicov and Lin. The Seebeck coefficient of antimony can be fitted with the simple, two parabolic band model.

Probably the closest solution to the true mobility values in antimony is that given in table 6.7 -(a) (page 103): the Seebeck coefficient and changes in resistivity on alloying with tin are best explained with mobility ratios, μ_z/ν_z = 0.94 and μ_x/ν_x = 0.47, which are very close to the values found for this solution.

In semimetals with overlapping bands and electron and hole effective masses of similar magnitudes, the Fermi level is constrained towards the centre of the region of the band overlap and is closer to the edge of that band containing the heavier carriers. When the temperature increases, the tendency of the Fermi level in each band to decrease is compensated by the thermal excitation of more carriers. Hence, while the number of carriers increases in the two bands, the Fermi level should stay at about the same position at all temperatures; the carriers in each band will be at least partially degenerate. The present finding of increases in

Table 8.3.

Comparison between Fermi energies estimated (i) from carrier
densities assuming 3 or 6 ellipsoids in each band and (ii) from the

Seebeck coefficient

Number of ellipsoids		Electrons		Holes	
		3	6	3	6
(i) Fermi energy estimated from carrier densities and density of states effective masses ($m_e^T = 0.20 \pm 0.01$ and $m_h^T = 0.15 \pm 0.01$)	77°K	0.101 ± 0.005	0.055 ± 0.006	0.139 ± 0.009	0.084 ± 0.006
	273°K	0.089 ± 0.004	0.050 ± 0.004	0.121 ± 0.007	0.073 ± 0.006
(ii) Fermi energies calculated from Seebeck coefficients. (Constant between 77°K and 273°K)		0.095 ± 0.006		0.062 ± 0.004	

Fermi energies above room temperature can be understood by the shift of the band edges, plausibly due in part to thermal expansion; when the lattice spacing changes, the band structure is altered and results in an increased overlap. Similar temperature dependences of the Fermi and overlap energies have been obtained for bismuth from the thermoelectric power (Gallo et al 1963). The concept of degeneracy temperature, defined by setting the Fermi energy equal to kT_D, can have no physical significance, if the band overlap increases, while the Fermi level remains practically pinned between the two band edges. In antimony the carrier populations always remain at least partially degenerate below $700^{\circ}K$ and ξ_e and ξ_h never fall below 3.5 and 2.0 respectively.

8.3.   Relationship Between the Galvanomagnetic Effects
         and the Band Structure of Antimony.

The features of the galvanomagnetic data have been interpreted quantitatively on the basis of a two multi-valley band model. Carrier mobilities obtained in the solution D match the cyclotron resonance effective masses of Datars and Vanderkooy (1964), if an isotropic relaxation time is assumed. Furthermore, the Seebeck coefficient can be fitted with the model and mobility ratios found in this solution. The conclusive feature is the agreement between the tilt angles of solution D and those obtained by other methods. In table 8.4 two groups of tilt angles are collected, the first group containing data from experiments of

Table 8.4.

Tilt angles in antimony. In some cases tilt away from the bisectrix axis was referred to originally but, for an ellipsoidal model, can be considered as equivalent to tilt away from the trigonal axis in the adjacent quadrant. For compilation of this table, the basic rotation in the y-z plane away from the trigonal axis is taken through ΓL. Data from Windmiller and Priestley refer to the tilt angle of the maximum Fermi surface area while in the present work tilt is considered for the minor ellipsoid axis $(3')$ corresponding to the largest carrier mobility in the mirror plane.

Reference	First Carrier	Second Carrier	Electrons	Holes
de Haas-van Alphen oscillations:				
Shoenberg (1952)		35°		
Saito (1964)	0°			
Ishizawa and Tanuma (1965)				36°
Windmiller and Priestley (1965)	6.5^O	31°		
de Haas – Shubnikov Effect:				
Ketterson and Eckstein (1963)	4°	36°		
Cyclotron resonance:				
Datars and Dexter (1961)			36°	
Datars and Vanderkooy (1964)	4°	36°		
Galvanomagnetic effects:				
Freedman and Juretschke (1961)			60°	27°
Epstein and Juretschke (1963)			10°	20°
Present experiment			5°	24°
Ultrasonic attenuation:				
Eriksson et al (1964)	2.5^O	35°		
Theoretical; using a pseudopotential technique:				
Falicov and Lin (1966)			2.5^O	49°

which the assignment of carriers into one of the two sets of ellipsoids is not possible, while the second group shows data obtained from methods which allowed correct placement of the carriers. One set of pockets has a small tilt angle of about 4°, while the tilt angle of the second set is about 35°. Previously, the large tilt angle ellipsoids have been assumed to contain electrons. However, for this case there are no solutions to the galvanomagnetic effects. A direct experiment carried out (Ishizawa and Tanuma 1965) on the de Haas-van Alphen effect in tin-doped antimony first indicated that holes should be assigned to the large tilt pockets. The recent theoretical determination of the band structure by the pseudopotential technique verifies this new carrier assignment (Falicov and Lin 1966).

The preliminary analysis of galvanomagnetic data in antimony-tin alloys, based on the rigid valence band model adds authority to this placement of the holes in the highly tilted pockets and demonstrates that the major contribution to the conductivity σ_{ij} in the alloys come from holes sited in similar pockets to those in antimony itself. But the discrepancies (B_{ij} cal. ~ 0.4 B_{ij} exp.) between the experimental and calculated values of the magnetoconductivity tensor coefficients suggest that the valence band structure in the alloys is more complicated. Calculations, mentioned previously, have shown that the galvanomagnetic effects in the alloys can

be interpreted if a second set of more mobile holes is present (G.A. Saunders - private communication).

Some light is shed on the possible presence of a third set of carriers by the self consistency of solution D over the temperature range. If a third carrier is present in antimony, then changes in the population ratio between the two valence bands might be expected. This effect must distort the values of the tilt angles and carrier densities. This is not observed. Minority carriers can play at most a minimal role in transport processes over the temperature range 77^OK - 273^OK.

In the present work the small tilt angle (3° to 6°) found accords with the results of other workers, shown in table 8.4. But the other tilt angle of 24° is not in close agreement with the usual value of about 35°. Assumptions made in the model must give rise to this discrepancy. It has been assumed that the constant energy surfaces are ellipsoidal. However, it is known that both sets of ellipsoids are in fact warped; the deviation is more marked for the hole pockets, as discussed in the first chapter. The effective tilt angle measured by the galvanomagnetic effects is only a mean value. Tilt angles measured by the de Haas-van Alphen effect are those of a different property, that of the extremal cross-section of the Fermi surface. Assumptions made in carrier scattering and isotropic relaxation times might be responsible in part for the discrepancy.

8.4.   Summary

The galvanomagnetic effects in antimony measured between 77^OK and 273^OK are found to be in reasonable agreement with the theoretical model of the Fermi surface determined by Falicov and Lin (1966). This theoretical work shows that there are three electron pockets, having a tilt angle of about 5°, located at the centres L of the six pseudo-hexagon faces of the Brillouin zone, illustrated in figures 1.10 and 1.14, and six hole pockets, those with a large angle of tilt, contained on the trigonal-bisectrix planes close to points T.

Carrier densities, equal for electrons and holes, are essentially temperature independent up to 273^OK. There are 1.4×1.0^{19} electrons/cm^3 in each electron pocket and 0.7×10^{19} holes/cm^3 in each hole extremum. Both sets of carriers have almost identical temperature dependences of mobility, $T^{-1.42}$ for electrons and $T^{-1.48}$ for holes.

The Seebeck coefficient data can be analysed on the basis of a two parabolic band model from the mobility ratios obtained in solution D. The partial Fermi ($\mathcal{E}_F^e = 0.098$ eV and $\mathcal{E}_F^h = 0.067$ eV) and the band overlap (0.165 eV) energies remain constant between 77^OK and 300^OK but increase rapidly as temperature rises above room temperature.

APPENDIX A

Experimental values for the twelve coefficients of the magnetoresistivity tensor obtained from each specimen at 273°K, 225°K, 183°K, 139°K and 77°K.

Units: ρ_{ij}, 10^{-6} ohm.cm; R_{ijk}, 10^{-7} ohm.cm.kG^{-1}; A_{ij}, 10^{-9} ohm.cm.kG^{-2}.

273°K

Sample	ρ_{11}	ρ_{33}	$-R_{123}$	$-R_{231}$	A_{11}	A_{12}	A_{13}	A_{31}	A_{33}	$-A_{44}$	A_{24}	A_{42}
S-90°-1	40.8		2.45			20.7	6.3					
S-90°-2	41.0				8.1						3.4	
S-0°-1		30.4		2.24				13.0				
S-90°-3	41.8		2.51	2.20		21.5	6.1					
S-90°-4	41.7				8.35		6.0			1.9		2.8
S-0°-2		33.1						15.5	2.18	1.7	2.4	2.3

$225^O K$

Sample	ρ_{11}	ρ_{33}	$-R_{123}$	$-R_{231}$	A_{11}	A_{12}	A_{13}	A_{31}	A_{33}	$-A_{44}$	A_{24}	A_{42}
S-90°-1	31.1		2.69			30.8	8.5				6.8	
S-90°-2	31.0											
S-0°-1		22.9		2.45				17.3				
S-90°-3	31.9			2.40								
S-90°-4	31.9				12.9		8.1			2.3		3.2
S-0°-2		25.0						19.8	3.16	1.9		3.15

$183^O K$

Sample	ρ_{11}	ρ_{33}	$-R_{123}$	$-R_{231}$	A_{11}	A_{12}	A_{13}	A_{31}	A_{33}	$-A_{44}$	A_{24}	A_{42}
S-90°-1	23.5		2.87			42.2	12.5				7.8	
S-900-2	23.3				18							
S-0°-1		17.2		2.65				24.4				
S-90°-3	24.5			2.59		44	12					
S-90°-4	24.2				18.6		11.7			3.2		4.8
S-0°-2		18.8						27.4	4.5	2.8		4.3

139°K

Sample	ρ_{11}	ρ_{33}	$-R_{123}$	$-R_{231}$	A_{11}	A_{12}	A_{13}	A_{31}	A_{33}	$-A_{44}$	A_{24}	A_{42}
S-90°-1	16.4		3.09	2.82		64.4	19.7				12.7	
S-90°-2	16.5				28.4							
S-0°-1		11.6		2.86				37.6				
S-90°-3	16.7			2.74								
S-90°-4	16.6				30.7		17.5			5.6		6.7
S-0°-2		12.8						39.5	7.0	5.1		6.3

77°K

Sample	ρ_{11}	ρ_{33}	$-R_{123}$	$-R_{231}$	A_{11}	A_{12}	A_{13}	A_{31}	A_{33}	$-A_{44}$	A_{24}	A_{42}
S-90°-1	7.12		3.47			150.8	45.8				30	
S-90°-2	7.13				61							
S-0°-1		5.08		3.10				91				
S-90°-3	7.20		3.40	2.90		156	45					15
S-90°-4	7.16				65.6		44.6			15.5		18.4
S-0°-2		5.47						87.5	16.6	12.4		14.5

APPENDIX B1

The Computer programme used to calculate the band
parameters of antimony. Some symbols employed in the programme
are different from those given in the equations 6.1 to 6.11.
The definitions are as follows:

In the equations	in the programme
f	F
α_1	CE
β_1	SE
α_2	CH
β_2	SH
μ_1	E1
μ_2	E2
μ_3	E3
ν_1	H1
ν_2	H2
ν_3	H3
μ_x	EX
ν_x	HX
μ_z	EZ
ν_z	HZ
$\widetilde{\sigma}_{11}$	D11
$\widetilde{\sigma}_{33}$	D33

Since only capital letters are available on the teleprinter, the other symbols such as K_{1e}, L_{1e}, x_e, etc. are written as K1E, L1E, XE, etc. The identifiers D11, D33, P123, etc. are used for the calculated values of the magnetoconductivity coefficients and D11E, D33E, P123E etc. for the experimental values. The mean values of K1E, K1H, K3E and K3H are obtained from the relations

$$K1E + K3E = 1$$

$$K1H + K3H = 1$$

If the calculated values of these four related unknowns obtained from the two sets of equations (6.10 and 6.11, pages 88 and 89) are represented by K1EA, K3EA, K1HA and K3HA, then the averages are found from the following relations

$$K1E = \frac{K1EA + (1 - K3EA)}{2}$$

$$K3E = \frac{K3EA + (1 - K1EA)}{2}$$

$$K1H = \frac{K1HA + (1 - K3HA)}{2}$$

$$K3H = \frac{K3HA + (1 - K1HA)}{2}$$

Here, for instance, K1EA is the value of K1E obtained from the set 6.10 and (1-K3EA) is that found from the second set 6.11.

The equations are given in electrostatic Gaussian units, i.e. conductivities and mobilities in e.s.u. and magnetic fields in gauss. The computer programme is presented on the following pages and a typical set of results from the computer in Appendix B2.

```
"0 "OKTU "CALCULATION OF "BAND "PARAMETERS OF "ANTIMONY, 31 "MAY 1966;
\BEGIN \REAL N,F,S1,S3,S4,S5,S6,S7,S8,S9,S0,S,T,
            FI,FO,DF,NI,NO,DN,
            K1EA,K1HA,K3EA,K3HA,
            L1E,L1H,L3E,L3H,K1E,K1H,K3E,K3H,
          ' XE,YE,ZE,CE,SE,XH,YH,ZH,CH,SH,
            X1E,X2E,X1H,X2H,DISXE,DISXH,DISYE,DISYH,
            E1,E2,E3,E4,E5,H1,H2,H3,H4,H5,EX,EZ,HX,HZ,
            D11,D33,P123,P231,B13,B31,B11,B12,B33,B44,B24,B42,
            D11E,D33E,P123E,P231E,B11E,B12E,B13E,B31E,
            A,G,H,I,J,R,U,V;
     \SWITCH SSS:=Q1,Q2,Q3,Q4,Q5,Q6;
     \READ T,S1,S4,S5,S6,S3,S7,S8,S9,S0,FI,FO,DF,NI,NO,DN,
            D11E,D33E,P123E,P231E,B11E,B12E,B13E,B31E,
            A,G,H,I,J,R,U,V;
     F:=FI;
     Q1:\IF F<FO \THEN F:=F+DF \ELSE \GOTO Q3;
     N:=NI;
     Q2:\IF N<NO \THEN N:=N+DN
                     \ELSE \BEGIN \PRINT ##L3??;
                           \GOTO Q1;
                           \END;
     L1E:=(N*(1-F)*S4+N↑2*(S5+S6))/F↑2;
     L1H:=(N↑2*(S5+S6)-N*F*S4)/(1-F)↑2;
     L3E:=(N*(1-F)*S7+N↑2*(S8+S9))/F↑2;
     L3H:=(N↑2*(S8+S9)-N*F*S7)/(1-F)↑2;
     K1EA:=(S1*(1-F)↑2*L1H-N↑2*S6)/(F*(1-F)↑2*L1H-F↑3*L1E);
     K1HA:=(N↑2*S6-F↑2*L1E*S1)/((1-F)↑3*L1H-(1-F)*F↑2*L1E);
     K3EA:=(S3*(1-F)↑2*L3H-N↑2*S8)/(F*(1-F)↑2*L3H-F↑3*L3E);
     K3HA:=(N↑2*S8-F↑2*L3E*S3)/((1-F)↑3*L3H-(1-F)*F↑2*L3E);
     \IF K1EA>1 \OR K1EA<0 \OR K3EA>1 \OR K3EA<0 \OR K1HA>1
     \OR K1HA<0 \OR K3HA>1 \OR K3HA<0 \OR L3E<0 \OR L1E<0
     \THEN \GOTO Q2;
     K1E:=(1+K1EA-K3EA)/2;  K3E:=(1+K3EA-K1EA)/2;
     K1H:=(1+K1HA-K3HA)/2;  K3H:=(1+K3HA-K1HA)/2;
     DISXE:=1-4*L3E/K1E↑2;
     \IF DISXE<0
     \THEN \BEGIN \PRINT ##L3?DISXE:=?,SAMELINE,PREFIX(##S2??),
                           DISXE,F,N,L3E,K1EA,K1E;
           \GOTO Q2;
           \END
     \ELSE \BEGIN X1E:=0.5*K1E*(1+SQRT(DISXE));
                  X2E:=0.5*K1E*(1-SQRT(DISXE));
           \END;
     DISXH:=1-4*L3H/K1H↑2;
     \IF DISXH<0
     \THEN \BEGIN \PRINT ##L3?DISXH:=?,SAMELINE,PREFIX(##S2??),
                           DISXH,F,N,L3H,K1HA,K1H;
           \GOTO Q2;
           \END
     \ELSE \BEGIN X1H:=0.5*K1H*(1+SQRT(DISXH));
                  X2H:=0.5*K1H*(1-SQRT(DISXH));
           \END;
```

```
        \BEGIN
        \FOR XE:=X1E,X2E \DO
            \BEGIN DISYE:=1-4*(L1E-XE*K3E)/(1-XE)↑2;
            \IF DISYE<0 \OR DISYE>1 \THEN \GOTO Q4
            \ELSE \BEGIN YE:=0.5*(1-XE)*(1-SQRT(DISYE));
                          ZE:=0.5*(1-XE)*(1+SQRT(DISYE));
                    \IF YE>K3E \OR YE>ZE \THEN \GOTO Q4
                    \ELSE CE:=SQRT((K3E-YE)/(ZE-YE));
                    \IF CE>1 \THEN \GOTO Q4;
                \END;
        \FOR XH:=X1H,X2H \DO
            \BEGIN DISYH:=1-4*(L1H-XH*K3H)/(1-XH)↑2;
            \IF DISYH<0 \OR DISYH>1 \THEN \GOTO Q5
            \ELSE \BEGIN YH:=0.5*(1-XH)*(1-SQRT(DISYH));
                          ZH:=0.5*(1-XH)*(1+SQRT(DISYH));
                    \IF YH>K3H \OR YH>ZH \THEN \GOTO Q5
                    \ELSE CH:=SQRT((K3H-YH)/(ZH-YH));
                    \IF CH>1 \THEN \GOTO Q5;
                \END;
\BEGIN
        SE:=SQRT(1-CE↑2);
        SH:=SQRT(1-CH↑2);
        S:=SO/N;
        E1:=F*S*XE;
        E2:=F*S*YE;
        E3:=F*S*ZE;
        H1:=(1-F)*S*XH;
        H2:=(1-F)*S*YH;
        H3:=(1-F)*S*ZH;
        EX:=0.5*(E1+CE↑2*E2+SE↑2*E3);
        EZ:=SE↑2*E2+CE↑2*E3;
        E4:=E2*E3+E1*EZ;
        E5:=E1*(CE↑2*E2+SE↑2*E3);
        HX:=0.5*(H1+CH↑2*H2+SH↑2*H3);
        HZ:=SH↑2*H2+CH↑2*H3;
        H4:=H2*H3+H1*HZ;
        H5:=H1*(CH↑2*H2+SH↑2*H3);
    D11:=4.8*10↑(-10)*N*(EX+HX);
    D33:=4.8*10↑(-10)*N*(EZ+HZ);
    P231:=8*10↑(-21)*N*(H4-E4);
    P123:=1.6*10↑(-20)*N*(H5-E5);
    B13:=5.33*10↑(-31)*N*(EX*E5+HX*H5);
    B31:=2.66*10↑(-31)*N*(EZ*E4+HZ*H4);
    B11:=6.66*10↑(-32)*N*(E1↑2*(SE↑2*E2+CE↑2*E3)+CE↑2*E2↑2*(3*SE↑2*E1+
E3)+SE↑2*E3↑2*(3*CE↑2*E1+E2)-E1*E2*E3*(2+6*CE↑2*SE↑2)+H1↑2*(SH↑2*H2+
CH↑2*H3)+CH↑2*H2↑2*(3*SH↑2*H1+H3)+SH↑2*H3↑2*(3*CH↑2*H1+H2)-H1*H2*H3*
(2+6*CH↑2*SH↑2));
    B12:=6.66*10↑(-32)*N*(3*E1↑2*(SE↑2*E2+CE↑2*E3)+CE↑2*E2↑2*(SE↑2*E1+
3*E3)+SE↑2*E3↑2*(CE↑2*E1+3*E2)+E1*E2*E3*(2-2*CE↑2*SE↑2)+3*H1↑2*(SH↑2*
H2+CH↑2*H3)+CH↑2*H2↑2*(SH↑2*H1+3*H3)+SH↑2*H3↑2*(CH↑2*H1+3*H2)+H1*H2*H3*
(2-2*CH↑2*SH↑2));
    B33:=5.33*10↑(-31)*N*(CE↑2*SE↑2*E1*(E2-E3)↑2+CH↑2*SH↑2*H1*(H2-H3)↑
2);
```

```
    B44:=-2.66*10↑(-31)*N*(EZ*E5+HZ*H5);
    B24:=1.33*10↑(-31)*N*(CE*SE*E1*(E2-E3)*(-E1+CE↑2*E2+SE↑2*E3)+CH*
SH*H1*(H2-H3)*(-H1+CH↑2*H2+SH↑2*H3));
    B42:=1.33*10↑(-31)*N*(CE*SE*(E2-E3)*(E2*E3-E1*(SE↑2*E2+CE↑2*E3))+
CH*SH*(H2-H3)*(H2*H3-H1*(SH↑2*H2+CH↑2*H3)));
    \IF  D11<D11E*(1-0.01*A)  \OR  D11>D11E*(1+0.01*A)  \OR  D33<D33E*(1-
0.01*G)  \OR  D33>D33E*(1+0.01*G)  \OR  P123<P123E*(1-0.01*H)  \OR  P123>
⌐123E*(1+0.01*H)  \OR  P231<P231E*(1-0.01*I)  \OR  P231>P231E*(1+0.01*I)
  \OR  B11<B11E*(1-0.01*J)  \OR  B11>B11E*(1+0.01*J)  \OR  B12<B12E*(1-0.01
*R)  \OR  B12>B12E*(1+0.01*R)  \OR  B13<B13E*(1-0.01*U)  \OR  B13>B13E*(1+
0.01*U)  \OR  B31<B31E*(1-0.01*V)  \OR  B31>B31E*(1+0.01*V)
    \THEN \GOTO Q6;
      \BEGIN \PRINT ##L3??;
      \PRINT T,SAMELINE,PREFIX(##S3??),N,F;
      \PRINT XE,SAMELINE,PREFIX(##S3??),YE,ZE,XH,YH,ZH;
      \PRINT E1,SAMELINE,PREFIX(##S3??),E2,E3,CE,EX,EZ;
      \PRINT H1,SAMELINE,PREFIX(##S3??),H2,H3,CH,HX,HZ;
      \PRINT D11,SAMELINE,PREFIX(##S3??),D33,P123,P231,B11,B12;
      \PRINT B13,SAMELINE,PREFIX(##S3??),B31,B33,B44,B24,B42; \END;
Q6:\END;
                Q5:\END;
          Q4:\END;
      \GOTO Q2;
      \END;
Q3:\END;
```

APPENDIX B2

A typical set of results obtained at $183^{O}K$ from the computer programme presented in Appendix B1. All four types of solutions are shown : the best fits to types A and D are framed. To compare the calculated values of magnetoconductivity coefficients with the experimental data, the experimental values of the magnetoconductivity coefficients at $183^{O}K$ are transformed to Gaussian units, as follows

$D11 = 3.78 \times 10^{16}$ e.s.u. conductivity

$D33 = 5.00 \times 10^{16}$

$-P123 = 4.58 \times 10^{11}$ e.s.u. conductivity $gauss^{-1}$

$-P231 = 5.51 \times 10^{11}$

$B_{11} = 29.1 \times 10^{6}$ e.s.u. conductivity $gauss^{-2}$

$B12 = 73.6 \times 10^{6}$

$B13 = 24.7 \times 10^{6}$

$B31 = 78.8 \times 10^{6}$

$B33 = 12.5 \times 10^{6}$

$-B44 = 9.63 \times 10^{6}$

$B24 = 12.4 \times 10^{6}$

$B42 = 9.46 \times 10^{6}$

183,00000	$3,700_{10}+19$	,39000000				
,00498281	,27070109	,72431610	,07746891	,21565586	,70687523	
13734,383	746147,32	1996469,6	,61159136	771264,23	1213822,9	
333985,20	929739,04	3047492,0	,56218919	1356073,6	1599069,0	B
$3,778_{10}+16$	$4,996_{10}+16$	$4,578_{10}+11$	$5,509_{10}+11$	20322561	73543921	
21560656	70992166	6484594,7	−12751105	−3369961,4	−15526235	

183,00000	$4,000_{10}+19$	,39000000				
,54013571	,01137960	,44848469	,54171672	,01957058	,43871270	
1377143,5	29013,705	1143467,8	,99463682	709039,60	1131545,8	
2160298,6	78045,018	1749531,4	,91268376	1258747,9	1470379,2	D
$3,778_{10}+16$	$4,996_{10}+16$	$4,578_{10}+11$	$5,509_{10}+11$	29171245	76493485	
21560656	70992167	18287268	−12751105	14041632	11012659	

183,00000	$4,000_{10}+19$	,39000000				
,54013571	,01137960	,44848469	,08957082	,27654553	,63388365	
1377143,5	29013,705	1143467,8	,99463682	709039,60	1131545,8	
357197,23	1102829,0	2527848,8	,50786454	1258747,9	1470379,2	A
$3,778_{10}+16$	$4,996_{10}+16$	$4,578_{10}+11$	$5,509_{10}+11$	17969385	72759532	
21560656	70992167	3345847,1	−12751105	−1013785,0	−6574002,4	

183,00000	$4,000_{10}+19$	,39000000				
,01605557	,42608025	,55786418	,54171672	,01957058	,43871270	
40935,694	1086344,8	1422344,4	,36677894	709039,60	1131545,8	
2160298,6	78045,018	1749531,4	,91268376	1258747,9	1470379,2	C
$3,778_{10}+16$	$4,996_{10}+16$	$4,578_{10}+11$	$5,509_{10}+11$	28890508	76399905	
21560656	70992167	17912811	−12751105	12885903	9168247,7	

183,00000	$4,000_{10}+19$	,39000000				
,01605557	,42608025	,55786418	,08957082	,27654553	,63388365	
40935,694	1086344,8	1422344,4	,36677894	709039,60	1131545,8	
357197,23	1102829,0	2527848,8	,50786454	1258747,9	1470379,2	B
$3,778_{10}+16$	$4,996_{10}+16$	$4,578_{10}+11$	$5,509_{10}+11$	17688648	72665952	
21560656	70992167	2971390,7	−12751105	−2169514,3	−8418413,5	

183,00000	$3,700_{10}+19$	,40000000				
,00648644	,25424865	,73926491	,08135952	,22950480	,68913568	
18337,328	718767,81	2089921,9	,61770923	792537,62	1241951,8	
345008,34	973224,43	2922307,8	,55377342	1334800,2	1570940,1	B
$3,778_{10}+16$	$4,996_{10}+16$	$4,578_{10}+11$	$5,509_{10}+11$	19701485	73336897	
21560656	70992166	5656181,6	−12751105	−3113649,8	−15030411	

APPENDIX   C1

The computer programme used to search through
solutions type D with fixed values of the tilt angles ψ_e
and ψ_h. Mobilities are varied within about 30%. The
calculations can be performed by writing the equations 6.14
(page 91) in the form

$$x_e = AE$$

$$y_e = \frac{1}{2} (1 - AE) (1 - BE)$$

$$z_e = \frac{1}{2} (1 - AE) (1 + BE)$$

where $\quad AE = \frac{1}{2} K_{1e} \left[1 + (1 - 4L_{3e}/K_{1e}^2)^{1/2} \right]$

and $\quad BE = \left[1 - 4(L_{1e} - x_e K_{3e}/(1 - x_e)^2 \right]^{1/2}$

Once the approximate values of the new variables AE and BE
are determined, the three dimensionless quantities x_e, y_e, z_e,
which are related to the principal mobilities μ_1, μ_2, μ_3
by the set of equations 6.6. (page 87), can be altered within
a required range. A set of similar relationships identical
in form hold for the hole ellipsoids. Use of equations 6.14
reduces the arbitrary selections of unknowns from six to four.

The computer programme is presented on the following
page and a set of typical output in the next Appendix.

```
"O "OKTU, "P"S7, 21 7 66;
\BEGIN \REAL N,F,S,SO,T,FI,FO,DF,NI,NO,DN,
              AE,AEI,DAE,AEO,BE,BEI,DBE,BEO,
              AH,AHI,DAH,AHO,BH,BHI,DBH,BHO,
              XE,YE,ZE,CE,SE,XH,YH,ZH,CH,SH,
              E1,E2,E3,E4,E5,H1,H2,H3,H4,H5,EX,EZ,HX,HZ,
              D11,D33,P123,P231,B13,B31,B11,B12,B33,B44,B24,B42,
              D11E,D33E,P123E,P231E,B11E,B12E,B13E,B31E,
              A,G,H,I,J,R,U,V;
      \SWITCH SSS:=Q1,Q2,Q3,Q6;
      \READ T,SO,CE,SE,CH,SH,FI,FO,DF,NI,NO,DN,
              AEI,AEO,DAE,BEI,BEO,DBE,AHI,AHO,DAH,BHI,BHO,DBH,
              D11E,D33E,P123E,P231E,B11E,B12E,B13E,B31E,
              A,G,H,I,J,R,U,V;
      F:=FI;
      Q1:\IF F<FO \THEN F:=F+DF \ELSE \GOTO Q3;
      N:=NI;
      Q2:\IF N<NO \THEN N:=N+DN \ELSE \GOTO Q1;
      S:=SO/N;
\BEGIN \FOR AE:=AEI \STEP DAE \UNTIL AEO \DO
      \BEGIN \FOR BE:=BEI \STEP DBE \UNTIL BEO \DO
              \BEGIN XE:=AE;
                     YE:=0.5*(1-AE)*(1-BE);
                     ZE:=0.5*(1-AE)*(1+BE);
              \END;
              \BEGIN \FOR AH:=AHI \STEP DAH \UNTIL AHO \DO
                     \BEGIN \FOR BH:=BHI \STEP DBH \UNTIL BHO \DO
                             \BEGIN XH:=AH;
                                    YH:=0.5*(1-AH)*(1-BH);
                                    ZH:=0.5*(1-AH)*(1+BH);
                     \END;
\BEGIN E1:=F*S*XE;
      E2:=F*S*YE;
      E3:=F*S*ZE;
      H1:=(1-F)*S*XH;
      H2:=(1-F)*S*YH;
      H3:=(1-F)*S*ZH;
      EX:=0.5*(E1+CE↑2*E2+SE↑2*E3);
      EZ:=SE↑2*E2+CE↑2*E3;
      E4:=E2*E3+E1*EZ;
      E5:=E1*(CE↑2*E2+SE↑2*E3);
      HX:=0.5*(H1+CH↑2*H2+SH↑2*H3);
      HZ:=SH↑2*H2+CH↑2*H3;
      H4:=H2*H3+H1*HZ;
      H5:=H1*(CH↑2*H2+SH↑2*H3);
```

```
    D11:=4.8*10↑(-10)*N*(EX+HX);
    D33:=4.8*10↑(-10)*N*(EZ+HZ);
    P231:=8*10↑(-21)*N*(H4-E4);
    P123:=1.6*10↑(-20)*N*(H5-E5);
    B13:=5.33*10↑(-31)*N*(EX*E5+HX*H5);
    B31:=2.66*10↑(-31)*N*(EZ*E4+HZ*H4);
    B11:=6.66*10↑(-32)*N*(E1↑2*(SE↑2*E2+CE↑2*E3)+CE↑2*E2↑2*(3*SE↑2*E1+
E3)+SE↑2*E3↑2*(3*CE↑2*E1+E2)-E1*E2*E3*(2+6*CE↑2*SE↑2)+H1↑2*(SH↑2*H2+
CH↑2*H3)+CH↑2*H2↑2*(3*SH↑2*H1+H3)+SH↑2*H3↑2*(3*CH↑2*H1+H2)-H1*H2*H3*
(2+6*CH↑2*SH↑2));
    B12:=6.66*10↑(-32)*N*(3*E1↑2*(SE↑2*E2+CE↑2*E3)+CE↑2*E2↑2*(SE↑2*E1+
3*E3)+SE↑2*E3↑2*(CE↑2*E1+3*E2)+E1*E2*E3*(2-2*CE↑2*SE↑2)+3*H1↑2*(SH↑2*
H2+CH↑2*H3)+CH↑2*H2↑2*(SH↑2*H1+3*H3)+SH↑2*H3↑2*(CH↑2*H1+3*H2)+H1*H2*H3*
(2-2*CH↑2*SH↑2));


    \IF D11<D11E*(1-0.01*A) \OR D11>D11E*(1+0.01*A) \OR D33<D33E*(1-
0.01*G) \OR D33>D33E*(1+0.01*G) \OR P123<P123E*(1-0.01*H) \OR P123>
P123E*(1+0.01*H) \OR P231<P231E*(1-0.01*I) \OR P231>P231E*(1+0.01*I)
 \OR B11<B11E*(1-0.01*J) \OR B11>B11E*(1+0.01*J) \OR B12<B12E*(1-0.01
*R) \OR B12>B12E*(1+0.01*R) \OR B13<B13E*(1-0.01*U) \OR B13>B13E*(1+
0.01*U) \OR B31<B31E*(1-0.01*V) \OR B31>B31E*(1+0.01*V)
    \THEN \GOTO Q6;
    \BEGIN
    B33:=5.33*10↑(-31)*N*(CE↑2*SE↑2*E1*(E2-E3)↑2+CH↑2*SH↑2*H1*(H2-H3)↑
2);
    B44:=-2.66*10↑(-31)*N*(EZ*E5+HZ*H5);
    B24:=1.33*10↑(-31)*N*(CE*SE*E1*(E2-E3)*(-E1+CE↑2*E2+SE↑2*E3)+CH*
SH*H1*(H2-H3)*(-H1+CH↑2*H2+SH↑2*H3));
    B42:=1.33*10↑(-31)*N*(CE*SE*(E2-E3)*(E2*E3-E1*(SE↑2*E2+CE↑2*E3))+
CH*SH*(H2-H3)*(H2*H3-H1*(SH↑2*H2+CH↑2*H3)));
        \PRINT ##L3??;
        \PRINT T,SAMELINE,PREFIX(##S3??),N,F,BE,BH;
        \PRINT XE,SAMELINE,PREFIX(##S3??),YE,ZE,XH,YH,ZH;
        \PRINT E1,SAMELINE,PREFIX(##S3??),E2,E3,CE,EX,EZ;
        \PRINT H1,SAMELINE,PREFIX(##S3??),H2,H3,CH,HX,HZ;
        \PRINT D11,SAMELINE,PREFIX(##S3??),D33,P123,P231,B11,B12;
        \PRINT B13,SAMELINE,PREFIX(##S3??),B31,B33,B44,B24,B42;
    \END;
Q6:\END;
                        \END;
                    \END;
        \END;
\GOTO Q2;\END;
Q3:\END;
```

APPENDIX   C2

A typical output obtained from the programme given in Appendix C1 for $\psi_e = 4^{\,o}$ and $\psi_h = 28^{o}$; the best fit is framed.

183.00000	$4.300_{10}+19$	.38000000	.94000000	.97000000	
.40000000	.02100000	.57900000	.57000000	.00860000	.42140000
924372.09	48529.534	1338028.6	.99756000	489588.28	1331743.2
2149165.1	32425.998	1588874.0	.88295000	1262317.8	1245834.0
$3.616_{10}+16$	$5.320_{10}+16$	$5.203_{10}+11$	$4.930_{10}+11$	26575619	62972718
23914309	58628866	20673843	-12270561	14477757	10287695

183.00000	$4.300_{10}+19$	.38000000	.94000000	.97000000	
.42000000	.02030000	.55970000	.55000000	.00900000	.44100000
970590.69	46911.883	1293427.7	.99756000	511784.17	1287351.7
2073755.8	33934.184	1662775.1	.88295000	1233345.0	1303779.8
$3.602_{10}+16$	$5.348_{10}+16$	$5.252_{10}+11$	$4.988_{10}+11$	26779986	62543810
23636512	60452924	21834374	-12908693	13901118	10811983

183.00000	$4.300_{10}+19$	.38000000	.94000000	.97000000	
.42000000	.02030000	.55970000	.57000000	.00860000	.42140000
970590.69	46911.883	1293427.7	.99756000	511784.17	1287351.7
2149165.1	32425.998	1588874.0	.88295000	1262317.8	1245834.0
$3.662_{10}+16$	$5.228_{10}+16$	$5.198_{10}+11$	$4.881_{10}+11$	26794169	63605682
23948994	58180061	20670631	-12256028	14507079	10279020

183.00000	$4.300_{10}+19$	.38000000	.94000000	.97000000	
.44000000	.01960000	.54040000	.55000000	.00900000	.44100000
1016809.3	45294.232	1248826.7	.99756000	533980.06	1242960.3
2073755.8	33934.184	1662775.1	.88295000	1233345.0	1303779.8
$3.648_{10}+16$	$5.256_{10}+16$	$5.248_{10}+11$	$4.953_{10}+11$	26992692	63154288
23669903	59933403	21830460	-12890988	13929597	10800496

183.00000	$4.300_{10}+19$	.38000000	.94000000	.97000000	
.44000000	.01960000	.54040000	.57000000	.00860000	.42140000
1016809.3	45294.232	1248826.7	.99756000	533980.06	1242960.3
2149165.1	32425.998	1588874.0	.88295000	1262317.8	1245834.0
$3.708_{10}+16$	$5.137_{10}+16$	$5.194_{10}+11$	$4.846_{10}+11$	27006875	64216160
23982384	57660540	20666716	-12238323	14535558	10267532

APPENDIX D1

Calculation of the band parameters of antimony-tin alloys.

Define $\nu_1+\nu_2+\nu_3 = \dfrac{2\,\widetilde{\sigma}_{11}+\widetilde{\sigma}_{33}}{eN} = S$ (1)

and

$$x = \frac{\nu_1}{S}$$

$$y = \frac{\nu_2}{S}$$

$$z = \frac{\nu_3}{S}$$ (2)

where $x + y + z = 1$. Then, the first four equations ($\widetilde{\sigma}_{11}$, $\widetilde{\sigma}_{33}$, $-P_{123}$, $-P_{231}$) of the set 7.2 (page 112) can be rewritten in terms of the following variables

$$K_1 = x + \alpha^2 y + \beta^2 z$$

$$K_3 = \beta^2 y + \alpha^2 z$$

$$L_1 = yz + x(\beta^2 y + \alpha^2 z)$$

$$L_3 = x(\alpha^2 y + \beta^2 z)$$ (3)

Here $K_1 + K_3 = 1$. The values of K_1, K_3, L_1 and L_3 can be obtained from the experimental values of the coefficients by

the relations

$$K_1 = \frac{2\tilde{\sigma}_{11}}{2\tilde{\sigma}_{11} + \tilde{\sigma}_{33}} = S_1$$

$$K_3 = \frac{\tilde{\sigma}_{33}}{2\tilde{\sigma}_{11} + \tilde{\sigma}_{33}} = S_3$$

$$L_1 = \frac{2eNcP_{231}}{(2\tilde{\sigma}_{11} + \tilde{\sigma}_{33})^2} = NS_4$$

$$L_3 = \frac{eNcP_{123}}{(2\tilde{\sigma}_{11} + \tilde{\sigma}_{33})^2} = NS_5 \qquad (4)$$

Thus the dimensionless parameters x, y and z, and the tilt angle ψ_h are found by solving the relations (3); the solution is

$$x = \frac{1}{2} K_1 \left[1 + (1 - 4L_3/K_1^2)^{1/2} \right]$$

$$y = \frac{1}{2}(1 - x) \left\{ 1 - \left[1 - 4(L_1 - xK_3)/(1 - x)^2 \right]^{1/2} \right\}$$

$$z = \frac{1}{2}(1 - x) \left\{ 1 + \left[1 - 4(L_1 - xK_3)/(1 - x)^2 \right]^{1/2} \right\}$$

$$\alpha^2 = \frac{K_3 - y}{z - y} \qquad (5)$$

The principal mobilities are then obtained by using the relations (2). Numerical calculations were carried out by a computer. The computer programme is presented on the next page and a typical ouput in Appendix D2.

```
DOPED ANTIMONY,FEB.1967 NO.104;
\BEGIN \REAL T,N,NI,ND,NO,S,SO,K1,K3,L1,L3,C,
            DISX,DISY,X,Y,Z,CE,SE,E1,E2,E3,EX,EZ,E4,E5,
            D11,D33,P123,P231,B11,B12,B13,B31,B33,
            B24,B42,B44,D11E,D33E,P123E,P231E;
        \SWITCH SSS:=Q1,Q2;
        \READ T,C,NI,NO,ND,D11E,D33E,P123E,P231E;
            SO:=2*D11E+D33E;
\BEGIN \FOR N:=NI \STEP ND \UNTIL NO \DO
        \BEGIN K1:=2*D11E/SO; K3:=D33E/SO;
            L1:=28.8*N*P231E/SO↑2; L3:=14.4*N*P123E/SO↑2;
        DISX:=1-4*L3/K1↑2; \IF DISX<0 \OR DISX>1 \THEN \GOTO Q1 \ELSE
        \BEGIN X:=0.5*K1*(1+SQRT(DISX));\IF X>0.99 \THEN \GOTO Q1;\END;
\BEGIN DISY:=1-4*(L1-X*K3)/(1-X)↑2;
        \IF DISY<0 \OR DISY>1 \THEN \GOTO Q2 \ELSE \BEGIN
        Y:=0.5*(1-X)*(1-SQRT(DISY)); Z:=0.5*(1-X)*(1+SQRT(DISY));
        \IF Y>K3 \OR Y>Z \THEN \GOTO Q2
        \ELSE CE:=SQRT((K3-Y)/(Z-Y)); \IF CE>1 \THEN \GOTO Q2;\END;
        SE:=SQRT(1-CE↑2);
        S:=20.83*10↑8*SO/N;
        E1:=S*X; E2:=S*Y; E3:=S*Z;
        EX:=0.5*(E1+CE↑2*E2+SE↑2*E3);
        EZ:=SE↑2*E2+CE↑2*E3;
        E4:=E2*E3+E1*EZ;
        E5:=E1*(CE↑2*E2+SE↑2*E3);
    D11:=4.8*10↑(-10)*N*EX; D33:=4.8*10↑(-10)*N*EZ;
    P231:=8*10↑(-21)*N*E4; P123:=1.6*10↑(-20)*N*E5;
    B13:=5.33*10↑(-31)*N*EX*E5; B31:=2.66*10↑(-31)*N*EZ*E4;
    B11:=6.66*10↑(-32)*N*(E1↑2*(SE↑2*E2+CE↑2*E3)+CE↑2*E2↑2*(3*SE↑2*E1+
E3)+SE↑2*E3↑2*(3*CE↑2*E1+E2)-E1*E2*E3*(2+6*CE↑2*SE↑2));
    B12:=6.66*10↑(-32)*N*(3*E1↑2*(SE↑2*E2+CE↑2*E3)+CE↑2*E2↑2*(SE↑2*E1+
3*E3)+SE↑2*E3↑2*(CE↑2*E1+3*E2)+E1*E2*E3*(2-2*CE↑2*SE↑2));
    B33:=5.33*10↑(-31)*N*(CE↑2*SE↑2*E1*(E2-E3)↑2);
    B44:=-2.66*10↑(-31)*N*EZ*E5;
    B24:=1.33*10↑(-31)*N*(CE*SE*E1*(E2-E3)*(-E1+CE↑2*E2+SE↑2*E3));
    B42:=1.33*10↑(-31)*N*(CE*SE*(E2-E3)*(E2*E3-E1*(SE↑2*E2+CE↑2*E3)));
\BEGIN \PRINT ##L3??;
\PRINT ALIGNED(3,2),T,SAMELINE,##S5??,C;\PRINT ##L1??;
\PRINT ##S2??,SAMELINE,SCALED(3),N,##S3??,ALIGNED(1,3),X,PREFIX(##S6??)
        Y,Z,CE;\PRINT ##L1??;
\PRINT ##S2??,SAMELINE,SCALED(3),E1,PREFIX(##S3??),E2,E3,EX,EZ;
        \PRINT ##L1??;
\PRINT ##S2??,SAMELINE,SCALED(3),D11,PREFIX(##S3??),D33,P123,P231,
        B11,B12;\PRINT ##L1??;
\PRINT ##S2??,SAMELINE,SCALED(3),B0,PREFIX(##S3??),B31,B33,B44,B24,
        B42; \END;
Q2:\END;
Q1:\END;\END;
\END;
```

APPENDIX   D2

A typical ouput of the programme given in Appendix
D1.   The results are those obtained at 77°K for the compos-
ition 2.5 at.% Sn.   The best fit is framed.   To compare the
calculated values of the magnetoconductivity coefficients with
the experimental data, the experimental values are presented
in Gaussian units :

$$\widetilde{\sigma_{11}} = 3.62 \times 10^{16} \quad \text{e.s.u. conductivity}$$

$$\widetilde{\sigma_{33}} = 2.33 \times 10^{16}$$

$$-P_{123} = 0.65 \times 10^{11} \quad \text{e.s.u. conductivity gauss}^{-1}$$

$$-P_{231} = 1.00 \times 10^{11}$$

$$B_{12} = 1.78 \times 10^{6} \quad \text{e.s.u. conductivity gauss}^{-2}$$

$$B_{13} = 1.00 \times 10^{6}$$

$$B_{31} = 1.45 \times 10^{6}$$

```
77,00        2,50
 4,00,+20    0,661      0,001      0,338      0,864
 2,99,+05    4,48,+02   1,53,+05   1,69,+05   1,15,+05
 3,25,+16    2,20,+16   7,50,+10   1,10,+11   3,78,+05   8,57,+05
 4,33,+05    4,19,+05   2,82,+05  -1,43,+05   2,75,+05   1,21,+05
```

```
77,00        2,50
 4,10,+20    0,658      0,016      0,326      0,874
 2,91,+05    6,98,+03   1,44,+05   1,65,+05   1,12,+05
 3,25,+16    2,20,+16   7,50,+10   1,10,+11   3,24,+05   8,21,+05
 4,12,+05    4,09,+05   2,15,+05  -1,39,+05   2,32,+05   1,00,+05
```

```
77,00        2,50
 4,20,+20    0,656      0,032      0,312      0,888
 2,83,+05    1,38,+04   1,35,+05   1,61,+05   1,09,+05
 3,25,+16    2,20,+16   7,50,+10   1,10,+11   2,75,+05   7,88,+05
 4,03,+05    3,99,+05   1,55,+05  -1,36,+05   1,90,+05   8,02,+04
```

```
77,00        2,50
 4,30,+20    0,653      0,050      0,297      0,906
 2,75,+05    2,10,+04   1,25,+05   1,57,+05   1,07,+05
 3,25,+16    2,20,+16   7,50,+10   1,10,+11   2,30,+05   7,57,+05
 3,93,+05    3,90,+05   1,00,+05  -1,33,+05   1,48,+05   6,09,+04
```

```
77,00        2,50
 4,40,+20    0,651      0,070      0,279      0,925
 2,68,+05    2,90,+04   1,15,+05   1,54,+05   1,04,+05
 3,25,+16    2,20,+16   7,50,+10   1,10,+11   1,90,+05   7,28,+05
 3,84,+05    3,81,+05   5,08,+04  -1,30,+05   1,02,+05   4,09,+04
```

```
77,00        2,50
 4,50,+20    0,648      0,095      0,257      0,928
 2,61,+05    3,84,+04   1,03,+05   1,50,+05   1,02,+05
 3,25,+16    2,20,+16   7,50,+10   1,10,+11   1,53,+05   7,01,+05
 2,76,+05    3,72,+05   5,90,+03  -1,27,+05   3,35,+04   1,31,+04
```

End of program

REFERENCES

Abeles, B. and Meiboom, S., 1954, Phys. Rev., 95, 31.

Abeles, B. and Meiboom, S., 1956, Phys. Rev., 101, 544.

Chandrasekhar, B.S., 1959, J. Phys. Chem. Solids, 11, 268.

Cohen, M. H., Falicov, L.M. and Golin, S., 1964, IBM. J.
    Res. Develop., 8, 215.

Datars, W.R. and Dexter, R.N., 1961, Phys. Rev., 124, 75.

Datars, W.R. and Vanderkooy, J., 1964, IBM. J. Res.
    Develop., 8, 247.

Drabble, J.R. and Wolfe, R., 1956, Proc. Phys. Soc., B69, 1101.

Epstein, S., 1962, J. Electrochem. Soc., 109, 738.

Epstein, S. and Juretschke, H.J., 1963, Phys. Rev., 129, 1148.

Eriksson, L., Beckman, O. and Hörnfeldt, S., 1964, J. Phys.
    Chem. Solids, 25, 1339.

Falicov, L.M. and Lin, P.J., 1966, Phys. Rev., 141, 562.

Freedman, S.J. and Juretschke, H.J., 1961, Phys. Rev.,
    124, 1379.

Gallo, C.F. Chandrasekhar, B.S. and Sutter, P.H. 1963, J.
    Appl. Phys., 34, 144.

Guinier, A., 1963, Metallic Solid Solutions (Benjamin) ed.
    J. Friedel and A. Guinier, article XXXVII - 1.

Hall, J.J. and Koenig, S.H., 1964, IBM. J. Res. Develop, 8, 241.

Hansen, M., 1958, Constitution of Binary Alloys, (McGraw-Hill
    Book Company) p.1175.

Hasler, M.F., 1933, Rev. Sci. Instr., 4, 656.

Herring, C. and Vogt, E., 1956, Phys. Rev., 101, 944.

Ishizawa, Y. and Tanuma, S., 1965, J. Phys. Soc. Japan,
    20, 1278.

Jones, H., 1936, Proc. Roy. Soc., A155, 653.

Jones, H., 1960, The Theory of Brillouin Zones and Electronic States in Crystals, (North-Holland) p.198.

Jones, H. and Zener, C., 1934, Proc. Roy. Soc., A145, 268.

Juretschke, H.J., 1955, Acta Cryst., 8, 716.

Kapitza, P., 1928, Proc. Roy. Soc., 119-A, 358.

Kechin, V.V., Likhter, A.I. and Pospelov, Yu.A., 1966, Soviet Physics JETP, 22, 26.

Ketterson, J. and Eckstein, Y., 1963, Phys. Rev., 132, 1885.

Lane, C.T. and Dodd, W.A., 1942, Phys. Rev., 61, 183.

Morimoto, T. and Takamura, J., 1967, J. Phys. Soc. Japan, 22, 89.

Mott, N.F. and Jones, H., 1936, The Theory of the Properties of Metals and Alloys, (Oxford University Press).

Nanney, C., 1962, Phys. Rev., 129, 109.

Priestley, M.G., Windmiller, L.R., Ketterson, J.B. and Eckstein, Y., 1967, Phys. Rev., 154, 471.

Putley, E.H., 1960, The Hall Effect and Related Phenomena, (Butterworths, London).

Rao, G.N. Zebouni, N.H., Grenier, C.G. and Reynolds, J.M., 1964, Phys. Rev., 133, A141.

Rausch, K., 1947, Ann. Physik, 1, 190.

Saito, Y., 1964, J. Phys. Soc. Japan, 19, 1319.

Saunders, G.A., Miziumski, C., Cooper, G.S. and Lawson, A.W., 1965, J. Phys. Chem. Solids, 26, 1299.

Shoenberg, D., 1952, Phil. Trans. Roy. Soc. London, A245, 1.

Sondheimer, E.H., 1952, Proc. Phys. Soc., A65, 561.

Soule, D.E., 1958, Phys. Rev., 112, 698.

Volger, J., 1950, Phys. Rev., 79, 1023.

Wernick, J.H., Hobstetter, J.N., Lovell, L.C., and
     Dorsi, D., 1958, J. Appl. Phys., 29, 1013.

White, G.K., 1959, Experimental Techniques in Low-
     Temperature Physics, (Oxford University Press)p.163.

Wilson, A.H., 1953, The Theory of Metals (Cambridge
     University Press)

Windmiller, L.R. and Priestley, M.G., 1965, Solid State
     Communications, 3, 199.

Windmiller, L.R., 1966, Phys. Rev., 149, 472.

shown in table 7 in contrast with an order of magnitude of anisotropy obtained from solution C. Most important and conclusive is the agreement between the tilt angles of solution D and those measured by other methods. In table 8 two groups of tilt angles are

Table 8. Tilt angles in antimony

Reference	First carrier	Second carrier	Electrons	Holes
de Haas–van Alphen oscillations:				
Shoenberg 1952		35°		
Saito 1964	0°	38°		
Ishizawa and Tanuma 1965				36°
Windmiller and Priestley 1965	6·5°	31°		
de Haas–Shubnikov effect:				
Ketterson and Eckstein 1963	4°	36°		
Cyclotron resonance:				
Datars and Dexter 1961			36°	
Datars and Vanderkooy 1964	4°	36°		
Galvanomagnetic effects:				
Freedman and Juretschke 1961			60°	27°
Epstein and Juretschke 1963			10°	20°
			54°	22°
Present experiment			5°	24°
Ultrasonic attenuation:				
Eriksson *et al.* 1964	2·5°	35°		
Theoretical, using a pseudo-potential technique:				
Falicov and Lin 1966			2·5°	49°

In some cases tilt away from the bisectrix axis was referred to originally but, for an ellipsoidal model, can be considered as equivalent to tilt away from the trigonal axis in the adjacent quadrant. The ambiguity in the sense of tilt angle is dealt with only by Windmiller and Priestley (1965) and Falicov and Lin (1966) and in the present work. For compilation of this table, the basic rotation in the yz plane away from the trigonal axis is taken through ΓL. Data from Windmiller and Priestley refer to the tilt angle of the maximum Fermi surface area, while in the present work tilt is considered for the minor ellipsoid axis (3′) corresponding to the largest carrier mobility in the mirror plane.

collected, the first group comprising data from experiments intractable to categorical assignment of carriers into one of the two sets of Fermi surface extrema, while the second group shows data obtained from methods which allowed correct placement of the carriers. Clearly in one set the pockets have a small tilt angle ($\sim$4°), while that of the others is about 35°. Previous practice has been to assume that the holes occupy the former ellipsoids and electrons the latter. However, for this case there are no solutions to the magnetoconductivity tensor analysis. The present results demonstrate that the electrons in fact occupy the extrema with low tilt angles. Independent evidence is forthcoming for this configuration, including the recent theoretical determination of the band structure through the pseudo-potential approach (Falicov and Lin 1966). Ishizawa and Tanuma (1965) find, when antimony is doped with 0·1 at. % tin, a decrease in the period of the de Haas–van Alphen oscillations corresponding to carriers in the ellipsoids of tilt angle 35° while the periods due to extrema with a small tilt angle increase. Thus, tin doping, which intro-duces holes at the expense of electrons, results in enlargement of the cross-sectional area of Fermi surface pockets with angle 35°, which must then contain holes.

In the present work the measured small tilt angle (3° to 6°) accords with the results of other workers, shown in table 8. But the other tilt angle of 24° is not in close agreement with the usual value of about 35°. Assumptions made in the model must give rise to this discrepancy. The postulates used in the treatment of carrier scattering, discussed previously, can have only a minimal effect on the tilt angles. Also, as we have seen, the data appear consistent with the two-band model; little evidence is available for the presence of minority carriers. From the way in which the problem is set up, it is clear that the origin of the discrepancy results from the assumption of ellipsoidal Fermi surfaces. Both sets of ellipsoids are now known to be warped, the deviation being most marked for the hole pockets (Windmiller and Priestley 1965, Falicov and Lin 1966). Warping is such that the effective tilt angle measured by the galvanomagnetic effects can only be a mean value. In a qualitative way, this can be readily seen by considering the theoretically calculated shape of the hole ellipsoids in figure 7 of Falicov and Lin (1966). Tilt angles measured by the de Haas–van Alphen effect are those of a different property, that of the extremal cross section of the Fermi surface.

To conclude, the galvanomagnetic effects are found to be in reasonable agreement with the theoretical model of the Fermi surface determined by Falicov and Lin (1966). This theoretical work shows that the electron pockets, having a tilt angle of about 5°, are located at the centres L of the six pseudo-hexagon faces of the Brillouin zone, illustrated in figure 1, while the hole pockets, those with a large angle of tilt, are contained with the Brillouin zone on the trigonal–bisectrix planes close to points such as T. While the present measurements provide no details of the number of pockets, once this is known the number of carriers in each pocket is manifested. Symmetry considerations (Falicov and Lin 1966), combined with numerous experimental observations that both sets of pockets have at least binary or mirror symmetry, eliminates the possibility of twelve equivalent pockets for either set of carriers. From measurements of the de Haas–van Alphen effect Windmiller and Priestley (1965) find a 2 : 1 ratio of volumes between single ellipsoids of small and large tilt angles, and, as the electron and hole densities are equal, suggest that the ellipsoid multiplicities should be three for the electrons and six for the holes. Thus the galvanomagnetic data from table 4 show that there are $1\cdot4 \times 10^{19}$ electrons/cm^3 in each electron pocket and $0\cdot7 \times 10^{19}$ holes/cm^3 in each hole extremum.

References

DATARS, W. R., and DEXTER, R. N., 1961, *Phys. Rev.*, **124**, 75.
DATARS, W. R., and VANDERKOOY, J., 1964, *IBM J. Res. Dev.*, **8**, 247.
DRABBLE, J. R., and WOLFE, R., 1956, *Proc. Phys. Soc.* B, **69**, 1101.
EPSTEIN, S., 1962, *J. Electrochem. Soc.*, **109**, 738.
EPSTEIN, S., and JURETSCHKE, H. J., 1963, *Phys. Rev.*, **129**, 1148.
ERIKSSON, L., BECKMAN, O., and HÖRNFELDT, S., 1964, *J. Phys. Chem. Solids*, **25**, 1339.
FALICOV, L. M., and LIN, P. J., 1966, *Phys. Rev.*, **141**, 562.
FREEDMAN, S. J., and JURETSCHKE, H. J., 1961, *Phys. Rev.*, **124**, 1379.
GALLO, C. F., CHANDRASEKHAR, B. S., and SUTTER, P. H., 1963, *J. Appl. Phys.*, **34**, 144.
HALL, J. J., and KOENIG, S. H., 1964, *IBM J. Res. Dev.*, **8**, 241.
HERRING, C., and VOGT, E., 1956, *Phys. Rev.*, **101**, 944.
ISHIZAWA, Y., and TANUMA, S., 1965, *J. Phys. Soc. Japan*, **20**, 1278.
JURETSCHKE, H. J., 1955, *Acta Cryst.*, **8**, 716.
KETTERSON, J., and ECKSTEIN, Y., 1963, *Phys. Rev.*, **132**, 1885.
RAO, G. N., ZEBOUNI, N. H., GRENIER, C. G., and REYNOLD, J. M., 1964, *Phys. Rev.*, **133**, A141.
SAITO, Y., 1964, *J. Phys. Soc. Japan*, **19**, 1319.
SAUNDERS, G. A., MIZIUMSKI, C., COOPER, G. S., and LAWSON, A. W., 1965, *J. Phys. Chem. Solids*, **26**, 1299.
SHOENBERG, D., 1952, *Phil. Trans. Roy. Soc.* A, **245**, 1.
SONDHEIMER, E. H., 1952, *Proc. Phys. Soc.* A, **65**, 561.
SOULE, D. E., 1958, *Phys. Rev.*, **112**, 698.
WERNICK, J. H., HOBSTETTER, J. N., LOVELL, L. C., and DORSI, D., 1958, *J. Appl. Phys.*, **29**, 1013.
WHITE, G. K., 1959, *Experimental Techniques in Low-Temperature Physics* (Oxford: Clarendon Press), p. 163.
WILSON, A. H., 1953, *The Theory of Metals* (London: Cambridge University Press), p. 264.
WINDMILLER, L. R., 1966, *Phys. Rev.*, **149**, 472.
WINDMILLER, L. R., and PRIESTLEY, M. G., 1965, *Solid St. Commun.*, **3**, 199.

Galvanomagnetic properties of single-crystal antimony between 77 °K and 273 °K

Ö. ÖKTÜ and G. A. SAUNDERS

Department of Applied Physics, University of Durham

MS. received 7th August 1966, *in revised form* 19*th December* 1966

Abstract. Galvanomagnetic measurements as a function of temperature between 77 °K and 273 °K in single crystals of antimony are presented. Results are interpreted in terms of the two-carrier multi-valley band model to obtain carrier mobilities, densities and details of the nature of the Fermi surface. The temperature dependences of the mobilities of holes and electrons are found to be $T^{-1\cdot48}$ and $T^{-1\cdot42}$ respectively. Contrary to the usual assumption, the electrons are sited in pockets with a small angle of tilt (5°) away from the trigonal axis, while the extrema containing holes have a large tilt angle (24°). Carrier densities are almost independent of temperature, ranging from $3\cdot9 \times 10^{19}$ cm^{-3} at 77 °K to $4\cdot2 \times 10^{19}$ cm^{-3} at 273 °K for both electrons and holes. If, as recent work indicates, there are three pockets of electrons and six of holes, then at 273 °K each electron ellipsoid contains $1\cdot4 \times 10^{19}$ electrons/cm^3 and each hole pocket $0\cdot7 \times 10^{19}$ holes/cm^3.

1. Introduction

Antimony is a semimetal. The crystal structure is rhombohedral (R3m) with two pentavalent atoms in each unit cell. The fifth Brillouin zone overlaps the sixth: about 10^{-3} electrons/atom spill over into the conduction band to leave an equal number of holes in the valence band. Carrier populations are degenerate and effective masses low. These features dominate the transport properties, the present concern.

In semimetals with low carrier densities ellipsoidal Fermi surfaces are the rule. Antimony is not an exception. The hole and electron surfaces can be described by two sets of closed, somewhat warped, prolate ellipsoids that enclose only a small part of the total Brillouin zone volume. Recently the number and arrangement of these surfaces have been a subject of some conjecture. Certainly, in the most probable configuration, the ellipsoids lie in the set of three trigonal–bisectrix planes exemplified by TZLNUXΓ in the Brillouin zone illustrated in figure 1. Symmetry requires that each ellipsoid be orientated, as shown in figure 2, with one principal axis coincident with the binary axis while the other two lie in the mirror plane. In each band there are either three or six ellipsoids. Development and experimental verification of this model of the Fermi surface have followed from extensive studies, among others, of the de Haas–van Alphen effect (Shoenberg 1952, Saito 1964, Windmiller and Priestley 1965), the de Haas–Shubnikov effect (Ketterson and Eckstein 1963, Rao *et al.* 1964), cyclotron resonance (Datars and Dexter 1961, Datars and Vanderkooy 1964) and ultrasonic attenuation (Eriksson *et al.* 1964).

One major distinguishing feature between the two families of ellipsoids is the angle of tilt (ψ), away from the trigonal axis ΓT in figure 1 towards the bisectrix axis ΓN, of one of the principal ellipsoid axes in the mirror plane. In the yz plane rotation from the trigonal axis towards the bisectrix axis can be taken either through the point X or through the point L, rotations by identical amounts not being equivalent. Therefore, to avoid ambiguity, the sense of the tilt angles must be defined through specification of the direction of this rotation. Experimentally this is made easier from back-reflection Laue photographs taken along the bisectrix axis: the direction ΓL shows as a prominent pseudo-trigonal point in the mirror plane and the direction ΓX is readily found from the pseudo-fourfold point. The symmetry properties have been detailed extensively by Windmiller (1966), who defined the tilt angles in the sense of rotation away from the trigonal axis ΓT towards ΓX, to analyse his de Haas-van Alphen data. In contrast, during the present work, we have defined the angles of tilt in the sense of a rotation away from the trigonal axis ΓT

through ΓL towards ΓN. Tilt angles have usually been referred to the angle between the bisectrix axis and the major ellipsoid axis 2′ in the yz plane; for an ellipsoidal model this is equivalent to our definition of tilt as the angle between the trigonal axis and the minor ellipsoidal axis 3′, as shown in figure 2. Wherever pertinent, data of other workers have been transformed to fit our definition.
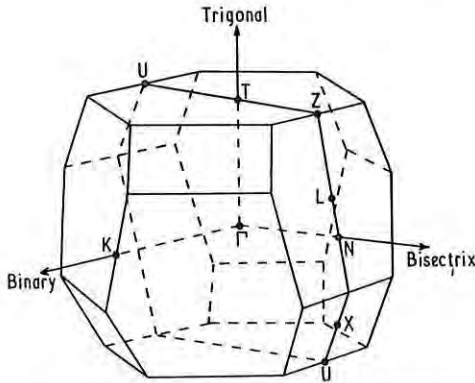
Figure 1. The Brillouin zone for antimony, showing those points of symmetry, in standard notation, prerequisite to the positioning of the Fermi surface extrema.
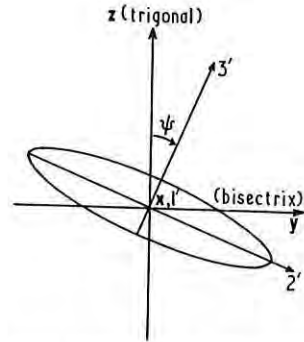
Figure 2. Cross section of an ellipsoid surface in the trigonal–bisectrix plane to illustrate the orientation relative to the crystal axes of the axes (1′, 2′, 3′) of the principal ellipsoid. The binary axis of the crystal coincides with the 1′ ellipsoid axis. The angle ψ refers to rotation away from the trigonal axis in the quadrant containing ΓT, ΓL and ΓN.

Two types of pockets occur, a set with a large tilt angle (about 35°) first observed by Shoenberg (1952) and another with a tilt angle close to 0°. Little evidence is available to assign the electrons and holes to these two sets. Previously Shoenberg's carriers have been alluded to as electrons. Experimental measurements of the Hall coefficient and the Seebeck effect, both positive in sign, should allow direct discrimination between the carriers. However, the Seebeck coefficient data of antimony cannot be fitted by the two-band model, if it is assumed that the highly tilted ellipsoids contain electrons (Saunders *et al.* 1965).

Freedman and Juretschke (1961) and Epstein and Juretschke (1963) have determined the low-field galvanomagnetic coefficients of antimony at room temperature. Results were interpreted in terms of a nine-parameter multi-valley model of the Fermi surface with tilt angles ψ_e and ψ_h for the electron and hole ellipsoids respectively. The other parameters are the total carrier densities, assumed equal for both sets of carriers, and the mobilities μ_i and ν_i of electrons and holes respectively. Here $i (= 1', 2', 3')$ defines the directions along the principal axes of one representative ellipsoid, as illustrated in figure 2, direction '1″ being along a binary axis while directions '2″ and '3″ lie in the mirror plane.

In the present work systematic measurements have been completed between 77 °K and 273 °K of all twelve components of the magnetoresistivity tensor to second order in the magnetic field. Results are interpreted in terms of the ellipsoid model of the Fermi surface. There were two principal objectives—firstly, to clarify the tilt angle situation, and, secondly, to provide detailed information of the carrier transport processes in antimony. Thus the temperature dependences of carrier mobilities and densities for both holes and electrons are resolved.

2. Experimental design

In an anisotropic medium, such as antimony with point-group symmetry $R\bar{3}m$, the fundamental equation for the conduction of electricity in a magnetic field $\mathbf{H}$ is the generalized form of Ohm's law relating the current density $\mathbf{J}$ to the applied field $\mathbf{E}$:

$$J_i = \sigma_{ij}(\mathbf{H})E_j \quad \text{or} \quad E_i = \rho_{ij}(\mathbf{H})J_j \tag{1}$$

where the resistivity tensor $\rho_{ij}(\mathbf{H})$ is the reciprocal of the conductivity tensor $\sigma_{ij}(\mathbf{H})$; both are general functions of $\mathbf{H}$ and obey the Onsager relation. When the effects of crystal symmetry on Hall coefficients and magnetoresistance are being studied, it is necessary to resort to a phenomenological treatment by expanding the resistivity tensor components in terms of rapidly converging series of increasing powers of the magnetic field H. For terms up to second order in H, Juretschke (1955) represents this expansion as

$$\rho_{11} = \rho_{11}{}^0 + A_{11}H_1{}^2 + A_{12}H_2{}^2 + A_{13}H_3{}^2 - 2A_{24}H_2H_3$$
$$\rho_{22} = \rho_{11}{}^0 + A_{12}H_1{}^2 + A_{11}H_2{}^2 + A_{13}H_3{}^2 + 2A_{24}H_2H_3$$
$$\rho_{33} = \rho_{33}{}^0 + A_{31}H_1{}^2 + A_{31}H_2{}^2 + A_{33}H_3{}^2$$
$$\rho_{23} = R_{231}H_1 - A_{42}H_1{}^2 + A_{42}H_2{}^2 + 2A_{44}H_2H_3 \tag{2}$$
$$\rho_{31} = R_{231}H_2 + 2A_{44}H_3H_1 - 2A_{42}H_1H_2$$
$$\rho_{12} = R_{123}H_3 - 2A_{24}H_3H_1 + (A_{11} - A_{12})H_1H_2$$

the remaining components of $\rho_{ij}(\mathbf{H})$ being obtainable from the Onsager relation

$$\rho_{ij}(\mathbf{H}) = \rho_{ji}(-\mathbf{H}).$$

Antimony then has twelve independent, isothermal, galvanomagnetic coefficients to second order in the magnetic field, there being two resistivity components $\rho_{11}{}^0$ and $\rho_{33}{}^0$, two Hall coefficients R_{231} and R_{123}, taken as the negatives of the conventionally defined Hall coefficients, and eight magnetoresistance coefficients A_{11} (the short notation for $\rho_{11,11}$), $A_{12}(\rho_{11,22})$, $A_{13}(\rho_{11,33})$, $A_{31}(\rho_{33,11})$, $A_{44}(\rho_{23,23})$, $A_{24}(\rho_{22,23})$, $A_{33}(\rho_{33,33})$ and $A_{42}(\rho_{23,22})$. These coefficients are defined conveniently with respect to the usual orthogonal coordinate system used for the trigonal semimetals Bi, Sb and As, having 1 along the binary (x) axis, 2 along the bisectrix (y) axis and 3 along the trigonal (z) axis.

These twelve components of the resistivity tensor, previously determined by Freedman and Juretschke (1961) and Epstein and Juretschke (1963) at room temperature, have been measured as a function of temperature during the present work. There are a number of possible alternatives for estimating the tensors when working with samples of rectangular cross section. The experimental configurations used, illustrated in figure 3, are based
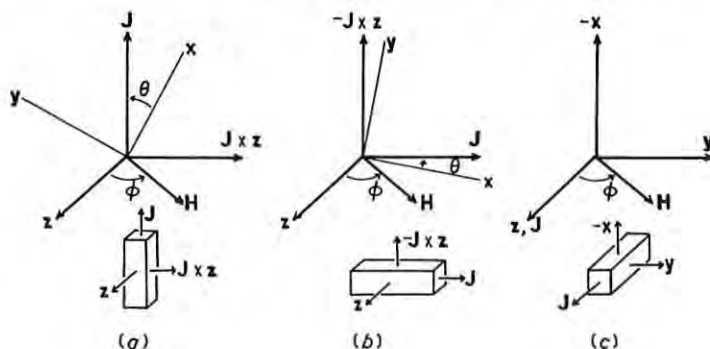
Figure 3. The specimen configurations relative to the directions of the current and the applied magnetic field used in the experimental determination of the magneto-resistivity tensor coefficients. The magnetic field direction was fixed and the samples were rotated about the vertical axis. The angle θ is that between the current direction and the binary axis, and the angle ϕ is that between the direction of the magnetic field and the trigonal axis.

upon those described by Epstein and Juretschke (1963) who obtained all the coefficients from two differently oriented, single-crystal rods. However, one difference in the present work is that the crystals were rotated in the magnetic field rather than the magnet itself being rotated and it was found that a set of three crystals was convenient. Overlap occurs: most coefficients have been measured twice for each set. Two complete sets of readings

were made on two independent groups of samples. Pertinent equations (3), (4) and (5) from Epstein and Juretschke (1963) were used to calculate the magnetoresistivity coefficients from the experimental data.

3. Crystal growth and experimental details

Square-sectioned (0·25 cm × 0·25 cm) single-crystal rods up to 10 cm long were grown in a nitrogen atmosphere from 99·9999% purity, zone-refined antimony by a method due to Epstein (1962). Precast rods were seeded in the crystallographic directions prerequisite for the measurements. Furnace and crucible were kept stationary. The separable partly enclosed crucible was made from three long (15 cm), thin (0·25 cm), baked, pyrophyllite slats held rigidly together so as to leave a square-sectioned channel to contain the antimony. The furnace was constructed from two concentric clear quartz tubes with Kanthal wire wound loosely spaced on the inner tube to develop a temperature gradient of up to 5 degc cm^{-1} along the axis. The precast antimony rod, cleaned by etching with CP4 and subsequent washing with distilled water, was placed in the crucible channel and covered, save for about 2 mm exposed to view at the 'cooler' end, with a loose, light, pyrophyllite lid. A single-crystal seed, accurately orientated from Laue back-reflection photographs and cut by spark erosion to be a snug fit in the groove, was placed about 1 cm from the exposed end of the rod. This seed was of sufficient size to allow about 2 mm of it to melt, yet leave enough solid to maintain orientation; should the seed be too small, the melt surface tension would tend to displace it. The furnace temperature was slowly increased while the protruding end of the melt was observed. About 500 w sufficed to melt the antimony (melting point 630 °c). At the instant when the exposed end melted, the seed was pushed along the groove up to the molten metal. Surface tension rounded the melt beyond the edge of the roof, and, to preserve seed orientation, the blob size was kept to a minimum by pushing the seed just into contact with the melt so that surface tension drew the melt over the seed face. If the seed was pushed right into the melt, orientation was lost. When about 2 mm of the seed had melted, the furnace power was sharply reduced so as to sweep the temperature gradient along the rod. The growth rate was about 5 cm min^{-1}. To delineate any grain structure, the rods, when cold, were chemically polished with a solution composed of 1 part HF, 3 parts concentrated HNO$_3$, 12 parts glacial acetic acid and a few drops of bromine.

As evidenced by lack of splitting of the spots on back-reflection Laue photographs, relatively unstrained crystals were obtained. Crystals were etched with CP4 etching reagent. The number of dislocation etch pits on the mirror-like, (111) cleavage planes were of the order of 10^4 cm^{-2} in accord with the results obtained by Wernick *et al.* (1958) for zone-refined crystals. Specimens showing low-angle grain boundaries on the (111) plane were discarded.

Specimens were orientated to within 1° of the required direction, trimmed with a spark erosion cutter into true rectangular parallelopipeds 2·5 cm long and mounted on, but insulated from, a flat face machined into the heavy copper cylinder employed as the sample holder. A kinematic adjustment of this sample holder with respect to the axis of the supporting stainless-steel rod allowed final accurate specimen alignment in the magnetic field through magnetoresistance measurements. The collinear cylinder and support rod axes defined the rotation axis of the sample. Current leads were soldered to the crystal ends. Two sets of three voltage probes of enamelled, 36 gauge, copper wire were spot welded to each pair of opposite faces. To prevent end effects, distances between voltage probes on the same face were kept to within the central third of each sample. The cryostat, designed specifically to avoid spurious thermal e.m.f.'s in the leads, consisted of a double-walled, German silver Dewar, with a brass tail to facilitate heat transfer, placed inside an outer glass Dewar filled with liquid nitrogen. For measurements at 139 °K and 183 °K the samples, sited in the metal Dewar, were immersed in the non-flammable, five-component, organic liquid mixture of 14·5% chloroform, 25·3% methylene chloride, 33·4% ethyl bromide, 10·4% transdichloroethylene and 16·4% trichloromethylene which remains liquid to below 130 °K (White 1959). Because this mixture develops an appreciable conductivity above about 200 °K, if left standing in contact with current-carrying metals, normal hexane was used as the liquid bath at 225 °K and 273 °K. Direct immersion of the

sample in the cryogenic liquid served a dual purpose. Isothermal conditions were attained; temperature gradients in the sample were reduced below 0·1 degK, making thermomagnetic effects negligible. Also the large volume of the liquid sealed within the metal Dewar facilitated control of temperature to better than 0·05 degK over long intervals. A standard vacuum system was used to pump the metal Dewar interspace, the bath temperature being controlled by adjustment of the interspace pressure through a needle valve and fine control achieved by electrical heating. Temperature was read from calibrated copper–constantan thermocouples adjacent to the sample.

Potential measurements were made using a precision potentiometer, a galvanometer preamplifier and a galvanometer, capable of definition down to 10^{-8} v following extrapolation procedures beyond 10^{-7} v. Although measurements were carried through at the former accuracy, they are only quoted to 10^{-7} v. Sample current densities, up to 75 A cm^{-2}, were kept constant to better than 1 part in 10^4 through a separate potentiometric system monitoring across a 0·01 Ω standard resistance.

All potential measurements were made under standard reversal conditions of the current and the magnetic field. Magnetoresistivity measurements were made for magnetic fields up to 3000 Oe at 77 °K and up to 5000 Oe at 273 °K. In general the angle ϕ (see figure 3) was chosen so that only one coefficient up to H^2 contributed to the measured voltages. Each magnetoresistance coefficient was determined as the intercept, from the linear region at low magnetic fields, on the graph of the average value of $\{V(H)-V(0)\}/dJH^2$ for both magnetic field directions ($\pm H$) plotted against H^2. Here, d is the distance between the potential probes, J is the current density and $V(H)$ and $V(0)$ are the measured potentials in or out of the magnetic field respectively. A specimen set of results is illustrated in figure 4 by reference to the coefficient A_{11}. At higher magnetic fields the curves evidence a contribution, particularly at lower temperatures, of higher-order coefficients. Similarly the Hall coefficients R_{123} and R_{231} were estimated as the intercept of the plot of V_H/tJH
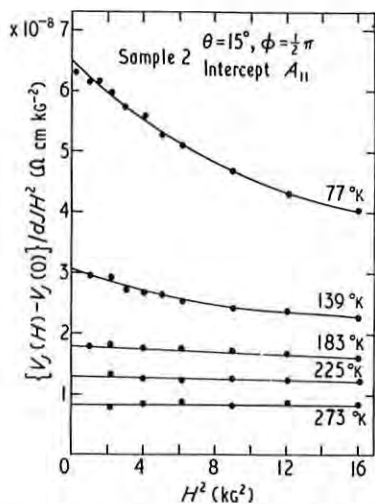
Figure 4. To illustrate a typical determination of a magnetoresistivity coefficient, in this case A_{11}. This graph shows the temperature and magnetic field dependence of the magneto-resistivity. The experimental configuration is that shown in figure 3(b) with ϕ equal to $\frac{1}{4}\pi$.
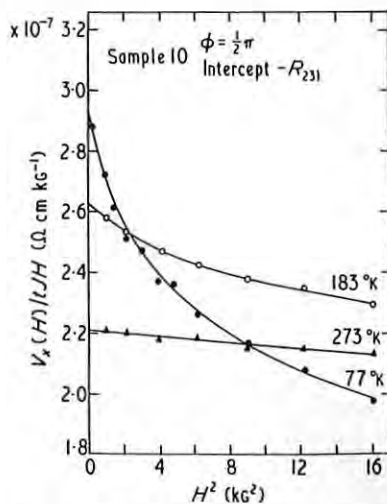
Figure 5. To illustrate a typical determination of a Hall coefficient ($-R_{231}$) at different temperatures. In this instance the experimental configuration is that of figure 3(c) with ϕ equal to $\frac{1}{4}\pi$.

against H^2, the Hall voltage V_H being the average of the four $\pm H \pm J$ values. Results are exemplified by reference to the coefficient R_{231} in figure 5. In all cases the curves in the linear region were fitted by the method of least squares. All coefficients were determined as the mean of measurements of angles ϕ and $\phi + \pi$.

4. Experimental results

In table 1 are presented the average values of data obtained from several specimens of the magnetoresistivity coefficients ρ_{ij}, R_{ijk} and A_{ij} as a function of temperature. The Hall

Table 1. Experimental values of the magnetoresistivity tensor components of antimony between 77 °K and 273 °K

Temp. (°K)	Resistivity		Hall		Magnetoresistivity							
	ρ_{11}	ρ_{33}	$-R_{123}$	$-R_{231}$	A_{11}	A_{12}	A_{13}	A_{31}	A_{33}	$-A_{44}$	A_{42}	A_{24}
273	41·3	31·7	2·47	2·22	8·35	21·0	6·1	13·6	2·2	1·8	2·4	3·4
225	31·5	24·0	2·69	2·42	12	30·8	8·3	18	3·1	2·1	3·2	6·0
183	23·8	18·0	2·88	2·62	18·3	42·5	12·1	25·5	4·5	3·0	4·5	7·8
139	16·5	12·2	3·09	2·80	30·5	64·4	18·6	38·5	7·0	5·3	6·5	12·7
77	7·15	5·27	3·43	3·0	63·5	151	45·2	91	16·6	13·5	16·5	30
Estimated error (%)	3	6	5	5	7	7	7	7	15	20	20	20

Units: resistivity, $10^{-6}\,\Omega$ cm; Hall coefficients, $10^{-7}\,\Omega$ cm kG^{-1}; magnetoresistivity, $10^{-9}\,\Omega$ cm kG^{-2}.

coefficients, as measured, are positive. The crystallographic binary and bisectrix axes, and hence the signs of A_{42} and A_{24}, cannot be uniquely defined: these two coefficients change sign on the transformation $\theta \to \theta + \frac{1}{3}n\pi$, where n can be 1, 3, 5, etc. But, for a particular choice of axes, both have the same sign. In the right-handed Cartesian coordinate system defined by rotation in the yz plane away from the trigonal axis through the pseudo-trigonal point towards the bisectrix axis, A_{42} and A_{24} turn out from the experiments to have positive signs. All the other A_{ij} except A_{44} are positive. Marked anisotropy of the magnetoresistivity is evident. But the anisotropy ratios ρ_{11}/ρ_{33}, R_{123}/R_{231} and $A_{ij}/A_{i'j'}$ remain reasonably constant throughout the temperature range.

Maximum errors on these results were calculated from the spread of values from different specimens. When the results are extrapolated to room temperature, reasonable agreement is found with the data of Epstein and Juretschke (1963). While the magnetoresistivity tensor coefficients are the measured quantities, theory is concerned with the magnetoconductivity tensor components obtainable from the relations derived by Juretschke (1955).

$$\sigma_{11} = \frac{1}{\rho_{11}}, \qquad \sigma_{33} = \frac{1}{\rho_{33}}$$

$$P_{123} = \frac{R_{123}}{\rho_{11}^2}, \qquad P_{231} = \frac{R_{231}}{\rho_{11}\rho_{33}}$$

$$B_{11} = \frac{A_{11}}{\rho_{11}^2}, \qquad B_{33} = \frac{A_{33}}{\rho_{33}^2}$$

$$B_{24} = \frac{A_{24}}{\rho_{11}^2}, \qquad B_{42} = \frac{A_{42}}{\rho_{11}\rho_{33}} \tag{3}$$

$$B_{12} = \frac{A_{12}}{\rho_{11}^2} + \frac{R_{231}^2}{\rho_{11}^2\rho_{33}}, \qquad B_{13} = \frac{A_{13}}{\rho_{11}^2} + \frac{R_{123}^2}{\rho_{11}^3}$$

$$B_{31} = \frac{A_{31}}{\rho_{33}^2} + \frac{R_{231}^2}{\rho_{11}\rho_{33}^2}, \qquad B_{44} = \frac{A_{44}}{\rho_{11}\rho_{33}} - \frac{1}{2}\frac{R_{123}R_{231}}{\rho_{11}^2\rho_{33}}.$$

Results are shown in table 2. For all the magnetoconductivity tensor coefficients B_{ij}, plots of log B_{ij} against log T are found to be straight lines with slopes lying between $-4\cdot2$ and $-4\cdot4$; this indicates similar temperature dependences close to $T^{-1.5}$ for all the carrier mobilities, as is confirmed by the detailed calculations presented in the next section.

6

Table 2. Magnetoconductivity tensor components

Temp. (°K)	Conductivity		Inverse Hall		Magnetoconductivity							
	σ_{11}	σ_{33}	$-P_{123}$	$-P_{231}$	B_{11}	B_{12}	B_{13}	B_{31}	B_{33}	$-B_{44}$	B_{42}	B_{24}
273	2·42	3·15	1·45	1·70	0·49	1·32	0·44	1·47	0·22	0·19	0·18	0·19
225	3·17	4·16	2·71	3·20	1·20	3·35	1·07	3·45	0·54	0·42	0·42	0·60
183	4·20	5·56	5·08	6·12	3·23	8·20	2·75	8·76	1·38	1·07	1·05	1·38
139	6·06	8·20	11·4	13·9	11·2	26·0	8·96	29·0	4·7	3·9	3·2	4·6
77	13·9	18·9	67·1	79·5	124	329	120	374	59·9	54·9	43·7	58·7

Units: conductivity, $10^4 \, \Omega^{-1} \, cm^{-1}$; inverse Hall coefficients, $10^2 \, \Omega^{-1} \, cm^{-1} \, kG^{-1}$; magnetoconductivity, $10 \, \Omega^{-1} \, cm^{-1} \, kG^{-2}$.

5. Calculations

In the absence of intravalley scattering, the magnetoconductivity tensor components of a semimetal of crystal class R3m with a many-valley band structure, as described in § 1, are related to the principal carrier mobilities μ_i and ν_i (where i is 1′, 2′, 3′) of electrons and holes respectively by the set of equations (Drabble and Wolfe 1956, Freedman and Juretschke 1961)

$$2\sigma_{11} = Ne\{(\mu_1 + \alpha_1{}^2\mu_2 + \beta_1{}^2\mu_3) + (\nu_1 + \alpha_2{}^2\nu_2 + \beta_2{}^2\nu_3)\}$$

$$\sigma_{33} = Ne\{(\beta_1{}^2\mu_2 + \alpha_1{}^2\mu_3) + (\beta_2{}^2\nu_2 + \alpha_2{}^2\nu_3)\}$$

$$-2cP_{231} = Ne[\{\nu_2\nu_3 + \nu_1(\beta_2{}^2\nu_2 + \alpha_2{}^2\nu_3)\} - \{\mu_2\mu_3 + \mu_1(\beta_1{}^2\mu_2 + \alpha_1{}^2\mu_3)\}] \quad (4a)$$

$$-cP_{123} = Ne[\{\nu_1(\alpha_2{}^2\nu_2 + \beta_2{}^2\nu_3)\} - \{\mu_1(\alpha_1{}^2\mu_2 + \beta_1{}^2\mu_3)\}].$$

The rest of the equations are written more conveniently by including only the contributions from electrons, those from the holes being identical in form and simply added on:

$$2c^2B_{13} = Ne(\mu_1 + \alpha_1{}^2\mu_2 + \beta_1{}^2\mu_3)\{\mu_1(\alpha_1{}^2\mu_2 + \beta_1{}^2\mu_3)\}$$

$$2c^2B_{31} = Ne(\beta_1{}^2\mu_2 + \alpha_1{}^2\mu_3)\{\mu_2\mu_3 + \mu_1(\beta_1{}^2\mu_2 + \alpha_1{}^2\mu_3)\}$$

$$-2c^2B_{44} = Ne(\beta_1{}^2\mu_2 + \alpha_1{}^2\mu_3)\{\mu_1(\alpha_1{}^2\mu_2 + \beta_1{}^2\mu_3)\}$$

$$c^2(3B_{12} - B_{11} - 2B_{44}) = Ne(\mu_1 + \alpha_1{}^2\mu_2 + \beta_1{}^2\mu_3)\{\mu_2\mu_3 + \mu_1(\beta_1{}^2\mu_2 + \alpha_1{}^2\mu_3)\} \quad (4b)$$

$$8c^2B_{11} = Ne\{\beta_1{}^2\mu_2(\mu_1 - \mu_3)^2 + \alpha_1{}^2\mu_3(\mu_1 - \mu_2)^2 + 3\alpha_1{}^2\beta_1{}^2\mu_1(\mu_2 - \mu_3)^2\}$$

$$8c^2B_{12} = Ne\{3\beta_1{}^2\mu_2(\mu_1{}^2 + \mu_3{}^2) + 3\alpha_1{}^2\mu_3(\mu_1{}^2 + \mu_2{}^2) + \alpha_1{}^2\beta_1{}^2\mu_1(\mu_2 - \mu_3)^2$$
$$+ 2\mu_1\mu_2\mu_3\}$$

$$2c^2B_{33} \equiv c^2(-B_{12} + 3B_{11} - 2B_{44}) = 2Ne\alpha_1{}^2\beta_1{}^2\mu_1(\mu_2 - \mu_3)^2$$

$$4c^2B_{24} = Ne\alpha_1\beta_1\mu_1(\mu_2 - \mu_3)(-\mu_1 + \alpha_1{}^2\mu_2 + \beta_1{}^2\mu_3)$$

$$4c^2B_{42} = Ne\alpha_1\beta_1(\mu_2 - \mu_3)\{\mu_2\mu_3 - \mu_1(\beta_1{}^2\mu_2 + \alpha_1{}^2\mu_3)\}.$$

Here the carrier densities N of holes and electrons are assumed equal and α and β are the cosine and sine of the tilt angles ψ_e and ψ_h. These equations can be referred to both rotation systems in the yz plane; the set of operations $\alpha \rightleftarrows \beta$, $\mu_2 \rightleftarrows \mu_3$, $\nu_2 \rightleftarrows \nu_3$ correspond to transformation from one rotation system to the other, the only variation in the equations being simultaneous changes of sign of B_{24} and B_{42}. As the contribution from each pocket is additive, the equations apply equally to a three- or six-ellipsoid model for each carrier species, in the latter case the number of carriers in each pocket simply being halved. Plausibly the requirement of an isotropic relaxation time may be relaxed somewhat and the relaxation time written as a tensor, each component being a separate function of energy (Herring and Vogt 1956). Therefore

$$\mu = e\tau/m^*. \quad (5)$$

Equivalent results to those in equation (4) are extant because the only change is the replacement of τ/m^* by $\boldsymbol{\tau}/\mathbf{m}^*$ in the Boltzmann equation. When $\boldsymbol{\tau}$ is not too anisotropic, this

approach is a good approximation; certainly it follows when the magnitudes of the tensor components differ by as much as a factor of 2.

To calculate the band and mobility parameters denoted by N, ψ_e, ψ_h, μ_i and ν_i the experimentally determined magnetoconductivity tensor coefficients presented in table 2 were inserted into the set of equations (4). An exact solution cannot be obtained; therefore, somewhat along the lines followed by Freedman and Juretschke (1961), a computer (Elliot 803) was programmed to produce self-consistent fits to the experimental data. By transforming to new variables, some of the equations (4) can be rewritten in simpler form to obtain two sets of four equations in ten variables. Two of these variables, namely N, the number of carriers, and f, which is defined by the equations

$$\mu_1 + \mu_2 + \mu_3 = fs$$
$$\nu_1 + \nu_2 + \nu_3 = (1-f)s \qquad (6)$$
$$s = \frac{2\sigma_{11} + \sigma_{33}}{eN}$$

are chosen arbitrarily. Four distinct acceptable types of solution, denoted by A, B, C and D arise, each over a narrow range of values for f and N. To check each solution the magneto-conductivity coefficients were recalculated from the band and mobility parameters and compared with the experimental values. In particular extensive calculations for all solutions were performed for the data obtained at 183 °K to assist in the determination of the best solution. Overall fits for the magnetoconductivity coefficients were so poor for solutions of types A and B, having tilt angles for the best fit of $\psi_e = 4°$, $\psi_h = 62°$ and $\psi_e = 52°$,

Table 3. Calculated band parameters of antimony for solution type C ($f = 0.420$)

Temp. (°K)	273	225	183	139	77
N	4·13	3·90	3·78	3·70	3·60
μ_1	0·11	0·10	0·11	0·19	0·37
μ_2	1·54	1·86	2·37	3·43	7·66
μ_3	3·43	5·13	7·20	10·7	26·1
ψ_e	59°	51°	51°	52°	52°
ν_1	3·60	5·42	7·20	10·1	23·6
ν_2	0·26	0·28	0·39	0·77	2·20
ν_3	3·15	4·06	5·80	8·96	21·3
ψ_h	23°	23°	23°	23°	23°

Units: N, 10^{19} cm^{-3}; mobilities, 10^3 cm^2 v^{-1} sec^{-1}.

Table 4. Calculated band parameters of antimony for solution type D

Temp. (°K)	273	225	183	139	77
N	4·22	4·12	4·00	3·92	3·86
f	0·405	0·397	0·390	0·387	0·385
μ_1	2·74	3·34	4·59	6·91	16·2
μ_2	0·11	0·09	0·10	0·17	0·38
μ_3	1·95	2·90	3·81	5·46	12·6
ψ_e	3°	5°	6°	6°	5°
ν_1	3·63	5·34	7·20	10·2	23·6
ν_2	0·18	0·33	0·26	0·44	1·70
ν_3	3·22	3·93	5·83	9·16	21·4
ψ_h	24°	22°	24°	24°	24°

Units: N, 10^{19} cm^{-3}; mobilities, 10^3 cm^2 v^{-1} sec^{-1}.

Table 5. Comparison of the recalculated magnetoconductivity tensor components for solution type D with the experimental values

	273 °K Calc.	273 °K $\frac{\text{Calc.}}{\text{Exp.}}$	225 °K Calc.	225 °K $\frac{\text{Calc.}}{\text{Exp.}}$	183 °K Calc.	183 °K $\frac{\text{Calc.}}{\text{Exp.}}$	139 °K Calc.	139 °K $\frac{\text{Calc.}}{\text{Exp.}}$	77 °K Calc.	77 °K $\frac{\text{Calc.}}{\text{Exp.}}$
σ_{11}	2·41	0·99	3·17	1·00	4·19	0·99	6·05	0·99	13·9	1·00
σ_{33}	3·15	1·00	4·16	1·00	5·55	0·99	8·20	1·00	18·9	1·00
$-P_{123}$	1·44	0·99	2·70	0·99	5·08	1·00	11·3	0·99	67·0	1·00
$-P_{231}$	1·69	0·99	3·19	0·99	6·12	1·00	13·9	1·00	79·5	1·00
B_{11}	0·49	1·02	1·16	0·96	3·24	1·00	10·2	0·91	120	0·97
B_{12}	1·37	1·04	3·43	1·02	8·50	1·04	26·7	1·02	339	1·03
B_{13}	0·38	0·87	0·95	0·89	2·40	0·87	7·85	0·88	106	0·89
B_{31}	1·33	0·90	3·14	0·91	7·88	0·90	26·3	0·90	340	0·91
B_{33}	0·30	1·40	0·56	1·04	2·02	1·45	7·01	1·48	78·6	1·31
$-B_{44}$	0·24	1·30	0·53	1·28	1·41	1·31	4·98	1·27	68·2	1·24
B_{42}	0·18	1·00	0·38	0·91	1·22	1·16	4·13	1·28	47·5	1·08
B_{24}	0·21	1·08	0·53	0·89	1·55	1·13	4·75	1·02	54·1	0·92

Units: σ, $10^4\ \Omega^{-1}\ \text{cm}^{-1}$; P, $10^2\ \Omega^{-1}\ \text{cm}^{-1}\ \text{kG}^{-1}$; B, $10\ \Omega^{-1}\ \text{cm}^{-1}\ \text{kG}^{-2}$.

$\psi_{\text{h}} = 58°$ respectively, that they were deemed unacceptable. Furthermore, there is no evidence from the numerous Fermi surface studies in antimony to justify such tilt angles; this is true also for solution C. But good fits were obtained through the temperature range for solutions C, shown in table 3, and D (see table 4). For the solution D, the true physical answer, the fit, demonstrated in table 5, was excellent; at all temperatures ψ_{h} is 24° while ψ_{e} is close to 5°. The excellent agreement between the tilt angles at different temperatures is remarkable. For reasons clarified in the next section, recalculations were made to attempt, within the limits of experimental error, extension of the tilt of the hole pockets towards the Shoenberg (1952) value of 36°; these were unsuccessful.

We refer the solution D to the rotational system in the yz plane taken from the trigonal axis through ΓL; the calculated values of B_{24} and B_{42}, in agreement with the experimental data for A_{24} and A_{42}, are positive. Thus, the fit is consistent in the quadrant containing ΓT, ΓL and ΓN. Tilt angles correspond to the direction of largest carrier mobility in the yz plane and, hence, to the minor axis 3′ of a Fermi ellipsoid, as illustrated in figure 2. The result is in agreement with that of Falicov and Lin (1966) and that of Windmiller (1966) for both tilt angles, if we take into account our rather low angle of tilt for the hole ellipsoid: the sum of the tilt angles from the two rotational systems is about 90°. Furthermore, the mobilities, equal to $e\tau/m^*$, compare qualitatively along each ellipsoid axis with the effective mass data of Windmiller; thus, the largest mobilities lie along the equivalent direction with the lowest effective mass.

Some light is shed on the possible presence of a third set of carriers by the self-consistency of solution D over the temperature range. Recent work, particularly on cyclotron resonance (Datars and Vanderkooy 1964), the de Haas–van Alphen effect (Windmiller and Priestley 1965) and ultrasonic attenuation (Eriksson *et al.* 1964) has produced no evidence for such carriers. If, as postulated by Hall and Koenig (1964), low-mobility heavy holes are present in antimony, then the population ratio in the two valence bands would be a function of temperature—an effect which would distort the values of the tilt angles and carrier densities. This is not observed. Minority carriers can play at most a minimal role in transport process over the temperature range 77–273 °K.

No physically acceptable solutions were obtained for the model with electrons in pockets with large tilt angles and holes in extrema with small tilt angles. A special computer programme was written to allow diligent search and verification of this most important point.

The carrier densities calculated in solution D (see table 4) are in agreement with those obtained by other methods and reproduced in table 6. Carrier density is essentially temperature independent, as would be expected from the comparatively high degeneracy temperatures of 940 °K for electrons and 1430 °K for holes estimated from the Fermi energy data tabulated by Rao *et al.* (1964).

Table 6. Carrier densities in antimony

Reference	Carrier density (cm^{-3})	Temperature ($^\circ$K)
Eriksson *et al.* 1964	$N_e = 4\cdot2 \times 10^{19}$	1·5
	$N_h = 4\cdot4 \times 10^{19}$	1·5
Epstein and Juretschke 1963	$N_e = N_h = 4\cdot3 \times 10^{19}$	293
Ketterson and Eckstein 1963	$N_e = N_h = 4\cdot07 \times 10^{19}$	1·15
Rao *et al.* 1964	$N_e = N_h = 5\cdot05 \times 10^{19}$	4·2
Present work	$N_e = N_h = 4\cdot22 \times 10^{19}$	273
(solution D)	$= 4\cdot12 \times 10^{19}$	225
	$= 4\cdot00 \times 10^{19}$	183
	$= 3\cdot92 \times 10^{19}$	139
	$= 3\cdot86 \times 10^{19}$	77
Windmiller and Priestley 1965	$N_e = N_h = 5\cdot5 \times 10^{19}$	1·26

The temperature dependences of the carrier mobilities μ_1 and μ_3, which together with μ_2 should be equal, as a result of the assumptions made in the development of the set of equations (4), are plotted from solution D in figure 6. Similarly the hole mobilities are
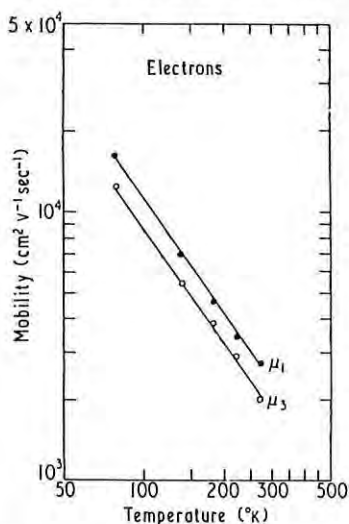

Figure 6. The temperature dependence of the electron mobility along the 1′ and 3′ directions of the electron ellipsoids, obtained from solution D.
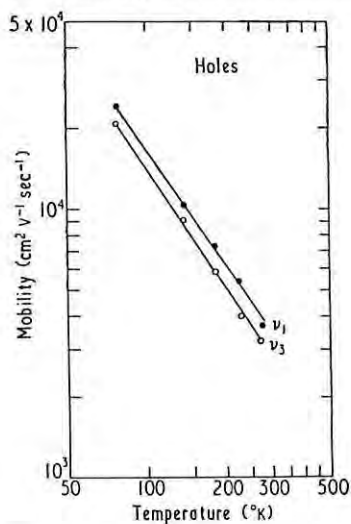

Figure 7. The temperature dependence of the hole mobility along the 1′ and 3′ directions of the hole ellipsoids, obtained from solution D.

illustrated in figure 7. Both sets of carriers have almost identical temperature dependences of mobility ($T^{-1\cdot42}$ for electrons and $T^{-1\cdot48}$ for holes). Very similar results (about $T^{-1\cdot5}$ for both hole and electron mobilities) were obtained for solution C: certainly, whichever solution is correct, the temperature dependences for both hole and electron mobilities in antimony are close to $T^{-1\cdot5}$. We proceed now to a brief discussion of the carrier mobilities before returning in conclusion to the problem of the tilt angles.

6. Discussion

Carrier mobilities and densities are disclosed directly from the low-field galvano-magnetic effects. Furthermore, the carrier signs can be determined, and the carriers assigned to the correct set of ellipsoids.

The formal theory of conductivity (Wilson 1953) demonstrates that only long-wave-length acoustical branch phonons can scatter electrons in semimetals. The expression for the isotropic relaxation time τ given by Wilson for intravalley lattice scattering in a

degenerate semimetal reduces to the approximate form

$$\tau = aT^{-1}E^{-1/2} \tag{7}$$

where a is a constant. The present finding of a $T^{-1.5}$ law for scattering of both holes and electrons, together with the similar orders of magnitude of both electron and hole mobilities μ_i and ν_i, evidence, not surprisingly, similar scattering mechanisms for both types of carrier. The exponent may be compared with that of -2.1 for bismuth (Gallo *et al.* 1963) and -1.2 for single-crystal graphite (Soule 1958). In a semimetal the scattering power, the inverse of the relaxation time, should be proportional to the product of the phonon density and the carrier density of states. Now the first factor is proportional to temperature, and the second, a measure of the vacant sites available for occupancy by scattered carriers, depends upon the carrier density. The average density of states near the Fermi surface in semimetals has only a weak temperature dependence, although being constant in a metal and in an ideal semiconductor obeying a $T^{1/2}$ law. Thus for acoustic-mode intravalley scattering, a mobility temperature dependence closer to $T^{-1.0}$ would be expected. Further theoretical studies should clarify the situation and assess possible contributions from other mechanisms such as intervalley scattering, electron–hole collisions or two-phonon processes.

From a comparison of the effective mass tensor data of Datars and Vanderkooy (1964) and the diagonalized mobilities determined by the present authors, which are given in table 4, the carrier relaxation times have been estimated and are shown in table 7. Carrier signs assumed by Datars and Vanderkooy were inverted. These relaxation times are not highly anisotropic, and are an order of magnitude larger than those in metals at the same temperature. The carrier mean free paths $l\,(= u_{\mathrm{F}}\tau)$, about 1000 Å at 273 °K and about 6000 Å at 77 °K, are also rather longer than those in metals. For semimetals, in which the

Table 7. Relaxation times for electrons and holes in antimony calculated from the cyclotron effective masses (Datars and Vanderkooy 1964) and mobility data from solution D

Relaxation times	273 °K	225 °K	183 °K	139 °K	77 °K
Electrons					
τ_1	1·4	1·7	2·4	3·6	8·6
τ_2	0·7	0·6	0·7	1·1	2·5
τ_3	1·0	1·5	1·9	2·7	6·3
Holes					
τ_1	1·4	2·0	2·7	3·9	9·1
τ_2	1·0	1·7	1·4	2·3	8·9
τ_3	0·9	1·1	1·6	2·6	6·1

Relaxation times are quoted in units of 10^{-13} sec.

number of effective conduction electrons N_{eff} is small, Sondheimer (1952) has shown that, because only the longest-wavelength phonons scatter the carriers, the relaxation times and mean free paths should be larger than those in metals. Furthermore, the relaxation times, dependent upon the factor $4N_{\mathrm{eff}}^{-4/3}$, should decrease with increasing carrier concentration; this follows qualitatively through the sequence of semimetals, at 77 °K, for example, bismuth:

$$N_e = 4.6 \times 10^{17} \text{ cm}^{-3}, \qquad \tau_{\mathrm{av}} \sim 10^{-11} \text{ sec}$$

graphite:

$$N_e = 2.2 \times 10^{18} \text{ cm}^{-3}, \qquad \tau_{\mathrm{av}} \sim 2.0 \times 10^{-12} \text{ sec}$$

and antimony:

$$N_e = 3.9 \times 10^{19} \text{ cm}^{-3}, \qquad \tau_{\mathrm{av}} \sim 7 \times 10^{-13} \text{ sec}.$$

Now let us discuss the problem of the Fermi surface of antimony. Solution D is considered to be the true one. Certainly this solution gives the best fit throughout to the experimental galvanomagnetic data. Both the electron and hole mobilities can be compared with the cyclotron resonance effective masses to give reasonably isotropic relaxation times